DEVELOPMENT AND EVALUATION OF A VISCOELASTIC BOUNDARY ELEMENT METHOD TO PREDICT ASPHALT PAVEMENT CRACKING

By

BOONCHAI SANGPETNGAM

A DISSERTATION PRESENTED TO THE GRADUATE SCHOOL
OF THE UNIVERSITY OF FLORIDA IN PARTIAL FULFILLMENT
OF THE REQUIREMENTS FOR THE DEGREE OF
DOCTOR OF PHILOSOPHY

UNIVERSITY OF FLORIDA

2003

Copyright 2003

by

BOONCHAI SANGPETNGAM

To my parents, brothers, sister, and Meena.

ACKNOWLEDGMENTS

First of all, I would like to acknowledge Dr. Bjorn Birgisson, my chair person, for his support, encouragement, and precious guidance in both academic and life throughout my course of study. I also thank Dr. Reynaldo Roque, my cochair, for the generous contribution of his discussion and thinking to this work. Many thanks should be given to my past and present colleagues, Dr. Zhiwang Zhang, Dr. Leslie Myers, Marc Novak, Adam Jajliardo, and Chote Soranakom, for their assistance and valuable contributions to my research study.

I also would like to send my appreciation to the Florida Department of Transportation and the Federal Highway Administration, especially to Mr. Gale Page, Mr. Bruce Dietrich, Mr. Greg Sholar, and Mr. Greg Schiess for the ongoing financial and technical support of the study of cracking mechanisms in asphalt pavements and mixtures.

And lastly, I would like to thank my parents, brothers and sister for understanding and supporting my long pursuit of the Ph.D. degree, and special thanks to noo+ Meen for her support, encouragement, and artworks in this dissertation.

TABLE OF CONTENTS

Page

ACKNOWLEDGMENTS iv

LIST OF TABLES ix

LIST OF FIGURES x

ABSTRACT xvi

CHAPTER

1 INTRODUCTION 1

- 1.1 Background 1
- 1.2 Statement of problem 2
  - 1.2.1 Identification of Complexity of HMA Cracking Mechanisms 2
  - 1.2.2 Identification of Critical Pavement Design Conditions 3
  - 1.2.3 Numerical Considerations 3
- 1.3 Hypothesis 4
- 1.4 Objectives 4
- 1.5 Scope 4
- 1.6 Research Approach 5

2 LITERATURE REVIEW 8

- 2.1 Classical Fatigue Cracking 8
- 2.2 Continuum Damage 10
- 2.3 Hot Mix Asphalt Fracture Mechanics 16
  - 2.3.1 Background 16
  - 2.3.2 Conventional Fracture Mechanics 17
  - 2.3.3 Crack Growth and Fracture Threshold in Hot Mix Asphalt 20
  - 2.3.4 HMA Fracture Mechanics 24

3 TWO-DIMENSIONAL DISPLACEMENT DISCONTINUITY METHOD 30

- 3.1 Fundamental Considerations 32
- 3.2 Displacement Discontinuity Element Formulation 38
- 3.3 Numerical Formulation 41
- 3.4 Modeling of Geometry and Boundary Conditions 45
- 3.5 Crack-Tip Element 47

3.6 Comparison to Finite Element Method 48
3.7 Higher Order Element Formulation 49
3.8 Multi-Layer Structure 51
3.9 Verification and Examples 54
  3.9.1 A Crack in Rectangular Plate 55
  3.9.2 Crack Propagation in the Superpave Indirect Tension Test 57
  3.9.3 Annulus Inside a Circular Hole in a Large Plate 59
  3.9.4 A Three-Layer Pavement 61
3.10 Summary of the DD Method 72

4 VISCOELASTIC DISPLACEMENT DISCONTINUITY METHOD 73

4.1 Viscoelastic Boundary Value Problem 73
4.2 The Correspondence Principle 76
4.3 Transformed Boundary Conditions 78
  4.3.1 Constant Step Function 79
  4.3.2 Continuous Sine Function 80
  4.3.3 Haversine Function 81
4.4 Transformed Material Property 81
  4.4.1 Burgers Model 84
  4.4.2 Power Law Model 89
4.5 Transformed Displacement Discontinuity Equations 92
4.6 Numerical Laplace Inversion 96
4.7 Strain Energy in One Direction 99
4.8 Verification and Examples 102
  4.8.1 One-Dimensional Problem 102
  4.8.2 Modeling Creep Behavior in Superpave Indirect Tension Test 104
  4.8.3 Thick-Walled Viscoelastic Tube 108
    4.8.3.1 Case 1: Kelvin model 108
    4.8.3.2 Case 2: Maxwell model 113
    4.8.3.3 Case 3: Burgers model 114
    4.8.3.3 Case 4: constant Poison ratio 119
4.9 Viscoelasticity of Hot Mix Asphalt Mixtures 125
4.10 Dissipated Creep Strain Energy 127
4.11 Response of Viscoelastic Material to Cyclic Loading 130

5 HOT MIX ASPHALT FRACTURE MECHANICS-BASED CRACK GROWTH SIMULATOR 135

5.1 Hot-Mixed Asphalt Fracture Simulator Framework 137
5.2 Assumptions and Limitations 138
5.3 Critical Zone 140
5.4 Damage in Critical Zone 146
  5.4.1 DCSE at Location Away from Crack Tip 149
  5.4.2 DCSE at Location of Crack Tip 152
  5.4.3 Average DCSE in the Critical Zone 153
5.5 Strain History during Crack Propagation 155

5.6 Critical Zone Vicinity and Direction of Crack Growth 165
    5.6.1 Three-Zone Grid: Case 1 167
    5.6.2 Three-Zone Grid: Case 2 169
5.7 Verification of HMA Fracture Simulator 171

6 ANALYSIS AND FINDINGS 177

6.1 Verification with Field Pavement Sections 177
    6.1.1 Pavement Sections 177
    6.1.2 Pavement Modeling 182
    6.1.3 Crack Growth Prediction 187
    6.1.4 Crack Growth Simulation 193
        6.1.4.1 First crack growth step 193
        6.1.4.2 Second crack growth step 195
        6.1.4.3 Subsequent crack growth steps 197
    6.1.5 Interpretation of Results 201
        6.1.5.1 I10 sections 201
        6.1.5.2 I75 sections 202
        6.1.5.3 US301 sections 202
6.2 Direction of Crack Growth in Asphalt Pavement 203
6.3 Residual Stress in Flexible Asphalt Pavements 207
    6.3.1 Investigation Approach 207
    6.3.2 Interpretation of Time-Dependent Response in Asphalt Concrete Layer 211
6.4 Effect of Stiffness Gradient 218
    6.4.1 Investigation Approach 219
        6.4.1.1 Stiffness Gradients 219
        6.4.1.2 Pavement modeling 221
        6.4.1.3 Stress intensity factor (K_I) 227
        6.4.1.4 Reference sections for critical stiffness gradients 229
    6.4.2 Intrepretation of Results 233

7 CONCLUSIONS AND RECOMMENDATIONS 235

7.1 Conclusions 235
7.2 Recommendations 238

APPENDIX

A HOOKE'S LAW 240

B FORMULATION FOR DISPLACEMENT DISCONTINUITY ELEMENT 242

Quadratic Element 242
Constant Element 247
Crack-Tip Element 248

C SOLUTIONS OF ONE-DIMENSIONAL VISCOELASTIC PROBLEMS 249

Viscoelastic Material under Continuous Sine Stress 249
Viscoelastic Material under a Half-Sine Stress 250

D DAMAGE ACCUMULATION AND CRACK GROWTH 251

Single Haversine Load 251
Cyclic Haversine Loads 255
Crack Geometry Change 260

LIST OF REFERENCES 263

BIOGRAPHICAL SKETCH 269

LIST OF TABLES

Table page

4-1 Material Properties in Correspondence Principle....83

4-2 Integration Points and Coefficients for 3-Point Gauss Quadrature....102

4-3 Viscoelastic Properties for Thick-Walled Tube Example....110

5-1 Superpave Coarse-Graded and Fine-Graded Gradations....173

5-2 Input Properties of the Superpave Coarse-Graded and Fine-Graded Mixes....173

6-1 Location of Sections....178

6-2 General Description of Field Sections....179

6-3 Layer Thickness and Modulus of Field Sections....180

6-4 Properties of Asphalt Concrete Layers at 10°C....181

6-4 Continued....182

6-5 Location of Maximum Tensile Stress at Surface of Pavement....190

6-6 Material Properties of a Flexible Pavement Structure....208

6-7 Resilient Modulus at Three Temperatures for I10MW2 and I75-1C....220

LIST OF FIGURES

Figure page

2-1. Application of Correspondence Principle to Cyclic Data with Negligible Damage: a) Stress-Strain; b) Stress-Pseudo Strain. (Lee and Kim 1998b) 12

2-2. Stress-Pseudo Strain Behavior and Pseudo Stiffness Changes in: a) Controlled-Strain Mode; b) Controlled-Stress Mode. (Lee and Kim 1998b)............................14

2-3. Change in Pseudo Stiffness Before and After Rest Period. (Lee and Kim 1998b)..14

2-4. Finite Element Model of IDT Sample with Hole and Vertical Crack......................18

2-5. Theoretical Relationship between Normalized Crack Length and Normalized Horizontal Displacement from IDT. 19

2-6. Fracture Test Results for the Mixtures from Eight Field Sections...........................19

2-7. Crack Growth Rate at $K=8MPa*mm^{0.5}$ for all Mixtures 20

2-8. Illustration of Crack Propagation in Asphalt Mixtures. 22

2-9. Illustration of Potential Loading Condition (Continuous Loading). 22

2-10. Determination of Dissipated Creep Strain Energy. 23

2-11. The Superpave Indirect Tension Test (IDT)...23

2-12. Crack Growth Process. 27

2-13. Fracture Energy Density of Superpave Mixtures @ 10 C......................................28

2-14. Fracture Energy Density of Eight Field Sections @ 10 C......................................29

3-1. Interior and Exterior Regions of Boundary S...34

3-2. Displacement Discontinuity Elements. 35

3-3. A Constant DD Element Illustrating Positive Displacement Discontinuity.............39

3-4. Directions of Positive Stress Components 41

3-5. Modeling of Structural Geometry and Boundary Conditions 46

3-6. Structural Models in Boundary Element Method and Finite Element Method........49

3-7. Diagram of Inhomogeneous Body and its Representative Model............................53

3-8. A Crack in a Rectangular Plate and its Closed Form Solution. A) Physical Geometry, and B) The Representative DD Model. 55

3-9. A Plot of Longitudinal Stress Around the Crack Tip of the Rectangular Plate Problem. 56

3-10. Superpave IDT with Vertical Crack and its Representative DD Model..................58

3-11. Relations Between Normalized Crack Length and Normalized Horizontal Displacements from Superpave IDT. 58

3-12. Annulus inside a Circular Large Plate 60

3-13. Radial and Tangential Stresses in Annulus and Plate..60

3-14. Pavement Model in Displacement Discontinuity Method.......................................64

3-15. Pavement Model in ABAQUS Finite Element Method 65

3-16. Vertical Deformation at Surface of Pavement..66

3-17. Vertical and Horizontal Stresses at Bottom of Asphalt Concrete Layer 67

3-18. Vertical and Horizontal Stresses at Top of Subgrade Layer 68

3-19. Pavement Model in Displacement Discontinuity Method Without Side Boundaries...69

3-20. Deformation and Stress at Surface of Pavement from DDM with Different Side Boundaries...70

3-21. Stresses at Bottom of Asphalt Layer from DDM with Different Side Boundaries.. 71

4-1. Time-Dependent Boundary Functions 80

4-2. Representative Burgers model 84

4-3. Maxwell Model and Creep Response..87

4-4. Kelvin Model and Creep Response...88

4-5. Burgers Creep and Recovery Response 88

4-6. Constant Creep Stress Conditions 89

4-7. Solutions of One-Dimensional Viscoelastic Problem 103

4-8. Strain Energy of One-Dimensional Problem under Sinusoidal Stress 104

4-9. Superpave Indirect Tension Creep Test and its Representative DD Model. 106

4-10. Comparison of Creep Compliance Curves Obtained from Measured Laboratory Data and from the DD Method with Burgers-Viscoelasticity. 107

4-11. Thick-Walled Tube and Its DDM Model. 109

4-12. Radial Displacement of Thick-Walled Viscoelastic Tube: Case 1 111

4-13. Radial and Circumferential Stresses of Thick-Walled Viscoelastic Tube: Case 1 and 2 112

4-14. Radial Displacement of Thick-Walled Viscoelastic Tube: Case 2 114

4-15. Radial Displacement of Thick-Walled Viscoelastic Tube: Case 3 117

4-16. Radial Stress of Thick-Walled Viscoelastic Tube: Case 3 118

4-17. Circumferential Displacement of Thick-Walled Viscoelastic Tube: Case 3 119

4-18. Radial Displacements of Thick-Walled Viscoelastic Tube. A) Case 4 Constant Poison Ratio, and B) Case 3 Time-Dependent Poison Ratio. 122

4-19. Radial Stresses of Thick-Walled Viscoelastic Tube. A) Case 4 Constant Poison Ratio, and B) Case 3 Time-Dependent Poison Ratio. 123

4-20. Circumferential Stresses of Thick-Walled Viscoelastic Tube. A) Case 4 Constant Poison Ratio, and B) Case 3 Time-Dependent Poison Ratio. 124

4-21 Stress and Strain Induced by a Single Loading Cycle. 132

4-22. Stress for Cyclic Haversine Loading. 132

4-23. Total Strain Response due to Cyclic Haversine Stress. 133

5-1. Flowchart Diagram of the HMA Fracture Simulator 139

5-2. Superpave Indirect Tension Fracture Test 142

5-3. Diagram Illustrating the Concept of Equal-Sized Critical Zone Length 143

5-4. Effects of Different Zone Length Definitions on Crack Growth Characteristics...145

5-5. Diagrams of IDT Crack Growth Test and the Time-Dependent Loading.............147

5-6. Stress Distributions Ahead of Crack Tip. A) Stress Singularities from Linear Elastic Fracture Mechanics-Based Solutions, and B) Stress Concentrations Limited by Limit Stress...147

5-7. Stresses and Creep Strains ahead of Crack Tip in the IDT Crack Growth Test. A) Location A, and B) Location B..149

5-8. Stresses in the Critical Zone...150

5-9. Tensile Stress and Dissipated Creep Strain Energy in Front of Crack Tip............154

5-10. Dissipated Creep Strain Energy in the Critical Zone. 155

5-11. History of Crack Growth and Damage Accumulation. 157

5-12. Cracking Damage Accumulation in the Critical Zone-i..158

5-13. Stress and Strain Induced by a Single Haversine Load...160

5-14. Stress Function of Cyclic Haversine Loading...160

5-15. History of Strain is Composed of a Superposition of Individual Strains Induced at Different Time...163

5-16. History of Stress and Strain During the Crack Propagation..................................164

5-17. Geometry of Grid of Critical Zones. Seven Zones (ABCDEFG) Locate in Front of Crack Tip...166

5-18. DCSE Variation in the Critical Zone Vicinity Caused by One Load Cycle...........166

5-19. Location of a Grid of Three Critical Zones: Case 1. 168

5-20. DCSE Variation for Three-Zone Grid: Case 1..168

5-21. Location of a Grid of Three Critical Zones: Case 2. 170

5-22. DCSE Variation for Three-Zone Grid: Case 2..170

5-23. Superpave IDT with Vertical Crack and its Representative DD Model................174

5-24. Crack Growth Characteristics of the Superpave Coarse-Graded Mix Obtained from Laboratory Results and from the HMA Fracture Simulator..........................175

5-25. Crack Growth Characteristics of the Superpave Fine-Graded Mix Obtained from Laboratory Results and from the HMA Fracture Simulator..........................176

6-1. Displacement Discontinuity Method Model for All Pavement Sections. 183

6-2. Time-Dependent Characteristic of Traffic Loads. 186

6-3. The Critical Condition of Top-Down Longitudinal Surface Cracking. 188

6-4. Horizontal Stresses at the Surface of Pavements. 188

6-4. Continued 189

6-5. Horizontal Stresses at the Bottom of Asphalt Layers..190

6-5. Continued. 191

6-6. Vertical Deformations at the Surface of Pavements. 192

6-6. Continued. 193

6-7. Top-Down Cracking Development in Asphalt Pavements. 197

6-8. Geometry of Crack Growth Prediction for Pavement Section I10MW1. 198

6-8. Continued. 199

6-9. Prediction of Crack Growth Rate for Pavement Sections I10MW1, I10MW2, US301BN, and US301BS. 200

6-10. Prediction of Crack Growth Rate for Pavement Sections I75-1U and I75-1C.......201

6-11. Crack Growth Geometry of Section I10MW1 for Crack Located 381 mm. (15 Inches) Closer to the Tire...205

6-11. Continued...206

6-12. Model of Three-Layer Pavement...209

6-13. Time-Dependent Characteristic of Load Applications...211

6-14. Horizontal Stress at Bottom of Asphalt Layer Below Center of Tire Caused by One Loading Cycle. A) Overall Scale, B) Enlarged Scale for Residual Stress. 213

6-15. Horizontal Stress at Surface of Pavement Below Center of Tire Caused by One Loading Cycle. A) Overall Scale, B) Enlarged Scale for Residual Stress. 214

6-16. Horizontal Stress at Bottom of Asphalt Layer Below Center of Tire Caused by Multiple Loading Cycles. A) Overall Scale, B) Enlarged Scale for Residual Stress. 215

6-17. Horizontal Stress at Surface of Pavement Below Center of Tire Caused by Multiple Loading Cycles. A) Overall Scale, B) Enlarged Scale for Residual Stress. 216

6-18. Pavement Responses During and After a Load Application. 217

6-19. Stiffness Gradients in Asphalt Concrete Sub-layers....223

6-20. Pavement Structure of I75-1C for Stiffness Gradient Case and Uniform Stiffness Case. 224

6-21. Pavement Structure of I10MW2 for Stiffness Gradient Case and Uniform Stiffness Case. 225

6-22. DDM Model of Pavement Section I10MW2 with Sub-Layers.. 226

6-23. Tensile Stress Distribution in Front of Crack Tip for Section I10MW2. 226

6-24. Tensile Stress Distribution in Front of Crack Tip for Section I75-1C. 227

6-25. Determination of the Stress Intensity Factor for Section I75-1C.. 228

6-26. Stress Intensity Factors of Sections I10MW2 and I75-1C. 228

6-27. Pavement Structures for Stiffness Gradient Case and Uniform Stiffness Case According to Myers (2000). 231

6-28. Stress Intensity Factors Obtained from DDM for the Reference Section (Myers 2000). 232

6-29. Stress Intensity Factors as Presented by Myers (2000) for the Reference Section (Myers 2000). 232

D-1. Stress in Sine Function. 251

D-2. Haversine Stress Function. 252

D-3. Stress and Strain Induced by a Single Haversine Load. 254

D-4. Stress Function of Cyclic Haversine Loading....256

D-5. History of Strain is Composed of a Superposition of Individual Strains Induced at Different Time. 258

D-6. Strain and total DCSE Under the Current Crack Geometry is Composed of Strain History of the Previous Crack Geometry....262

Abstract of Dissertation Presented to the Graduate School
of the University of Florida in Partial Fulfillment of the
Requirements for the Degree of Doctor of Philosophy

DEVELOPMENT AND EVALUATION OF A VISCOELASTIC BOUNDARY ELEMENT METHOD TO PREDICT ASPHALT PAVEMENT CRACKING

By

BOONCHAI SANGPETNGAM

May 2003

Chair: Dr. Bjorn Birgisson
Cochair: Dr. Reynaldo Roque
Major Department: Civil and Coastal Engineering

It has long been accepted that cracking of hot-mix asphalt (HMA) pavements is a major mode of premature failure. Many state agencies have verified that pavement cracking not only occurred from fatigue in which a crack initiates from the bottom of the asphalt layer but also in other modes such as low temperature and the most recently identified top-down cracking. Recent work at the University of Florida has led to the development of a viscoelastic fracture mechanics-based crack growth law that is capable of fully describing both initiation and propagation of cracks in asphalt mixtures. The model requires the determination of only four fundamental mixture parameters that can be obtained from less than one hour of testing using the SuperPave□ Indirect Tension Test (IDT). These parameters can account for micro-damage, crack propagation, and healing for stated loading conditions, temperatures, and rest periods.

In this dissertation, the hot mix asphalt fracture mechanics-based crack growth simulator is developed. The framework of the simulator is based on the viscoelastic displacement discontinuity boundary element method. The framework components and details of crack growth mechanism are fully described. The resulting fracture simulator is shown to predict reasonably the crack propagation of coarse-graded and fine-graded mixtures in a laboratory under cyclic loading conditions. A case study of using the newly developed fracture simulator to describe how cracking damage develops in asphalt pavement is also included.

CHAPTER 1
INTRODUCTION

1.1 Background

It has long been accepted that cracking of hot-mix asphalt (HMA) pavements is a major mode of premature failure. Currently, four major failure mechanisms associated with cracking in HMA pavements are recognized: 1) fatigue cracking, starting at the bottom of the flexible pavement and propagating upward, 2) low temperature cracking, 3) reflective cracking, in which existing cracks or joints provide stress concentrations that result in crack propagation through an HMA overlay layer, and the more recently identified, 4) top-down cracking, which is initiated at the top of the asphalt pavement layer in a direction along the wheel path, and grows into the pavement layer (Roque, Myers, and Birgisson 2000; Myers, Roque, and Birgisson 2001; Uhlmeyer et al. 2000; Komoriya et al. 2001). A solid understanding of the mechanisms of crack initiation and crack growth are essential to predict pavement performance in the context of thickness design, as well as in the design and optimization of mixtures. Any hope of developing more crack resistant mixes relies on improved understanding of the mechanics of crack initiation and crack growth in HMA mixtures. Unfortunately, the complexity of modeling crack initiation and crack growth has been an obstacle to the incorporation of fracture mechanics-based approaches in the bituminous pavement area.

The Displacement Discontinuity (DD) boundary element method is a numerical method that offers a potential solution to the crack growth problems (e.g. Crouch and Starfield 1990; Shou and Crouch 1995; Siebrits and Crouch 1994). An advantage of the DD method is the flexibility associated with meshing is required only on the boundaries of an object or pavement, including cracks. This means that the number of elements required is significantly smaller than for domain-based methods like the finite element method. Also, the stress singularity at the crack tip can be naturally included in the DD method by using an element with a representative displacement distribution around the crack tip. Moreover, crack growth is addressed simply by adding DD elements in regions of crack growth. Most importantly, the success of the DD method in other fields, such as rock mechanics, mining, and the oil industry, leaves no apparent reason why it should not be applicable to problems common to asphalt pavements (Napier 1999; Einstein and Bobet 1999; Siebrits et al. 1997, 2000, 2001; Guzina 2001).

1.2 Statement of problem

Fracture modeling in asphalt pavement is a very challenging topic that requires an intensive study since there are many related factors that affect the mechanism on where and when cracks start, how fast and in what direction cracks develop. The hot mix asphalt (HMA) fracture mechanics framework (Zhang 2000; Zhang, Roque, and Birgisson 2001; Zhang, Roque, Birgisson and Sangpetngam 2001) has revealed a fundamental energy-based fracture threshold and an associated crack growth rule based on the Superpave indirect tension (IDT) test, yet, there are problems to be addressed in the numerical modeling side in order to simulate laboratory and field cracking performance. Some of the key issues to be addressed are listed below.

1.2.1 Identification of Complexity of HMA Cracking Mechanisms

Mechanism of crack initiation and propagation:

- What factor causes the crack to start?
- Where will crack start to initiate?

- What will be the initial crack length?
- How to account for stress gradients when determining whether a crack will initiate?

Characteristics of cracking:

- Whether multiple cracks are allowed to develop simultaneously at relatively different locations, or
- Will there be one location where the mixture is weakest such that one predominant crack will develop and propagate.

Perhaps, it is most important for laboratory tests where uniform stress conditions are used. In the field, stress gradients are more common, so there will generally be points of maximum stress.

1.2.2 Identification of Critical Pavement Design Conditions

Effect of loading conditions such as:

- Surface contact of traffic vehicles
- Wandering pattern of tire positions in transverse direction
- Speed of vehicles

Effect of environment:

- Temperature changes cause gradient of expansion or contraction in asphalt layer
- Stiffness gradient due to temperature
- The variations of loading and environment may cause the critical condition for cracking to move from a position to another position, which affects the crack initiation and propagation.

Effect of pavement structure on the cracking performance, and

Effect of healing: damage recovery after rest periods

1.2.3 Numerical Considerations

- Since the critical condition leading to cracking may change in location within the material, it raises a question on how to keep track of damage history at all points in the potential cracking area, and how far the area should be extended.

- Viscoelasticity representation of HMA materials.
- Loading functions: how to represent the characteristics of vehicle loads in the field pavement and loads applied to specimens in laboratory.
- Layering representation of the pavement structure.

1.3 Hypothesis

It is possible to predict the cracking performance of mixtures in the laboratory and in the field through the use of a boundary element based numerical simulator that incorporates HMA fracture mechanics and appropriate key pavement design conditions.

1.4 Objectives

- Develop a HMA pavement fracture simulator that integrates the HMA fracture mechanics into a viscoelastic displacement discontinuity boundary element method.
- Identify a rational approach for pavement-cracking analysis using the HMA pavement fracture simulator that adequately addresses fracture initiation and crack growth in mixture.
- Use the approach developed to demonstrate for key design conditions what factors force a crack to initiate and how the crack will propagate under those conditions.
- Evaluate the approach to the most possible extent whether it can relate to the cracking performance observed in the field pavement and laboratory data.

1.5 Scope

One of the goals of this research is to develop a numerical simulator that integrates the HMA fracture mechanics so that it can analyze the cracking performance of the HMA. Definitely, it will be ideal to develop the ultimate model such that it can analyze an arbitrary crack initiation and propagation under the many complicated factors such as load-position variation, temperature gradient, healing, etc. However, this tremendous task will be too great to accomplish within a limited period of time. In fact, there are many components such as healing behavior that have not been fully understood yet. In order to achieve the research objectives, the study will be focused on limited conditions and some assumptions must be made to reduce the level of complication.

The research will focus primarily on using the displacement discontinuity boundary element method as a mechanical analysis platform with the integrated HMA fracture mechanics to identify the rational approach that governs where cracks initiate and how they propagate. The limitations and assumptions of the hypothesis in this study are as follows:

- Two-dimensional analysis will be used throughout the study. This condition allows for a reduction in the complications associated with the crack growth in three-dimensional media and the three-dimensional displacement discontinuity method. Plane strain conditions will be used in the pavement-related studies, while plane stress conditions will be applied to the analysis of the indirect tension test.
- The research will be conducted based on a set of predefined conditions of
    - Critical locations for the initiation of crack growth
    - Pavement structure: thickness and properties of layers
    - Environmental effect: temperature and stiffness gradient
    - Variation of surface loading: position, speed and surface contact of tire loads
- The theory of fracture mechanics was utilized to obtain the response related to cracking discontinuities, such as stress singularity, crack-opening displacement, and dissipated creep strain energy.
- Linear viscoelasticity is assumed sufficient to represent the time-dependent response of the HMA material.
- Assumption of linear elasticity is used in the model for describing the behavior of aggregate/soil materials in response to the vehicle and environmental loading.

1.6 Research Approach

The purpose of this research is mainly to develop a numerical method for crack growth analysis in HMA. Based on its superior performance on modeling discontinuities, the displacement discontinuity boundary element method was chosen as the numerical platform for the implementation of HMA fracture mechanics. The research approach to develop such a system is described in the following areas:

1. Review literature: the theory of the displacement discontinuity method, and the existing crack growth theories: classical fatigue, continuum damage, fracture mechanics related methods.
2. Develop the viscoelastic displacement discontinuity method from the existing elastic DD method. In order to model the crack growth behavior for HMA pavement, an addition of many essential features is necessary for the existing method. Those features include
    - Crack-tip element: upgrade the existing displacement discontinuity boundary element method to capture the stress singularity at the crack tip by introducing a crack-tip element that has a displacement discontinuity of $1/\sqrt{r}$ (where r is the distance from the notch end of the crack-tip element).
    - Incorporate a linear viscoelasticity constitutive model into the DD method to capture time-dependent behavior of HMA. The two selected constitutive models are 1) the power law equation and 2) Burgers model. The power law equation explains the time-dependent compliance (D) in a power form, D(t)=D0+D1 tm , where the constants are obtained by a curve fitting method. The laboratory measurement of parameters in the power law equation was described by Roque and Buttlar (1992) and Buttlar and Roque (1994). The Burgers model is a physical model that illustrates the viscoelastic behavior by a combination of springs and dashpots.

The developing scheme involves applying the viscoelastic correspondence principle that converts the time-dependent problem to the Laplace-transformed domain, solving the transformed stress-displacement problem in the transformed domain (all equations are linear elastic sense) using the DD method, and inverting the solutions back to the time domain.

- Loading function: the method should be able to address characteristics of time-dependent tire loads, load-unload functions that are applied in laboratory such as sinusoidal function and a load-unload stepwise function.
- Multi-layer system: the introduction of layering (Crouch and Starfield 1990) can be implemented in the DD code to enable the modeling of pavement structure, which

typically has four or more layers of different materials: surface, base, subbase, and subgrade.

- Higher order element: unlike the constant DD element that assumes constant displacement over an element, the higher order element has linear or quadratic distribution of displacement over an element resulting in more accurate stress-displacement solutions at locations close to the DD elements.

3. Identify a rational approach for determining where and when the crack will initiate, how much it is going to grow initially, and how the crack will propagate in terms of rate and direction based on the HMA fracture mechanics. The approach may be obtained from the theoretical relationship to the mechanical quantities (e.g. dissipated creep strain energy, etc.) At the most possible extent, the approach should correlate well with the observation in laboratory and field data.

4. Implement the approach into the viscoelastic displacement discontinuity method.

5. Define a set of key design conditions to limit the variation of the influenced factors. The predefined conditions include

    - Critical locations for the initiation of crack growth
    - Pavement structure including layer thicknesses and material properties
    - Design loading condition and its variation in positions
    - Environmental effect such as temperature gradient

Validate the developed simulator with the integrated approach and evaluate whether it is able to describe or relate the cracking observation in the laboratory and field pavement based on a limited basis with existing data.

CHAPTER 2
LITERATURE REVIEW

2.1 Classical Fatigue Cracking

Fatigue cracking in flexible pavements is traditionally associated with a mode of pavement failure corresponding to the repeated tensile strains at the bottom of the asphalt surface layer due to the bending effect of the layer subjected to traffic loadings. The fatigue cracking consists of 2 phases: crack initiation and crack propagation. The initiation phase involves formation, growth, densification, and coalescence of distributed microcracks under repeated loads. The propagation phase starts with cracks growing outward from the tensile zone where the microcracks formed and eventually develops from small but visible flaws into full depth cracks in the asphalt layer.

Many researchers developed equations to quantify the number of load repetitions that asphalt materials can tolerate until fatigue failure. The early developments quantified the number of cycles to failure (N_f) as a function of the repeated tensile strain at the bottom of the asphalt layer (ε_t) alone. Later on, the equations have been improved by including other related variables such as mixture stiffness and volume of bitumen in the mix.

Pavement life equations provide the simple relationship between mechanical responses i.e., stress, strain, deflection and pavement performance and are the essence of the mechanical-empirical design. However, they cannot address some important issues such as crack initiation and propagation, stress redistribution due to the presence of a crack, rate of crack growth, and effects of healing (damage recovery after a rest period).

The equations are empirical in nature and applicable only for fatigue cracks at the bottom of surface layer and must be used with caution since they were developed based on specific materials and testing conditions and may not be widely applicable. It is important that they be carefully calibrated to local conditions to provide for a reliable estimation of pavement fatigue life. Some famous fatigue equations are explained below.

The general strain based equation has a simple form often expressed as

$$N_f = k_1 \left(\frac{1}{\varepsilon_t} \right)^{k_2} \tag{2-1}$$

where N_f is number of repeated loads until fatigue failure,

ε_t is repeated tensile strain,

k_1, k_2 are experimentally determined constants.

Research work related to the determination of k_1, k_2 values were presented by e.g. Myre (1990), Cooper and Pell (1974), Rauhut, Lytton and Darter (1984).

The Illinois Department of Transportation used the strain-based function in their thickness design for fatigue resistance based on the studies of Thompson and Cation (1986), Gomez and Thompson (1984), and Thompson (1987). The function had accounted for mixture composition factors, field calibration and split strength characteristics. The fatigue function for a typical dense graded Illinois DOT hot mix asphalt pavement was

$$N_f = 5*10^{-6}(1/\varepsilon_t)^{3.0} \tag{2-2}$$

Monismith and Epps (1969) proposed a laboratory model that related the number of repeated loads until fatigue failure (N_f) to the tensile strain at the bottom of the surface layer (ε_t) and modulus of the asphalt bound material (E_{ac}) as follows:

$$\log N_f = 14.82 - 3.291*\log(\varepsilon_t/10^{-6}) - 0.854*\log(E_{ac}/1000) \qquad (2\text{-}3)$$

Newcomb, Bu-bushait, Mahoney and Sharma (1983) used Monismith's formula but applied a shift factor (SHF) to replicate the field measurements:

$$N_{field} = N_{lab} * SHF \qquad (2\text{-}4)$$

The shift factor was a function of void ratio, asphalt cement content, viscosity, layer thickness and pavement loading conditions.

The equation used in the 1981 MS-1 Asphalt Institute Thickness Design Manual accounted for the air void content (V_a), volumetric asphalt content (V_b), stiffness of the mixture (E_1) and tensile strain (ε_t):

$$N_f = 10^M\,(18.4)(0.00432)(1/\varepsilon_t)^{3.291}(1/E_1)^{0.854} \qquad (2\text{-}5)$$

where $M = 4.84(\frac{V_b}{V_a + V_b} - 0.69)$.

Research by Sousa, Way and Harvey (1996) during the SHRP program yielded a fatigue life equation expressed as

$$N_f = S_f*2.738*10^5*e^{0.077(VFB)}*(\varepsilon_t)^{-3.624}*S_0^{-2.720} \qquad (2\text{-}6)$$

where

S_f	is a factor converting laboratory measurements to the field results,
VFB	is the voids filled with bitumen,
S_0	is the loss stiffness.

2.2 Continuum Damage

The general idea of the continuum damage mechanics deals with pictures the fatigue crack growth as the progressive reduction in the material stiffness due to the repeated loads. The theory described the behavior of hot mix asphalt (HMA) subjected to traffic loadings in terms of three mechanisms:

- Relaxation or creep due to viscoelastic behavior of bituminous materials,
- Any amount of response beyond the viscoelastic part is considered as damage accumulation (i.e. stiffness reduction),
- Healing of damage due to resting periods (i.e. recovery of stiffness reduction).

Since the viscoelastic response does not contribute to the damage part, Lee and Kim (1998a) eliminated the viscoelastic strain from the total strain by applying the following procedures:

For linear viscoelasticity, a uniaxial stress-strain relationship is

$$\sigma(t) = \int_0^t E(t-\tau)\frac{d\varepsilon}{d\tau}d\tau \qquad (2\text{-}7)$$

where E(t) is relaxation modulus at time t.

They used pseudo strain, introduced by Schapery (1984), instead of general strain to separate the viscoelastic part from the overall response. The pseudo strain (ε^R) is defined as

$$\varepsilon^R = \frac{1}{E_R}\int_0^t E(t-\tau)\frac{d\varepsilon}{d\tau}d\tau \qquad (2\text{-}8)$$

where E_R is reference modulus (an arbitrary constant).

If there is no damage contributed in the loading response as shown in Figure 2-1, the stress-pseudo strain relationship becomes a linear elastic-like equation:

$$\sigma = E_R\,\varepsilon^R \qquad (2\text{-}9)$$

This process of reducing the problem from time-dependence to a corresponding linear-elasticity (time-independence) is known as the Correspondence Principle.

Lee and Kim (1998b) observed three basic characteristics from the stress-pseudo strain relationship of a cyclic uniaxial tensile test during the damage process as shown in Figure 2-2:

- Nonlinear behavior of the loading and unloading paths in each cycle,
- Change in slope of each σ-ε^R cycle (i.e. reduction in pseudo stiffness) as cyclic loading continues,
- Accumulation of permanent pseudo strain ($\varepsilon^R{}_S$) in the controlled stress mode of loading (i.e. shift of the σ-ε^R loop from the origin as cyclic loading continues).

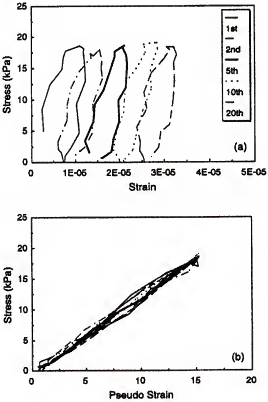

Figure 2-1. Application of Correspondence Principle to Cyclic Data with Negligible Damage: a) Stress-Strain; b) Stress-Pseudo Strain. (Lee and Kim 1998b)

In Figure 2-3, the secant pseudo stiffness (S^R)--called pseudo stiffness for simplicity--was defined to characterize the change in the slope of each σ-ε^R cycle.

$$S^R = \frac{\sigma_m}{\varepsilon^R_m} \tag{2-10}$$

where

$\varepsilon^R{}_m$ is peak pseudo strain in each stress-pseudo strain cycle, and

σ_m is the stress corresponding to ε^R_m.

Lee and Kim (1998a) proposed a constitutive model for the stress-pseudo strain relationship of the uniaxial tensile cyclic test without rest periods as

$$\sigma = I\,(\varepsilon^R_e)\,(F+G) \qquad (2\text{-}11)$$

where

I is initial pseudo stiffness,

F is damage function representing pseudo stiffness reduction,

G is hysteresis function representing nonlinearity of loading and unloading cycle,

ε^R_e is effective pseudo strain accounting for the permanent pseudo strain accumulated in the controlled-stress mode; $\varepsilon^R_e = \varepsilon^R - \varepsilon^R_S$.

Later, Lee and Kim (1998b) proposed the simpler form of reduced constitutive equation as

$$\sigma_m = I\,C(S)\,(\varepsilon^R_m) \qquad (2\text{-}12)$$

where C(S) is coefficient of secant pseudo stiffness reduction, i.e. $C \leq 1$, and

S is internal state variable (ISV) representing damage.

The S parameter at a current N^{th} cycle may be obtained by the numerical scheme as

$$S \cong \sum_{i=1}^{N}\left[\frac{I}{2}(\varepsilon_i^R)^2(C_{i-1}-C_i)\right]^{\alpha/(1+\alpha)}(t_i-t_{i-1})^{1/(1+\alpha)} \qquad (2\text{-}13)$$

where α is a material constant.

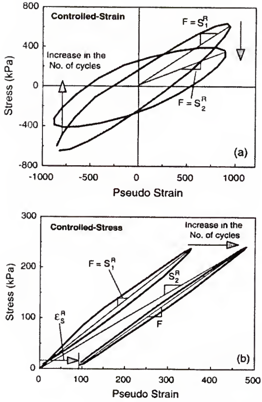

Figure 2-2. Stress-Pseudo Strain Behavior and Pseudo Stiffness Changes in: a) Controlled-Strain Mode; b) Controlled-Stress Mode. (Lee and Kim 1998b)

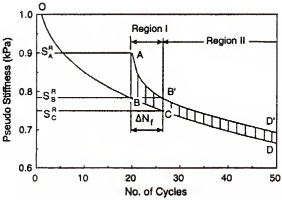

Figure 2-3. Change in Pseudo Stiffness Before and After Rest Period. (Lee and Kim 1998b)

Figure 2-3 shows the change in pseudo stiffness or C(S) as a product of increasing number of loading cycles. Line OBCD represents pseudo stiffness reduction without a rest period. AB represents recovery of pseudo stiffness in the case of having a rest period at the 20th cycle. AB'D' represents the pseudo stiffness reduction curve after the rest period.

According to laboratory results from Lee and Kim (1998a, 1998b) and Lee, Daniel and Kim (2000), the continuum damage equation predicts well the stress-strain response observed in the uniaxial tension test in both stress-controlled and strain-controlled modes.

Application of the continuum damage method to real pavement performance was found in the work by Lee, Daniel and Kim (2000) in which the laboratory performance of modified asphalt mixtures for Inchon airport pavements in Korea was evaluated. In this work, the continuum damage approach was able to predict the number of cycles to failure (N_f) based on the continuum damage equation. For example:

$$N_{f\text{ without rest periods}} = A\,\varepsilon_0^{-2\alpha} \tag{2-14}$$

where

A is a function of dynamic modulus and the parameters in the continuum damage equation such as S, I, C as mentioned earlier,

ε_0 is tensile strain amplitude obtained from a mechanical analysis method,

$\alpha = 1/(1+n)$, and n is slope of the creep compliance versus time curve in log-log scale.

The resulting prediction can be considered to be a mechanical-empirical method since the subjected strain must be calculated from mechanical modeling, then is used as the input for the continuum damage equation to predict the pavement life. Therefore, the implementation of the continuum damage approach directly into a mechanics-based analyzer is still in question. In effect, the continuum damage approach is effectively a phenomenological method, requiring calibration to given material conditions before use in predicting pavement fatigue life.

The disadvantage of the continuum damage method is the requirement of numerous functions such as relaxation modulus to determine pseudo strain, as well as the F and G functions to describe the damage process. The functions are unique properties of an asphalt mix and are obtained from laboratory tests. In fact, there is no detail presented on how to determine these functions. The continuum damage approach also does not consider a real physical crack in a material; therefore it cannot specifically address the stress redistribution due to the crack and the mechanics of crack propagation. Moreover, the approach assumes that damage grows continuously, but Zhang et al. (2001) have shown that cracks in asphalt mixtures grow in a discontinuous manner. The assumption that damage develops continuously with load repetitions was found to be inadequate to describe the contradiction that samples from a highly cracked pavement section turned out to show better cracking resistance in the laboratory than another sample from a pavement section that has better performance (Zhang 2000). In addition, damage mechanics does not provide a realistic physical interpretation of damage: Failure is generally assumed to coincide with a 50 percent reduction in pseudo-stiffness.

2.3 Hot Mix Asphalt Fracture Mechanics

2.3.1 Background

Many researchers believe that only studying the mechanics of real crack growth in HMA will resolve the puzzles of cracking damage in asphalt pavement. The research performed on the causes of top-down cracking on asphalt pavement by Roque, Myers and Birgisson (2000), and Myers, Roque and Birgisson (2001) indicated that the tearing-apart actions from the contact pressures between the ribs of the truck tire and the pavement surface can induce a sufficient level of tensile stress at a discontinuity (i.e. a crack) located at the pavement surface to cause the crack to propagate. This discovery has emphasized the importance of having a physical crack in the study of cracking damage in HMA.

2.3.2 Conventional Fracture Mechanics

Because of the difficulty of measuring the real crack length in the laboratory, Roque, Zhang and Sankar (1999) initiated a method of measuring a theoretical crack length instead. By using the linear elastic finite element method to simulate the samples under an indirect tension test condition at different crack length series, they established a relationship between the theoretical crack length and the deformation between two gauge points located across the crack line. Figure 2-4 illustrates the finite element model of the indirect tension test. The theoretical crack length allowed them to monitor the crack growth corresponding to the increment of cyclic loading. Figure 2-5 shows the relationship between the gauge deformation and the crack length.

The conventional linear elastic fracture mechanics presumes there are intrinsic flaws or micro-cracks in a material. At a critical condition, a crack initiates from the flaws and propagates continuously. Crack growth rate of linear elastic materials commonly is assumed to follow Paris's law, in which $\frac{da}{dN} = A(\Delta K)^n$, where a is crack length, N is number of repeated loads, K is stress intensity factor, A and n are constants. Zhang (2000) found that although the Paris law may be able to characterize the crack growth rate of Superpave laboratory samples in the cyclic Indirect Tension Test, its characterization of continuous crack growth cannot match observed field performance.

The contradiction was observed in the fracture test results (Figure 2-6) in which the samples from I95DuvalW exhibited significantly higher laboratory crack growth rate than the samples from US301 sections, but the I95DuvalW section was considered to be an excellent performer in the field, while the US301 sections had the most severe load-associated cracking in the field. Laboratory results from Honeycutt (2000) also reported a discrepancy between the cracking behavior of aged and unaged mixtures in the laboratory. Figure 2-7 shows that for three of four mixtures tested, da/dN was higher for the unaged than for the aged mixtures. These key observations inferred the limitation of the crack growth theory of the linear elastic fracture mechanics.

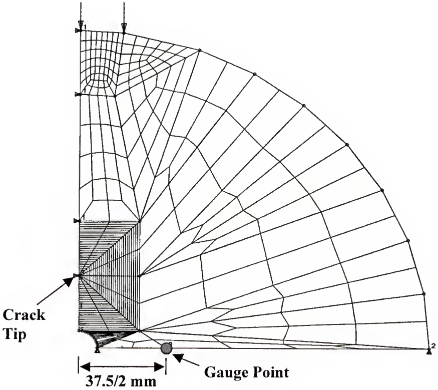

Figure 2-4. Finite Element Model of IDT Sample with Hole and Vertical Crack

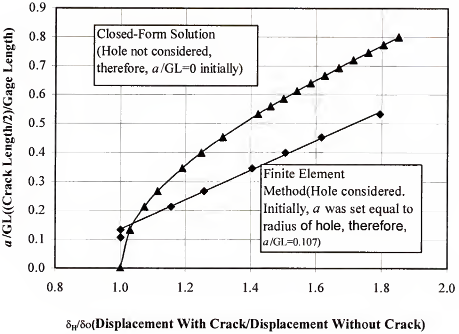

Figure 2-5. Theoretical Relationship between Normalized Crack Length and Normalized Horizontal Displacement from IDT.

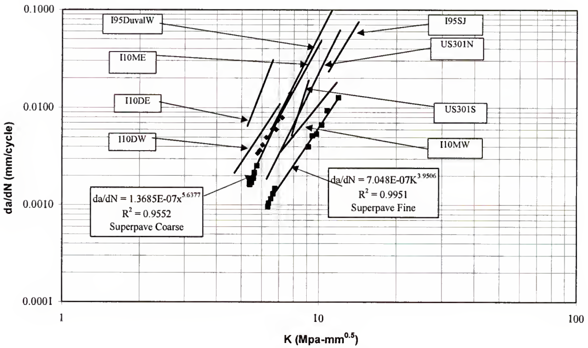

Figure 2-6. Fracture Test Results for the Mixtures from Eight Field Sections.

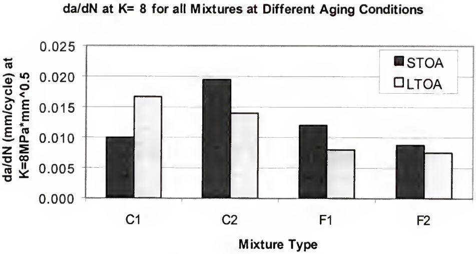

Figure 2-7. Crack Growth Rate at K=8MPa*mm$^{0.5}$ for all Mixtures

2.3.3 Crack Growth and Fracture Threshold in Hot Mix Asphalt

Zhang, Roque and Birgisson (2001) observed that a crack in HMA grows in a stepwise rather than a continuous manner (Figure 2-8). They indicated there is a certain threshold below which damage is considered micro-damage (i.e., damage not associated with crack initiation or crack growth) and fully healable after a rest period, while the non-healable macro-damage (i.e., damage associated with crack initiation or growth) occurs when the threshold is reached or exceeded. Zhang (2000) had investigated many potential models to explain the observed cracking behavior, such as yield strength and strain energy and found the dissipated creep strain energy (DCSE) limit as the fundamental threshold for crack propagation that is independent of mode of loading (strength mode or cyclic mode).

Figure 2-9 illustrates two possible ways that fracture (crack initiation or crack growth) can develop in asphalt mixtures. First (case 1), a number of continuous repeated loads using stresses significantly below the tensile strength would cause damage accumulation due to creep strain energy and lead to fracture if the dissipated creep strain energy (DCSE) threshold is reached. It is important that the mixture may never crack if loading and healing conditions are such that the induced energy does not exceed the energy threshold regardless of the number of loads applied. This may occur in mixtures with high fracture energy thresholds, low rates of micro-damage accumulation, and/or high rates of healing. Second (case 2), during the loading cycle, fracture would occur if any large single load exceeds the fracture energy (FE) threshold. The FE threshold for a large single load is generally higher than the DCSE threshold in case 1 in an amount equal to elastic energy (EE) of the single load. This is because the applied energy of the single load consists of elastic energy and creep strain energy, only creep strain energy is considered towards the fracture development. Case 3 shows that fracture would not occur during a single load application unless the upper threshold is exceeded, even when the lower threshold is exceeded.

It has been determined that the dissipated creep strain energy (DCSE) limit and the fracture energy limit (FE) of asphalt mixtures suitably define the lower and upper threshold values for cases 1 and 2, respectively. These parameters can be easily determined from the stress-strain response of a tensile strength test, as shown in Figure 2-10. The fracture energy limit is determined as the area under the stress-strain curve, while the dissipated creep strain energy limit is the fracture energy minus the elastic energy at the time of fracture. It is necessary to know the elastic modulus of the mixture to determine the elastic energy at fracture. The fracture threshold values and the modulus can be accurately determined using the Superpave Indirect Tensile Test (IDT: Figure 2-11) following the procedures developed by Roque and Buttlar (1992) and Buttlar and Roque (1994).

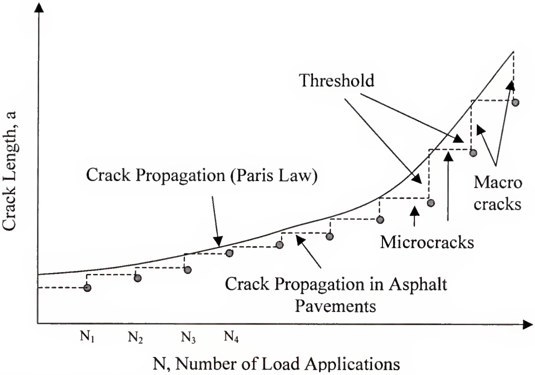
Threshold
Crack Length, a
Crack Propagation (Paris Law)
Macro cracks
Microcracks
Crack Propagation in Asphalt Pavements
N_1
N_2
N_3
N_4
N, Number of Load Applications

Figure 2-8. Illustration of Crack Propagation in Asphalt Mixtures.

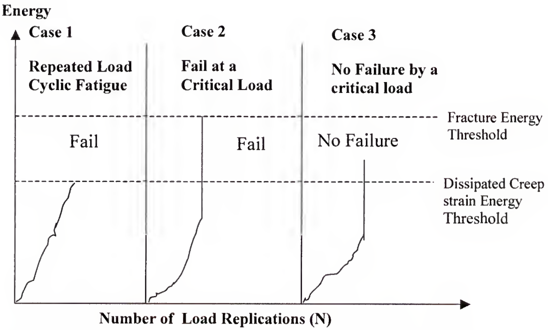
Energy
Case 1
Repeated Load Cyclic Fatigue
Case 2
Fail at a Critical Load
Case 3
No Failure by a critical load
Fracture Energy Threshold
Fail
Fail
No Failure
Dissipated Creep strain Energy Threshold
Number of Load Replications (N)

Figure 2-9. Illustration of Potential Loading Condition (Continuous Loading).

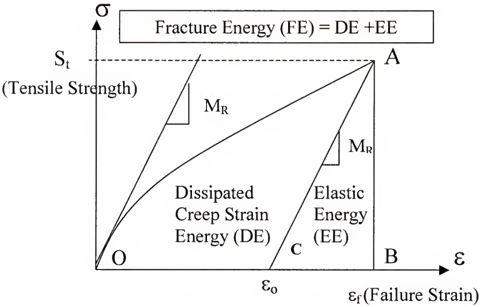

Figure 2-10. Determination of Dissipated Creep Strain Energy.

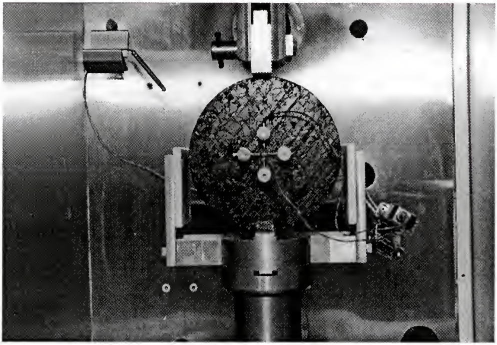

Figure 2-11. The Superpave Indirect Tension Test (IDT).

2.3.4 HMA Fracture Mechanics

Zhang, Roque, Birgisson and Sangpetngam (2001) applied the concept of energy threshold to form a simple predictive model for cyclic indirect tension test based on the following processes:

- A crack starts initiation from the circular hole at the center of IDT sample because of high stress concentration around the hole. The crack initiation phase was assumed 10-mm in length based on the typical aggregate size of typical asphalt mixtures.
- The applied repeated loads cause an accumulation of DCSE in the initiation zone. Each cycle of load induces DCSE at an amount of

$$\text{DCSE/cycle} = \frac{1}{20}\sigma_{AVE}^{2}\, D_1\, m\,(100)^{m-1} \qquad (2\text{-}15)$$

  where σ_{AVE} is the average stress in the zone, D1 and m are creep compliance parameters.

- The continuous cyclic loading will increase the accumulative DCSE in the initiation zone until it reaches the DCSE threshold at which the crack will initiate by the length of the zone (10-mm) as shown in Figure 2-12a.
- After initiation, the stress singularity at the crack tip will draw a high rate of DCSE accumulation in the zone next to the crack tip (Figure 2-12b). The length of this zone is defined by the tensile strength (S_t), applied uniform stress (σ_{FA}), and the current crack length (a_i)

$$\text{Zone length} = \frac{1}{2}\left(\frac{\sigma_{FA}}{S_t}\right)^{2} a_i \qquad (2\text{-}16)$$

- Once the DCSE in this zone builds up and exceeds the threshold, the crack propagates by the length of the zone.
- The DCSE accumulation process continues to grow the crack to the next zone length (Figure 2-12c) at the faster crack growth rate (i.e. fewer number of load cycles to fail the next zone), since the latter zones are always weaker than the earlier zones due to the prolonged DCSE accumulation from the beginning. It means the applied loads not only damage the initiation zone or the zone next to crack tip, but they also cause smaller damage throughout the crack growth path.

The method was successful in predicting crack growth behavior similar to that observed in laboratory results of the cyclic indirect tension test performed on a typical Florida Superpave coarse-graded mix.

Based on the threshold concept and HMA fracture model, there appear to be three key parameters that govern the cracking performance of asphalt mixtures:

- DCSE limit: dissipated creep strain energy to failure,
- m-value: parameter governing the creep strain rate,
- h: healing rate parameter.

In addition, mixture stiffness, as described by modulus, will affect stress distribution in the pavement system.

These parameters can be used not only to predict damage and crack growth in mixtures subjected to generalized loading conditions, but they are also suitable for use in mixture design and optimization. For example, it is clear that cracking performance improves as the DCSE limit increases. Similarly, a lower m-value will result in a lower rate of damage accumulation. However, a lower m-value does not necessarily assure improved cracking performance, since mixtures with lower m-values may also have lower DCSE limits and lower rates of healing.

This appears to explain why age-hardened mixtures exhibit slower rates of crack growth in the laboratory, but perform poorly in the field. The m-value decreases significantly as age-hardening progresses; therefore, for conditions of controlled cracking, the rate of damage accumulation and crack growth decreases as age-hardening increases. However, for random loading conditions occurring in the field, the higher stiffness age-hardened mixture will attract more stress and is very likely to be subjected to individual loading cycles that will exceed the diminished energy limits of the mixture

(Figure 2-13). In addition, age-hardened mixtures will not heal as readily as non-aged mixture, which is a disadvantage that will not be revealed in controlled laboratory crack growth tests.

This hypothesis also explains the discrepancy between the field performance and laboratory results in the case of US301 and I95Duval sections. Fracture tests indicated that I95Duval section had higher threshold than US301 sections did (Figure 2-14). Therefore, US301 sections were likely to experience more non-healable damage, which resulted in severe load-associated cracking in the field. In comparison, the I95Duval section showed more healable damage, which resulted in better performance in the field. However, laboratory results reported that US301 sections had a lower crack growth rate than the I95Duval section. This is because samples were not allowed to heal during the continuous cyclic loadings, so micro-damage was forced to form macro-damage. For this case, the I95Duval section probably had a higher m-value (i.e. higher DCSE increasing rate) than US301, which resulted in a higher crack growth rate in I95Duval samples than in US301 samples.

The HMA fracture mechanics model was developed as a prototype under assumptions of simplified conditions of the IDT test. This hypothesis must be generalized in order to implement into a mechanistic-based analysis system.

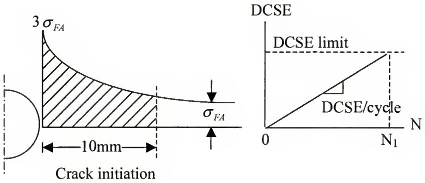

(a) step 1

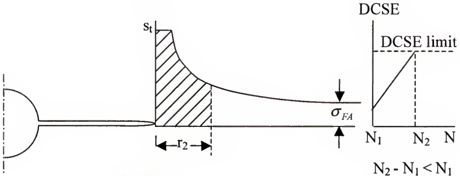

(b) step 2

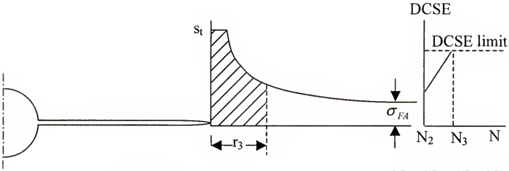

(c) step 3

Figure 2-12. Crack Growth Process.

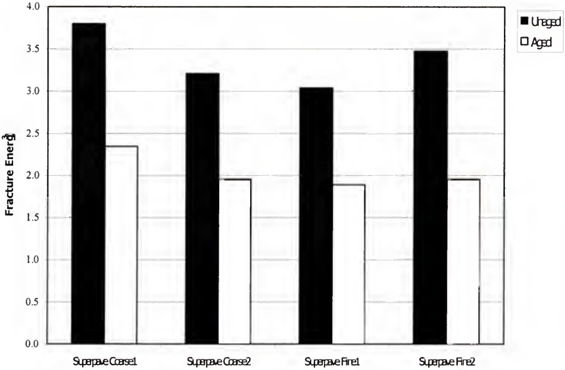

Figure 2-13. Fracture Energy Density of Superpave Mixtures @ 10 C

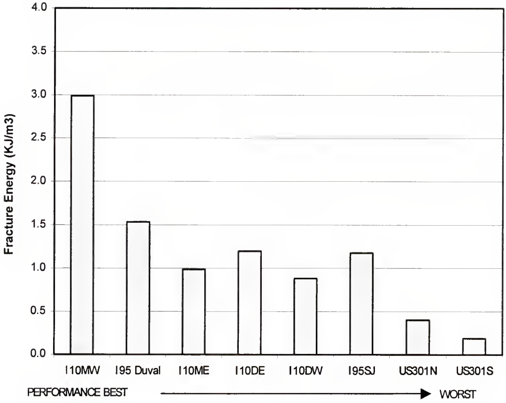

Figure 2-14. Fracture Energy Density of Eight Field Sections @ 10 C.

CHAPTER 3
TWO-DIMENSIONAL DISPLACEMENT DISCONTINUITY METHOD

In this chapter, the fundamentals of the Displacement Discontinuity Method (DDM), along with its capabilities of modeling cracks, and layered pavement structure are explained. In addition, some examples of using the DDM to solve cracking problems are illustrated.

In general, numerical methods for solving boundary value problems can be divided into two types, the domain type, which requires approximations to be made through the domain, and the boundary type, which only requires approximations on the boundary of the domain. Finite difference and finite element methods are examples of the first type, and boundary element methods fall into the second type. Boundary element methods (BEM) only require discretization on the boundaries of the problem; thus have the advantage of reducing the dimension of the problem by one. Boundary element methods are also potentially more accurate than finite difference and finite element methods because their formulation is based on an analytical solution, which holds throughout the domain.

The finite element method (FEM) is a very popular tool for the evaluation of stresses and displacements in many engineering fields. However, the FEM tends to be extremely cumbersome, if not prohibitive with respect to addressing cracking in asphalt pavements because of the need for highly refined meshes around the cracking area. Improper mesh generation will result in a failure to capture the very important stress singularity at the crack tip. Also, to simulate crack growth, an elaborate remeshing corresponding to the growing crack geometry is required.

As an example of the numerical intensity required to solve the relatively simple problem of simulating crack growth in the Superpave Indirect Tension Test (IDT) with the finite element method, researchers have found that up to 11,000 (eleven thousand) elements are needed for each crack length to obtain reasonable stress intensity factors (Roque et al.1999; Zhang 2000). In addition, once the crack is ready to grow, the problem has to be re-meshed and resolved. The computational intensity required puts these types of problems out of the realm of reasonableness for the typical capabilities of personal computers, which means that only select research organizations and major universities have the capabilities to perform these types of calculations.

The displacement discontinuity method (DDM) is a boundary element-based method that may offer a potential solution to the requirement of having a very refined mesh, with a large number of elements, as well as the requirement for elaborate re-meshing with crack growth (Crouch and Starfield 1990; Shou and Crouch 1995; Siebrits and Crouch 1994). The DDM requires meshes only on the boundaries of an object or pavement, including cracks. This means that the number of elements required is reduced significantly. Also, the stress singularity at the crack tip is naturally included in the DDM by using a representative displacement distribution around the crack tip. Crack growth is addressed simply by adding more DDM elements in regions of crack growth. Most importantly, the success of the DDM in other fields, such as rock mechanics, mining, and the oil industry leaves no apparent reason why it should not be applicable to problems common to asphalt pavements (Napier 1999; Einstein and Bobet 1999; Siebrits et al. 1997, 2001; Guzina 2001; Siebrits and Peirce 2000).

The displacement discontinuity (DD) boundary element method is a numerical method for analysis of stresses and displacements. Its features are comparable to the well-known finite element method (FEM). In fact, the DD method can solve any elastic problem that is solved by FEM.

The basis for the DD method is the well-known linear elasticity concept that a known displacement of a point anywhere in a body allows for the solution of displacements and stresses at all other points. Rather than expressing the known displacement in absolute terms, it can be expressed in terms of discontinuous displacements. Examples of discontinuous displacements include cracks, fissures, and joints. Thus, the DD method solves for stresses and displacements within an elastic solid in terms of constant normal and shear displacement discontinuities over one or more elements in a body. This means that the DD method can be used to directly calculate the displacement normal and along any crack surface, making it uniquely suitable for crack problems.

3.1 Fundamental Considerations

The boundary element method uses the fundamental solutions of linear elasticity that relate displacement at any given location to the application of a unit force at another location. The Kelvin's solution (Sokolnikoff 1956), provides the basis for the fundamental solution, $U_{ij}(\underline{x},\underline{\xi})$ used in this work. $U_{ij}(\underline{x},\underline{\xi})$ represents the i-component of the displacement at point $\underline{x}$ due to a unit force e_j acting in the j-direction at point $\underline{\xi}$. While the fundamental solution $T_{ij}(\underline{x},\underline{\xi})$ represents the i-component of the traction at point $\underline{x}$ due to a unit force e_j acting in the j-direction at point $\underline{\xi}$. Thus, each component of displacements and tractions at point $\underline{x}$ on boundary of the reference state caused by the unit line force e_j acting at point $\underline{\xi}$ can be written in the form:

$$u'_i(\underline{x}) = U_{ij}(\underline{x},\underline{\xi})\, e_j(\underline{\xi}) \tag{3-1}$$

$$t'_i(\underline{x}) = T_{ij}(\underline{x},\underline{\xi})\, e_j(\underline{\xi}) \tag{3-2}$$

Substitution Equations (3-2) and (3-3) into Somigliana's formula (e.g. Love 1944) leads to

$$\varepsilon(\underline{\xi})\, u_i(\underline{\xi}) = \int_S t_j(\underline{x})\, U_{ij}(\underline{x},\underline{\xi})\, ds(\underline{x}) - \int_S u_j(\underline{x})\, T_{ij}(\underline{x},\underline{\xi})\, ds(\underline{x}) \tag{3-3}$$

where ε is defined as

$$\varepsilon(\underline{\xi}) = \begin{cases} 0 & \underline{\xi} \notin V \\ 1 & \underline{\xi} \in V \\ 0.5 & \underline{\xi} \in S \end{cases} \tag{3-4}$$

Equation (3-3) can be applied to interior and exterior regions of boundary S in Figure 3-1. For the interior domain R_{int}, let the boundary displacements and tractions be u_i and t_i respectively. The boundary integral equation (3-3) for region R_{int} is

$$\varepsilon(\underline{\xi})\, u_i(\underline{\xi}) = \int_S t_j(\underline{x})\, U_{ij}(\underline{x},\underline{\xi})\, ds(\underline{x}) - \int_S u_j(\underline{x})\, T_{ij}(\underline{x},\underline{\xi})\, ds(\underline{x}) \tag{3-5}$$

Now let the boundary displacements and tractions for the exterior region R_{ext} be $\hat{u}$ and $\hat{t}$ respectively. Application of the boundary integral equation (3-4) for region R_{ext} gives

$$\varepsilon(\underline{\xi})\, u_i(\underline{\xi}) = -\left[\int_S \hat{t}_j(\underline{x})\, U_{ij}(\underline{x},\underline{\xi})\, ds(\underline{x}) - \int_S \hat{u}_j(\underline{x})\, T_{ij}(\underline{x},\underline{\xi})\, ds(\underline{x}) \right] \tag{3-7}$$

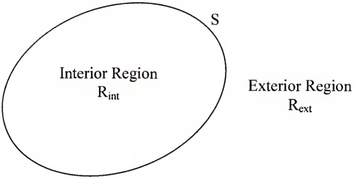

Figure 3-1. Interior and Exterior Regions of Boundary S.

The negative sign in the right hand side of equation appears because the normal to the boundary of exterior region is in the opposite direction of the normal to the boundary for the interior region. If the boundaries of interior and exterior are taken as the upper and lower surfaces of a closed-loop crack, t_j and $\hat{t}_j$ then become the tractions acting inside the crack and are equal but in opposite direction on boundary S. Addition of Equations (3-5) and (3-6) results in the following equation:

$$u_i(\underline{\xi}) = \int_S [u_j(\underline{x}) - \hat{u}_j(\underline{x})]\, T_{ij}(\underline{x}, \underline{\xi})\, ds(\underline{x}) \tag{3-7}$$

The $\underline{x}$ and $\underline{\xi}$ in Equation (3-7) can be interchanged to result in the following equation.

$$u_i(\underline{x}) = \int_S [u_j(\underline{\xi}) - \hat{u}_j(\underline{\xi})]\, T_{ij}(\underline{\xi}, \underline{x})\, ds(\underline{\xi}) \tag{3-8}$$

where $\underline{x}$ is any point in the domain including boundary, $u_j(\underline{\xi}) - \hat{u}_j(\underline{\xi})$ is the relative displacement between two surfaces of crack at point $\underline{\xi}$ in j-direction, which is referred as displacement discontinuity. Applying Hooke's law and kinematic equation to Equation (3-8), one can obtain the equation for stresses as

$$\sigma_{ij}(\underline{x}) = \int_S [u_j(\underline{\xi}) - \hat{u}_j(\underline{\xi})]\, G_{ij}(\underline{\xi}, \underline{x})\, ds(\underline{\xi}) \tag{3-9}$$

Equations (3-8) and (3-9) form the basis of the displacement discontinuity method. The next step is to determine the fundamental solutions for a unit displacement discontinuity $[u_j(\underline{\xi}) - \hat{u}_j(\underline{\xi})]$.

Now let us consider an element of crack in which opposing surfaces can be displaced relative to one another, as shown in Figures 3-2. The displacement discontinuity is the displacement of one surface relative to the opposing surface of the same element and it can be in direction of: normal or tangential to the elemental surfaces.

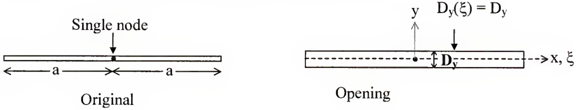

(a) Constant Element

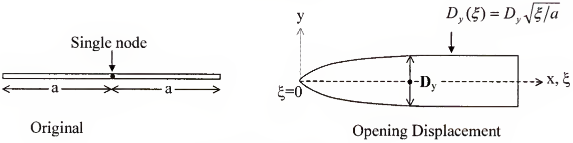

(b) Crack-Tip Element

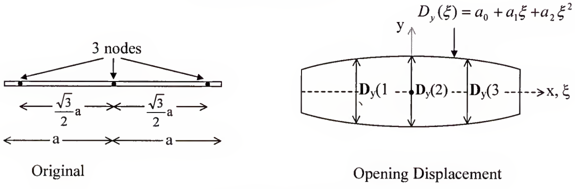

(c) Quadratic Element

Figure 3-2. Displacement Discontinuity Elements.

The variable displacement discontinuities over the element are defined as

$$D_y(x) = u_y(x, 0_-) - u_y(x, 0_+)\,, \qquad |x| < a \tag{3-10}$$

$$D_x(x) = u_x(x, 0_-) - u_x(x, 0_+)\,, \qquad |x| < a \tag{3-11}$$

where a is one half of the element length.

Based on the equilibrium equations and stress-strain relations for an isotropic linearly elastic material, Crouch (1976) developed a set of stress-displacement solutions induced by the displacement discontinuities of a crack (element) under plane strain conditions:

$$u_x = [-2(1-\nu)\,\psi_{,y} + y\,\psi_{,xx}] + [\,(1-2\nu)\,\phi_{,x} + y\,\phi_{,xy}]$$

$$u_y = [-(1-2\nu)\,\psi_{,x} + y\,\psi_{,xy}] + [-2(1-\nu)\,\phi_{,y} + y\,\phi_{,yy}] \tag{3-12}$$

$$\sigma_{xx} = 2G\,[-2\,\psi_{,xy} - y\,\psi_{,xyy}] + 2G\,[-\phi_{,yy} - y\,\phi_{,yyy}]$$

$$\sigma_{yy} = 2G\,[y\,\psi_{,xyy}] + 2G\,[-\phi_{,yy} + y\,\phi_{,yyy}] \tag{3-13}$$

$$\sigma_{xy} = 2G\,[-\psi_{,yy} - y\,\psi_{,yyy}] + 2G\,[y\,\phi_{,xyy}]$$

where

x, y are the local coordinates measured from the center of the crack

u_x and u_y are solutions of two displacement components at a location (x, y)

σ_{xx} , σ_{yy} and σ_{xy} are solutions of stress state at a location (x, y)

G, ν are shear modulus and Poisson ratio of the solid material

ψ and ϕ are potential functions.

$f_{,ab} = \dfrac{\partial^2 f}{\partial a \partial b}$ is the second derivative of function f in respective to a and b

$f_{,abc} = \dfrac{\partial^3 f}{\partial a \partial b \partial c}$ is the third derivative of function f in respective to a, b and c

$D_x(\xi)$, $D_y(\xi)$ are variations of shear and normal displacement discontinuities over the DD element.

Crouch (1976) found the potential functions that satisfy the stresses and displacements at boundary of crack as follows:

$$\phi_{,x} = \frac{1}{4\pi(1-\nu)} \int_{-a}^{a} D_y(\xi) \frac{x-\xi}{(x-\xi)^2+y^2} d\xi \tag{3-14}$$

$$\phi_{,y} = \frac{1}{4\pi(1-\nu)} \int_{-a}^{a} D_y(\xi) \frac{y}{(x-\xi)^2+y^2} d\xi \tag{3-15}$$

$$\psi_{,x} = \frac{1}{4\pi(1-\nu)} \int_{-a}^{a} D_x(\xi) \frac{x-\xi}{(x-\xi)^2+y^2} d\xi \tag{3-16}$$

$$\psi_{,y} = \frac{1}{4\pi(1-\nu)} \int_{-a}^{a} D_x(\xi) \frac{y}{(x-\xi)^2+y^2} d\xi \tag{3-17}$$

Thus, the relations between the stress/displacement and the displacement discontinuities become

$$\begin{aligned} u_x = {} & \frac{-2(1-\nu)}{4\pi(1-\nu)} \int_{-a}^{a} D_x(\xi) \frac{y}{(x-\xi)^2+y^2} d\xi + \frac{y}{4\pi(1-\nu)} \frac{\partial}{\partial x} \int_{-a}^{a} D_x(\xi) \frac{x-\xi}{(x-\xi)^2+y^2} d\xi \\ & + \frac{1-2\nu}{4\pi(1-\nu)} \int_{-a}^{a} D_y(\xi) \frac{x-\xi}{(x-\xi)^2+y^2} d\xi + \frac{y}{4\pi(1-\nu)} \frac{\partial}{\partial y} \int_{-a}^{a} D_y(\xi) \frac{x-\xi}{(x-\xi)^2+y^2} d\xi \end{aligned} \tag{3-18}$$

$$\begin{aligned} u_y = {} & \frac{-(1-2\nu)}{4\pi(1-\nu)} \int_{-a}^{a} D_x(\xi) \frac{x-\xi}{(x-\xi)^2+y^2} d\xi + \frac{y}{4\pi(1-\nu)} \frac{\partial}{\partial y} \int_{-a}^{a} D_x(\xi) \frac{x-\xi}{(x-\xi)^2+y^2} d\xi \\ & \frac{-2(1-\nu)}{4\pi(1-\nu)} \int_{-a}^{a} D_y(\xi) \frac{y}{(x-\xi)^2+y^2} d\xi + \frac{y}{4\pi(1-\nu)} \frac{\partial}{\partial y} \int_{-a}^{a} D_y(\xi) \frac{y}{(x-\xi)^2+y^2} d\xi \end{aligned} \tag{3-19}$$

$$\sigma_{xx} = \frac{2G}{4\pi(1-\nu)} \left[-2\frac{\partial}{\partial y} \int_{-a}^{a} D_x(\xi) \frac{x-\xi}{(x-\xi)^2+y^2} d\xi - y\frac{\partial^2}{\partial y^2} \int_{-a}^{a} D_x(\xi) \frac{x-\xi}{(x-\xi)^2+y^2} d\xi \right] +$$

$$\frac{2G}{4\pi(1-\nu)}[-\frac{\partial}{\partial y}\int_{-a}^{a} D_y(\xi)\frac{y}{(x-\xi)^2+y^2}d\xi - y\frac{\partial^2}{\partial y^2}\int_{-a}^{a} D_y(\xi)\frac{y}{(x-\xi)^2+y^2}d\xi] \quad (3\text{-}20)$$

$$\sigma_{yy} = \frac{2G}{4\pi(1-\nu)}[y\frac{\partial^2}{\partial y^2}\int_{-a}^{a} D_x(\xi)\frac{x-\xi}{(x-\xi)^2+y^2}d\xi] +$$

$$\frac{2G}{4\pi(1-\nu)}[-\frac{\partial}{\partial y}\int_{-a}^{a} D_y(\xi)\frac{y}{(x-\xi)^2+y^2}d\xi + y\frac{\partial^2}{\partial y^2}\int_{-a}^{a} D_y(\xi)\frac{y}{(x-\xi)^2+y^2}d\xi] \quad (3\text{-}21)$$

$$\sigma_{xy} = \frac{2G}{4\pi(1-\nu)}[-\frac{\partial}{\partial y}\int_{-a}^{a} D_x(\xi)\frac{y}{(x-\xi)^2+y^2}d\xi - y\frac{\partial^2}{\partial y^2}\int_{-a}^{a} D_x(\xi)\frac{y}{(x-\xi)^2+y^2}d\xi] +$$

$$\frac{2G}{4\pi(1-\nu)}[y\frac{\partial^2}{\partial y^2}\int_{-a}^{a} D_y(\xi)\frac{x-\xi}{(x-\xi)^2+y^2}d\xi] \quad (3\text{-}22)$$

If a crack with length 2a covers the boundary in the domain, Equations (3-18) to (3-22) are equivalent to Equations (3-9) and (3-10). The term $D_j(\xi)$ in Equations (3-18) to (3-22) is the term $[u_j(\underline{\xi}) - \hat{u}_j(\underline{\xi})]$ in Equations (3-9) and (3-10). The remaining parts of coefficient and geometrical terms in Equations (3-18) to (3-22) then represent the term $T_{ij}(\underline{\xi}, \underline{x})$ and $G_{ij}(\underline{\xi}, \underline{x})$ in Equations (3-9) and (3-10). Thus the displacement discontinuity equation for a portion of crack boundary is now established. In the following, the details of extending Equations (3-18) to (3-22) to cover the whole boundary of a problem will be described.

3.2 Displacement Discontinuity Element Formulation

For illustrative purposes, the constant DD element formulation will be described below. A constant DD element is composed of two surfaces that displace equally relative to one another. Figure 3-2a illustrates the constant displacement discontinuity in its normal direction. The displacement discontinuity over the element is defined as

$$D_s = u_s^- - u_s^+ \quad (3\text{-}23)$$

$$D_n = u_n^- - u_n^+ \tag{3-24}$$

where

D_s and D_n are constant shear and normal displacement discontinuities

u_s^+ and u_n^+ are shear and normal displacements of the upper surface of crack

u_s^- and u_n^- are shear and normal displacements of the lower surface of crack

In reality, D_s represents sliding deformation and D_n represents opening (D_n is negative) or closing (D_n is positive) of the crack segment.

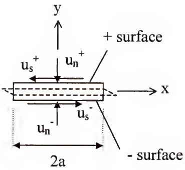

Figure 3-3. A Constant DD Element Illustrating Positive Displacement Discontinuity.

For a constant DD element, substitute $D_x(\xi) = D_s$, $D_y(\xi) = D_n$ into Equations (3-18 to 3-22) to obtain

$$u_x = [-2\,II + \frac{y}{1-v}\,I_{,x}]\,D_s + [\frac{1-2v}{1-v}\,I + \frac{y}{1-v}\,I_{,y}]\,D_n \tag{3-25}$$

$$u_y = [-\frac{1-2v}{1-v}\,I + \frac{y}{1-v}\,I_{,y}]\,D_s + [-2\,II + \frac{y}{1-v}\,II_{,y}]\,D_n \tag{3-26}$$

$$\sigma_{xx} = \frac{2G}{1-v}[-2\,I_{,y} - y\,I_{,yy}]\,D_s + \frac{2G}{1-v}\,[-II_{,y} - y\,II_{,yy}]\,D_n \tag{3-27}$$

$$\sigma_{yy} = \frac{2G}{1-\nu}\ [y\ I_{,yy}]\ D_s + \frac{2G}{1-\nu}\ [-II_{,y} + y\ II_{,yy}]\ D_n \tag{3-28}$$

$$\sigma_{xy} = \frac{2G}{1-\nu}\ [-II_{,y} - y\ II_{,yy}]\ D_s + \frac{2G}{1-\nu}\ [\ y\ I_{,yy}]\ D_n \tag{3-29}$$

where

$$I = \frac{1}{4\pi} \int_{-a}^{a} \frac{x-\xi}{(x-\xi)^2 + y^2} d\xi \tag{3-30}$$

$$II = \frac{1}{4\pi} \int_{-a}^{a} \frac{y}{(x-\xi)^2 + y^2} d\xi \tag{3-31}$$

The functions I, II and their derivatives are given in Appendix B. By the compatibility equations, the normal strains can be obtained by taking geometrical derivatives of equation (3-25 and 3-26) to obtain

$$\varepsilon_{xx} = u_{x\ ,x} = [-2II_{,x} + \frac{y}{1-\nu} I_{,xx}]\ D_s + [\frac{1-2\nu}{1-\nu} I_{,x} + \frac{y}{1-\nu}\ I_{,xy}]\ D_n \tag{3-32}$$

$$\varepsilon_{yy} = u_{y\ ,y} = [-\frac{1-2\nu}{1-\nu} I_{,y} + \frac{1}{1-\nu} I_{,y} + \frac{y}{1-\nu}\ I_{,yy}]\ D_s + [-2\ II_{,y} + \frac{1}{1-\nu} II_{,y} + \frac{y}{1-\nu}\ II_{,yy}]\ D_n \tag{3-33}$$

After rearranging the order of derivatives, we can obtain

$$\varepsilon_{xx} = [-2\ I_{,y} - \frac{y}{1-\nu} I_{,yy}]\ D_s + [\frac{1-2\nu}{1-\nu} I_{,x} - \frac{y}{1-\nu} II_{,yy}]\ D_n \tag{3-34}$$

$$\varepsilon_{yy} = [\frac{2\nu}{1-\nu} I_{,y} + \frac{y}{1-\nu} I_{,yy}]\ D_s + [\ -\frac{1-2\nu}{1-\nu} II_{,y} + \frac{y}{1-\nu} II_{,yy}]\ D_n \tag{3-35}$$

The shear strain is obtained by

$$\varepsilon_{xy} = \sigma_{xy}/2G = [-\frac{1}{1-\nu} II_{,y} - \frac{y}{1-\nu}\ II_{,yy}]\ D_s + \ [\frac{y}{1-\nu}\ I_{,yy}]\ D_n \tag{3-36}$$

If the point of interest is located on the line of another DD element, it is usual to calculate stresses and displacements and transform them in the directions normal and tangential to the DD element as normal and shear stresses, σ_n and σ_s , normal and shear displacements, u_n and u_s.

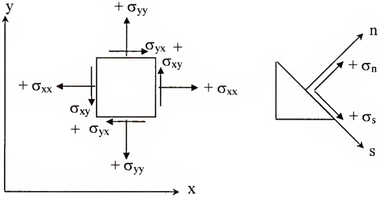

Figure 3-4. Directions of Positive Stress Components

Figure 3-4 shows the sign convention used for stresses and strains. A positive sign means tension, a negative sign means compression for normal stress and strain. The relationship between sign and direction of shear stresses is shown in Figure 3-4.

3.3 Numerical Formulation

Let us assume there are N constant DD elements in a representative model. Each element has normal and shear displacement discontinuities. The DDs of element j will induce stresses and displacements at any other point in the solid body including at other element locations. Let us consider a pair of elements j and i. From Equation (3-27) to (3-29), the DDs of element j induce stresses at the center of element i as

$$\sigma_{xx}{}^{i} = \frac{2G}{1-\nu}\,[-2\,I_{,y} - y\,I_{,yy}]\,D_s^j + \frac{2G}{1-\nu}\,[-II_{,y} - y\,II_{,yy}]\,D_n^j \qquad (3\text{-}37)$$

$$\sigma_{yy}{}^{i} = \frac{2G}{1-\nu}\,[y\,I_{,yy}]\,D_s^j + \frac{2G}{1-\nu}\,[-II_{,y} + y\,II_{,yy}]\,D_n^j \qquad (3\text{-}38)$$

$$\sigma_{xy}{}^{i} = \frac{2G}{1-\nu}\,[-II_{,y} - y\,II_{,yy}]\,D_s^j + \frac{2G}{1-\nu}\,[\,y\,I_{,yy}]\,D_n^j \qquad (3\text{-}39)$$

The x and y coordinates in the above equations are the distance from center of element i to center of element j, i.e. $x = x^i - x^j$, $y = y^i - y^j$. The stresses at element i presented above are in the local coordinate system of element j. To obtain the shear and normal stresses at element i, the coordinate transformations are applied

$$\sigma_s{}^i = -(\sigma_{xx}{}^i - \sigma_{yy}{}^i) \sin\beta \cos\beta + \sigma_{xy}{}^i (\cos^2\beta - \sin^2\beta) \tag{3-40}$$

$$\sigma_n{}^i = \sigma_{xx}{}^i \sin^2\beta - 2\sigma_{xy}{}^i \sin\beta \cos\beta + \sigma_{yy}{}^i \cos^2\beta \tag{3-41}$$

where β is the angle between the line of element i and the line of element j.

After substituting Equations (3-37 to 3-39) into Equations (3-40 and 3-41) and rearranging the terms, we can obtain

$$\sigma_s{}^i = A_{ss}{}^{ij} D_s{}^j + A_{sn}{}^{ij} D_n{}^j \tag{3-42a}$$

$$\sigma_n{}^i = A_{ns}{}^{ij} D_s{}^j + A_{nn}{}^{ij} D_n{}^j \tag{3-42b}$$

$$A_{ss}{}^{ij} = \frac{2G}{1-\nu} [\sin(2\beta)\, I_{,y} + \cos(2\beta)\, I_{,x} + y\, (\sin(2\beta)\, I_{,yy} - \cos(2\beta)\, II_{,yy})] \tag{3-43a}$$

$$A_{sn}{}^{ij} = \frac{2G}{1-\nu} [\, y\, (\cos(2\beta)\, I_{,yy} + \sin(2\beta)\, II_{,yy})] \tag{3-43b}$$

$$A_{ns}{}^{ij} = \frac{2G}{1-\nu} [-2 \sin^2\beta\, I_{,y} - \sin(2\beta)\, I_{,x} + y\, (\cos(2\beta)\, I_{,yy} + \sin(2\beta)\, II_{,yy})] \tag{3-43c}$$

$$A_{nn}{}^{ij} = \frac{2G}{1-\nu} [\, I_{,x} - y\, (\sin(2\beta)\, I_{,yy} - \cos(2\beta)\, II_{,yy})] \tag{3-43d}$$

Similarly, the displacements at element i induced by DDs of element j are

$$u_x{}^i = [-2\, II + \frac{y}{1-\nu} I_{,x}]\, D_s{}^j + [\frac{1-2\nu}{1-\nu} I + \frac{y}{1-\nu} I_{,y}]\, D_n{}^j \tag{3-44}$$

$$u_y{}^i = [-\frac{1-2\nu}{1-\nu} I + \frac{y}{1-\nu} I_{,y}]\, D_s{}^j + [-2\, II + \frac{y}{1-\nu} II_{,y}]\, D_n{}^j \tag{3-45}$$

Applying the following coordinate transformations for displacements:

$$u_s^{\,i} = u_x^{\,i} \cos\beta + u_y^{\,i} \sin\beta \tag{3-46}$$

$$u_n^{\,i} = -u_x^{\,i} \sin\beta + u_y^{\,i} \cos\beta \tag{3-47}$$

and substituting Equations (3-44 and 3-45) into Equations (3-46 and 3-47) and rearranging the terms, we can obtain

$$u_s^{\,i} = B_{ss}^{\,ij}\, D_s^{\,j} + B_{sn}^{\,ij}\, D_n^{\,j} \tag{3-48a}$$

$$u_n^{\,i} = B_{ns}^{\,ij}\, D_s^{\,j} + B_{nn}^{\,ij}\, D_n^{\,j} \tag{3-48b}$$

$$B_{ss}^{\,ij} = -2\ \mathrm{II} \cos\beta - \frac{1-2\nu}{1-\nu}\ \mathrm{I} \sin\beta + \frac{y}{1-\nu}\ (\ \mathrm{I}_{,y} \sin\beta + \mathrm{I}_{,x} \cos\beta) \tag{3-49a}$$

$$B_{sn}^{\,ij} = -2\ \mathrm{II} \sin\beta + \frac{1-2\nu}{1-\nu}\ \mathrm{I} \cos\beta + \frac{y}{1-\nu}\ (\ \mathrm{I}_{,y} \cos\beta + \mathrm{II}_{,y} \sin\beta) \tag{3-49b}$$

$$B_{ns}^{\,ij} = 2\ \mathrm{II} \sin\beta - \frac{1-2\nu}{1-\nu}\ \mathrm{I} \cos\beta + \frac{y}{1-\nu}\ (\ \mathrm{I}_{,y} \cos\beta + \mathrm{II}_{,y} \sin\beta) \tag{3-49c}$$

$$B_{nn}^{\,ij} = -2\ \mathrm{II} \cos\beta - \frac{1-2\nu}{1-\nu}\ \mathrm{I} \sin\beta - \frac{y}{1-\nu}\ (\ \mathrm{I}_{,y} \sin\beta + \mathrm{I}_{,x} \cos\beta) \tag{3-49d}$$

The terms $A_{ss}^{\,ij}$, $A_{sn}^{\,ij}$, $A_{ns}^{\,ij}$, $A_{nn}^{\,ij}$, $B_{ss}^{\,ij}$, $B_{sn}^{\,ij}$, $B_{ns}^{\,ij}$, $B_{nn}^{\,ij}$ are called influence coefficients and would be used to determine the unknown displacement discontinuities on each element.

Since there are N constant DD elements, it results in 2N unknown displacement discontinuities in the problem. However, these unknown displacement discontinuities together must induce stresses or displacements equal to the prescribed values at all segments (elements) representing the boundary of the structure. For instance, the normal or shear tractions (t_n , t_s) are prescribed on the ith element, the sum of influences by element 1 to N must be

$$t_s^{\,i} = \sum_{j=1}^{N} A_{ss}^{\,ij}\, D_s^{\,j} + \sum_{j=1}^{N} A_{sn}^{\,ij}\, D_n^{\,j} \tag{3-50}$$

$$t_n{}^i = \sum_{j=1}^{N} A_{ns}{}^{ij} D_s^j + \sum_{j=1}^{N} A_{nn}{}^{ij} D_n^j \tag{3-51}$$

If the normal or shear displacements (bu_n , bu_s) are prescribed on the ith element, the sum of influences by element 1 to N must be

$$u_s^i = \sum_{j=1}^{N} B_{ss}{}^{ij} D_s^j + \sum_{j=1}^{N} B_{sn}{}^{ij} D_n^j \tag{3-52}$$

$$u_n^i = \sum_{j=1}^{N} B_{ns}{}^{ij} D_s^j + \sum_{j=1}^{N} B_{nn}{}^{ij} D_n^j \tag{3-53}$$

Thus a system of 2N linear equations can be formed:

$$b_s^i = \sum_{j=1}^{N} C_{ss}{}^{ij} D_s^j + \sum_{j=1}^{N} C_{sn}{}^{ij} D_n^j \qquad i = 1 \text{ to } N \tag{3-54}$$

$$b_n^i = \sum_{j=1}^{N} C_{ns}{}^{ij} D_s^j + \sum_{j=1}^{N} C_{nn}{}^{ij} D_n^j \qquad i = 1 \text{ to } N \tag{3-55}$$

where

$C_{ss}{}^{ij}$, $C_{sn}{}^{ij}$ are $A_{ss}{}^{ij}$, $A_{sn}{}^{ij}$, and $b_s^i = t_s{}^i$, if the shear traction is prescribed on element i

$C_{ss}{}^{ij}$, $C_{sn}{}^{ij}$ are $B_{ss}{}^{ij}$, $B_{sn}{}^{ij}$, and $b_s^i = u_s{}^i$, if the shear displacement is prescribed on element i

$C_{ns}{}^{ij}$, $C_{nn}{}^{ij}$ are $A_{ns}{}^{ij}$, $A_{nn}{}^{ij}$, and $b_n^i = t_n{}^i$, if the normal traction is prescribed on element i

$C_{ns}{}^{ij}$, $C_{nn}{}^{ij}$ are $B_{ns}{}^{ij}$, $B_{nn}{}^{ij}$, and $b_n^i = u_n{}^i$, if the normal displacement is prescribed on element i .

With the known values of normal- and shear- traction or displacement on each of the boundary elements, the solutions of 2N elemental displacement discontinuities can be obtained by an equation solving method such as the Gauss Elimination.

After solving for the 2N displacement discontinuities, they can be used to calculate stresses and displacements at any location inside the structure and along the boundary. By using the principle of superposition and Equations (3-25 to 3-29), the stresses and displacements at a location P in the problem are the sums of the effects due to displacement discontinuities of element 1 to element N.

$$u_x(P) = \sum_{j=1}^{N} [-2\,II + \frac{y}{1-\nu} I_{,x}]\, D_s^j + \sum_{j=1}^{N} [\frac{1-2\nu}{1-\nu} I + \frac{y}{1-\nu} I_{,y}]\, D_n^j \qquad (3\text{-}56)$$

$$u_y(P) = \sum_{j=1}^{N} [-\frac{1-2\nu}{1-\nu} I + \frac{y}{1-\nu} I_{,y}]\, D_s^j + \sum_{j=1}^{N} [-2\,II + \frac{y}{1-\nu} II_{,y}]\, D_n^j \qquad (3\text{-}57)$$

$$\sigma_{xx}(P) = \sum_{j=1}^{N} \frac{2G}{1-\nu} [-2\, I_{,y} - y\, I_{,yy}]\, D_s^j + \sum_{j=1}^{N} \frac{2G}{1-\nu} [-II_{,y} - y\, II_{,yy}]\, D_n^j \qquad (3\text{-}58)$$

$$\sigma_{yy}(P) = \sum_{j=1}^{N} \frac{2G}{1-\nu} [y\, I_{,yy}]\, D_s^j + \sum_{j=1}^{N} \frac{2G}{1-\nu} [-II_{,y} + y\, II_{,yy}]\, D_n^j \qquad (3\text{-}59)$$

$$\sigma_{xy}(P) = \sum_{j=1}^{N} \frac{2G}{1-\nu} [-II_{,y} - y\, II_{,yy}]\, D_s^j + \sum_{j=1}^{N} \frac{2G}{1-\nu} [\, y\, I_{,yy}]\, D_n^j \qquad (3\text{-}60)$$

where x, y in the above equations are the distance from location P to center of element j.

3.4 Modeling of Geometry and Boundary Conditions

When a number of DD elements are connected end-to-end, a closed loop is created. This allows for the creation of a representative model of a structure by placing a series of DD elements along the boundaries of the structure. For consistency purposes, the element must be placed in such a direction that its negative surface faces the inside of the structure. Figure 3-5 shows an example of a circular disk and its representative model. Accordingly, the following discretization convention is adopted: the boundary of a finite body is traversed in the clockwise sense, whereas the boundary of a cavity is traversed in the counterclockwise sense. Figure 3-5 illustrates the directions of elements for a finite body structure and a cavity in an infinite solid structure.

External tractions and restricted displacements that are applied on each portion of the boundaries of the real body are included by prescribing them at the corresponding boundary elements. The prescribed conditions are in the format of normal- and shear-tractions (t_n , t_s) or displacements (u_n , u_s) and are applied at the negative face of the elements.

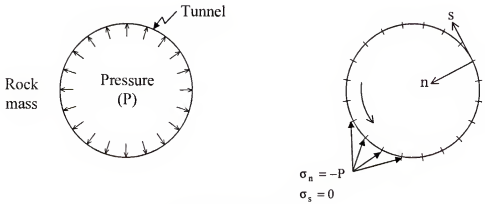

(a) Pressurized Tunnel

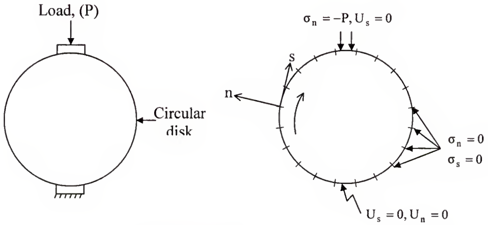

(b) Indirect Tension

Figure 3-5. Modeling of Structural Geometry and Boundary Conditions

To model a pressurized tunnel in the solid rock (Figure 3-5a), a tunnel model is created by placing N number of DD elements end-to-end, counterclockwise, on the perimeter of the circular tunnel. The area outside the closed elemental loop represents the rock body. Since the pressure in tunnel acts normal to the tunnel surface, every boundary element has the prescribed normal traction (σ_n) equal to the pressure (p) and the prescribed shear stress (σ_s) equal to zero.

On the other hand, a circular disk under indirect tension (Figure 3-5b) is also modeled by the same pattern of discretized circle as the tunnel problem, but in the clockwise direction. In this case, the area inside the closed contour represents the disk. The vertical loading is represented by applying σn equal to the applied vertical pressure at the uppermost and bottommost segments of the disk. The remaining segments are prescribed under zero normal- and shear- stresses.

3.5 Crack-Tip Element

To model a real crack with the DD method, the crack is simulated by a series of relatively few DD elements connected in series. To capture the very important singularity characteristic of a crack tip, a special crack-tip element must be placed at both ends of the line. Unlike a basic DD element in which opposing surfaces displace constantly over an entire segment, a crack-tip element has $\sqrt{r}$ distribution of displacement discontinuities (Figure 3-2c), which is more representative of a real crack tip opening. This displacement distribution leads to the fundamental solution of $1/\sqrt{r}$ stress singularity around the crack-tip element. Similarly, crack growth can be addressed by simply adding more constant-DD elements as the incremental crack length develops, rather than remeshing the whole mesh as in the finite element method. The I and II terms in Equations (3-25) to (3-29) for crack-tip element should become

$$\mathrm{I} = \frac{1}{4\pi} \int_{0}^{2a} \frac{x-\xi}{(x-\xi)^2 + y^2} \cdot \sqrt{\frac{\xi}{a}}\, \mathrm{d}\xi \tag{3-61}$$

$$\mathrm{II} = \frac{1}{4\pi} \int_{0}^{2a} \frac{y}{(x-\xi)^2 + y^2} \cdot \sqrt{\frac{\xi}{a}}\, \mathrm{d}\xi \tag{3-62}$$

The expansion of terms I and II is presented in Appendix B.

3.6 Comparison to Finite Element Method

The accuracy of finite element solutions is dependent on the number of elements used to describe the body. The greater the number of elements the problem has, the more accurate the solution, provided that the elements are placed in the right locations. However, more elements create more unknown equations, which require more computation time. The DD method only requires placing elements on the boundary of the body, as shown in Figure 3-6. In this context, cracks are considered boundaries as well. This reduces the number of elements significantly, as well as reducing the number of equations in the solving process.

Simulation of crack growth with the finite element method requires a separate mesh for each crack length. Each crack length simulation requires a highly refined mesh around the crack tip. This requires detailed re-meshing and optimization for each crack length as the crack is growing. In contrast, the use of the DD method for simulating crack growth only requires elements to be added where the crack is actually growing. The rest of the mesh stays the same.

The finite element method requires pavements to be represented by a finite mesh. However, pavement problems are semi-infinite in extent. The DD method accommodates problems of infinite or semi-infinite extent naturally through the use of the analytical solution upon which it is based (Birgisson et al. 1998). It should be noted that some finite element codes, such as ABAQUS, LSDYNA, and ADINA, include the option of infinite elements, which minimizes the effects of the finite mesh.

Finally, even though boundary element solutions have been formulated for just about any type of problem that can be solved by the finite element method, the formulation and use of the method for solving problems in plasticity remains complicated and cumbersome and is probably best left to the finite element method.

Recognition of the pros and cons of each of these numerical methods has led to the development of hybrid codes, in which the finite element method is used to solve for regions of plasticity, but the boundary element method is used for solving everything else, including cracks, within the domain.

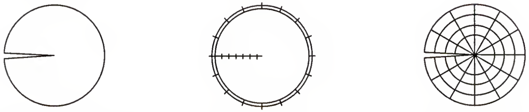

Circular plate with a crack BEM model FEM model

Figure 3-6. Structural Models in Boundary Element Method and Finite Element Method

3.7 Higher Order Element Formulation

Although the constant DD element was proven to be accurate enough for stress-displacement solutions for a general finite body including an infinite media, Crawford and Curran (1982) illustrated that the constant element was not precise enough to capture the bending action in a beam structure. In addition, they revealed through a number of examples, e.g. a cantilever beam, a pressurized crack, and a circular cavity, that the quadratic element gave better overall results than the constant element. It appeared that the quadratic element was able to capture the bending stress and displacement well with relatively few elements. Its solutions also converged to the exact analytical solutions faster than the constant element's at the same number of degree of freedom. Moreover, the accuracy of the quadratic element allows us to obtain the stress solutions at locations close to the element, which is impossible for the case of the constant element. This evidence can be found in the work done by Crawford and Curran (1982). The advantage on accuracy is useful when calculating the strain energy at locations close to the crack tip.

Unlike the constant element that the displacement discontinuity is assumed equally constant across the elemental length, the quadratic element has its displacement discontinuity variation in a quadratic shape (Figure 3-2 c). Thus, the displacement discontinuity, $u_i(\xi)$, in Equations (3-18) to (3-22) becomes

$$D_i(\xi) = a_0 + a_1\,\xi + a_2\,\xi^2 \tag{3-63}$$

It is necessary to specify three nodal points on the element so that the relation between a general displacement discontinuity along the element and the values of displacement at the three distinct points can be established. Crawford and Curran (1982) suggested that the most optimum locations of the nodes are at the Gauss-Chebyshev integration points; $-\frac{\sqrt{3}}{2}a$, 0, $\frac{\sqrt{3}}{2}a$ for quadratic equation. Thus, we can rewrite

$$D_i(\xi) = N_1(\xi)\,D_i(1) + N_2(\xi)\,D_i(2) + N_3(\xi)\,D_i(3) \tag{3-64}$$

where

$$N_1(\xi) = -\frac{1}{\sqrt{3}}\frac{\xi}{a} + \frac{2}{3}\left(\frac{\xi}{a}\right)^2 \tag{3-65}$$

$$N_2(\xi) = 1 - \frac{4}{3}\left(\frac{\xi}{a}\right)^2 \tag{3-66}$$

$$N_3(\xi) = \frac{1}{\sqrt{3}}\frac{\xi}{a} + \frac{2}{3}\left(\frac{\xi}{a}\right)^2 \tag{3-67}$$

$D_i(1)$, $D_i(2)$, $D_i(3)$ are displacement discontinuities at $-\frac{\sqrt{3}}{2}a$, 0, $\frac{\sqrt{3}}{2}a$.

The solutions of stress-displacement induced by the quadratic element are found to be the functions of $D_i(1)$, $D_i(2)$, $D_i(3)$ at the nodal points. In fact, the solutions are in the same format as Equations (3-25) to (3-29). Thus, it is possible to form a system of linear equations with coefficient matrix, unknown displacement discontinuity vector, and prescribed boundary condition vector as described in Section 3.3. The details of the formulas and their derivations are presented in Appendix B.

3.8 Multi-Layer Structure

The displacement discontinuity method discussed so far in this Chapter has been devised to solve general tow-dimensional boundary value problems for homogeneous, isotropic, linearly elastic bodies. In many situations in civil engineering, we face the composition of inhomogeneous bodies. Crouch and Starfield (1990) formulated the displacement discontinuity approach to solve inhomogeneous problems by simply rearranging the existing algorithm. Figure 3-7 illustrates an example of an inhomogeneous problem consisting of two finite subregions. The two subregions, R_1 and R_2, are each assumed to be homogeneous, isotropic and linearly elastic with elastic constants ν_1, E_1 and ν_2, E_2. The boundaries of the two subregions R_1 and R_2 are C_1 and C_2. The common portion of boundaries where the two subregions are coalescent is called the *interface*.

Let us assume that the boundary C_1 is discretized into N_1 elements and so for the boundary C_2 with N_2 elements. It is important that the elements along the interface must match exactly the elements on the opposite side in terms of geometry of elements, number of nodes, and nodal locations. At the element outside the interface, there are two prescribed boundary values associated with two unknown displacement discontinuities per node. At the elements along the interface, there are four unknown displacement discontinuities on one set of two matching node points. However, there are no prescribed boundary values on the interface. This problem can be resolved by utilizing the continuity conditions for the displacements and tractions along the interface between the subregions. The continuity conditions for a nodal point i and its opposite nodal point i* along the interface can be written as

$$\begin{aligned} \sigma_s^{i\,[1]} &= \sigma_s^{i*\,[2]} \\ \sigma_n^{i\,[1]} &= \sigma_n^{i*\,[2]} \\ u_s^{i\,[1]} &= -\,u_s^{i*\,[2]} \\ u_n^{i\,[1]} &= -\,u_n^{i*\,[2]} \end{aligned} \tag{3-68}$$

where the superscript in the bracket indicates the subregion of the nodal point.

The minus signs in the displacement equations are a consequence of the opposite directions of the local co-ordinates s_1, n_1 and s_2, n_2 along the interface.

The above equations can be rearranged as

$$\begin{aligned} \sigma_s^{i\,[1]} - \sigma_s^{i*\,[2]} &= 0 \\ \sigma_n^{i\,[1]} - \sigma_n^{i*\,[2]} &= 0 \\ u_s^{i\,[1]} + u_s^{i*\,[2]} &= 0 \\ u_n^{i\,[1]} + u_n^{i*\,[2]} &= 0 \end{aligned} \tag{3-69}$$

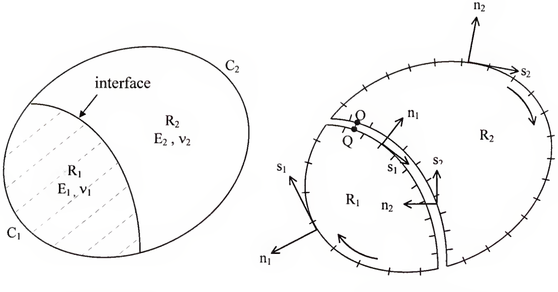

A finite body with two subregions

Boundary model of the inhomogeneous body

Figure 3-7. Diagram of Inhomogeneous Body and its Representative Model

Assuming that the number of nodes is 1 to N_1 in the subregion R1, and nodes N_1+1 to N in the subregion R2, the stresses and displacements along the interface of the subregion R_1 can be written

$$\begin{aligned}
\sigma_s^{i\,[1]} &= \sum_{j=1}^{N1} A_{ss}^{ij\,[1]} D_s^j + \sum_{j=1}^{N1} A_{sn}^{ij\,[1]} D_n^j \\
\sigma_n^{i\,[1]} &= \sum_{j=1}^{N1} A_{ns}^{ij\,[1]} D_s^j + \sum_{j=1}^{N1} A_{nn}^{ij\,[1]} D_n^j \\
u_s^{i\,[1]} &= \sum_{j=1}^{N1} B_{ss}^{ij\,[1]} D_s^j + \sum_{j=1}^{N1} B_{sn}^{ij\,[1]} D_n^j \\
u_n^{i\,[1]} &= \sum_{j=1}^{N1} B_{ns}^{ij\,[1]} D_s^j + \sum_{j=1}^{N1} B_{nn}^{ij\,[1]} D_n^j
\end{aligned} \tag{3-70}$$

For the interface on subregion R_2, the stresses and displacements are

$$\sigma_s^{i*\,[2]} = \sum_{j=N1+1}^{N} A_{ss}^{i*j\,[2]} D_s^j + \sum_{j=N1+1}^{N} A_{sn}^{i*j\,[2]} D_n^j$$

$$\begin{aligned} \sigma_n^{i^*[2]} &= \sum_{j=N1+1}^{N} A_{ns}^{i^*j\,[2]} D_s^j + \sum_{j=N1+1}^{N} A_{nn}^{i^*j\,[2]} D_n^j \\ u_s^{i^*[2]} &= \sum_{j=N1+1}^{N} B_{ss}^{i^*j\,[2]} D_s^j + \sum_{j=N1+1}^{N} B_{sn}^{i^*j\,[2]} D_n^j \\ u_n^{i^*[2]} &= \sum_{j=N1+1}^{N} B_{ns}^{i^*j\,[2]} D_s^j + \sum_{j=N1+1}^{N} B_{nn}^{i^*j\,[2]} D_n^j \end{aligned} \qquad (3\text{-}71)$$

After substituting the above equations of stresses and displacements into Equation (3-69), we now obtain four continuity equations per one nodal point. Thus, the four unknowns per one node set on the interface are now matched with the four continuity conditions, and the overall problem is soluble through the system of linear equations as discussed previously. The following matrix equation illustrates the pattern of the system of equations:

$$\begin{array}{cccccc} \left[\begin{array}{c|c} \mathbf{C}^{[1]} & \mathbf{0} \\ \hdashline \mathbf{A}^{[1]} & \mathbf{A}^{*[2]} \\ \hline \mathbf{B}^{*[1]} & \mathbf{B}^{[2]} \\ \hdashline \mathbf{0} & \mathbf{C}^{[2]} \end{array}\right] & N_1 & \left[\begin{array}{c} \mathbf{D}^{[1]} \\ \hline \mathbf{D}^{[2]} \end{array}\right] & = & \left[\begin{array}{c} \mathbf{b}^{[1]} \\ \hdashline \mathbf{0} \\ \hline \mathbf{0} \\ \hdashline \mathbf{b}^{[2]} \end{array}\right] & N_1 \\ N_1 \qquad\quad N & & & & & N \end{array} \qquad (3\text{-}72)$$

3.9 Verification and Examples

In the following, two examples are presented of the use of the displacement discontinuity method for solving crack related problems. Both examples include cracks in two-dimensional linear elastic isotropic materials. The results obtained with the DD method will be compared to closed form solutions and solutions obtained with the finite element method.

3.9.1 A Crack in Rectangular Plate

This problem deals with the calculation of stresses around a crack in a rectangular plate. The plate is 101.6-mm (4 in) wide by 152.4-mm (6 in) long, and it is under a uniaxial tension of 689 kPa (100 psi) in the longitudinal direction. A line crack, which is 10.16-mm (0.4 in) long is located at the middle of the plate. Figure 3-8 shows the rectangular plate and a representative DD model consisting of 112 elements. The longitudinal stresses around the crack tip along the x-direction obtained from the DD model and from the comparative closed form solution obtained from Broek (1986) are shown in Figure 3-9. The stress predicted with the DD method is comparable to the closed form solution in the critical area close to the crack tip.

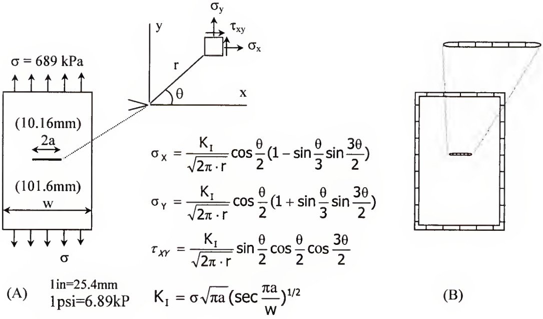
σ = 689 kPa
(10.16mm)
2a
(101.6mm)
W
σ
(A)
1in=25.4mm
1psi=6.89kP
σ_y
τ_{xy}
σ_x
y
r
θ
x
$\sigma_X = \frac{K_I}{\sqrt{2\pi \cdot r}} \cos\frac{\theta}{2}(1 - \sin\frac{\theta}{3}\sin\frac{3\theta}{2})$
$\sigma_Y = \frac{K_I}{\sqrt{2\pi \cdot r}} \cos\frac{\theta}{2}(1 + \sin\frac{\theta}{3}\sin\frac{3\theta}{2})$
$\tau_{XY} = \frac{K_I}{\sqrt{2\pi \cdot r}} \sin\frac{\theta}{2}\cos\frac{\theta}{2}\cos\frac{3\theta}{2}$
$K_I = \sigma\sqrt{\pi a}(\sec\frac{\pi a}{W})^{1/2}$
(B)

Figure 3-8. A Crack in a Rectangular Plate and its Closed Form Solution. A) Physical Geometry, and B) The Representative DD Model.

It should be noted that the closed form solution is only valid around the crack tip, whereas the DD solution is valid throughout, as can be seen by the closed form solution converging to zero stress away from the crack tip. However, the DD method is successfully converges to the external tensile stress (689 kPa or 100 psi) as distances far away from the crack tip.

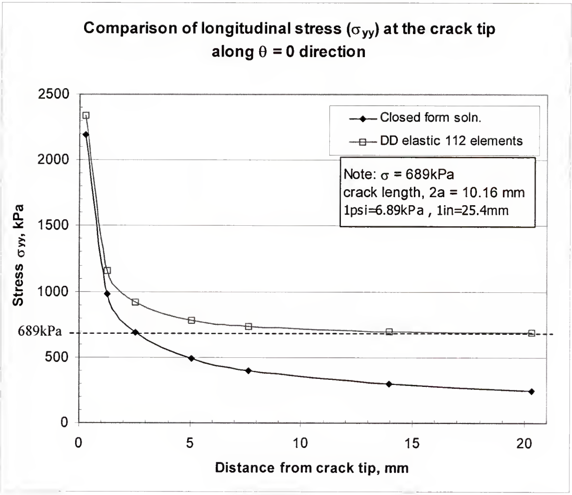

Figure 3-9. A Plot of Longitudinal Stress Around the Crack Tip of the Rectangular Plate Problem.

3.9.2 Crack Propagation in the Superpave Indirect Tension Test

This example deals with the simulation of crack growth in the Superpave IDT test. An IDT disk specimen with an 8 mm hole at the center was modeled with a crack initiated from the top and the bottom of the hole in the vertical direction as shown in Figure 3-10. The objective with the modeling was to determine a relationship between the crack length in the specimen and the horizontal deformation between the two gauge points across the center of the specimen (Roque et al.1999 and Zhang 2000).

Using the finite element method, several representative models had to be created to account for different crack lengths as the crack was growing. Each finite element model required about 11,000 (eleven thousand!) elements to capture the singularity around the crack tip, as shown in Figure 2-4.

The same problem was modeled with the DD method with only 132 elements. To simulate the crack growth, more elements were simply added to the end of the crack, without having to re-mesh the whole problem as in the finite element model.

Figure 3-11 shows the resulting relationship between the crack length and the horizonal deformation computed by the FEM and the DD method. As shown, the FEM and the DD method yielded similar results. As a note of interest, it took days on a workstation to complete the multiple remeshing and subsequent runs with the FEM analysis, whereas the full DD solution was obtained in less than 15 minutes total on a Pentium III 550 MHz computer (including the addition of elements to simulate the crack growth).

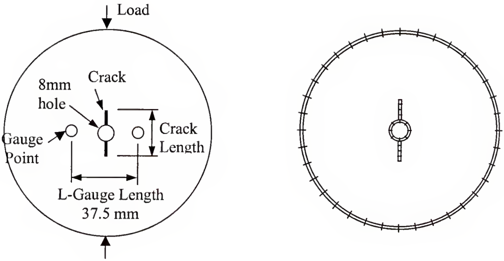

Figure 3-10. Superpave IDT with Vertical Crack and its Representative DD Model.

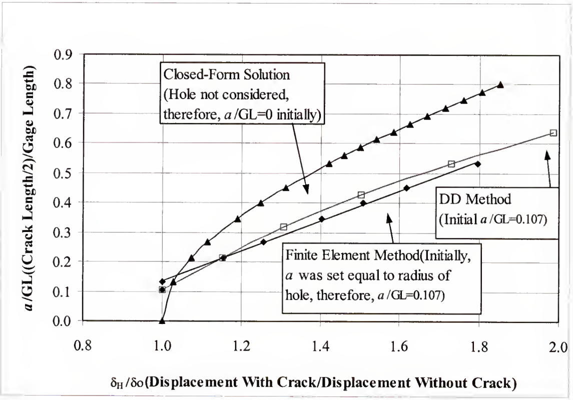

Figure 3-11. Relations Between Normalized Crack Length and Normalized Horizontal Displacements from Superpave IDT.

3.9.3 Annulus Inside a Circular Hole in a Large Plate

In this example, an annulus $a \le r \le b$ with elastic constants ν_1 and G_1 is embedded inside a circular hole of radius $r = b$ in a large plate with elastic constants ν_2 and G_2. The inside wall of the annulus is subjected to a compressive pressure $\sigma_{rr} = -p$ and the plate is unstressed at infinity. The annulus is in good contact with the plate without any slippage. Figure 3-12 illustrates the problem. The analytical solution to this problem is provided by Crouch and Starfield (1990):

For the region $a \le r \le b$, the radial and tangential stresses are

$$\sigma_{rr} = \frac{1}{1 - a^2/b^2} [\, (p\, a^2/b^2 - p') - (p - p')\, a^2/r^2 \,] \tag{3-73a}$$

$$\sigma_{\theta\theta} = \frac{1}{1 - a^2/b^2} [\, (p\, a^2/b^2 - p') + (p - p')\, a^2/r^2 \,] \tag{3-73b}$$

And for the region $r \ge b$, the stresses are

$$\sigma_{rr} = -p'\, b^2/r^2 \quad \text{(3-73c)}, \qquad \sigma_{\theta\theta} = p'\, b^2/r^2 \tag{3-73d}$$

in which $$p' = \frac{2(1-\nu_1)pa^2/b^2}{2(1-\nu_1) + (G_1/G_2 - 1)(1 - a^2/b^2)}. \tag{3-73e}$$

A numerical solution to this problem was obtained using the Displacement Discontinuity Method with two-subregion modeling. The conditions were selected such that $a/b = 0.5$, $\nu_1 = \nu_2 = 0.25$, $G_1 / G_2 = 2$, and $p / G_1 = 10^{-3}$. The inside boundary of annulus and the interface between annulus and plate each were divided into 100 constant elements. The results are compared with the analytical solution in Figure 3-13. The differences between the numerical and analytical values of both radial and tangential stresses were less than 3.3 percent.

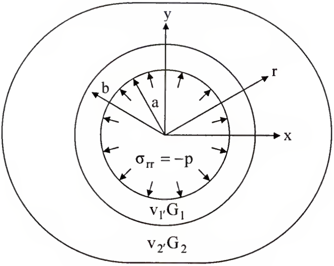

Figure 3-12. Annulus inside a Circular Large Plate

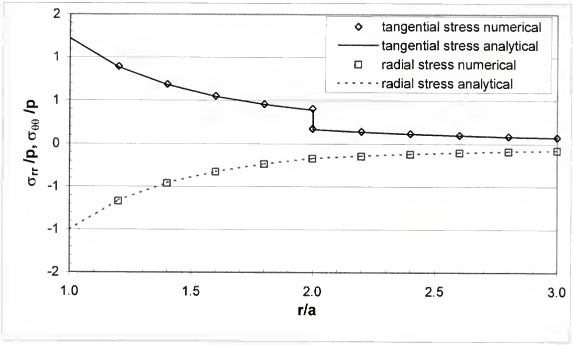

Figure 3-13. Radial and Tangential Stresses in Annulus and Plate

3.9.4 A Three-Layer Pavement

A three-layer flexible pavement was loaded by a single tire load. The pavement consists of a 254-mm (10-in) asphalt concrete and a 305-mm (12-in). stabilized base on top of subgrade. The material properties (Young modulus and Poisson's ratio) are E_1=1379 MPa (200,000 psi), $\nu_1 = 0.35$ for asphalt concrete, $E_2 = 345$ MPa (50,000 psi), $\nu_2 = 0.4$ for base material, and $E_3 = 69$MPa (10,000 psi), $\nu_3 = 0.45$ for subgrade. The tire load has uniform vertical pressure of 0.69 MPa (100 psi) and radius 127 mm (5 in).

The pavement was modeled as a plane strain three-layer structure. The dimension of model is 10.16 m (400 in.) width x 5.64 m (222 in.) total depth to extensively cover the pavement boundaries. The model represents the tire load by a strip of uniformly distributed pressure of 254 mm (10 in.) width. The DD method used 226 quadratic elements to model the pavement structure as shown in Figure 3-14. The purpose of using quadratic elements was to capture the bending effects in the upper layers. For boundary conditions, the elements along the bottom of pavement were restricted for zero shear and normal deformations to represent the rigid foundation. While the elements on the side boundaries were allowed to deform vertically but the horizontal displacement was not allowed. All elements on the top surface of pavement were prescribed as zero shear and normal stresses, except for the center element where the uniformly distributed tire pressure of 0.69 MPa (100 psi) was assigned to as the normal stress.

In order to verify the analysis results from the DD method, the pavement structure with same geometry and properties was also modeled by the ABAQUS finite element package. In this case, the three-layered pavement was treated as a two-dimensional structure under plane strain condition. The center of the pavement surface is loaded by a uniformly distributed pressure of 254-mm-width tire strip. Since the pavement geometry and loading condition are symmetry around the centerline of pavement, only one half of pavement is required in modeling. The three-layer pavement structure was constructed by 5,565 eight-node rectangular solid elements containing 16,940 nodes as presented in Figure 3-15. The extent of the meshes covers 5.64 m (222 in.) total depth from the top surface to the bottom of subgrade layer and 5.08 m (200 in.) width from center of pavement to the side boundary. Since the bending action concentrates in the top layer of pavement and especially in the area underneath the tire strip, the size of element meshes is smaller in the top layer underneath the tire strip and becomes larger in the lower layers and away from the tire area. In each layer, the linear-elastic material properties of young modulus and Poisson's ratio were assigned to elements located within its extent. For boundary conditions, the nodes located at the bottom of pavement were restricted for any deformation to represent the rigid foundation. The nodal points on both sides of model were restricted for horizontal movement and only allowed to move vertically. The nodes at the top of pavement were free of stresses, except for the nodes in the area underneath the tire strip where uniformly distributed forces were assigned.

Figure 3-16, 3-17 and 3-18 show the results of surface deformation, horizontal and vertical stresses at bottom of asphalt concrete layer and at top of subgrade. It appears that the stresses and deformation from the DD method match well with those from the finite element method.

Let us consider the pavement model in Figure 3-14. The DDM elements were placed on top, bottom, interlayer, and side boundaries to form a closed body. The pavement model in Figure 3-14 covers a considerably wide distance (10.16 m) comparing to its total depth (5.64 m). In this case, the elements on the side boundaries locate so far away from the tire area that they may have minimal influences on the area of interest at the center of pavement. Thus, there can be an alternative for DDM to model a pavement structure by placing elements only on extensive horizontal boundaries without any need for side boundaries. To verify this modeling approach, the same pavement model in Figure 3-14 is reused, but its side boundaries are excluded for the new analysis. The new pavement model is illustrated in Figure 3-19. The results of stresses and deformation at surface of pavement and at bottom of asphalt layer for the pavement model without side boundaries are shown in Figures 3-20 and 3-21 along with a comparison to the results based on pavement model with complete side boundaries. The stresses at the surface and bottom of asphalt layers are closely comparable for both approaches, especially at the center of pavement. The surface deformation of no-side boundaries model is greater than the deformation of complete-boundary model by a small value. However, their shapes of the deformed surface are approximately identical. Moreover, the no-side boundary model results in the vertical deformation close to zero at the distance far away from the center, which is more realistic than what occurs in the complete boundary model. Therefore, an alternative of DDM modeling with side boundaries excluded is possible for the case that the model cover a wide extent and the solutions at side boundary area are not in focus.

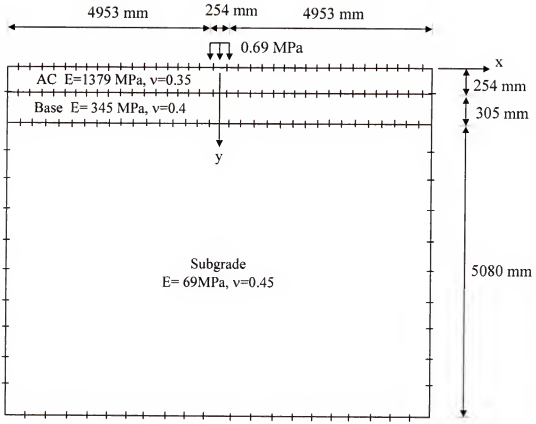

Figure 3-14. Pavement Model in Displacement Discontinuity Method

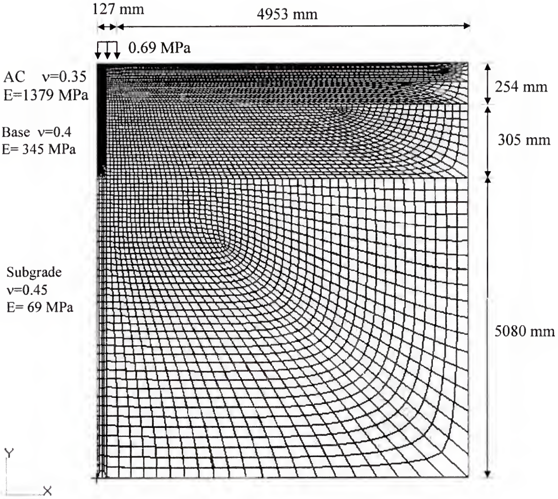

Figure 3-15. Pavement Model in ABAQUS Finite Element Method

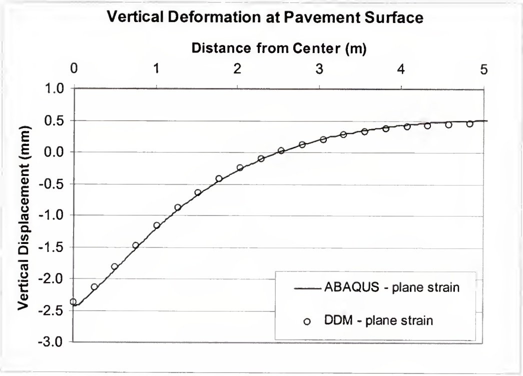

Figure 3-16. Vertical Deformation at Surface of Pavement

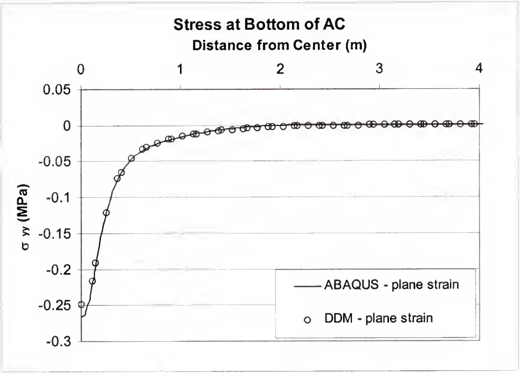

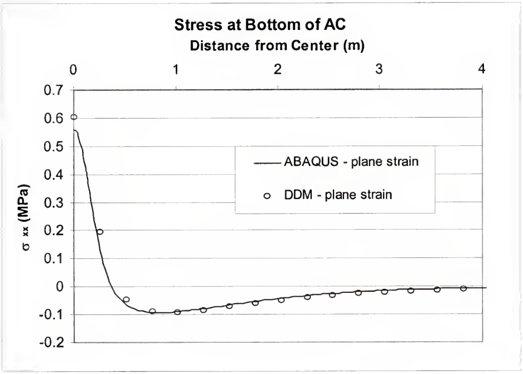

Figure 3-17. Vertical and Horizontal Stresses at Bottom of Asphalt Concrete Layer

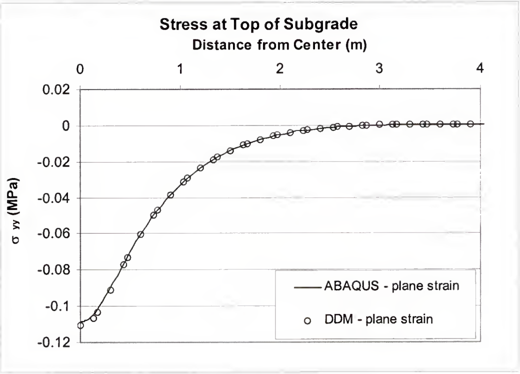

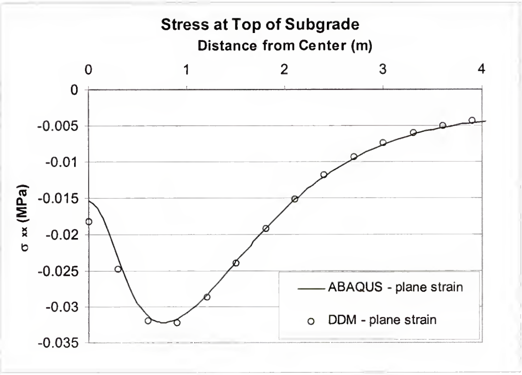

Figure 3-18. Vertical and Horizontal Stresses at Top of Subgrade Layer

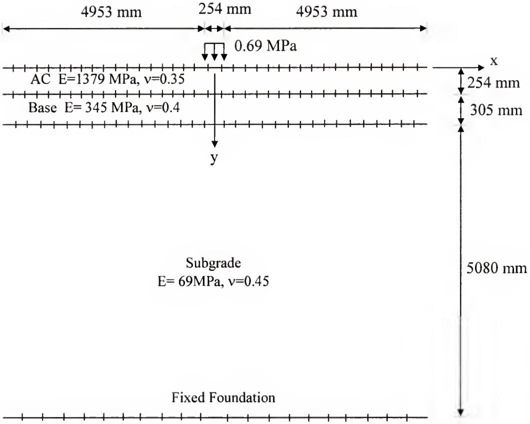

Figure 3-19. Pavement Model in Displacement Discontinuity Method Without Side Boundaries.

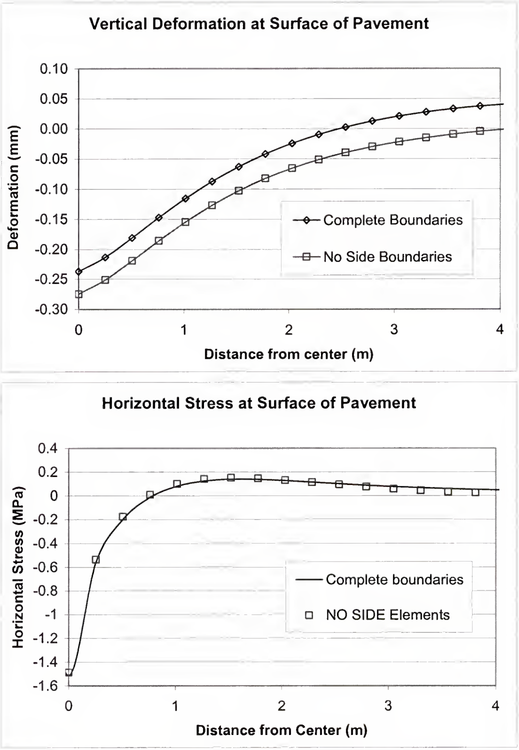

Figure 3-20. Deformation and Stress at Surface of Pavement from DDM with Different Side Boundaries.

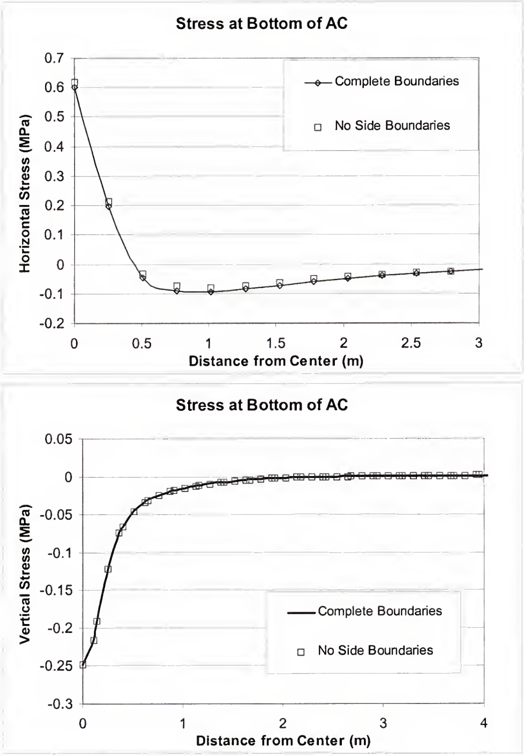

Figure 3-21. Stresses at Bottom of Asphalt Layer from DDM with Different Side Boundaries.

3.10 Summary of the DD Method

In this chapter, the foundation of the displacement discontinuity boundary element method was reviewed and covered to a great extent. A number of different examples involved in the physical crack and layered structure were presented. In all cases, the DD method was found to perform well compared to either the FEM, actual measurements, or analytical solutions. The examples clearly illustrate the potential benefits of using the DD method for simulating the cracking behavior of pavement structure. Below, some of the advantages of the DD boundary element method for use in the modeling of the cracking behavior of mixtures include

- A reduction of the dimension of the problem by one, since only the boundary is discretized. This translates into significant savings in computational effort.
- Potentially more accurate than finite element methods around crack tips, because of the explicit representation of cracks at the element level (each element can be regarded as a crack). In addition, the introduction of a relatively simple crack tip element at the crack tip captures the important stress singularity around a crack tip.
- Elaborate re-meshing is not required every time a crack grows. Rather, elements are simply added to the existing geometry to naturally represent crack growth.

CHAPTER 4
VISCOELASTIC DISPLACEMENT DISCONTINUITY METHOD

It is generally accepted that hot mix asphalt at low temperature can be described as a viscoelastic material—a material that responds in a time-dependent manner to the influenced excitation. This time-dependent characteristic is the cause of creep or permanent deformation, stress relaxation, and rate of loading dependency. The viscoelastic behavior of mixtures governs the performance against cracking damage from loads, and environmental changes as presented in many modern crack growth theories, such as continuum damage mechanics (Lee et al. 2000; Lee and Kim 1998b), thermal cracking (Roque et al. 1997) and HMA Fracture Mechanics (Roque et al. 2002; Zhang et al. 2001). Thus, it is important that a crack growth simulator is able to include the time-dependent nature of the hot mix asphalt.

In this Chapter, the development of a new viscoelastic displacement discontinuity boundary element method is described. Its components and the mechanical relationship between time dependent external load, material behavior, and induced response are explained.

4.1 Viscoelastic Boundary Value Problem

In elasticity, the material response is independent of time, which is known as static response. For a viscoelastic problem, the boundary condition and the material response are time-dependent. If an assumption of negligible acceleration of motion is made, the problem is referred to as a quasi-static or quasi-stationary problem. The time-dependency of the boundary regions falls into the following two categories.

- For fixed boundary condition, the traction history is known for all time over a fixed part of the boundary, while the time-dependent displacement is specified on the remainder of the boundary.
- For mixed boundary conditions, a change from traction boundary condition to displacement boundary condition occurs at some locations on the boundary. An example of this case is a rigid spherical indentor moving into a material, which causes an extension of contact area between the indentor and material.

The governing equations for an isotropic viscoelastic boundary value problem are as follows:

- For initial conditions, the body is assumed initially undisturbed, i.e. displacements, stresses, and strains are zero for $-\infty < t < 0$.
- For boundary conditions, the normal and shear tractions are time-dependent on a traction boundary, $T_i(x, t)$. The normal and shear displacements are also time-dependent on a displacement boundary, $u_i(x, t)$.
- The equilibrium equations for viscoelastic problem remains the same as in elasticity:

  $$\sigma_{ij,j} + b_j = 0$$

  where the body force, b_j, is not accounted in this study.
- The strain-displacement relations are

  $$\varepsilon_{ij}(t) = [u_{i,j}(t) + u_{j,I}(t)]/2$$
- The time-dependent stress-strain relations in terms of dilational and deviatoric forms can be written in the following convolutional integral forms:

$$\sigma_{ii}(t) = 3\int_0^t K(t-\tau)\,\frac{d\varepsilon_{ii}(\tau)}{d\tau}\,d\tau \qquad (4\text{-}1a)$$

$$\sigma_{ij}(t) = 2\int_0^t G(t-\tau)\,\frac{d\varepsilon_{ij}(\tau)}{d\tau}\,d\tau \qquad (4\text{-}1b)$$

where $K(t)$ and $G(t)$ are the relaxation functions of bulk modulus and shear modulus. Optional equations are also often seen as

$$\varepsilon_{ii}(t) = \int_0^t J_v(t-\tau)\,\frac{d\sigma_{ii}(\tau)}{d\tau}\,d\tau \qquad (4\text{-}2a)$$

$$\varepsilon_{ij}(t) = \int_0^t J_d(t-\tau)\,\frac{d\sigma_{ij}(\tau)}{d\tau}\,d\tau \qquad (4\text{-}2b)$$

where $J_v(t)$ and $J_d(t)$ are the compliance functions for volumetric and deviatoric components.

For the one-dimensional case, Equations (4-1) and (4-2) are reduced to

$$\varepsilon(t) = \int_0^t J(t-\tau)\,\frac{d\sigma}{d\tau}\,d\tau \qquad \text{or} \qquad (4\text{-}3)$$

$$\sigma(t) = \int_0^t E(t-\tau)\,\frac{d\varepsilon}{d\tau}\,d\tau \qquad (4\text{-}4)$$

where $J(t)$ is a creep compliance function, and $E(t)$ is a relaxation modulus function.

In order to solve the viscoelastic boundary value problem, the initial condition and the time-dependent boundary conditions must be prescribed as a well-posed problem. This implies that the prescribed initial and boundary conditions must allow for an existence of a unique, and continuously time-dependent solution. For fixed-type boundary conditions, there are two cases: 1) the stress at boundary is prescribed while the displacement at the same location is left unknown, or 2) the displacement at boundary is prescribed and the stress is unknown.

The displacement discontinuity method presented in Chapter 3 is a numerical method that is based on the linear elastic governing equations. Commonly, there are several approaches to allow the boundary element-type of method to obtain the viscoelastic solutions. For instance, Birgisson (1996) applied the utilization of a numerical time stepping scheme into a direct integral boundary element method to solve time-dependent governing equations incrementally through the whole history of solutions. Another important approach is to apply the Laplace transformation to the constitutive equations, and the boundary conditions, then solve the equations in the transformed domain, and invert the solutions in transformed domain back to time domain. This approach is known as the Correspondence Principle (Findley et al.1976; Tschoegl 1989; Haddad 1995).

4.2 The Correspondence Principle

> The Correspondence Principle: If an elastic solution to a stress analysis problem is known, substitution of the appropriate complex-plane transforms for the quantities employed in the elastic analysis immediately furnishes the viscoelastic solution in the transform plane. The time-dependent viscoelastic solution is then obtained by inverting the transform. The principle can only be applied if the boundaries themselves do not change with time. (Tschoegl 1989)

By using the correspondence principle, the viscoelastic governing equations are transformed into a set of corresponding elastic governing equations in forms of transform variable s. The Laplace transform forms of the governing equations are described as follows:

- The initial conditions of an undisturbed body stay the same.
- The Laplace-transformed forms of the boundary conditions are

For tractions, $T_i(x, t) \rightarrow \overline{T}_i(x, s)$

For displacements, $u_i(x,t) \rightarrow \overline{u}_i(x, s)$

where s is the Laplace transform variable, and the overbar designates the Laplace transform of the function, i.e.

$$L\{f(x, t)\} = \overline{F}(x, s) = \int_0^\infty f(x, t) \exp(-st)\, dt \tag{4-5}$$

- The Laplace transformed equilibrium equations are

$\sigma_{ij,j} + b_j = 0$ where the body force, $b_j = 0$ in this study.

- The transformed strain-displacement relations become

$$\varepsilon_{ij}(t) = [u_{i,j}(t) + u_{j,l}(t)]/2 \rightarrow \bar{\varepsilon}_{ij}(s) = [\bar{u}_{i,j}(s) + \bar{u}_{j,i}(s)]/2 \tag{4-6}$$

- The transformed stress-strain relations in terms of dilational and deviatoric forms become

For the dilatational equation,

$$L\{\sigma_{ii}(t)\} = L\{ 3\int_0^t K(t-\tau)\frac{d\varepsilon_{ii}(\tau)}{d\tau}d\tau \}$$

$$\bar{\sigma}_{ii}(s) = s\cdot 3\bar{K}(s)\cdot\bar{\varepsilon}_{ii}(s) \tag{4-7a}$$

For the deviatoric equation,

$$L\{\sigma_{ij}(t)\} = L\{ 2\int_0^t G(t-\tau)\frac{d\varepsilon_{ij}(\tau)}{d\tau}d\tau \}$$

$$\bar{\sigma}_{ij}(s) = s\cdot 2\bar{G}(s)\cdot\bar{\varepsilon}_{ij}(s) \tag{4-7b}$$

Similarly the transformed compliance equations for volumetric and deviatoric components become

$$\bar{\varepsilon}_{ii}(s) = s\cdot\bar{J}_v(s)\cdot\bar{\sigma}_{ii}(s) \tag{4-8a}$$

$$\bar{\varepsilon}_{ij}(s) = s\cdot\bar{J}_d(s)\cdot\bar{\sigma}_{ij}(s) \tag{4-8b}$$

At this point, the viscoelastic boundary value problem then becomes a corresponding elastic problem in the transform variable, s. Thus, the analogous problem can be solved in the same conventional way as an elastic problem to obtain the transformed stresses, $\bar{\sigma}_{ij}(s)$, and transformed displacements, $\bar{u}_i(s)$, throughout the body. A Laplace inversion would be applied to the transformed solutions afterward to determine the stresses, $\sigma_{ij}(t)$, and displacements, $u_i(t)$, in the original viscoelastic boundary value problem.

With this analogy, we now can modify the linear-elasticity-based displacement discontinuity method to solve the problem of linear viscoelasticity by replacing the time-dependent boundary condition and the material viscoelastic functions with the corresponding transformed functions. The time variable (represented by t) in those time functions is Laplace-transformed into the transformed variable (represented by '*s* '). The stress-displacement equations in the elastic displacement discontinuity method, such as Equations (3-25) to (3-29), become a set of transformed equations. However, all mechanical parameters that are possibly time-dependent, such as stresses, displacements, displacement discontinuities, shear modulus, and Poisson's ratio, become functions of the transformed variable (s). A boundary value problem in the transformed domain is then solved in the same manner using the displacement discontinuity method as in the elastic problem, consequently giving the solutions of displacement discontinuities, stresses and displacements as functions of the transformed parameters. Finally, the solutions in transformed variable space are inverted back to time domain to obtain the time-dependent viscoelastic solutions.

In the following, the details of applying the correspondence principle to the boundary condition, material properties, and displacement discontinuity equations are described.

4.3 Transformed Boundary Conditions

As discussed previously, the stress tractions and the displacements on the boundaries of the problem must be identified in order to form a well posed boundary value problem. For a well-posed boundary value problem, the displacements and/or tractions must be prescribed at the location of each displacement discontinuity element.

In viscoelastic problems, the boundary conditions are time-dependent functions. Since the correspondence principle is applicable to only the fixed boundary condition, a change in boundary conditions from a traction boundary to a displacement boundary at any location is restricted. This means we can only prescribe either tractions or displacements to a boundary component (shear or normal) of a DD element throughout the history. In addition, a geometrical extension of the boundaries during the history is not allowed.

The following time functions for boundary conditions that are used in this study are implemented into the viscoelastic DDM.

4.3.1 Constant Step Function

The constant step function represents the case of constant traction or displacement is applied to a location throughout the time history. Examples include: constant creep loading, fixed displacement boundary, and zero stress boundary. The unit step function or Heaviside unit function as shown in Figure 4-1a is defined as

$$H(t-a) = \begin{cases} 0 & \text{if } t < a \\ 0.5 & \text{if } t = a \\ 1 & \text{if } t > a \end{cases} \tag{4-9}$$

Any function f(t) when multiplied by H(t-a) will have a value of zero for $t < a$ and a value of f(t) in the region $t > a$. Thus a step change in stress from $\sigma = 0$ to $\sigma = \sigma_0$ may be represented by

$$\sigma(t) = \sigma_0 \, H(t-a) \tag{4-10}$$

Similarly for a step change in displacement:

$$u(t) = u_0 \, H(t-a) \tag{4-11}$$

The Laplace transform of the unit step function is

$$L\{ H(t-a)f(t) \} = f(s)\, e^{-a \cdot s} \tag{4-12}$$

again, f(s) = L{ f(t) } stands for the Laplace transform of function f(t).

4.3.2 Continuous Sine Function

The change in stress or displacement over time can be illustrated by a continuous sine function (Figure 4-1b):

$$f(t) = f_0 \sin \omega t \tag{4-13}$$

The corresponding Laplace transform is written as

$$\bar{f}(s) = f_0 \left(\frac{\omega}{s^2 + \omega^2} \right) \tag{4-14}$$

where f_0 is the maximum amplitude of stress or displacement. The continuous sine function can be applied to the cyclic boundary condition.

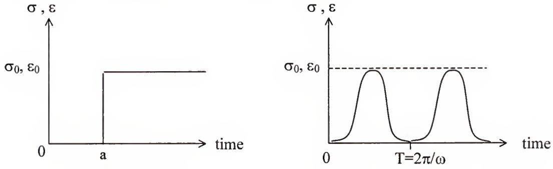

a) Step function

b) Non-reversal sine function

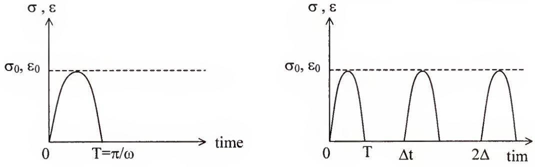

c) Haversine function

d) Repeated haversine function

Figure 4-1. Time-Dependent Boundary Functions

4.3.3 Haversine Function

The half sine function is equivalent to the sine function but only one half of the cycle (sin 0 to sin π) is considered. The diagram of a single half sine function is illustrated in Figure 4-1c. The single half sine function is written as

$$F(t) = f_0 \sin \omega\, t + H(t-T)\, f_0 \sin \omega\, (t-T) \tag{4-15}$$

$$\bar{F}(s) = \bar{f}(s) + \bar{f}(s) \exp(-s \cdot T) \tag{4-16}$$

$$\bar{f}(s) = f_0 \left(\frac{\omega}{s^2 + \omega^2}\right) \tag{4-17}$$

where $T = \pi/\omega$ is the time period from sin 0 to sin π. The repeated half sine function (Figure 4-1d) can be written by adding the single half sine functions at different durations as

$$F(t) = \sum_{i=0}^{N-1} \{ f_0 \sin \omega(t-i\Delta t) \cdot H(t-i\Delta t) + f_0 \sin \omega(t-i\Delta t-T) \cdot H(t-i\Delta t-T) \} \tag{4-18}$$

where Δt is the resting time between the beginning of two half-sine cycles. The Laplace transform of the repeated half sine function is

$$\bar{F}(s) = \sum_{i=0}^{N-1} \{ \bar{f}(s) \exp(-s \cdot i\Delta t) + \bar{f}(s) \exp(-s \cdot (i\Delta t + T)) \} \tag{4-19}$$

The repeated half sine function is used as the cyclic loading characteristic in the Indirect Tension Test (Roque et al. 1997; Roque and Buttlar 1992; Buttlar and Roque 1994).

4.4 Transformed Material Property

For a viscoelastic material, e.g. asphalt mixtures, the modulus and (in some cases) the Poisson's ratio are not constant with time. They are time-dependent, and usually represented by mathematical functions. The time-dependent characteristic consequently causes the stress-strain relationship to change with time and the history of the applied boundary conditions. As explained in Section 4.2, the stress-strain equations in transform variable are

$$\overline{\sigma}_{ii}(s) = s\cdot 3\,\overline{K}\,(s)\cdot \overline{\varepsilon}_{ii}(s) \tag{4-7a}$$

$$\overline{\sigma}_{ij}(s) = s\cdot 2\,\overline{G}\,(s)\cdot \overline{\varepsilon}_{ij}(s) \tag{4-7b}$$

Similarly, the viscoelastic convolutional integral equations for one-dimensional case should become

$$\varepsilon(t) = \int_0^t J(t-\tau)\,\frac{d\sigma(\tau)}{d\tau}\,d\tau \quad \rightarrow \quad \overline{\varepsilon}\,(s) = s\cdot \overline{J}\,(s)\cdot \overline{\sigma}\,(s) \tag{4-20}$$

$$\sigma(t) = \int_0^t E(t-\tau)\,\frac{d\varepsilon(\tau)}{d\tau}\,d\tau \quad \rightarrow \quad \overline{\sigma}\,(s) = s\cdot \overline{E}\,(s)\cdot \overline{\varepsilon}\,(s) \tag{4-21}$$

Equations 4-20 and 4-21 are analogous to linear elastic equations: $\varepsilon = J\,\sigma$, and $\sigma = E\,\varepsilon$. The elastic stress and strain, σ and ε, are replaced by the transformed stress and strain, $\overline{\sigma}\,(s)$ and $\overline{\varepsilon}\,(s)$. The elastic modulus and compliance, E and J, are replaced by the transformed modulus and compliance, $s\cdot \overline{E}\,(s)$ and $s\cdot \overline{J}\,(s)$. If the governing equation involves the Poison ratio, the transformed Poison ratio, $\overline{\nu}\,(s)$, must be used. This s-multiplication evidence can be found in Tschoegl (1989). Table 4-1 gives the elastic-transform relationship of some material properties.

The relationship between the material properties in transform domain can be obtained by the same analogy as in elasticity. For instance, in elasticity, the young modulus, E, and Poison ratio can be written in terms of shear and bulk modulus (G and K):

$$E = \frac{9KG}{3K + G} \tag{4-22}$$

$$\nu = \frac{3K - 2G}{6K + 2G} \tag{4-23}$$

In the correspondence principle, substitute the s-multiplied terms from Table 4-1 into above equations to obtain the relationships for transform young modulus and transform Poison ratio.

$$s\cdot \overline{E}(s) = \frac{9\, s\overline{K}(s)\, s\overline{G}(s)}{3\, s\overline{K}(s) + s\overline{G}(s)} \quad \rightarrow \quad \overline{E}(s) = \frac{9\, \overline{K}(s)\overline{G}(s)}{3\, \overline{K}(s) + \overline{G}(s)} \tag{4-24}$$

$$\overline{v}(s) = \frac{3\, s\overline{K}(s) - 2\, s\overline{G}(s)}{6\, s\overline{K}(s) + 2\, s\overline{G}(s)} \quad \rightarrow \quad \overline{v}(s) = \frac{3\, \overline{K}(s) - 2\, \overline{G}(s)}{6\, \overline{K}(s) + 2\, \overline{G}(s)} \tag{4-25}$$

Table 4-1. Material Properties in Correspondence Principle.

	Time Domain	Transform Domain	Appearance in σ-ε Equations
Compliance	$J(t)$	$\overline{J}(s) = L\{J(t)\}$	$s\cdot \overline{J}(s)$
Young Modulus	$E(t)$	$\overline{E}(s) = L\{J(t)\}$	$s\cdot \overline{E}(s)$
Shear Modulus	$G(t)$	$\overline{G}(s) = L\{G(t)\}$	$s\cdot \overline{G}(s)$
Bulk Modulus	$K(t)$	$\overline{K}(s) = L\{K(t)\}$	$s\cdot \overline{K}(s)$
Poison Ratio	$v(t)$	$\overline{v}(s) = L\{v(t)\}$	$\overline{v}(s)$

In general, the material properties are described in terms of mathematical functions. These material functions can be obtained from the stress-strain relationship of a representative model, or from the laboratory measurement of stress and strain of the material. In this study, two material models—the Burgers model and the power law model—are implemented.

4.4.1 Burgers Model

The Burgers viscoelastic model is made up of a combination of mechanical springs and dashpots as depicted in Figure 4-2. There are four components mechanically representing the time-dependent behavior of the compliance function. The Burgers model is comprised of a Kelvin model connecting to a Maxwell model.

- The Maxwell model is composed of one spring representing the initial elastic response of the material, and one dashpot representing the permanent deformation (creep) of the material.
- The Kelvin model is a parallel set of one spring and one dashpot. It represents the delayed elastic response of the material.

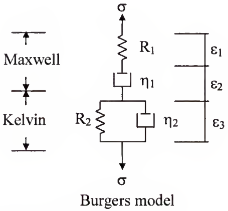

Figure 4-2. Representative Burgers model

The Maxwell and Kelvin models are the most fundamental elements of linear viscoelasticity. Figure 4-3, 4-4 and 4-5 illustrate the time-dependent responses under a constant creep condition of the Maxwell, Kelvin, and Burgers models respectively.

The constitutive differential equation of the Burgers model in one-dimensional case is written as

$$\sigma(t)+\left[\frac{\eta_1}{R_1}+\frac{\eta_1}{R_2}+\frac{\eta_2}{R_2}\right]\dot{\sigma}(t)+\frac{\eta_1\eta_2}{R_1R_2}\ddot{\sigma}(t)=\eta_1\dot{\varepsilon}(t)+\frac{\eta_1\eta_2}{R_2}\ddot{\varepsilon}(t) \tag{4-26}$$

where

σ is axial stress; $\dot{\sigma}, \ddot{\sigma}$ are its 1st and 2nd derivative with respect to time,

$\varepsilon, \dot{\varepsilon}, \ddot{\varepsilon}$ are axial strain and its 1st and 2nd derivative with respect to time,

R_1, R_2, η_1, η_2 are coefficients of springs and dashpots.

The differential equation can be written in the form of an operator equation as

$$(1 + p_1 \frac{\partial}{\partial t} + p_2 \frac{\partial^2}{\partial t^2})\sigma(t) = (q_1 \frac{\partial}{\partial t} + q_2 \frac{\partial^2}{\partial t^2})\varepsilon(t) \tag{4-27}$$

where

$$p_1 = \frac{\eta_1}{R_1} + \frac{\eta_1}{R_2} + \frac{\eta_2}{R_2} \qquad p_2 = \frac{\eta_1 \eta_2}{R_1 R_2} \qquad q_1 = \eta_1 \qquad q_2 = \frac{\eta_1 \eta_2}{R_2}$$

The Laplace transformation of the operator Equation (4-27) leads to

$$(1 + p_1\, s + p_2\, s^2)\, \bar{\sigma}(s) = (q_1\, s + q_2\, s^2)\, \bar{\varepsilon}(s) \tag{4-28}$$

or

$$P(s) \cdot \bar{\sigma}(s) = Q(s) \cdot \bar{\varepsilon}(s) \tag{4-29}$$

where

$$Q(s) = q_1\, s + q_2\, s^2 \qquad \text{and } P(s) = 1 + p_1\, s + p_2\, s^2 \tag{4-30}$$

In one-dimensional problems, it is usual to apply a Burgers model to represent either the modulus or compliance of the viscoelastic material.

For a transform modulus:

$$s \cdot \bar{E}(s) = \frac{\bar{\sigma}(s)}{\bar{\varepsilon}(s)} = \frac{q_1 s + q_2 s^2}{1 + p_1 s + p_2 s^2} \tag{4-31}$$

For a transform compliance:

$$s \cdot \bar{J}(s) = \frac{\bar{\varepsilon}(s)}{\bar{\sigma}(s)} = \frac{1 + p_1 s + p_2 s^2}{q_1 s + q_2 s^2} = \frac{1}{R_1} + \frac{1}{\eta_1 s} + \frac{1}{\eta_2 (s + R_2/\eta_2)} \tag{4-32}$$

Equation (4-32) leads to the most seen one-dimensional compliance function:

$$\bar{J}(s) = \frac{1}{sR_1} + \frac{1}{\eta_1 s^2} + \frac{1}{\eta_2 s(s + R_2/\eta_2)} \tag{4-33}$$

$$J(t) = L^{-1}\{\ \bar{J}(s)\ \} = \frac{1}{R_1} + \frac{t}{\eta_1} + \frac{1}{R_2}\left(1 - \exp\left(-\frac{R_2}{\eta_2}t\right)\right) \tag{4-34}$$

where

$$L^{-1}\{\ \bar{F}(s)\ \} = \frac{1}{2\pi\pi}\int_{c-i\infty}^{c+i\infty}\bar{F}(s)\cdot\exp(st)ds \text{ is Laplace inversion of } \bar{F}(s), \tag{4-35}$$

c denotes an abscissa located to the right of any singularity that $\bar{F}(s)$ may possess,

$\frac{1}{R_1}$ represents the immediate response,

$\frac{1}{R_2}\left(1 - \exp\left(-\frac{R_2}{\eta_2}t\right)\right)$ represents the delayed response,

and $\frac{t}{\eta_1}$ represents the permanent response.

In a general viscoelastic problem, two Burgers elements can be used to describe the three-dimensional stress-strain relation. Each of the volumetric and deviatoric responses is individually represented by one Burgers model. The first element is applied to represent the deviatoric stress-strain relation:

$$2\, s\cdot \bar{G}(s) = \frac{\bar{\sigma}_{ij}(s)}{\bar{\varepsilon}_{ij}(s)} = \frac{Q'(s)}{P'(s)} = \frac{q_1's + q_2's^2}{1 + p_1's + p_2's^2} \tag{4-36}$$

where the first set of constants are

$$p'_1 = \frac{\eta_1'}{R_1'} + \frac{\eta_1'}{R_2'} + \frac{\eta_2'}{R_2'} \quad p'_2 = \frac{\eta_1'\eta_2'}{R_1'R_2'} \quad q'_1 = \eta'_1 \quad q'_2 = \frac{\eta_1'\eta_2'}{R_2'}$$

The second set of constants represents the volumetric stress-strain relation:

$$3\,s\cdot\bar{K}(s)=\frac{\bar{\sigma}_{ii}(s)}{\bar{\varepsilon}_{ii}(s)}=\frac{Q''(s)}{P''(s)}=\frac{q''_1 s+q''_2 s^2}{1+p''_1 s+p''_2 s^2} \tag{4-37}$$

where the second set of constants are

$$p''_1=\frac{\eta''_1}{R''_1}+\frac{\eta''_1}{R''_2}+\frac{\eta''_2}{R''_2} \qquad p''_2=\frac{\eta''_1\eta''_2}{R''_1R''_2} \qquad q''_1=\eta''_1 \qquad q''_2=\frac{\eta''_1\eta''_2}{R''_2}$$

The transform young modulus and transform Poison ratio can be obtained by substituting the transform bulk modulus and transform shear modulus into Equations (4-24) and (4-25).

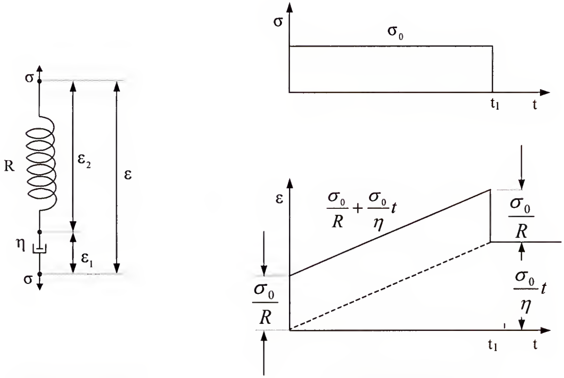

(a) Maxwell Model

(b) Creep and Recovery

Figure 4-3. Maxwell Model and Creep Response

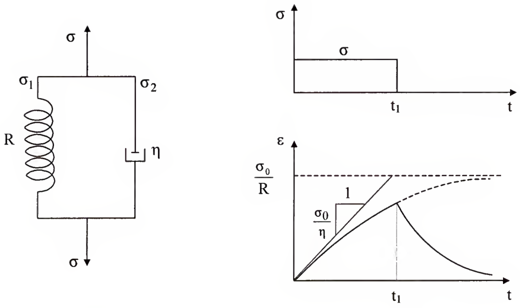

(a) Kelvin Model

(b) Creep and Recovery

Figure 4-4. Kelvin Model and Creep Response

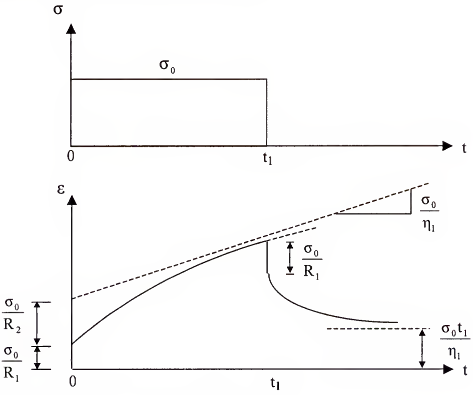

Figure 4-5. Burgers Creep and Recovery Response

4.4.2 Power Law Model

The power law model uses the following equation to represent the compliance of a viscoelastic material.

$$D(t) = D_0 + D_1 t^m \tag{4-38}$$

where D(t) is time-dependent compliance,

D_0, D_1 and m are constants. (m<1 for asphalt mixtures).

The D_0 constant in the power law equation describes the immediate elastic response. The $D_1 t^m$ term represents the time-dependent response.

The compliance is normally used to describe the time-dependent response of a viscoelastic material that is subjected to a constant applied load, i.e. creep condition. For a one-dimensional creep, the compliance is simply a ratio of measured uniaxial strain response, ε(t), divided by the constant uniaxial stress, σ.

$$J(t) = \frac{\varepsilon(t)}{\sigma} = D(t) = D_0 + D_1 t^m \tag{4-39}$$

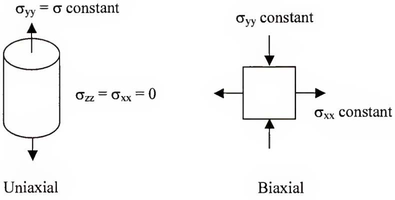
$\sigma_{yy} = \sigma$ constant
$\sigma_{zz} = \sigma_{xx} = 0$
Uniaxial
σ_{yy} constant
σ_{xx} constant
Biaxial

Figure 4-6. Constant Creep Stress Conditions

For a biaxial plane stress condition, the applied stresses in two directions are constant, while there is no normal stress acting on the plane of interest. The compliance is obtained by considering the time dependent strain in one direction as follows:

$$\varepsilon_{xx}(t) = \sigma_{xx}\, D(t) - \nu\, \sigma_{yy}\, D(t)$$

$$J(t) = D(t) = \frac{\varepsilon_{xx}(t)}{\sigma_{xx} - \nu\sigma_{yy}} = D_0 + D_1\, t^{\,m} \tag{4-40}$$

The power law equation for compliance is usually obtained by applying a nonlinear curve-fitting method to the graphs of compliance versus time that are obtained from measurement in laboratory tests. For instance, with the Superpave indirect tension creep test, the post-data interpreting program applies a nonlinear curve-fitting method to the average measured compliance data obtained from the creep tests performed on three samples. Complete details of curve fitting method can be found in Roque and Buttlar (1992), Buttlar and Roque (1994), Roque et al. (1997).

The Laplace transform of the compliance is written as

$$\bar{J}(s) = \bar{D}(s) = L\{D_0 + D_1\, t^{\,m}\}$$

$$\bar{J}(s) = \bar{D}(s) = \frac{D_0}{s} + \frac{D_1\Gamma(m+1)}{s^{m+1}} \tag{4-41}$$

$$s\cdot \bar{J}(s) = s\cdot \bar{D}(s) = \frac{D_0 s^m + D_1\Gamma(m+1)}{s^m} \tag{4-42}$$

where $\Gamma(z)$ is the Euler Gamma function: $\Gamma(z) = \int_0^\infty t^{\,z-1}\, e^{-t}\, dt$ (4-42a)

In a general viscoelastic problem, two power law equations can be used to describe the three-dimensional stress-strain relation. Each of volumetric and deviatoric responses is individually represented by one power law equation. The first equation is applied to represent the deviatoric stress-strain relation:

$$\frac{1}{2s\cdot\overline{G}(s)}=\frac{\overline{\varepsilon}_{ij}(s)}{\overline{\sigma}_{ij}(s)}=\frac{D'_0 s^{m'}+D'_1\Gamma(m'+1)}{s^{m'}} \tag{4-43a}$$

where the first set of constants are D'$_0$, D'$_1$, and m'

$$\frac{1}{3s\cdot\overline{K}(s)}=\frac{\overline{\varepsilon}_{ii}(s)}{\overline{\sigma}_{ii}(s)}=\frac{D''_0 s^{m''}+D''_1\Gamma(m''+1)}{s^{m''}} \tag{4-43b}$$

where the second set of constants are D''$_0$, D''$_1$, and m''

The power law equation is simple and requires only 3 constants (D_0, D_1 and m). However, it is unable to distinguish the permanent component from the equation, which is required in determining cracking damage according to the HMA Fracture mechanics. To resolve the permanent component issue, Zhang et al. (2001b) used the rate of compliance function, D(t), at the maximum time of testing period in creep test (t_{max}) to represent the constant rate of permanent deformation in the power law equation. The rate of permanent compliance is determined by taking derivative of Equation 4-39 with time:

$$D(t) = D_0 + D_1\, t^{\,m}$$

$$\frac{dD(t)}{dt} = m\, D_1\, (t)^{m-1}$$

At t_{max}

$$\frac{dD(t_{max})}{dt} = m\, D_1\, (t_{max})^{m-1} \tag{4-44}$$

Thus, the permanent component in the compliance is

$$D_p(t) = \frac{dD(t_{max})}{dt}\, t = m\, D_1\, (t_{max})^{m-1}\, t \tag{4-45}$$

In Burgers model, the external dashpot, η_1, is the only representative part of the permanent response. The creep part of compliance for Burgers model can be written as

$$D_p(t) = \frac{t}{\eta_1} \tag{4-46}$$

The constant rate of permanent component at t_{max} is analogous to the external dashpot part in the Burgers model. Their strain responses to the constant creep stress are linear with time. Thus, the dashpot constant is equivalent to the compliance rate at t_{max}.

$$(\eta_1)^{-1} = m\, D_1\, (t_{max})^{m-1} \tag{4-47}$$

4.5 Transformed Displacement Discontinuity Equations

The displacement discontinuity equations for elastic boundary value problem are Equations (3-54) and (3-55) from Chapter 3:

$$b_s^{\,i} = \sum_{j=1}^{N} C_{ss}^{\,ij}\, D_s^{\,j} + \sum_{j=1}^{N} C_{sn}^{\,ij}\, D_n^{\,j} \qquad i = 1 \text{ to } N \tag{3-54}$$

$$b_n^{\,i} = \sum_{j=1}^{N} C_{ns}^{\,ij}\, D_s^{\,j} + \sum_{j=1}^{N} C_{nn}^{\,ij}\, D_n^{\,j} \qquad i = 1 \text{ to } N \tag{3-55}$$

where the influence coefficients $C_{ss}^{\,ij}$, $C_{sn}^{\,ij}$, $C_{ns}^{\,ij}$, $C_{nn}^{\,ij}$ are the influence of displacement discontinuity at element j on boundary stress/displacement at element i. For stress boundary condition, $C_{ss}^{\,ij}$, $C_{sn}^{\,ij}$, $C_{ns}^{\,ij}$, $C_{nn}^{\,ij}$ become $A_{ss}^{\,ij}$, $A_{sn}^{\,ij}$, $A_{ns}^{\,ij}$, $A_{nn}^{\,ij}$. For displacement boundary condition, $C_{ss}^{\,ij}$, $C_{sn}^{\,ij}$, $C_{ns}^{\,ij}$, $C_{nn}^{\,ij}$ become $B_{ss}^{\,ij}$, $B_{sn}^{\,ij}$, $B_{ns}^{\,ij}$, $B_{nn}^{\,ij}$.

Once we apply the correspondence principle to Equations (3-54) and (3-55), the prescribed time-dependent boundary condition terms become $\overline{b}_s^{\,i}(s)$ and $\overline{b}_n^{\,i}(s)$, the unknown time-dependent displacement discontinuities become $\overline{D}_n(s)$ and $\overline{D}_n(s)$. Also, the following material property terms are transformed into the functions of variable s.

From Table 4-1, $G \rightarrow s\cdot\overline{G}(s)$ and $\nu \rightarrow \overline{\nu}(s)$

$$\frac{2G}{1-\nu} \rightarrow \qquad \frac{2\,s\overline{G}(s)}{1-\overline{\nu}(s)} \tag{4-48}$$

$$\frac{1-2\nu}{1-\nu} \rightarrow \qquad \frac{1-2\,s\bar{\nu}(s)}{1-\bar{\nu}(s)} \tag{4-49}$$

$$\frac{1}{1-\nu} \rightarrow \qquad \frac{1}{1-\bar{\nu}(s)} \tag{4-50}$$

If only shear modulus and bulk modulus are available, the term $\bar{\nu}(s)$ can be replaced by $\bar{\nu}(s) = \frac{3\,\bar{K}(s) - 2\,\bar{G}(s)}{6\,\bar{K}(s) + 2\,\bar{G}(s)}$ from Equation (4-25). Apply $\bar{\nu}(s)$ term into Equations (4-48) to (4-50) would result in

$$\frac{2\,s\bar{G}(s)}{1-\bar{\nu}(s)} = 2\,s\cdot\bar{G}\,(s)\,\frac{6\bar{K}(s)+2\bar{G}(s)}{3\bar{K}(s)+4\bar{G}(s)} \tag{4-51}$$

$$\frac{1-2\,\bar{\nu}(s)}{1-\bar{\nu}(s)} = \frac{6\bar{G}(s)}{3\bar{K}(s)+4\bar{G}(s)} \tag{4-52}$$

$$\frac{1}{1-\bar{\nu}(s)} = \frac{6\bar{K}(s)+2\bar{G}(s)}{3\bar{K}(s)+4\bar{G}(s)} \tag{4-53}$$

Substitute (4-48) to (4-50) into the elastic influence coefficients in Equations (3-43) and (3-49), the transformed influence coefficients become

$$\bar{A}_{ss}^{ij}(s) = \frac{2\,s\bar{G}(s)}{1-\bar{\nu}(s)}\,[\sin(2\beta)\,I_{,y} + \cos(2\beta)\,I_{,x} + y\,(\,\sin(2\beta)\,I_{,yy} - \cos(2\beta)\,II_{,yy})] \tag{4-54a}$$

$$\bar{A}_{sn}^{ij}(s) = \frac{2\,s\bar{G}(s)}{1-\bar{\nu}(s)}\,[\,y\,(\,\cos(2\beta)\,I_{,yy} + \sin(2\beta)\,II_{,yy})] \tag{4-54b}$$

$$\bar{A}_{ns}^{ij}(s) = \frac{2\,s\bar{G}(s)}{1-\bar{\nu}(s)}\,[-2\,\sin^2\beta\,I_{,y} - \sin(2\beta)\,I_{,x} + y\,(\,\cos(2\beta)\,I_{,yy} + \sin(2\beta)\,II_{,yy})] \tag{4-54c}$$

$$\bar{A}_{nn}^{ij}(s) = \frac{2\,s\bar{G}(s)}{1-\bar{\nu}(s)}\,[\,I_{,x} - y\,(\,\sin(2\beta)\,I_{,yy} - \cos(2\beta)\,II_{,yy})] \tag{4-54d}$$

$$\bar{B}_{ss}^{ij}(s) = -2\,II\,\cos\beta - \frac{1-2\,\bar{\nu}(s)}{1-\bar{\nu}(s)}\,I\,\sin\beta + \frac{y}{1-\bar{\nu}(s)}(\,I_{,y}\,\sin\beta + I_{,x}\,\cos\beta) \tag{4-55a}$$

$$\overline{B}_{sn}^{ij}(s) = -2\ II\sin\beta + \frac{1-2\,\overline{v}(s)}{1-\overline{v}(s)}\ I\cos\beta + \frac{y}{1-\overline{v}(s)}\ (\ I_{,y}\cos\beta + II_{,y}\sin\beta) \tag{4-55b}$$

$$\overline{B}_{ns}^{ij}(s) = 2\ II\sin\beta - \frac{1-2\,\overline{v}(s)}{1-\overline{v}(s)}\ I\cos\beta + \frac{y}{1-\overline{v}(s)}\ (\ I_{,y}\cos\beta + II_{,y}\sin\beta) \tag{4-55c}$$

$$\overline{B}_{nn}^{ij}(s) = -2\ II\cos\beta - \frac{1-2\,\overline{v}(s)}{1-\overline{v}(s)}\ I\sin\beta - \frac{y}{1-\overline{v}(s)}\ (\ I_{,y}\sin\beta + I_{,x}\cos\beta) \tag{4-55d}$$

Note that the terms I and II and their derivatives are functions of geometry of elements; thus, they are not affected by the transformed variable. Thus the transform version of displacement discontinuities equations become

$$\overline{b}_s^{\,i}(s) = \sum_{j=1}^{N} \overline{C}_{ss}^{ij}(s)\,\overline{D}_s^{\,j}(s) + \sum_{j=1}^{N} \overline{C}_{sn}^{ij}(s)\,\overline{D}_n^{\,j}(s) \qquad i = 1 \text{ to } N \tag{4-56}$$

$$\overline{b}_n^{\,i}(s) = \sum_{j=1}^{N} \overline{C}_{ns}^{ij}(s)\,\overline{D}_s^{\,j}(s) + \sum_{j=1}^{N} \overline{C}_{nn}^{ij}(s)\,\overline{D}_n^{\,j}(s) \qquad i = 1 \text{ to } N \tag{4-57}$$

The system of displacement discontinuity equations now becomes a system of complex number equations (variable s). The transformed boundary conditions $\overline{b}_s^{\,i}(s)$ and $\overline{b}_n^{\,i}(s)$ on an element-i are prescribed as explained earlier in Section 4.3. The only unknowns in the equations are the transformed displacement discontinuities $\overline{D}_s^{\,j}(s)$ and $\overline{D}_n^{\,j}(s)$. At a given complex number of s variable, the equation $\underline{\underline{C}}\ \underline{D} = \underline{b}$ is in a general complex-number form, in which $\underline{\underline{C}}$ is the matrix of influence coefficients, $\underline{b}$ is the vector of prescribed boundary conditions, and $\underline{D}$ is the vector of unknown displacement discontinuities. A numerical algorithm is implemented to solve this complex-number equation. The algorithm solves a system of linear algebraic equations with a complex general coefficient matrix. It first computes an LU factorization of the coefficient matrix $\underline{\underline{C}}$ with pivoting option. $\underline{\underline{L}}$ and $\underline{\underline{U}}$ are the lower and upper triangular matrixes of $\underline{\underline{C}}$ such that $\underline{\underline{L}}\ \underline{\underline{U}} = \underline{\underline{C}}$. The solution $\underline{\underline{C}}\ \underline{D} = \underline{b}$ is found by solving the triangular system $\underline{\underline{L}}\ \underline{y} = \underline{b}$ and $\underline{\underline{U}}\ \underline{D} = \underline{y}$. More detail of this solving technique can be found in many references such as Atkinson (1989); Maron (1987).

After the displacement discontinuities, $\bar{D}_s^j(s)$ and $\bar{D}_n^j(s)$, are determined, they can be applied to the transformed Equations (3-56) to (3-60) to obtain the stresses and displacements at a location of interest, P, in terms of transform variable, s as follows:

$$\bar{u}_x(s) = \sum_{j=1}^{N} \left[-2\,II + \frac{y}{1-\bar{v}(s)} I_{,x}\right] \bar{D}_s^j(s) + \sum_{j=1}^{N} \left[\frac{1-2\bar{v}(s)}{1-\bar{v}(s)} I + \frac{y}{1-\bar{v}(s)} I_{,y}\right] \bar{D}_n^j(s) \qquad (4\text{-}58a)$$

$$\bar{u}_y(s) = \sum_{j=1}^{N} \left[-\frac{1-2\bar{v}(s)}{1-\bar{v}(s)} I + \frac{y}{1-\bar{v}(s)} I_{,y}\right] \bar{D}_s^j(s) + \sum_{j=1}^{N} \left[-2\,II + \frac{y}{1-\bar{v}(s)} II_{,y}\right] \bar{D}_n^j(s) \qquad (4\text{-}58b)$$

$$\bar{\sigma}_{xx}(s) = \sum_{j=1}^{N} \frac{2s\bar{G}(s)}{1-\bar{v}(s)} \left[-2\, I_{,y} - y\, I_{,yy}\right] \bar{D}_s^j(s) + \sum_{j=1}^{N} \frac{2s\bar{G}(s)}{1-\bar{v}(s)} \left[-II_{,y} - y\, II_{,yy}\right] \bar{D}_n^j(s) \qquad (4\text{-}58c)$$

$$\bar{\sigma}_{yy}(s) = \sum_{j=1}^{N} \frac{2s\bar{G}(s)}{1-\bar{v}(s)} \left[y\, I_{,yy}\right] \bar{D}_s^j(s) + \sum_{j=1}^{N} \frac{2s\bar{G}(s)}{1-\bar{v}(s)} \left[-II_{,y} + y\, II_{,yy}\right] \bar{D}_n^j(s) \qquad (4\text{-}58d)$$

$$\bar{\sigma}_{xy}(s) = \sum_{j=1}^{N} \frac{2s\bar{G}(s)}{1-\bar{v}(s)} \left[-II_{,y} - y\, II_{,yy}\right] \bar{D}_s^j(s) + \sum_{j=1}^{N} \frac{2s\bar{G}(s)}{1-\bar{v}(s)} \left[\, y\, I_{,yy}\right] \bar{D}_n^j(s) \qquad (4\text{-}58e)$$

Again the terms I and II and their derivatives are functions of geometry and are not affected by the transformed variable.

In order to obtain the solutions of stresses and displacements at any point in the time domain, the Laplace inversion can be applied to the transformed solutions, which inverts the functions of transform variable, s, back to functions of time variable, i.e.

$$u_i(t) = L^{-1}\{\bar{u}_i(s)\} \quad \text{and} \quad \sigma_{ij}(t) = L^{-1}\{\bar{\sigma}_{ij}(s)\} \qquad (4\text{-}59)$$

where $L^{-1}\{\bar{F}(s)\}$ is Laplace inversion of transform function $\bar{F}(s)$.

$$f(t) = L^{-1}\{\ \overline{F}(s)\ \} = \frac{1}{2\pi i}\int_{c-i\infty}^{c+i\infty}\overline{F}(s)\cdot\exp(st)ds \qquad (4\text{-}60)$$

4.6 Numerical Laplace Inversion

If the transform solutions $\overline{u}_i(s)$ and $\overline{\sigma}_{ij}(s)$ are presented in mathematical in terms of the variable s, their Laplace inversion may be carried out analytically by the use of the table of Laplace transform pairs. However, it is practically impossible to obtain the solutions $\overline{u}_i(s)$ and $\overline{\sigma}_{ij}(s)$ in a closed analytical form, because they are functions of transformed displacement discontinuities $\overline{D}_s^j(s)$ and $\overline{D}_n^j(s)$ which are the results of solving a system of linear equations (4-56) and (4-57). Analytical solutions in mathematical form cannot be obtained from the matrix-solving process. Thus, only numerical solutions of $\overline{u}_i(s)$ and $\overline{\sigma}_{ij}(s)$ at any specific value of variable s are available.

An optional strategy to resolve this inversion problem is to apply a numerical Laplace inversion scheme. Generally, there are several numerical-inversion methods available based on various mathematical techniques such as the Fast Fourier transform, numerical integration, series of polynomials, etc. Narayanan and Beskos (1982) summarized a number of inversion techniques in their work. All numerical inversion schemes require the determination at numerous times of $\overline{D}_s^j(s)$, $\overline{D}_n^j(s)$, $\overline{u}_i(s)$ and $\overline{\sigma}_{ij}(s)$ at different values of the variable s. The numerical scheme uses these transform solutions at various s-values to create the approximate functions of the transform solutions. The solutions in terms of the s-variable are then numerically inverted by the scheme to arrive at the solutions at the user-defined set of time.

In this study, we apply a programming algorithm DINLAP that is provided by IMSL mathematical library (2003). In the algorithm, the computation of the Laplace inversion is based on the complex Fourier series proposed by Crump (1976). Fundamentally, if F(s) is the Laplace transformed of a time function, f(t), then the function f(t) can also be obtained by the following equation:

$$f(t) \cong (e^{\alpha t}/T)\, R\left\{\frac{1}{2}F(\alpha) + \sum_{k=1}^{\infty} F(\alpha + \omega_k i)\exp(i\omega_k \cdot t)\right\} \tag{4-61}$$

where $\omega_k = \frac{k\pi}{T}$, k = 1 to ∞, are the frequencies of Fourier series, i is the unit imaginary part of complex number, and α is an estimate of the maximum of the real parts of the singularities of function F(s).

Equation (4-61) is the real part of the complex Fourier series. In this equation, the transform function F(s) is approximated by the complex Fourier series $\frac{1}{2}F(\alpha) + \sum_{k=1}^{\infty} F(\alpha + \omega_k i)\exp(i\omega_k \cdot t)$. The complex Fourier series is created from a discrete set of transformed function, F(s), at various values of s-variable: $s = \alpha + \omega_k i$, k =1 to ∞. The algorithm approximates the inversion of a transform function F(s) = L{f(t)} by Equation (4-61). The full detail of this algorithm can be found in Crump (1976) and IMSL library (2003).

Therefore, the algorithm requires the input of solutions of the stresses and displacements in transform domain, $\overline{\sigma}_{ij}(s)$ and $\overline{u}_i(s)$, at various numbers of s-variable ($s = \alpha + \omega_k i$, k =1 to ∞) to be able to calculate the stresses and displacements in time domain, $u_i(t)$ and $\sigma_{ij}(t)$ by Equation (4-61). The inversion algorithm begins with assigning a complex value of $s = \alpha + \omega_{k*} i$ at one k value (k*). The assigned value of s-variable is substituted into the functions of transform boundary conditions $\overline{b}(s)$ and transform material properties $\overline{G}(s)$, $\overline{v}(s)$ to obtain the corresponding functions at this assigned s-value. Now the transform displacement discontinuities at the assigned s-value can be obtained by solving the system of Equations (4-56) and (4-57).

$$s = \alpha + \omega_{k*}i; \quad \overline{b}_s^{\,i}(s) = \sum_{j=1}^{N} \overline{C}_{ss}^{\,ij}(s)\,\overline{D}_s^{\,j}(s) + \sum_{j=1}^{N} \overline{C}_{sn}^{\,ij}(s)\,\overline{D}_n^{\,j}(s) \quad i = 1 \text{ to } N \qquad (4\text{-}56)$$

$$s = \alpha + \omega_{k*}i; \quad \overline{b}_n^{\,i}(s) = \sum_{j=1}^{N} \overline{C}_{ns}^{\,ij}(s)\,\overline{D}_s^{\,j}(s) + \sum_{j=1}^{N} \overline{C}_{nn}^{\,ij}(s)\,\overline{D}_n^{\,j}(s) \quad i = 1 \text{ to } N \qquad (4\text{-}57)$$

where the influence coefficients $\overline{C}(s)$ are functions of $\overline{G}(s)$, $\overline{v}(s)$.

The complex-number solver that was described in Section 4.5 is applied to solve for displacement discontinuities, $\overline{D}_s^{\,j}(s)$ and $\overline{D}_n^{\,j}(s)$, in the above equations. Once the terms $\overline{D}_s^{\,j}(s)$ and $\overline{D}_n^{\,j}(s)$ at a value of $s = \alpha + \omega_{k*}i$ are known, the transform stresses and displacements at the assigned s-value are obtained by substituting $\overline{D}_s^{\,j}(s), \overline{D}_n^{\,j}(s)$ $\overline{G}(s)$ and $\overline{v}(s)$ for the assigned $s = \alpha + \omega_{k*}i$ into Equations (4-58).

$$\overline{u}_x(s) = \sum_{j=1}^{N} \left[-2\,II + \frac{y}{1 - s\overline{v}(s)} I_{,x}\right] \overline{D}_s^{\,j}(s) + \sum_{j=1}^{N} \left[\frac{1 - 2s\overline{v}(s)}{1 - s\overline{v}(s)} I + \frac{y}{1 - s\overline{v}(s)} I_{,y}\right] \overline{D}_n^{\,j}(s) \qquad (4\text{-}58a)$$

$$\overline{u}_y(s) = \sum_{j=1}^{N} \left[-\frac{1 - 2s\overline{v}(s)}{1 - s\overline{v}(s)} I + \frac{y}{1 - s\overline{v}(s)} I_{,y}\right] \overline{D}_s^{\,j}(s) + \sum_{j=1}^{N} \left[-2\,II + \frac{y}{1 - s\overline{v}(s)} II_{,y}\right] \overline{D}_n^{\,j}(s) \qquad (4\text{-}58b)$$

$$\overline{\sigma}_{xx}(s) = \sum_{j=1}^{N} \frac{2s\overline{G}(s)}{1 - s\overline{v}(s)} [-2\,I_{,y} - y\,I_{,yy}]\, \overline{D}_s^{\,j}(s) + \sum_{j=1}^{N} \frac{2s\overline{G}(s)}{1 - s\overline{v}(s)} [-II_{,y} - y\,II_{,yy}]\, \overline{D}_n^{\,j}(s) \qquad (4\text{-}58c)$$

$$\overline{\sigma}_{yy}(s) = \sum_{j=1}^{N} \frac{2s\overline{G}(s)}{1 - s\overline{v}(s)} [y\,I_{,yy}]\, \overline{D}_s^{\,j}(s) + \sum_{j=1}^{N} \frac{2s\overline{G}(s)}{1 - s\overline{v}(s)} [-II_{,y} + y\,II_{,yy}]\, \overline{D}_n^{\,j}(s) \qquad (4\text{-}58d)$$

$$\overline{\sigma}_{xy}(s) = \sum_{j=1}^{N} \frac{2s\overline{G}(s)}{1 - s\overline{v}(s)} [-II_{,y} - y\,II_{,yy}]\, \overline{D}_s^{\,j}(s) + \sum_{j=1}^{N} \frac{2s\overline{G}(s)}{1 - s\overline{v}(s)} [\,y\,I_{,yy}]\, \overline{D}_n^{\,j}(s) \qquad (4\text{-}58e)$$

After that, the inversion algorithm will assigned a new value of k* to the $s = \alpha + \omega_{k*}i$. The solving process for the $\bar{\sigma}_{ij}(s)$ and $\bar{u}_i(s)$ is then repeated for several times at various assigned values of $s = \alpha + \omega_{k*}i$ until the complex Fourier series of the transform stress or displacement function is created. Lastly, the inversion algorithm computes the stresses or displacements in time domain $u_i(t)$ or $\sigma_{ij}(t)$ based on Equation (4-61).

4.7 Strain Energy in One Direction

The strain energy at a location in a viscoelastic material at a certain time (t) is determined by the following equation (Findley et al. 1976, p.95; Tschoegl, 1989):

$$W(t) = \int_0^t \sigma_{ij}(\tau) \frac{d\varepsilon_{ij}}{d\tau} d\tau \qquad (4\text{-}62)$$

where W(t) is the strain energy,

$\sigma_{ij}(\tau)$ is the stress tensor—with six normal and shear components—as a function of time, and

$d\varepsilon_{ij}(\tau)/d\tau$ is time derivative of the strain tensor as a function of time.

The HMA fracture mechanics revealed that only the dissipated creep strain energy in tensile mode contributed to tensile cracking (opening mode). Thus, only the tensile component of stress and strain tensors that is perpendicular to the crack growth plane in Equation (4-62) is of interest. Let us assume that the tensile stress locates on a y-direction, Equation (4-62) can be reduced to the strain energy equation for y-direction:

$$W(t) = \int_0^t \sigma_{yy}(\tau)\, \dot{\varepsilon}_{yy}(\tau)\, d\tau \qquad (4\text{-}63)$$

where $\sigma_{yy}(\tau)$ and $\dot{\varepsilon}_{yy}(\tau)=d\varepsilon_{yy}(\tau)/d\tau$ are the tensile stress and tensile strain rate that are normal to the plane of crack growth (in x-direction).

The time history of tensile stress at a location P can be determined by the viscoelastic displacement discontinuity method. First, obtain the stress tensor at the location P in terms of the transformed variable, $\bar{\sigma}_{ij}(s)$ by using Equations (4-58). To obtain the strain in transform domain, we can use the stress-strain relationship from Hooke's law.

For two-dimensional plane strain condition,

$$\varepsilon_{yy} = \frac{1}{2G}\left[\sigma_{yy} - \nu\left(\sigma_{xx} + \sigma_{yy}\right)\right] \tag{4-64}$$

Apply the correspondence principle to the above equation and obtain

$$\bar{\varepsilon}_{yy}(s) = \frac{1}{2\,s\bar{G}(s)}\left[\bar{\sigma}_{yy}(s) - s\cdot\bar{\nu}(s)\cdot\left(\bar{\sigma}_{xx}(s) + \bar{\sigma}_{yy}(s)\right)\right] \tag{4-65}$$

The derivative property of Laplace transform theorem states that a time derivative of a function, df(t)/dt, equals s·F(s) in Laplace transform, where F(s) is the Laplace transform of f(t). Therefore, the transform strain rate is

$$\bar{\dot{\varepsilon}}_{yy}(s) = s\cdot\bar{\varepsilon}_{yy}(s) \tag{4-66}$$

$$\bar{\dot{\varepsilon}}_{yy}(s) = s\cdot\frac{1}{2\,s\bar{\bar{G}}(s)}\left[\bar{\sigma}_{yy}(s) - s\cdot\bar{\nu}(s)\cdot\left(\bar{\sigma}_{xx}(s) + \bar{\sigma}_{yy}(s)\right)\right] \tag{4-67}$$

Next, we apply a numerical Laplace inversion to the transformed normal stress, $\bar{\varepsilon}_{yy}(s)$, and normal strain rate in Equation (4-67) to obtain $\sigma_{yy}(t)$ and $\dot{\varepsilon}_{yy}(t)$.

Although in many cases the Laplace inversion can yield the solution of time function in an analytical equation format. The viscoelastic DD method gives the solutions of stress, strain, and displacement based on solving a system of equations. Thus, it is not possible to obtain the solutions in term of analytical time functions. Only a set of solutions at the requested time periods can be provided. In order to determine the strain energy, a numerical integration method must be applied to Equation (4-63). In this study, the author applied the 3-point Gauss quadrature numerical integration to Equation (4-63).

The Gauss quadrature numerical integration (Atkinson 1989; Maron 1987) approximates an integration by a numerical evaluation:

$$\int_{-1}^{1} f(x)\,dx \cong \sum_{k=1}^{n} A_k\, f(x_k) \tag{4-68}$$

where n is the number of Gauss points which is three in this case, x_k are the integration points, $f(x_k)$ are the functions at the integration points, and A_k are the weighting coefficients of the functions at corresponding integration points.

For the integration range of a to b, a transformation can be made from

$$a \leq x \leq b \quad \text{to} \quad -1 \leq \xi \leq 1 \quad \rightarrow \quad x = \frac{b+a}{2} + \frac{b-a}{2}\xi \tag{4-69}$$

$$\text{Thus } x_k = \frac{b+a}{2} + \frac{b-a}{2}\xi_k \tag{4-70}$$

$$\int_{a}^{b} f(x)\,dx \cong [\sum_{k=1}^{n} A_k\, f(x_k)] \left(\frac{b-a}{2}\right) \tag{4-71}$$

The Gauss quadrature yields an exact integration if f(x) is a polynomial of 2n-1 degree or lower. Thus for 3-point Gauss quadrature, the integration is exact for a 5th degree polynomial. The integration points and weighting coefficients for the 3-point quadrature are given in Table 4-2.

Apply the 3-point Gauss quadrature to evaluate the integration in Equation (4-63)

$$W(t) = \int_{0}^{t} \sigma_{yy}(\tau)\,\dot{\varepsilon}_{yy}(\tau)\,d\tau \cong [\sum_{k=1}^{3} A_k\, f(\tau_k)] \cdot 0.5\,t \tag{4-72}$$

where $\tau_k = 0.5\,t + 0.5\,t\,\xi_k$, and $f(\tau_k) = \sigma_{yy}(\tau_k)\,\dot{\varepsilon}_{yy}(\tau_k)$.

Therefore, the three values of $\sigma_{yy}(\tau_k)$ and $\dot{\varepsilon}_{yy}(\tau_k)$ at time $\tau_k = 0.5\,t + 0.5\,t\,\xi_1$, $0.5\,t + 0.5\,t\,\xi_2$, and $0.5\,t + 0.5\,t\,\xi_3$ are required in the calculation.

An example of calculating strain energy for a one-dimensional problem is presented later in this chapter.

Table 4-2. Integration Points and Coefficients for 3-Point Gauss Quadrature.

k	ξ_k	A_k
1	-0.774597	0.555556
2	0.0	0.888889
3	0.774597	0.555556

4.8 Verification and Examples

4.8.1 One-Dimensional Problem

A problem of the viscoelastic material under one-dimensional uniform tensile stress is presented. The sinusoidal tensile stress with a full period of 0.2 second is applied to a Burgers-type viscoelastic material. The viscoelastic constants of the Burgers model are given as $R_1 = 2.5$ Gpa, $\eta_1 = 86.33$ GPa·sec, $R_2 = 0.5$ Gpa, and $\eta_2 = 50$ GPa·sec. The stress function can be written as

$$\sigma(t) = \sigma_0 \sin \omega t$$

where $\omega = 10\pi$ and $\sigma_0 = 1.0$ Gpa.

The analytical solution of viscoelastic strain response by the material is

$$\varepsilon(t) := \sigma_0 \cdot \left[\frac{1}{R_1} \cdot \sin(\omega \cdot t) + \frac{1}{\eta_1 \cdot \omega} \cdot (1 - \cos(\omega \cdot t)) + \frac{1}{\eta_2 \cdot (\omega^2 + \alpha^2)} \cdot \left(\alpha \cdot \sin(\omega \cdot t) - \omega \cdot \cos(\omega \cdot t) + \omega \cdot e^{-\alpha \cdot t} \right) \right] \tag{4-73}$$

where $\alpha = R_2/\eta_2$. The details of this analytical solutions are presented in Appendix C.

The solutions of strain and strain rate can also be obtained by using the Viscoelastic Displacement Discontinuity Method (VEDDM). In the VEDDM, the one-dimensional problem was modeled by applying faraway uniform stress with a sinusoidal function to the infinite medium. The solutions of one-dimensional case were then obtained at any location in the medium as shown in Figures 4-7 and 4-8.

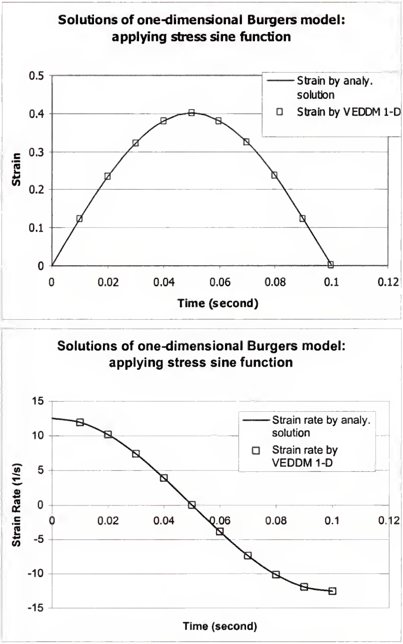

Figure 4-7. Solutions of One-Dimensional Viscoelastic Problem

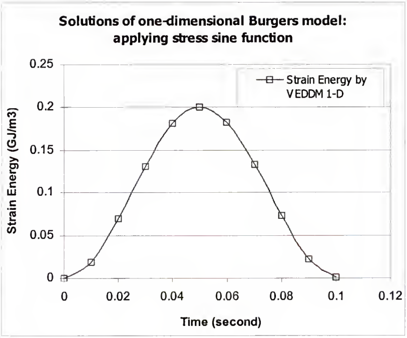

Figure 4-8. Strain Energy of One-Dimensional Problem under Sinusoidal Stress

Figure 4-7 shows that the results from the Viscoelastic Displacement Discontinuity Method exactly match the one-dimensional analytical solutions. The calculated strain energy from the Viscoelastic Displacement Discontinuity Method is illustrated in Figure 4-8.

4.8.2 Modeling Creep Behavior in Superpave Indirect Tension Test

This example deals with the simulation of the creep response of a HMA mix obtained from the Superpave IDT creep test. The mix tested was previously tested by Honeycutt (2000) and Zhang (2000). The aggregate used was oolitic limestone from South Florida. This is an aggregate commonly used in Florida mixes. The mix was a 12.5-mm nominal maximum aggregate size coarse-graded Superpave mix. The gradation is given in Table 5-1. The asphalt used was an AC-30 asphalt. The design asphalt content of 6.5 percent was determined at $N_{design} = 109$ revolutions according to Superpave specifications. The asphalt and the aggregate were mixed at 150°C and subjected to short-term oven aging for two hours at 135°C. Specimens were compacted using a Superpave gyratory compactor to produce three 4500g, 150-mm diameter gyratory-compacted specimen with an air void content of 7 percent (±0.5 percent). The mixture met all Superpave requirements, including all aggregate and volumetric requirements.

Gyratory-compacted specimens were sliced to obtain Superpave IDT test specimens that were approximately 50-mm thick for the creep compliance test. Two sets of gage points were glued on each side of the specimen. After the gage points were placed, the specimen was placed in a low relative humidity (about 40 percent) chamber for 72 hours to reduce moisture effects prior to testing. The creep test was conducted at 10°C under the SHRP Indirect Tension creep test procedure, presented by Roque et al. (1997) and Buttlar and Roque (1994). During the test, horizontal deformations were measured between two gauge-points located across the center of the specimen from both surfaces of the sample. The measurement between the two gage points represents the horizontal strain at the center of the specimen. The horizontal strains were averaged, and normalized by stress to obtain the creep compliance D(t):

$$D(t) = \frac{\varepsilon_x(t)}{\sigma_x - v\sigma_y} \tag{4-74}$$

where

D(t) is fitted compliance function

ε_x is horizontal strain

σ_x and σ_y is horizontal stress and vertical stress, respectively

v is Poisson's ratio

The DD model of the test specimen was made of about 100 DD elements connected end-to-end to form a closed circular boundary as shown in Figure 4-9. The external creep load was prescribed by a constant vertical pressure applied at the top-most elements as shown in Figure 4-9. For other elements, zero traction is applied to represent the free surface condition.

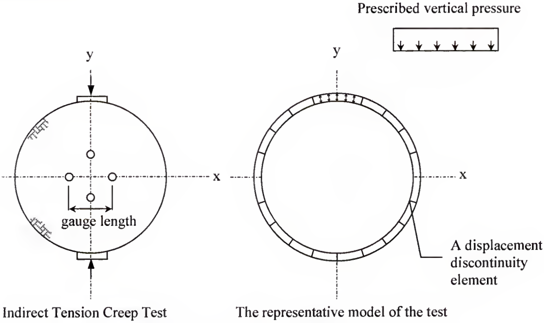
y
x
gauge length
Indirect Tension Creep Test
Prescribed vertical pressure
y
x
A displacement discontinuity element
The representative model of the test

Figure 4-9. Superpave Indirect Tension Creep Test and its Representative DD Model.

For this example, a Burger viscoelastic model was selected to represent the creep response of the mix. For the Burger model, four spring-dashpot parameters were extracted from the laboratory creep compliance curve. The Burger model parameters were R_1 = 1795 MPa (260.26 ksi), η_1 = 57550 MPa·sec (8345 ksi-second), R_2 = 333 MPa (48.33 ksi), and η_2 = 33300 MPa·sec (4833. ksi-second), respectively. The methodology for obtaining the Burger model properties followed that of Newcomb et al. (1993). The viscoelastic-DD analysis was based on the plane-stress analysis. Output stresses and displacements were then requested at the gauge point locations to simulate the actual creep test results more accurately.

Figure 4-10 shows a comparison of the measured and predicted creep compliance curves with time. The DD predicted creep compliance curve was calculated based on the output stresses and deformations. Figure 4-10 clearly shows that the DD method with a simple Burger-viscoelastic model was successful in predicting the creep response of the hot-mix asphalt.

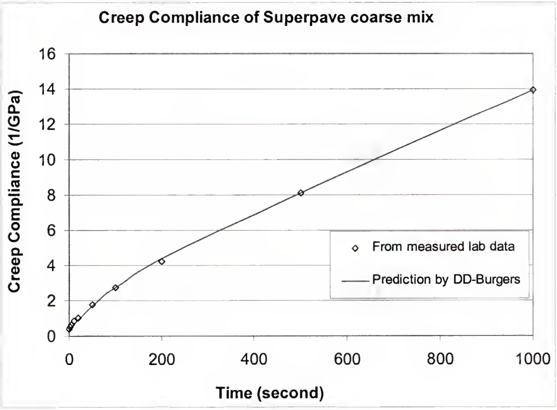

Figure 4-10. Comparison of Creep Compliance Curves Obtained from Measured Laboratory Data and from the DD Method with Burgers-Viscoelasticity.

4.8.3 Thick-Walled Viscoelastic Tube

An axially symmetric thick-walled tube with inside and outside radii of *a* and *b* respectively is subjected to a constant internal pressure *p*, while the outer boundary of the tube is free from stress. The tube is constructed of a linear-viscoelastic material; thus, it causes the tube to deform in timely manner. The geometry and boundary conditions for this example are shown in Figure 4-11. The analytical solutions to this problem (elasticity and viscoelasticity) including the derivation were given by Flugge (1975) and Findley et al. (1976). Crawford and Curran (1983) also found this problem to be a good testing example for their numerical method of creep analysis.

For a linear elastic material, the solutions of the radial displacement (u) and radial and tangential stresses (σ_r and σ_θ) under plane strain condition are as follows:

$$u = \frac{1}{2G}\frac{pa^2}{b^2 - a^2}\left[\,(1\text{-}2\nu)\,r + \frac{b^2}{r}\right] \tag{4-75}$$

$$\sigma_r = \frac{pa^2}{b^2 - a^2}\left(1 - \frac{b^2}{r^2}\right) \qquad \sigma_\theta = \frac{pa^2}{b^2 - a^2}\left(1 + \frac{b^2}{r^2}\right) \tag{4-76}$$

The equations of stresses are free of the elastic constants and therefore in accordance with the correspondence principle will be the same when the tube is made of viscoelastic material.

4.8.3.1 Case 1: Kelvin model

Let us consider the first case in which the tube is made of material whose behavior is elastic in dilatation and Kelvin-type viscoelastic in distortion:

Transformed bulk modulus $\quad s\overline{K}(s) = K$ (4-77)

Transformed shear modulus $\quad 2\,s\overline{G}(s) = \frac{1}{2}(\,R + \eta s)$ (4-78)

The bulk modulus and Kelvin constants are given in Table 4-3. The analytical solution of radial displacement given by Flugge (1975) for this case is

$$u(r, t) = \frac{pa^2}{b^2 - a^2}\left\{\frac{3r}{6K + R}\left[1 - \exp\left(-\frac{6K + R}{\eta}t\right)\right] + \frac{b^2}{rR}\left[1 - \exp\left(-\frac{R}{\eta}t\right)\right]\right\} \quad (4\text{-}79)$$

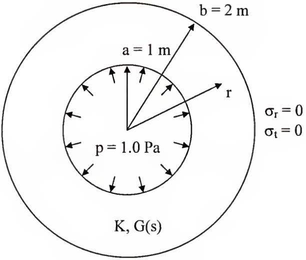

A. Thick-Walled Tube

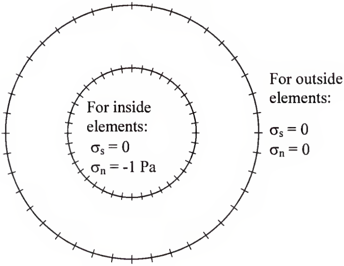

B. Model of Thick-Walled Tube

Figure 4-11. Thick-Walled Tube and Its DDM Model.

Table 4-3. Viscoelastic Properties for Thick-Walled Tube Example

Case 1	Case 2	Case 3	Case 4
Dilatation: Bulk Modulus K = 2000 Pa	Dilatation: Bulk Modulus K = 2000 Pa	Dilatation: Bulk Modulus K = 2000 Pa	Poison Ratio $\nu = 0.3846$
Distortion: Kelvin Material R = 1000 Pa η = 1000 Pa·sec	Distortion: Maxwell Material R = 1000 Pa η = 1000 Pa·sec	Distortion: Burgers Material R_1 = 1000 Pa η_1 = 1000 Pa·sec R_2 = 1000 Pa η_2 = 1000 Pa·sec	Distortion: Burgers Material R_1 = 1000 Pa η_1 = 1000 Pa·sec R_2 = 1000 Pa η_2 = 1000 Pa·sec

To apply the viscoelastic DD method to this problem, the tube is modeled by placing two series of 100 constant DD elements on inner and outer boundaries of the tube. The constant interior pressure in transformed domain is prescribed to the inner elements as $\frac{p}{s}$ for normal stress and zero for shear stress. While the prescribed normal and shear stresses on outer elements are kept at zero. For the material model, the Maxwell spring and dashpot constants in the Burgers model must be set at infinity to allow only the Kelvin components in action. The transformed Poison's ratio and shear modulus, which are required in the DD method now become

$$s\overline{G}(s) = \frac{1}{2}\left[\frac{1}{R_1} + \frac{1}{\eta_1 s} + \frac{1}{\eta_2(s + R_2/\eta_2)}\right]^{-1} \tag{4-80}$$

where R_1 and $\eta_1 \rightarrow \infty$, and the transform Poison ratio from relationship in Equation (4-24) now becomes

$$\overline{\nu}(s) = \frac{3\,s\overline{K}(s) - 2\,s\overline{G}(s)}{6\,s\overline{K}(s) + 2\,s\overline{G}(s)} \qquad \rightarrow \qquad \overline{\nu}(s) = \frac{3\,K - 2\,s\overline{G}(s)}{6\,K + 2\,s\overline{G}(s)} \tag{4-81}$$

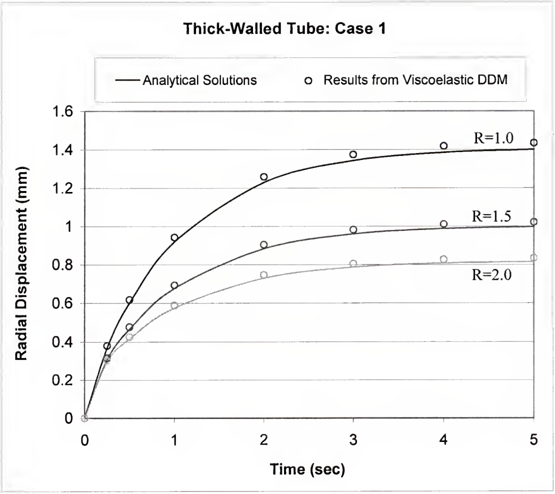

Figure 4-12. Radial Displacement of Thick-Walled Viscoelastic Tube: Case 1

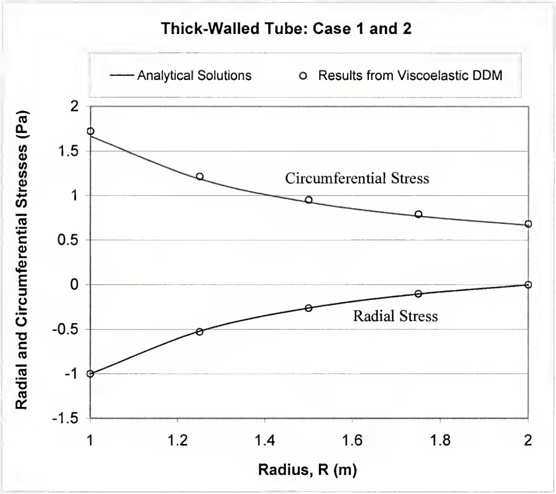

Figure 4-13. Radial and Circumferential Stresses of Thick-Walled Viscoelastic Tube: Case 1 and 2

Results of time-dependent radial displacements at different locations in the tube are plotted along with the analytical solutions in Figure 4-12. For t = 0, there is no deformation at all, since the Kelvin model does not admit an immediate elastic response. For $t \to \infty$, the radial deformation seems to converge to the value corresponding to that of an elastic material with bulk modulus K = 2000 Pa and shear modulus G = 1000 Pa. The results from viscoelastic DD method appear to agree well with the analytical solutions within an acceptable range of error. The distribution of radial and tangential stresses from the DD method shown in Figure 4-13 also matches with those from analytical solutions.

4.8.3.2 Case 2: Maxwell model

In another case, the tube is replaced with material whose volumetric behavior is still elastic, but its deviatoric response is Maxwell-type viscoelastic:

Transformed bulk modulus $$s\overline{K}(s) = K \tag{4-82}$$

Transformed shear modulus $$s\overline{G}(s) = \frac{\eta s}{1 + \frac{\eta}{R} s} \tag{4-83}$$

The bulk modulus and Maxwell constants are given in Table 4-3. The analytical solution of radial displacement given by Flugge (1975) for this case is

$$u(r, t) = \frac{pa^2}{b^2 - a^2} \left\{ \frac{r}{2K} + \left(\frac{3r\,\eta/R}{6K\,\eta/R + \eta} - \frac{r}{2K} \right) \cdot \exp\left(\frac{-6Kt}{6K\,\eta/R + \eta} \right) + \frac{b^2(\eta/R + t)}{r\,\eta} \right\} \tag{4-84}$$

To solve the problem with the viscoelastic DD method under this material case, an adjustment must be made to the transformed shear modulus by assigning the Maxwell constants (Table 4-3) to the Maxwell element in the Burgers model and setting the Kelvin-dashpot component to infinity to disable the Kelvin element. After changing the shear modulus and updating the transformed Poison's ratio, the solutions of stresses and displacement from the viscoelastic DD method can be obtained for this material case. Figure 4-14 illustrates the comparison of radial displacements from the viscoelastic DD method and from the analytical solution; once again they are in good agreement.

Up to this point in this thick-walled tube example, the individual Maxwell and Kelvin elements in the viscoelastic DD method has been verified to an acceptable level. Next we turn to the situation in which the full Burgers element will be tested.

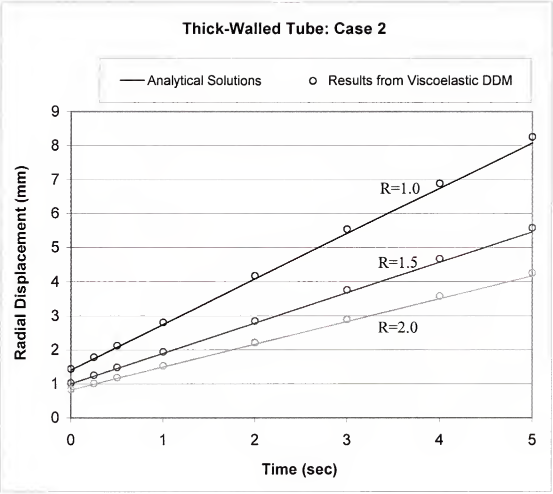

Figure 4-14. Radial Displacement of Thick-Walled Viscoelastic Tube: Case 2

4.8.3.3 Case 3: Burgers model

For this case, the thick-walled tube is made of a material with Burgers-type in distortion, and elastic type in dilation. The tube is still subjected to internal pressure, but at this time, its outside boundary is in contact with a medium so rigid that no deformation is allowed. The boundary conditions become

At $r = a$, $\sigma_r = -p$

At $r = b$, $u = 0$

Flugge (1975) gave the elastic solutions of this problem (where the upper sign is for σ_r and the lower for σ_θ):

$$\sigma_{r,\theta} = -\frac{pa^2}{(1-2\nu)b^2+a^2}\left[1 \pm (1-2\nu)\frac{b^2}{r^2}\right] \tag{4-85}$$

$$u = \frac{pba^2(1-2\nu)}{2G\left[(1-2\nu)\,b^2+a^2\right]}\left(\frac{b}{r}-\frac{r}{b}\right) \tag{4-86}$$

In this case, the Poison's ratio also appears in the stress function, thus the stresses in the viscoelastic tube are time-dependent. To find the stresses and displacement of the viscoelastic tube, we apply the correspondence principle to the elastic solutions as described in Flugge (1975):

$$\bar{\sigma}(s)_{r,\theta} = -\frac{\bar{p}(s)\cdot a^2}{(1-2\bar{\nu}(s))b^2+a^2}\left[1 \pm (1-2\bar{\nu}(s))\frac{b^2}{r^2}\right] \tag{4-87}$$

$$\bar{u}(s) = \frac{\bar{p}(s)ba^2(1-2\bar{\nu}(s))}{2\bar{G}(s)\left[(1-2\bar{\nu}(s))\,b^2+a^2\right]}\left(\frac{b}{r}-\frac{r}{b}\right) \tag{4-88}$$

The transformed function for the constant internal pressure is $\bar{p}(s) = \frac{p}{s}$. Apply the Burgers model equation (section 4.3.1) to the transformed shear modulus:

$$2\,\bar{G}(s) = Q(s)\,/\,P(s) = \frac{q_1 s + q_2 s^2}{1 + p_1 s + p_2 s^2} \tag{4-89}$$

where $p_1 = \frac{\eta_1}{R_1} + \frac{\eta_1}{R_2} + \frac{\eta_2}{R_2}$ $\quad p_2 = \frac{\eta_1\eta_2}{R_1R_2}$ $\quad q_1 = \eta_1$ $\quad q_2 = \frac{\eta_1\eta_2}{R_2}$.

And obtaining the transformed Poison ratio from Equation (4-81):

$$\bar{\nu}(s) = \frac{3K - 2\bar{G}(s)}{6K + 2\bar{G}(s)}$$

After substituting $\bar{p}(s)$, $\bar{G}(s)$ and $\bar{\nu}(s)$ into the $\bar{\sigma}(s)_{r,\theta}$ and $\bar{u}(s)$ equations, we apply the Laplace inversion to obtain the analytical solutions of time-dependent stresses and deformation:

$$u\,(r,t) = 3pba^2\left(\frac{b}{r}-\frac{r}{b}\right)\cdot\frac{1}{\beta_3}[\,A + B\exp(-\gamma_1 t) + C\exp(-\gamma_2 t)\,] \tag{4-90}$$

$$\bar{\sigma}(s)_{r,\theta}\,(r,t) = -\frac{pa^2}{r^2}\cdot\frac{1}{\beta_3}[\,D + E\exp(-\gamma_1 t) + F\exp(-\gamma_2 t)\,] \tag{4-91}$$

where

$$A = \frac{1}{\gamma_1\gamma_2} \qquad B = \frac{p_1 - \frac{1}{\gamma_1} - p_2\gamma_1}{\gamma_2 - \gamma_1} \qquad C = \frac{p_1 - \frac{1}{\gamma_2} - p_2\gamma_2}{\gamma_1 - \gamma_2}$$

$$D = \frac{\alpha_1}{\gamma_1\gamma_2} \qquad E = \frac{\alpha_2 - \frac{\alpha_1}{\gamma_1} - \alpha_3\gamma_1}{\gamma_2 - \gamma_1} \qquad F = \frac{\alpha_2 - \frac{\alpha_1}{\gamma_2} - \alpha_3\gamma_2}{\gamma_1 - \gamma_2}$$

$$\alpha_1 = 6Kr^2 \qquad \alpha_2 = 6Kr^2p_1 + q_1\cdot(r^2 \pm 3b^2) \qquad \alpha_3 = 6Kr^2p_2 + q_2\cdot(r^2 \pm 3b^2)$$

$$\beta_1 = 6Ka^2 \qquad \beta_2 = 6Ka^2p_1 + q_1\cdot(a^2 + 3b^2) \qquad \beta_3 = 6Ka^2p_2 + q_2\cdot(a^2 + 3b^2)$$

$$\gamma_1 = \frac{\beta_2 + \sqrt{\beta_2^2 - 4\beta_1\beta_3}}{2\beta_3} \qquad \gamma_2 = \frac{\beta_2 - \sqrt{\beta_2^2 - 4\beta_1\beta_3}}{2\beta_3}$$

To solve this problem, we assign the following boundary conditions to the elements representing the tube:

For inner elements ($r = a$): normal stress (σ_n) = -p, shear stress (σ_s) = 0.

For outer elements ($r = b$): normal and shear displacements (u_n and u_s) = 0.

For transformed material properties, $\overline{G}(s)$ and $\bar{\nu}(s)$, which are required in the DD analysis are obtained by equation (4-36), (4-37), and (4-25), with the viscoelastic constants given in Table 4-3. Figures 4-15, 4-16 and 4-17 show the analysis results of time-dependent stress and displacement in the tube at various locations. The plots also include the analytical solutions for comparison. It appears that the viscoelastic DD method yields very similar time-dependent stresses and displacements as compared to the analytical solutions with only a slight difference in predicted results.

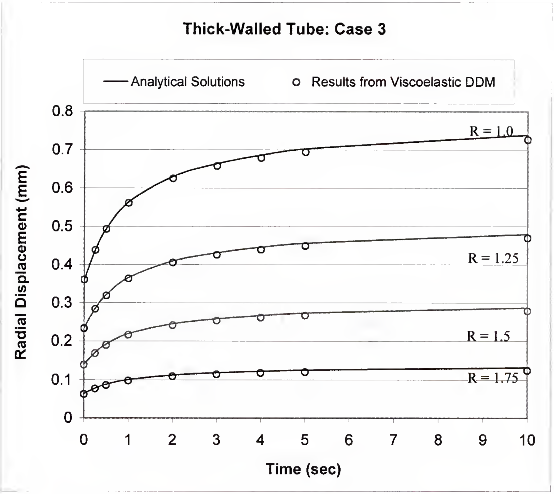

Figure 4-15. Radial Displacement of Thick-Walled Viscoelastic Tube: Case 3

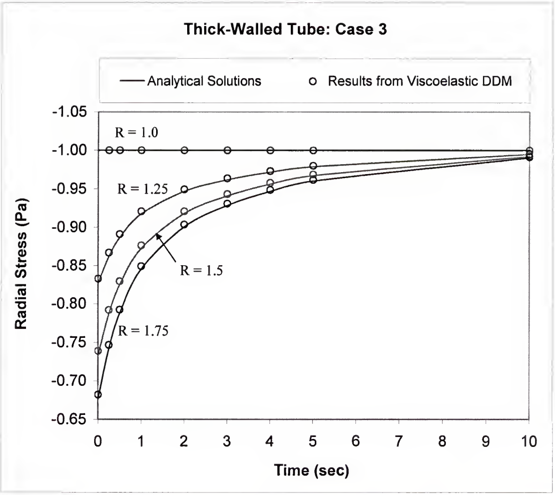

Figure 4-16. Radial Stress of Thick-Walled Viscoelastic Tube: Case 3

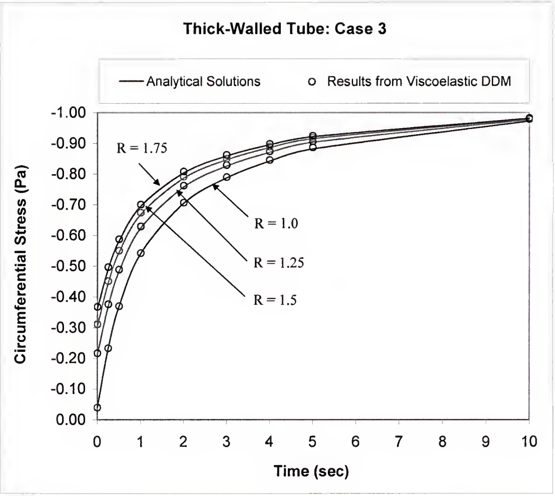

Figure 4-17. Circumferential Displacement of Thick-Walled Viscoelastic Tube: Case 3

4.8.3.3 Case 4: constant Poison ratio

In this case, we will consider the case of Poison ratio being constant with time. The same thick-walled tube with fixed outer boundary problem as presented in the case 3 is used in this problem. The tube is subjected to the constant internal pressure of p = 1 Pascal. The tube is made of a viscoelastic material with Burgers-type in distortion, and its Poison ratio is constant with time. As described in the case 3, the transform shear modulus of the Burgers-type distortion is represented by Equation (4-89):

$$2\overline{G}(s) = Q(s) / P(s) = \frac{q_1 s + q_2 s^2}{1 + p_1 s + p_2 s^2} \qquad (4\text{-}89)$$

where $p_1 = \frac{\eta_1}{R_1} + \frac{\eta_1}{R_2} + \frac{\eta_2}{R_2}$ $p_2 = \frac{\eta_1 \eta_2}{R_1 R_2}$ $q_1 = \eta_1$ $q_2 = \frac{\eta_1 \eta_2}{R_2}$.

The Burgers constants of R_1, R_2, η_1, and η_2 are given Table 4-3. The transform Poison ratio for this material is written as follows:

$$\bar{v}(s) = v \tag{4-90}$$

where v is the constant Poison ratio whose value for this problem is given in Table 4-3. Note that the given value of constant Poison ratio is equal to the initial Poison ratio at time zero for case-3 problem.

The elastic solutions to this problem are the same equations given in the case 3 (4-85) and (4-86):

$$\sigma_{r,\theta} = -\frac{pa^2}{(1-2v)b^2 + a^2}\left[1 \pm (1-2v)\frac{b^2}{r^2}\right] \tag{4-85}$$

$$u = \frac{pba^2(1-2v)}{2G\left[(1-2v)b^2 + a^2\right]}\left(\frac{b}{r} - \frac{r}{b}\right) \tag{4-86}$$

In order to obtain the viscoelastic solutions to this problem, we apply the correspondence principle to the elastic solutions resulting in Equations (4-87) and (4-88) as presented previously.

$$\bar{\sigma}(s)_{r,\theta} = -\frac{\bar{p}(s) \cdot a^2}{(1-2\bar{v}(s))b^2 + a^2}\left[1 \pm (1-2\bar{v}(s))\frac{b^2}{r^2}\right] \tag{4-87}$$

$$\bar{u}(s) = \frac{\bar{p}(s)ba^2(1-2\bar{v}(s))}{2\bar{G}(s)\left[(1-2\bar{v}(s))b^2 + a^2\right]}\left(\frac{b}{r} - \frac{r}{b}\right) \tag{4-88}$$

After substituting $2\overline{G}(s)$, $\overline{v}(s)$ from (4-89), (4-90), and the transformed constant internal pressure of $\overline{p}(s) = \frac{p}{s}$ into the above equation, we apply the Laplace inversion to obtain the analytical solutions in time domain as follows:

$$\sigma_{r,\theta} = -\frac{pa^2}{(1-2v)b^2 + a^2}\left[1 \pm (1-2v)\frac{b^2}{r^2}\right] \tag{4-91}$$

$$u = \frac{pba^2(1-2v)}{\left[(1-2v)b^2 + a^2\right]}\left(\frac{b}{r} - \frac{r}{b}\right)\left[\frac{1}{R_1} + \frac{t}{\eta_1} + \frac{1}{R_2}\left(1 - \exp(-\frac{R_2}{\eta_2}t)\right)\right] \tag{4-92}$$

The analytical solutions of time-dependent displacement and stresses for this case are shown in Figures 4-18 to 4-20.

The solutions to this viscoelastic tube with fixed outer boundary under constant internal pressure can also be obtained by using the viscoelastic DD method. The same DD model of the tube and its boundary conditions as applied earlier in the case 3 are used again in this problem case. But in this case, we use the transform material properties of $\overline{G}(s)$ and $\overline{v}(s)$ given in Equations (4-89) and (4-90). The results of time-dependent displacement and stresses in the tube analyzed by the viscoelastic DD method are illustrated in Figures 4-18 to 4-20. Again, the Figures show that solutions by the viscoelastic DD method agree well with the analytical solutions. For comparison, these figures also show the solutions for the previous case 3 in which the Poison ratio is time-dependent.

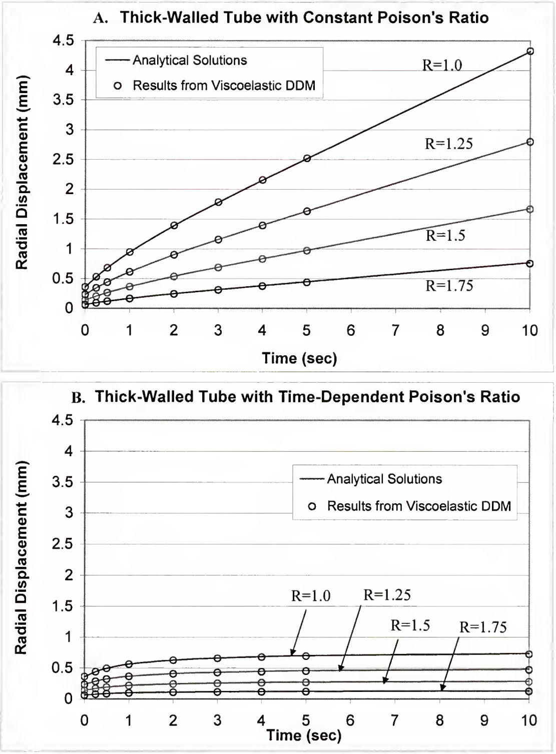

Figure 4-18. Radial Displacements of Thick-Walled Viscoelastic Tube. A) Case 4 Constant Poison Ratio, and B) Case 3 Time-Dependent Poison Ratio.

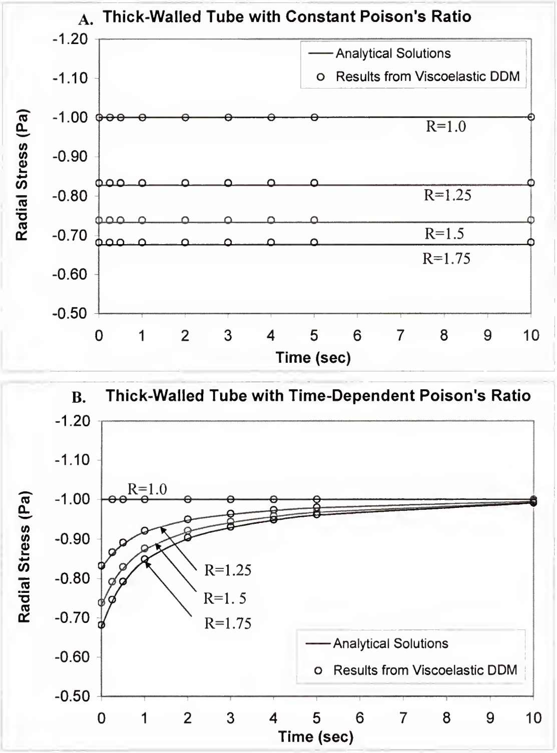

Figure 4-19. Radial Stresses of Thick-Walled Viscoelastic Tube. A) Case 4 Constant Poison Ratio, and B) Case 3 Time-Dependent Poison Ratio.

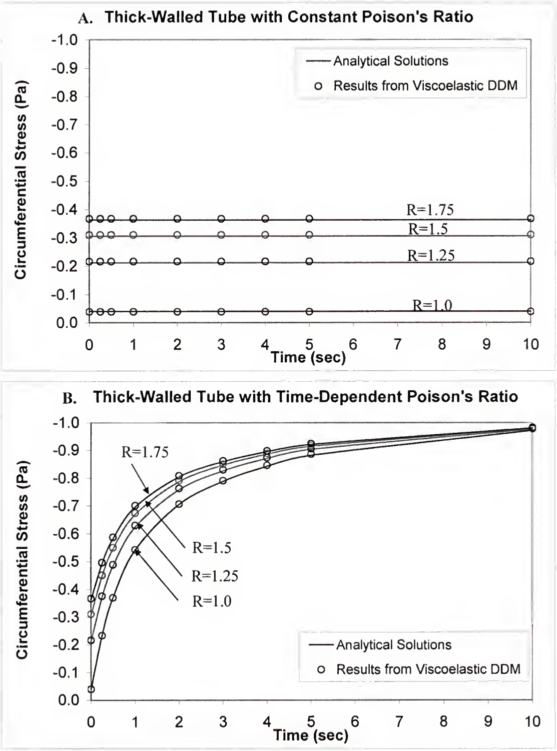

Figure 4-20. Circumferential Stresses of Thick-Walled Viscoelastic Tube. A) Case 4 Constant Poison Ratio, and B) Case 3 Time-Dependent Poison Ratio.

For the case of constant Poison ratio, the radial and circumferential stresses remain constant throughout the time. But for the time-dependent Poison ratio in case 3, the compressive stresses increase with time and converge to the value of internal pressure (-1 Pascal). The constant Poison ratio also has an effect on the radial displacement in the tube. The tube with constant Poison ratio gains significantly greater radial displacement that of the tube with time-dependent Poison ratio. This is because the Poison ratio is increasing with time in the case of time-dependent Poison ratio, which results in smaller radial displacement.

In this thick-walled tube problem, the material with time-dependent Poison ratio seems to be stiffer with time by gaining more resistance in stresses and allowing less deformation. While the material with constant Poison ratio behaves softer by yielding consistent rate of deformation and remaining its stress state. However, the effects of Poison ratio variation seem to be less significant at shorter time period. In some problems, it may make only slight difference in the solutions of stress and displacement when either the constant Poison ratio or the time-dependent Poison ratio is used.

4.9 Viscoelasticity of Hot Mix Asphalt Mixtures

The relaxation modulus and the compliance are the two fundamental parameters used for describing the time-dependent characteristic of viscoelastic materials. In hot mix asphalt mixtures, the compliance and the Poisson ratio are the common viscoelastic properties that can be simply obtained by performing a constant load creep test such as the Superpave indirect tension creep test (Roque and Buttlar 1992). The creep compliance is obtained from dividing the measured strain by the stresses at the measured location. The compliance obtained from the indirect tension creep test is equivalent to the one-dimensional compliance. According to the Superpave indirect tension creep test specification (Roque et al. 1997), the Poisson ratio is assumed constant throughout the test period. When the Poisson ratio is kept constant, it means the Poisson effect on the lateral strain has the same time-dependent characteristic as in the normal direction. This assumption was based on the observations in past experiments during the development of the test specification that the Poisson ratio of asphalt mixtures does not vary significantly with time. Thus, assuming a constant Poisson ratio would not significantly affect the overall predicted time dependent behavior of the asphalt materials.

For asphalt mixtures, the Poison ratio is

$$\nu(t) = \nu. \tag{4-93}$$

The one-dimensional compliance function is written in either of the following forms.

For Burgers model,
$$J(t) = \frac{1}{R_1} + \frac{t}{\eta_1} + \frac{1}{R_2}\left(1 - \exp\left(-\frac{R_2}{\eta_2}t\right)\right) \tag{4-94a}$$

For power law model,
$$J(t) = D(t) = D_0 + D_1\, t^m \tag{4-94b}$$

The transform compliance for asphalt mixture is then equivalent to the inverse transform Young modulus, i.e.

$$s\cdot \bar{J}(s) = \frac{1}{s\bar{E}(s)} \tag{4-95}$$

Since the Poisson's ratio is constant with time, the transform Poisson ratio, $s\cdot \bar{\nu}(s)$, is

$$\bar{\nu}(s) = \nu \tag{4-96}$$

While the compliance function in transform domain, $s\cdot \bar{J}(s)$, becomes

for Burgers model (Equation 4-32)
$$s\cdot \bar{J}(s) = \frac{1}{R_1} + \frac{1}{\eta_1 s} + \frac{1}{\eta_2(s + R_2/\eta_2)} \tag{4-97a}$$

for power law model (Equation 4-42)
$$s\cdot \bar{J}(s) = s\cdot \overline{D}(s) = \frac{D_0 s^m + D_1\Gamma(m+1)}{s^m} \tag{4-97b}$$

where $\Gamma(z)$ is the Euler Gamma function: $\Gamma(z) = \int_0^\infty t^{z-1} e^{-t} dt$.

By the Correspondence Principle, we can obtain the transformed shear modulus $s \cdot \overline{G}(s)$ from the equation:

$$s \cdot \overline{G}(s) = \frac{s\overline{E}(s)}{2(1+\overline{v}(s))} \tag{4-98}$$

where $$s \cdot \overline{E}(s) = \frac{1}{s\overline{J}(s)} .$$

Substitute $s \cdot \overline{J}(s)$ in (4-97) and $s \cdot \overline{v}(s)$ in (4-96) into the above equation to obtain the transform shear modulus.

For Burgers model, $$s \cdot \overline{G}(s) = \frac{1}{2(1+\nu)} \cdot \left[\frac{1}{R_1} + \frac{1}{\eta_1 s} + \frac{1}{\eta_2 (s + R_2/\eta_2)} \right]^{-1} \tag{4-99a}$$

For power law model, $$s \cdot \overline{G}(s) = \frac{1}{2(1+\nu)} \cdot \frac{s^m}{D_0 s^m + D_1 \Gamma(m+1)} \tag{4-99b}$$

Now, the transform shear modulus and Poison ratio in Equations (4-96) and (4-99) can be used in the displacement discontinuity equations.

4.10 Dissipated Creep Strain Energy

It was discussed earlier that the constitutive response for a viscoelastic material consists of three components: an elastic part, a delayed elastic part, and a permanent part. The strain energy that was explained in Section 4.7 is the total strain energy that includes total strain in the calculation. However, in the HMA fracture mechanics, the part of the strain energy that causes the cracking damage is the part that associates with permanent strain only, or known as dissipated creep strain energy (DCSE). The dissipated creep strain energy (DCSE) that contributes to cracking damage in asphalt mixture is the energy created by the tensile stress and permanent tensile strain that are acting on the crack growth plane. Now let us assume that the tensile stress is acting in a local y-direction. The dissipated creep strain energy on the y-direction is determined by the following equation:

$$\mathrm{DCSE} = W_p(t) = \int_0^t \sigma_{yy}(\tau)\,\dot{\varepsilon}_{p\,yy}(\tau)\,d\tau \tag{4-100}$$

where $\dot{\varepsilon}_{p\,yy}(\tau)$ is the rate of tensile creep strain in y-direction, and $\sigma_{yy}(\tau)$ is the tensile stress in y-direction.

The permanent strain is the amount of the strain that remains unrecoverable long after the loading was released. However, it is not practically appropriate to determine the permanent strain after the release of loading, since sometimes it is difficult to separate the permanent component from the total response, and in many cases the release of loading is not allowed in the problems. Alternatively, a more practical method to determine permanent strain is to apply the permanent part of material properties when calculating strain, which results in obtaining only the permanent strain. Let us refer to the permanent part of compliance-time function for Power law model in Equations (4-45):

$$J_p(t) = D_p\,(t) = \frac{dD(t_{max})}{dt}\,t = m\,D_1\,(t_{max})^{m-1}\,t \tag{4-101}$$

where t_{max} is the maximum period of creep test.

For Burgers model, the permanent compliance is due to the action of external dashpot and was presented earlier in Equation (4-46):

$$J_p(t) = \frac{t}{\eta_1} \tag{4-102}$$

The Laplace transform of the permanent compliance functions are

$$\bar{J}_p(s) = \bar{D}_p(s) = m\, D_1\, (t_{max})^{m-1}\, \frac{1}{s^2} \quad \text{for power law model} \qquad (4\text{-}103a)$$

$$\bar{J}_p(s) = \frac{1}{\eta_1 s^2} \quad \text{for Burgers model} \qquad (4\text{-}103b)$$

The transform permanent compliance, $s\,\bar{J}_p(s)$, becomes

$$s\,\bar{J}_p(s) = \bar{D}_p(s) = m\, D_1\, (t_{max})^{m-1}\, \frac{1}{s} \quad \text{for power law model} \qquad (4\text{-}104a)$$

$$s\,\bar{J}_p(s) = \frac{1}{\eta_1 s} \quad \text{for Burgers model} \qquad (4\text{-}104b)$$

Since the compliance is in one-dimensional sense, i.e. $s\cdot\bar{E}(s) = \frac{1}{s\bar{J}(s)}$, apply the transform permanent compliance to find the transform permanent shear modulus as follows:

$$s\cdot\bar{G}_p(s) = \frac{1}{2(1+\bar{\nu}(s))}\cdot\frac{1}{s\bar{J}(s)} \qquad (4\text{-}105)$$

For power law model, $$s\cdot\bar{G}_p(s) = \frac{1}{2(1+\nu)}\,\frac{s}{mD_1(t_{max})^{m-1}} \qquad (4\text{-}106a)$$

For Burgers model, $$s\cdot\bar{G}_p(s) = \frac{\eta_1 s}{2(1+\nu)} \qquad (4\text{-}106b)$$

After the transform permanent shear modulus is known, the dissipated creep strain energy in Equation (4-100) can be determined by the similar process in Section 4.7.

- Obtain the transform stresses tensor $\bar{\sigma}_{yy}(s)$ and $\bar{\sigma}_{xx}(s)$ by Equation (4-58)
- Obtain the permanent strain rate in transform domain by using $s\cdot\bar{G}_p(s)$ instead of $s\cdot\bar{G}(s)$ in Equation (4-67):

$$\bar{\dot{\varepsilon}}_{p\,yy}(s) = s\cdot\frac{1}{2\,s\bar{G}_p(s)}\left[\bar{\sigma}_{yy}(s) - s\cdot\bar{\nu}(s)\cdot(\bar{\sigma}_{xx}(s) + \bar{\sigma}_{yy}(s))\right] \qquad (4\text{-}107)$$

- Perform numerical inversion on $\bar{\sigma}_{yy}(s)$ and $\bar{\dot{\varepsilon}}_{p\,yy}(s)$ to obtain $\sigma_{yy}(\tau_k)$ and $\dot{\varepsilon}_{p\,yy}(\tau_k)$ at time $\tau_k = 0.5\,t + 0.5\,t\,\xi_1$, $0.5\,t + 0.5\,t\,\xi_2$, and $0.5\,t + 0.5\,t\,\xi_3$.

- Calculate the creep strain energy by the 3-point Gauss quadrature numerical integration:

$$\mathrm{DCSE} = W_p(t) = \int_0^t \sigma_{yy}(\tau)\,\dot{\varepsilon}_{p\,yy}(\tau)\,d\tau \cong \Big[\sum_{k=1}^{3} A_k\, f(\tau_k)\Big]\cdot 0.5\,t \tag{4-108}$$

where $f(\tau_k) = \sigma_{yy}(\tau_k)\,\dot{\varepsilon}_{p\,yy}(\tau_k)$.

4.11 Response of Viscoelastic Material to Cyclic Loading

In flexible asphalt pavements, asphalt mixtures are subjected to cyclic loading in most of the time. In the following, the time-dependent response of a viscoelastic material to application of cyclic loading is considered.

Let us consider a location A in a viscoelastic material. A cycle of haversine load is applied to the material and induces tensile stress at location A as follows:

$$\sigma(t) = \sigma_0\,[\sin\omega t + \sin\omega(t-T)\cdot H(t-T)] \tag{4-109}$$

where $\omega = \pi/T$, T is the period of the haversine, and H(t-T) is a unit step function. Figure 4-21 illustrates a cycle of haversine stress. If the viscoelastic material is represented by a Burgers model, a total strain response to one cycle of uniaxial haversine stress is

$$\varepsilon(t) = \varepsilon_{sin}(t) + \varepsilon_{sin}(t-T)\cdot H(t-T) \tag{4-110}$$

where

$$\varepsilon_{sin}(t) := \sigma_0\cdot\left[\frac{1}{R_1}\cdot\sin(\omega\cdot t) + \frac{1}{\eta_1\cdot\omega}\cdot(1-\cos(\omega\cdot t)) + \frac{1}{\eta_2\cdot(\omega^2+\alpha^2)}\cdot\left(\alpha\cdot\sin(\omega\cdot t) - \omega\cdot\cos(\omega\cdot t) + \omega\cdot e^{-\alpha\cdot t}\right)\right] \tag{4-111}$$

R_1, η_1, R_2, and η_2 are Burgers constants. $\varepsilon_{sin}(t-T)$ is the total strain response of Burgers material to a continuous sinusoidal stress. The detail of derivation of this solution is presented in Appendix C. Figure 4-21 also includes the diagram of the total strain response for one haversine cycle. In one cycle of haversine loading, the induced tensile stress fully deceases after the haversine period, T. The total strain response at a long time can be found by

$$\lim_{t\to\infty} \varepsilon(t) = \frac{2\sigma_0}{\eta_1\omega} \tag{4-112}$$

This is because the sine and cosine terms in $\varepsilon_{sin}(t) + \varepsilon_{sin}(t-T) \cdot H(t-T)$ disappear due to addition at a period shift (T). While the exponential terms become zero at long time. Only is the permanent strain, $\frac{2\sigma_0}{\eta_1\omega}$, left in the material.

Now let us consider the material responses due to multiple haversine loading cycles. The cyclic haversine stress at point A is shown in Figure 4-22. The stress function can be written by a superposition of multiple haversine cycles, each of which is shifted by a period of Δt:

$$\begin{aligned}\sigma(t) = \;& \sigma_0\,[\sin \omega t + \sin \omega(t-T)\cdot H(t-T)] + \\ & \sigma_0\,[\sin \omega(t-\Delta t)\cdot H(t-\Delta t) + \sin \omega(t-\Delta t-T)\cdot H(t-\Delta t-T)] + \\ & \sigma_0\,[\sin \omega(t-2\cdot\Delta t)\cdot H(t-2\cdot\Delta t) + \sin \omega(t-2\cdot\Delta t-T)\cdot H(t-2\cdot\Delta t-T)] + \ldots\end{aligned} \tag{4-113}$$

By using the Boltzmann's superposition principle (Findley et al. 1976), the solution of total strain due to multiple load steps is the superposition of multiple total strain responses due to cyclic haversine stresses presented at various periods. Figure 4-23 illustrates the superposition of multiple total strain responses. The total strain response can be written in the form:

$$\begin{aligned}\varepsilon(t) = \;& \varepsilon_{sin}(t) + \varepsilon_{sin}(t-T) \cdot H(t-T) + \\ & \varepsilon_{sin}(t-\Delta t) \cdot H(t-\Delta t) + \varepsilon_{sin}(t-\Delta t - T) \cdot H(t-\Delta t - T) +\end{aligned}$$

$$\varepsilon_{\sin}(t-2\cdot\Delta t)\cdot H(t-2\cdot\Delta t) + \varepsilon_{\sin}(t-2\cdot\Delta t - T)\cdot H(t-2\cdot\Delta t - T) + \ldots \qquad (4\text{-}114)$$

The supporting details of the above and the following equations are presented in Appendix D.

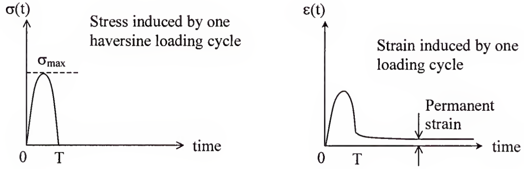

Figure 4-21 Stress and Strain Induced by a Single Loading Cycle.

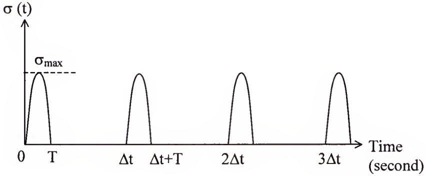

Figure 4-22. Stress for Cyclic Haversine Loading.

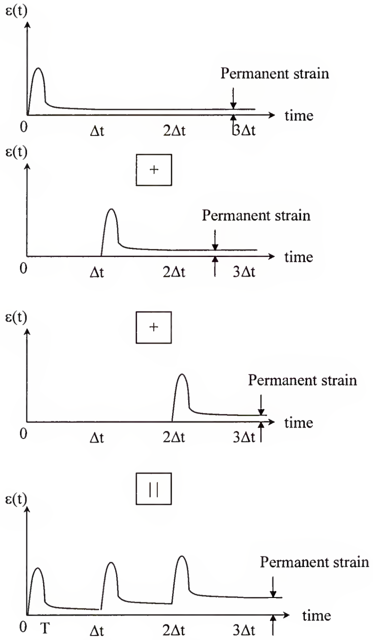

Figure 4-23. Total Strain Response due to Cyclic Haversine Stress.

The permanent strain response due to cyclic loading should become

$$\lim_{t\to\infty} \varepsilon(t) = \lim_{t\to\infty} [\ \varepsilon_{sin}(t) + \varepsilon_{sin}(t\text{-}T) \cdot H(t\text{-}T)\ ]+$$

$$\lim_{t\to\infty} [\ \varepsilon_{sin}(t\text{-}\Delta t) \cdot H(t\text{-}\Delta t) + \varepsilon_{sin}(t\text{-}\Delta t\ \text{-}T) \cdot H(t\text{-}\Delta t\ \text{-}T)\ ] +$$

$$\lim_{t\to\infty} [\ \varepsilon_{sin}(t\text{-}2\cdot\Delta t) \cdot H(t\text{-}2\cdot\Delta t) + \varepsilon_{sin}(t\text{-}2\cdot\Delta t\ \text{-}T) \cdot H(t\text{-}2\cdot\Delta t\ \text{-}T)\ ] + \ldots \quad (4\text{-}115)$$

$$\lim_{t\to\infty} \varepsilon(t) = \frac{2\sigma_0}{\eta_1\omega} + \frac{2\sigma_0}{\eta_1\omega} + \frac{2\sigma_0}{\eta_1\omega} + \ldots \quad (4\text{-}116)$$

Thus, the permanent strain response due to the cyclic haversine loading is the superposition of each permanent strain response due to each haversine cycle. This superposition concept can also be applied to the dissipated creep strain energy. The equation for dissipated creep strain energy in one dimension is

$$\text{DCSE} = W_p(t) = \int_0^t \sigma(\tau)\,\dot{\varepsilon}_p(\tau)\,d\tau \quad (4\text{-}117)$$

Since, the dissipated creep strain energy is calculated from the permanent strain, it is also an unrecoverable (permanent) quantity. The total dissipated creep strain energy induced by multiple haversine loading cycles then equals the superposition of dissipated creep strain energy due to each haversine loading cycle. This concept of accumulation of dissipated creep strain energy also appears in the HMA fracture mechanics (Zhang 2000; Zhang et al. 2001), and will be applied to the determination of cracking damage for asphalt mixture in the next Chapter.

CHAPTER 5
HOT MIX ASPHALT FRACTURE MECHANICS-BASED CRACK GROWTH SIMULATOR

Fatigue cracking due to repeated traffic loading is one of the major distresses in asphalt concrete pavements. These cracks may start as micro-cracks that later coalesce to form macro-cracks that propagate due to tensile or shear stress or combinations of both. Pavement serviceability is reduced as these cracks propagate. A mixture's resistance to crack development and propagation affects the cracking performance of asphalt pavements. The recognition of the importance of understanding of the cracking behavior of asphalt pavements, combined with a strong desire to have a practical and reliable system to determine a mixture's resistance to crack development and propagation lead the Florida Department of Transportation to sponsor a research program at the University of Florida to identify a suitable crack growth law for asphalt mixtures that could provide the foundation for the development of a pavement cracking prediction model (Birgisson et al. 2002b; Zhang et al. 2001b). This research effort has lead to an improved understanding of the cracking behavior of asphalt mixtures, resulting in the development of a new viscoelastic fracture mechanics-based crack growth law, entitled "HMA fracture mechanics (HMAFM)" (Zhang et al. 2001b; Roque et al. 2002). The HMA fracture mechanics framework uses a set of key mixture parameters that were found to govern both crack initiation and crack propagation.

Perhaps the most important feature of the HMA fracture mechanics crack growth law is the inclusion of a fundamental crack growth threshold, below which only healable micro-damage develops, and above which non-healable crack initiation or growth occurs. The introduction of a fundamental crack growth threshold allows for the simulation of discontinuous crack growth, which is consistent with observed crack growth behavior in hot mix asphalt mixtures (Birgisson et al. 2002b; Zhang et al. 2001b; Kim et al. 1997; Jacobs et al. 1996). In contrast, in conventional fracture mechanics, the crack growth is generally assumed to be continuous and initial crack sites must be selected for analysis and evaluation.

The HMA fracture mechanics model appears to provide a powerful tool for mixture optimization and design. The model can also be used as the foundation for the prediction of pavement performance for the purposes of specification development, mixture design, and pavement thickness design. Unfortunately, the prediction of crack initiation and crack growth for generalized pavement loading, environmental, and geometric configurations, requires numerical solutions, such as those obtained by the finite element method.

The complexity of modeling the mechanics of crack initiation and crack growth with traditional numerical methods, such as the finite element method (FEM) has been an obstacle to the incorporation of fracture mechanics-based approaches in the bituminous pavement area, as discussed by Birgisson et al. (2002a). The FEM requires highly refined meshes around the cracking area in order to simulate the stresses around the near crack tip area. Improper mesh generation will result in a failure to capture the very important stress singularity at the crack tip. The simulation of crack growth with the FEM also requires elaborate remeshing to simulate the geometry of a growing crack. The computational intensity required puts these types of problems out of the realm of reasonableness for the typical capabilities of personal computers, which means that only select research organizations and major universities have the capabilities to perform these types of calculations.

The displacement discontinuity method (DDM) provides a natural method for modeling crack initiation and crack growth, as discussed in chapter two. The DD method requires meshes only on the boundaries of an object or pavement, including cracks. This means that the number of elements required is reduced significantly. Also, the stress singularity at the crack tip is naturally included in the DD. Crack growth is addressed simply by adding more DD elements in regions of crack growth.

As a result, the new HMA fracture mechanics-based crack growth simulator was developed from the displacement discontinuity method under the HMA fracture mechanics crack growth law. In this chapter, the details of implementation of the fracture simulator and its key features are described.

5.1 Hot-Mixed Asphalt Fracture Simulator Framework

Figure 5-1 illustrates the diagram of the new HMA fracture simulator. The structure is modeled by placing the DD elements on the boundaries. The location(s) of possible crack initiation must be specified in the model. Knowing the critical location(s), the critical zone can be defined in front of those location(s). The DD method calculates the tensile-mode dissipated creep strain energy (if any) in the critical zone vicinity. The strain energy represents the amount of damage that is induced by one application of the loading spectrum. The loading spectrum is a time record of all loading applications; each can differ in magnitude and point of contact. Thus, it is necessary to determine amount of induced damage step by step according to the loading spectrum. This damage is accumulative as long as not exceeding the damage threshold (i.e. dissipated creep strain energy limit). Once the DCSE exceeds or reaches the DCSE limit, a macro-crack forms in the critical zone and causes the crack to grow by length of the zone in the direction of maximum DCSE.

The fracture simulator then places a few number of DD elements on the crack extension to represent the new crack length. At this point, the critical location for crack propagation moves to the tip of the new crack geometry. The new critical zone vicinity is determined. Before starting the process with the next loading application, an initial damage must be added to the new critical zone in order to account for the fact that damage has occurred in this area during the loadings on the previous crack geometry. With the new geometry and initial damage condition, the fracture simulator is now ready to continue calculate and accumulate DCSE in the current critical zone through the remaining of loading spectrum. Once the damage in the critical zone again reaches the threshold, the crack propagates another step.

Throughout the process of crack growth, the history of load applications at each step of crack length is recorded for illustrating the rate of crack growth.

5.2 Assumptions and Limitations

The limitations and assumptions of the hot mix asphalt fracture simulator are described as follows:

- Asphalt mixtures are treated as isotropic, piecewise-homogeneous, viscoelastic materials in the analysis. This means that the current formulation follows a traditional fracture mechanics-based framework, where it is well accepted that the influence of microstructure in granular materials (e.g. HMA, concrete, rock) can be captured through "homogenized" macro-properties, such as strength, stiffness, creep compliance, etc.

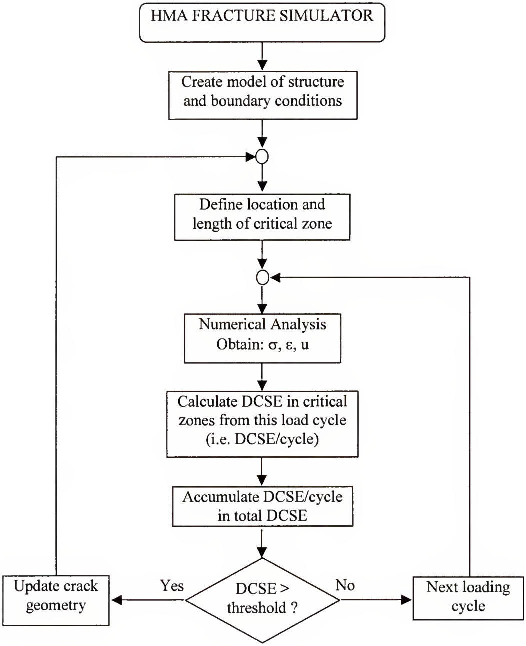
HMA FRACTURE SIMULATOR
Create model of structure and boundary conditions
Define location and length of critical zone
Numerical Analysis Obtain: σ, ε, u
Calculate DCSE in critical zones from this load cycle (i.e. DCSE/cycle)
Accumulate DCSE/cycle in total DCSE
DCSE > threshold ?
Yes
No
Update crack geometry
Next loading cycle

Figure 5-1. Flowchart Diagram of the HMA Fracture Simulator

- The DDM framework on which the fracture simulator is based is currently limited to two-dimensional analysis (plane stress or plane strain). Although cracking in hot-mix asphalt is generally three-dimensional, a firm understanding of the issues in two dimensions should precede any further analysis
- The HMA fracture mechanics crack growth law describes the load-initiated tensile mode of cracking. Its key parameters were obtained from standard test results (strength test, Mr test, and creep test) at low temperatures between 0 to15°C.
- Verification of the HMA fracture mechanics crack growth law has only been done with IDT crack growth in Superpave mixtures.

5.3 Critical Zone

A micro-mechanics study of hot mix asphalt cracking under indirect tension test by Birgisson et al. (2002c; 2003) indicated an evidence of cracks propagating by breaking through large aggregate particles in asphalt mixtures with its aggregate produced from weak limestone. On the other hand, Birgisson et al. (2002c; 2003) found that cracking can also develop around large aggregate particles through the mastic in mixtures produced from strong aggregates e.g. granite, limestone. Hence, crack growth patterns in hot mix asphalt seems to depend on the microscopic structure of the mixture. However the attempt to understand this microstructural phenomenon is beyond the scope of this study.

In the HMA fracture mechanics crack growth model, a critical zone is introduced ahead of the crack tip, representing the portion of the mixture being damaged by healable micro-damage. Once the cumulative micro-damage inside the critical zone reaches the cracking threshold, a macro-crack is formed, and the crack extends by the length of the critical zone immediately in front of the crack. Thus, the critical zone is a key feature governing the characteristic stepwise crack growth, observed in HMA mixtures.

Originally, the HMA fracture mechanics growth rule defined the length of the critical zone by the location at which the tensile stress reached the yield stress limit

(Zhang et al. 2001; Birgisson et al. 2002b). In other words, it is a stress-dependent definition. In general crack propagation problems, significant variations in stresses are expected, resulting in changes in the portions of the mixture under yield stress conditions, which in turn changes the zone length, making it impossible to consistently define the zones.

A potential solution to this problem is to apply a new definition for the length of the critical zone (i.e. the portion of the crack growth zone immediately next to the crack tip). Birgisson et al. (2002c and 2003) showed that a size effect related to the size and structure of the aggregates may exist in asphalt mixtures. This means that it is rational to define a critical zone length, independent of stress condition, throughout the crack growth process.

A study is conducted to evaluate the effect of equal zone length definitions on the crack growth characteristics of mixtures under a condition of the indirect tension fracture test (Roque et al. 1999) shown in Figure 5-2. The crack growth prediction is set to develop at an equal length in each step by introducing an equal-sized critical zone in front of the crack tip at every step of crack geometry. Thus, a series of zones with an equal length can be located on the crack growth path as presented in Figure 5-3, where c_1 , c_2 , c_3 , … are the lengths of zone 1, 2, 3, … correspondingly. A set of different lengths of the equal-sized zone is tested to evaluate the effect of the zone length.

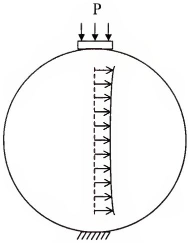

Conventional Indirect Tension

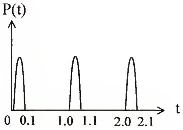

Haversine Cyclic Loads

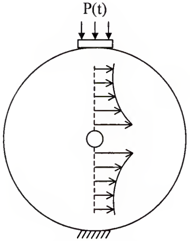

Indirect Tensile Fracture

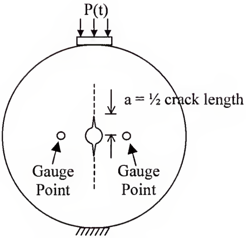

Crack Development

Figure 5-2. Superpave Indirect Tension Fracture Test.

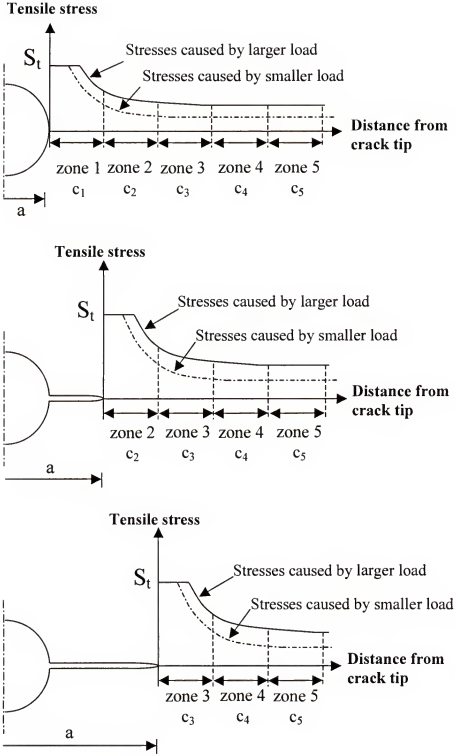
Tensile stress
S_t
Stresses caused by larger load
Stresses caused by smaller load
Distance from crack tip
zone 1 zone 2 zone 3 zone 4 zone 5
c_1 c_2 c_3 c_4 c_5
a
Tensile stress
S_t
Stresses caused by larger load
Stresses caused by smaller load
Distance from crack tip
zone 2 zone 3 zone 4 zone 5
c_2 c_3 c_4 c_5
a
Tensile stress
S_t
Stresses caused by larger load
Stresses caused by smaller load
Distance from crack tip
zone 3 zone 4 zone 5
c_3 c_4 c_5
a

Figure 5-3. Diagram Illustrating the Concept of Equal-Sized Critical Zone Length.

The following are the patterns of zone length used in the trials:

1. All zones have equal length of 1 millimeter, i.e. $c_1, c_2, c_3, \ldots = 1$ mm.
2. All zones have equal length of 2 millimeters, i.e. $c_1, c_2, c_3, \ldots = 2$ mm.
3. All zones have equal length of 5 millimeters, i.e. $c_1, c_2, c_3, \ldots = 5$ mm.
4. The first zone length is set to 5 millimeters to simulate a greater length of crack initiation. All other zones have equal length of 2 millimeters, i.e. $c_1 = 5$ mm. $c_2, c_3, c_4, \ldots = 2$ mm.
5. For comparison purpose, the original stress-dependent zone length as presented in the original HMA fracture mechanics model (Zhang et al. 2001; Birgisson et al. 2002b) is also included (detail presented in chapter 2). Each zone length is determined by

$$\text{Zone length, } c_i = \frac{1}{2}\left(\frac{\sigma_{FA}}{S_t}\right)^2 a \qquad (5\text{-}1)$$

where a is the one half of the current crack length, S_t is the tensile strength of the hot mix asphalt, and σ_{FA} is the far away tensile stress in the indirect tension test condition.

The crack growth predictions for all trials are performed by using the HMA fracture mechanics crack growth model (Zhang et al. 2001; Birgisson et al. 2002b) described in Chapter 2. All predictions are based on the same properties of the Superpave coarse-graded mix presented in Tables 5-1 and 5-2. The predicted crack length versus number of load cycles (a-N relationship) for each trial of zone lengths is presented in Figure 5-4.

The Results of predicted a-N relationships from various zone-length definitions are only slightly different. They are also only slightly different from the original stress dependent zone-length concept. This can be explained by the fact that the larger the equal-sized zone becomes, the lower the average tensile stress in that zone, which results in the smaller amount of cracking damage induced in each load cycle. Thus as the zone length increases, it takes more number of load repetitions for cracks to grow. Likewise, smaller equal-sized zone lengths require smaller number of load repetitions for cracks to propagate through the smaller zone length. Therefore, the overall crack growth characteristics remain similar for different sizes of equal zone lengths.

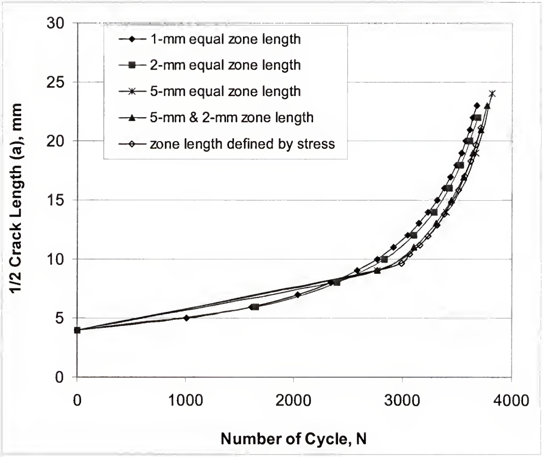

Figure 5-4. Effects of Different Zone Length Definitions on Crack Growth Characteristics.

Therefore, an equal zone length definition is implemented into the displacement discontinuity boundary element HMA fracture simulator to address the inconsistent zone length issue. The author believes that the appropriate equal size of the critical zone may be a function of aggregate size and structure, or possibly the geometry of the crack tip itself. However, the exact determination of the length of the critical zone is beyond the scope of this study. At this point, we will proceed with an equal zone length of one half of the maximum aggregate size, which ranges between 1.27 to 2.54 mm (0.5 to 1.0 inch) for most asphalt mixtures, for all crack growth predictions throughout the study.

5.4 Damage in Critical Zone

HMA fracture mechanics describes that healable micro-damage can be represented by dissipated creep strain energy (DCSE). The dissipated creep strain energy is the energy that is released to produce micro-cracks. The dissipated creep strain energy at a location in one direction (e.g. x-direction) due to a load application is determined by the tensile stress and the corresponding permanent strain rate as described earlier in Chapter 4 (equation 4-24):

$$\mathrm{DCSE} = \int_0^t \sigma_{xx}(\tau)\,\dot{\varepsilon}_{p\,xx}(\tau)\,d\tau \tag{5-2}$$

where t is the duration of a load application, $\sigma_{xx}(\tau)$ is the time-dependent tensile stress, $\dot{\varepsilon}_{p\,xx}(\tau)$ is the rate of permanent strain as a function of time, and τ is a time variable in the integral term.

Let us consider a cycle of haversine load that is applied to a simulated asphalt mixture sample under the indirect tensile test boundary conditions as shown in Figure 5-5. Figure 5-6 illustrates a typical plot of tensile stress distribution within a zone located in front of the crack tip. The haversine load cycle causes spatial and temporal variations of tensile stress induced in the zone ahead of the crack tip (Figure 5-5). The induced tensile stress reaches its peak magnitude at the half of haversine period. The tensile stress singularity ahead of the crack tip is limited by the maximum stress limit (i.e. tensile strength) of asphalt mixture.

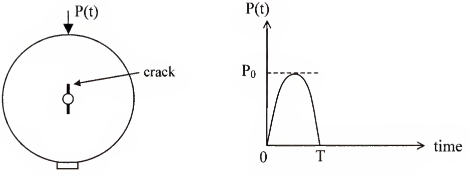

Half-sine loading function

Figure 5-5. Diagrams of IDT Crack Growth Test and the Time-Dependent Loading.

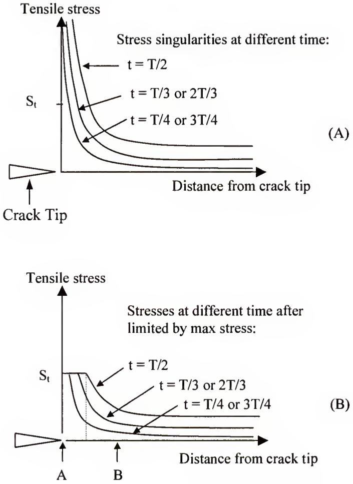

Figure 5-6. Stress Distributions Ahead of Crack Tip. A) Stress Singularities from Linear Elastic Fracture Mechanics-Based Solutions, and B) Stress Concentrations Limited by Limit Stress.

The location where the peak tensile stress reaches this stress limit can be approximated by

$$\text{Yield location} = \frac{1}{2}\left(\frac{\sigma_{FA}}{S_t}\right)^2 a \qquad (5\text{-}3)$$

where S_t is the tensile strength (the stress limit), a is one half of the crack length, and σ_{FA} is the far away uniform tensile stress field. This is the same equation that was used to define the critical zone in the original HMA fracture mechanics crack growth model (Zhang et al. 2001).

The spatial variation of tensile stress results in two different patterns of temporal strain responses inside the critical zone. For a location inside the area of tensile stress equal the maximum limit stress, the time-dependent stress is considered constant with time and equal to the stress limit. This time-dependent stress pattern is illustrated in Figure 5-7A. For a spot outside the area of tensile stress equal the limit stress, the time-dependent stress is below the stress limit and in the haversine pattern as illustrated in Figure 5-7B.

Since the equation of DCSE (5-2) is defined at a point location rather than on a portion of line, the DCSE that is required to represent the cracking damage in a critical zone can be obtained by averaging values of DCSE from several locations within the zone. As a result, a distribution of DCSE within the zone is required to evaluate the average DCSE in the zone.

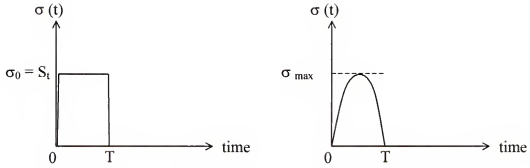

Stress at A induced by P(t)

Stress at B induced by P(t)

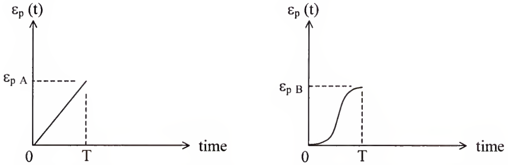

Creep strain at A induced by P(t)

Creep strain at B induced by P(t)

Figure 5-7. Stresses and Creep Strains ahead of Crack Tip in the IDT Crack Growth Test. A) Location A, and B) Location B.

In this study, the length of the equal-sized critical zone is greater than the location where stress exceeds the stress limit. Therefore, the determination of DCSE in the zone will involve the locations inside and outside the area where the stress exceeds the stress limit.

5.4.1 DCSE at Location Away from Crack Tip

Let us consider a location B away from the crack tip. At location B, the tensile stress normal to the critical zone line is lower than the limit stress throughout the loading period as illustrated in Figure 5-6. Figure 5-8 presents the two-dimensional stress state at the location B. In order to evaluate the DCSE at location B, we utilize the procedure presented in Chapter 4.10. The DCSE at a location B is determined by Equation (4-18):

$$\mathrm{DCSE} = \mathrm{W_p(t)} = \int_0^t \sigma_{nn}(\tau)\,\dot{\varepsilon}_{p\,nn}(\tau)\,d\tau \tag{5-4}$$

where $\dot{\varepsilon}_{p\,nn}(\tau)$ is the rate of tensile creep strain in the direction normal to the critical zone, and $\sigma_{yy}(\tau)$ is the tensile stress in the direction normal to the critical zone.

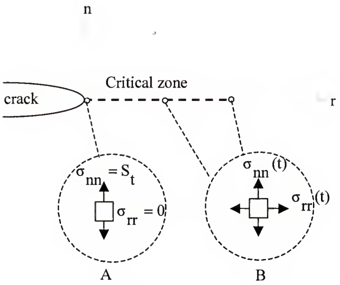

Figure 5-8. Stresses in the Critical Zone.

The time-dependent stress term in (5-4) can be determined by the viscoelastic displacement discontinuity method presented in Chapter 4. First, obtain the stress at location B in transform variable (s) by Equation (4-58):

$$\bar{\sigma}_{xx}(s) = \sum_{j=1}^{N} \frac{2\,s\bar{G}(s)}{1-\bar{v}(s)}[-2\,I_{,y} - y\,I_{,yy}]\,\bar{D}_s^{\,j}(s) + \sum_{j=1}^{N} \frac{2\,s\bar{G}(s)}{1-\bar{v}(s)}\,[-II_{,y} - y\,II_{,yy}]\,\bar{D}_n^{\,j}(s) \tag{5-5a}$$

$$\bar{\sigma}_{yy}(s) = \sum_{j=1}^{N} \frac{2\,s\bar{G}(s)}{1-\bar{v}(s)}\,[y\,I_{,yy}]\,\bar{D}_s^{\,j}(s) + \sum_{j=1}^{N} \frac{2\,s\bar{G}(s)}{1-\bar{v}(s)}\,[-II_{,y} + y\,II_{,yy}]\,\bar{D}_n^{\,j}(s) \tag{5-5b}$$

$$\bar{\sigma}_{xy}(s) = \sum_{j=1}^{N} \frac{2\,s\bar{G}(s)}{1-\bar{v}(s)}\,[-II_{,y} - y\,II_{,yy}]\,\bar{D}_s^{\,j}(s) + \sum_{j=1}^{N} \frac{2\,s\bar{G}(s)}{1-\bar{v}(s)}\,[\,y\,I_{,yy}]\,\bar{D}_n^{\,j}(s) \tag{5-5c}$$

where $\overline{G}(s)$ and $\overline{\nu}(s)$ are the transform shear modulus and transform Poison ratio, the terms I, II and their derivatives are the influence coefficients independent of time, and $\overline{D}_s^j(s)$, $\overline{D}_n^j(s)$ are the displacement discontinuities on the elements, which are determined by solving Equations (4-56, 4-57):

$$\overline{b}_s^{\,i}(s) = \sum_{j=1}^{N} \overline{C}_{ss}^{\,ij}(s)\overline{D}_s^{\,j}(s) + \sum_{j=1}^{N} \overline{C}_{sn}^{\,ij}(s)\overline{D}_n^{\,j}(s) \quad i = 1 \text{ to } N \tag{5-6a}$$

$$\overline{b}_n^{\,i}(s) = \sum_{j=1}^{N} \overline{C}_{ns}^{\,ij}(s)\overline{D}_s^{\,j}(s) + \sum_{j=1}^{N} \overline{C}_{nn}^{\,ij}(s)\overline{D}_n^{\,j}(s) \quad i = 1 \text{ to } N \tag{5-6b}$$

where the $\overline{C}^{\,ij}(s)$ related terms are the influence coefficients in transform domain. The full details were covered in Chapter 4.

The transform stresses at location B obtained from Equation (5-5) are in the global coordinate orientation (x-y). With a similar directional transformation presented in Equations (3-40, 3-41), the transform stresses in the direction of the critical zone are obtained

$$\overline{\sigma}_{nn}(s) = \overline{\sigma}_{xx}(s)\sin^2\beta - 2\overline{\sigma}_{xy}(s)\sin\beta\cos\beta + \overline{\sigma}_{yy}(s)\cos^2\beta \tag{5-7a}$$

$$\overline{\sigma}_{rr}(s) = \overline{\sigma}_{xx}(s)\cos^2\beta + 2\overline{\sigma}_{xy}(s)\sin\beta\cos\beta + \overline{\sigma}_{yy}(s)\sin^2\beta \tag{5-7b}$$

$$\overline{\sigma}_{nr}(s) = -(\overline{\sigma}_{xx}(s) - \overline{\sigma}_{yy}(s))\sin\beta\cos\beta + \overline{\sigma}_{xy}(s)(\cos^2\beta - \sin^2\beta) \tag{5-7c}$$

where $\overline{\sigma}_{nn}(s)$ is the component normal to the zone, $\overline{\sigma}_{rr}(s)$ is the component tangent to the zone, $\overline{\sigma}_{nr}(s)$ is the shear component on the zone, and β is the angle between the critical zone line and the coordinate x-direction.

After the transform stresses at location B are determined, the rate of creep strain at location B in the direction normal to the critical zone under two-dimensional plane strain condition can be obtained from Equation (4-107):

$$\bar{\dot{\varepsilon}}_{p\,nn}(s) = s \cdot \frac{1}{2\,s\overline{G}_p(s)} [\,\bar{\sigma}_{nn}(s) - \bar{\nu}(s) \cdot (\bar{\sigma}_{rr}(s) + \bar{\sigma}_{nn}(s)\,)\,] \qquad (5\text{-}8)$$

where $\bar{\nu}(s)$ is the transform Poison ratio, which is considered constant for hot mix asphalt as described in Chapter 4:

$$\bar{\nu}(s) \rightarrow \nu. \qquad (5\text{-}9)$$

$\overline{G}_p(s)$ is the permanent component for transform shear modulus discussed in Section 4.10 Chapter 4. It can be obtained by utilizing Equation (4-106):

For power law model, $$s \cdot \overline{G}_p(s) = \frac{1}{2(1+\nu)} \frac{s}{mD_1(t_{max})^{m-1}} \qquad (5\text{-}10a)$$

For Burgers model, $$s \cdot \overline{G}_p(s) = \frac{\eta_1 s}{2(1+\nu)} \qquad (5\text{-}10b)$$

where η_1 is the external dashpot constant representing the permanent response in Burgers model. For power law model, m and D_1 are the compliance constants in compliance equation, $D(t) = D_0 + D_1 t^m$; and t_{max} is the maximum period of creep test, from which m and D_1 were obtained.

Now the stress and rate of permanent strain at location B in time domain can be obtained by the numerical inversion of $\bar{\sigma}_{nn}(s)$ and $\bar{\dot{\varepsilon}}_{p\,yy}(s)$ to obtain $\sigma_{yy}(t)$ and $\dot{\varepsilon}_{p\,yy}(t)$ in time domain. The DCSE at the location B is obtained by the numerical integration presented in Chapter 4.

5.4.2 DCSE at Location of Crack Tip

Let us consider the location A at the crack tip shown in Figure 5-6. The tensile stress normal to the critical zone at location A remains at the maximum tensile stress (S_t) throughout the loading period, i.e. $\sigma_{nn}(t) = S_t$. While the tangential stress at location A (crack tip) remains at zero because the surface of crack is free of traction, i.e. $\sigma_{rr}(t) = 0$. The stress components at location A in transform domain become

$$\sigma_{nn}(t) = S_t \qquad \rightarrow \qquad \bar{\sigma}_{nn}(s) = \frac{S_t}{s} \qquad \text{(5-11a)}$$

$$\sigma_{rr}(t) = 0 \qquad \rightarrow \qquad \bar{\sigma}_{nn}(s) = 0 \qquad \text{(5-11b)}$$

This time-dependent stress pattern results in the permanent strain response at location A as shown in Figure 5-6A. The rate of permanent strain at the location A under the two-dimensional plane strain condition can be determined by substituting (5-11) into (5-8):

$$\bar{\dot{\varepsilon}}_{p\,nn}(s) = s \cdot \frac{1}{2\,s\bar{G}_p(s)}\left[\frac{S_t}{s} - \bar{v}(s)\cdot\left(0 + \frac{S_t}{s}\right)\right]$$

$$\bar{\dot{\varepsilon}}_{p\,nn}(s) = \frac{1}{2\,s\bar{G}_p(s)} S_t\,[1 - \bar{v}(s)] \qquad \text{(5-12)}$$

where $\bar{v}(s)$ is the transform Poison ratio presented in (5-9), and $\bar{G}_p(s)$ is the permanent component for transform shear modulus presented in (5-10).

Now the stress and rate of permanent strain at location A in time domain can be obtained by the numerical inversion of $\bar{\sigma}_{nn}(s)$ and $\bar{\dot{\varepsilon}}_{p\,yy}(s)$ to obtain $\sigma_{yy}(t)$ and $\dot{\varepsilon}_{p\,yy}(t)$ in time domain. The DCSE at the location A is obtained by the numerical integration presented in Chapter 4.

5.4.3 Average DCSE in the Critical Zone

An example of tensile stress and DCSE variation in front of the crack tip is shown in Figure 5-9. The plots represent a HMA sample under the indirect tension fracture test at one half of crack length, a, of 9 mm (0.3543 in.). The sample was a Superpave coarse-graded mix. Its maximum tensile stress limit is 2.55 MPa (370 psi).

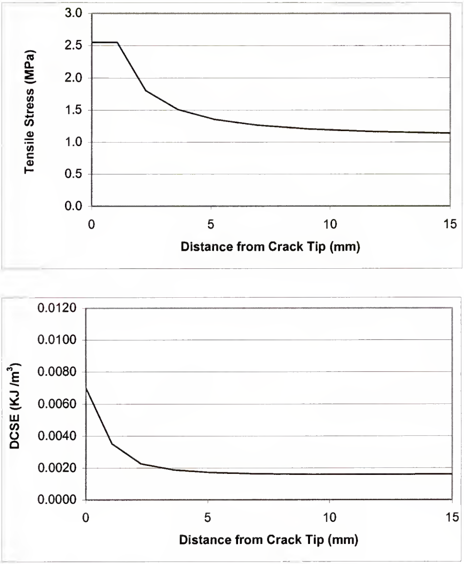

Figure 5-9. Tensile Stress and Dissipated Creep Strain Energy in Front of Crack Tip.

In this case, the length of the critical zone is set to one half of 1.27 mm (0.5-inch) maximum aggregate size. The average DCSE in the critical zone can be approximated by dividing the area under the 1-2-3 curve in Figure 5-10 by the length of the zone. The DCSE at three locations (1, 2, and 3) in the critical zone are required to approximate the area under DCSE curve by trapezoidal areas.

The DCSE at location (1), i.e. crack tip location, is determined by using the approach presented in Section 5.4.2. While the DCSEs at location (2) and (3) are obtained by using the approach illustrated in Section 5.4.1.

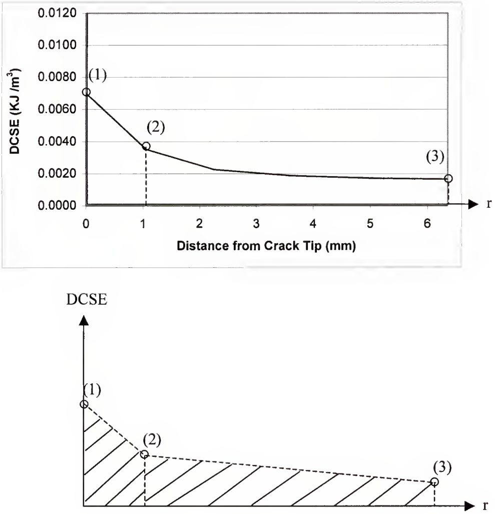

Figure 5-10. Dissipated Creep Strain Energy in the Critical Zone.

5.5 Strain History during Crack Propagation

It is important to mention that the micro-damage that exists in HMA material is not only healable, but it is also cumulative through the number of load applications. At any given moment of time, the total micro-damage in the critical zone located in front of the current crack geometry is actually comprised of the amount of micro-damage accumulated by the whole history of load applications. To explain this idea, let us consider diagram of crack growth history in Figure 5-11. The crack length a_2 is the current crack geometry with the critical zone (zone-i) in front of the crack tip (Figure 5-7c). Prior to the current crack geometry (a_2), the crack developed in stepwise manner from an initial crack length a_0 to crack length a_1, and continued from a_1 to the current crack a_2. From the beginning, the material with the initial crack (a_0) was damaged by a number of load cycles from the first cycle until the cycle N_1 when the initial crack length propagated to the length a_1. Besides causing the crack to grow the initial crack length, the load cycles from 1 to N_1 also created micro-damage to the area surrounding the initial crack which included the location of zone-i. Thus, the micro-damage was also accumulated in the zone-i in an amount of $DCSE_{(0\rightarrow N1)}$. After that, the load cycles from N_1+1 to N_2 caused micro-damage in front of crack geometry a_1 to develop into a macro-crack i.e. crack propagated to the crack length a_2. The load cycles from N_1+1 to N_2 also induced more micro-damage to the location of zone-i in an amount of $DCSE_{(N1\rightarrow N2)}$. Once the crack geometry arrives at the current stage (a_2), the critical zone-i already has an initial micro-damage of amount $DCSE_{(0\rightarrow N1)} + DCSE_{(N1\rightarrow N2)}$. Thus the total micro-damage in the critical zone i at current load application (N) equals $DCSE_{(0\rightarrow N1)} + DCSE_{(N1\rightarrow N2)} + DCSE_{(N2\rightarrow N)}$ as shown in Figure 5-12.

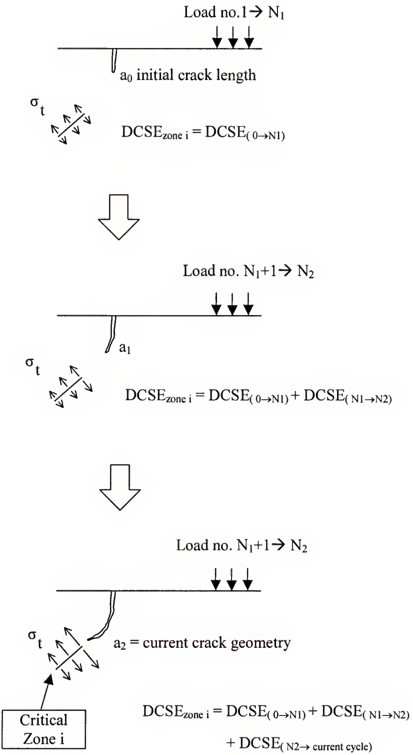
Load no.1→ N1
a0 initial crack length
σt
DCSEzone i = DCSE(0→N1)
Load no. N1+1→ N2
a1
σt
DCSEzone i = DCSE(0→N1) + DCSE(N1→N2)
Load no. N1+1→ N2
σt
a2 = current crack geometry
Critical Zone i
DCSEzone i = DCSE(0→N1) + DCSE(N1→N2) + DCSE(N2→ current cycle)

Figure 5-11. History of Crack Growth and Damage Accumulation.

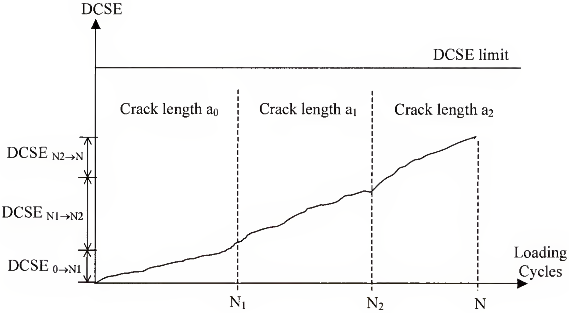

Figure 5-12. Cracking Damage Accumulation in the Critical Zone-i.

The fact that the cracking damage at an intact location from the previous state of crack geometry remains after the change of crack geometry, and serves as the initial damage at the new crack geometry can be proven by using the theory of viscoelasticity. Since the dissipated creep strain energy i.e. micro-damage is directly proportional to permanent creep strain, we can alternatively proof that the creep strain remains unchanged after crack geometry change, and then apply this analogy to the dissipated creep strain energy.

Strain history during crack propagation. Let us consider a crack in a viscoelastic material subjected to a uniform, one-dimensional tensile stress field. The tensile stress is applied in a haversine manner. As described earlier in Chapter 4, the tensile stress at the location A away from the crack tip and can be written in the following form:

$$\sigma(t) = \sigma_0 [\sin \omega t + \sin \omega(t-T) \cdot H(t-T)] \tag{5-13}$$

where σ_0 is the amplitude of haversine tensile stress, $\omega = \pi/T$ is the radial frequency, T is the period of the haversine, and H(t-T) is a unit step function.

If the viscoelastic material is represented by a Burgers model, a total strain response to the one-dimensional haversine stress is

$$\varepsilon(t) = \varepsilon_{\sin}(t) + \varepsilon_{\sin}(t-T) \cdot H(t-T) \qquad (5\text{-}14)$$

where

$$\varepsilon_{\sin}(t) := \sigma_0 \cdot \left[\frac{1}{R_1} \cdot \sin(\omega \cdot t) + \frac{1}{\eta_1 \cdot \omega} \cdot (1 - \cos(\omega \cdot t)) + \frac{1}{\eta_2 \cdot (\omega^2 + \alpha^2)} \cdot \left(\alpha \cdot \sin(\omega \cdot t) - \omega \cdot \cos(\omega \cdot t) + \omega \cdot e^{-\alpha \cdot t} \right) \right]$$

(5-15)

R_1, η_1, R_2, and η_2 are Burgers constants. $\varepsilon_{\sin}(t-T)$ is the total strain response of Burgers material to a continuous sinusoidal stress.

The permanent strain response that is left in the material after a long period can be found by

$$\varepsilon_p(\text{one cycle}) = \lim_{t \to \infty} \varepsilon(t) = \frac{2\sigma_0}{\eta_1 \omega} \qquad (5\text{-}16)$$

Figure 5-13 illustrates the diagram of the tensile stress and the total strain response for one haversine cycle. Now, the material is subjected to a multiple cycles of haversine stress shown in Figure 5-14. As described previously in Chapter 4, the stress and strain function at location A can be written by a superposition of each cycle with a shifted period of Δt.

$$\begin{aligned} \sigma(t) = \; & \sigma_0 [\sin \omega t + \sin \omega(t-T) \cdot H(t-T)] + \\ & \sigma_0 [\sin \omega(t-\Delta t) \cdot H(t-\Delta t) + \sin \omega(t-\Delta t-T) \cdot H(t-\Delta t-T)] + \\ & \sigma_0 [\sin \omega(t-2 \cdot \Delta t) \cdot H(t-2 \cdot \Delta t) + \sin \omega(t-2 \cdot \Delta t-T) \cdot H(t-2 \cdot \Delta t-T)] + \ldots \end{aligned} \qquad (5\text{-}17)$$

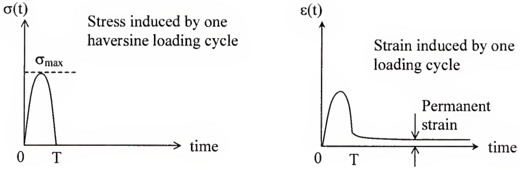

Figure 5-13. Stress and Strain Induced by a Single Haversine Load.

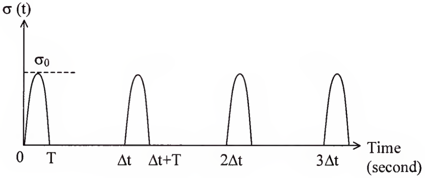

Figure 5-14. Stress Function of Cyclic Haversine Loading

$$\begin{aligned}\varepsilon(t) = {} & \varepsilon_{\sin}(t) + \varepsilon_{\sin}(t-T)\cdot H(t-T) + \\ & \varepsilon_{\sin}(t-\Delta t)\cdot H(t-\Delta t) + \varepsilon_{\sin}(t-\Delta t-T)\cdot H(t-\Delta t-T) + \\ & \varepsilon_{\sin}(t-2\cdot\Delta t)\cdot H(t-2\cdot\Delta t) + \varepsilon_{\sin}(t-2\cdot\Delta t-T)\cdot H(t-2\cdot\Delta t-T) + \ldots \qquad (5\text{-}18)\end{aligned}$$

The stress, total strain, and permanent strain induced by cyclic haversine load from 1 to N cycles can also be written in the summation term as

$$\sigma_A(t) = \sum_{i=0}^{N-1} \sigma_0\,[\sin\omega(t-i\cdot\Delta t)\cdot H(t-i\cdot\Delta t) + \sin\omega(t-i\cdot\Delta t-T)\cdot H(t-i\cdot\Delta t-T)] \qquad (5\text{-}19)$$

$$\varepsilon(t) = \sum_{i=0}^{N-1} \varepsilon_{\sin}(t-i\cdot\Delta t)\cdot H(t-i\cdot\Delta t) + \varepsilon_{\sin}(t-i\cdot\Delta t-T)\cdot H(t-i\cdot\Delta t-T) \qquad (5\text{-}20)$$

$$\varepsilon_p(\text{cycles 1 to N}) = \lim_{t\to\infty} \varepsilon(t) = \sum_{i=0}^{N-1} \frac{2\sigma_0}{\eta_1\omega} \tag{5-21}$$

The above equation indicates that the strain response to multiple haversine cycles is a result of superposition of a number of individual-cycle strain functions as illustrated in Figure 5-15.

Now considering the scenario of geometrical change due to crack growth, the initial crack length a_0 develops to a new crack length a_1 at the N_1^{th} load cycle. At the new crack length (a_1), the stress history at the location A away from the crack due to cyclic loads from cycles 1 to N ($N > N_1$) is written as

$$\sigma_A(t) = \sum_{i=0}^{N1-1} \sigma_0 \left[\sin \omega(t-i\cdot\Delta t)\cdot H(t- i\cdot\Delta t) + \sin \omega(t- i\cdot\Delta t-T)\cdot H(t- i\cdot\Delta t-T)\right] +$$

$$\sum_{i=N1}^{N-1} \sigma'_0 \left[\sin \omega(t-i\cdot\Delta t)\cdot H(t- i\cdot\Delta t) + \sin \omega(t- i\cdot\Delta t-T)\cdot H(t- i\cdot\Delta t-T)\right] \tag{5-22}$$

where σ_0 is the amplitude of haversine stress at location A under crack geometry of a_0, while σ'_0 is the amplitude of haversine stress when the crack geometry changes to a_1.

By using the Boltzmann's superposition principle (Findley et al. 1976), the solution of total strain due to multiple load cycles is the superposition of each total strain response due to a cyclic haversine load presented in the history as presented in Figure 5-16:

$$\varepsilon_A(t) = \sum_{i=0}^{N1-1} \varepsilon_{sin}(t- i\cdot\Delta t) \cdot H(t- i\cdot\Delta t) + \varepsilon_{sin}(t- i\cdot\Delta t -T) \cdot H(t- i\cdot\Delta t -T)$$

$$+ \sum_{i=N1}^{N-1} \varepsilon'_{sin}(t- i\cdot\Delta t) \cdot H(t- i\cdot\Delta t) + \varepsilon'_{sin}(t- i\cdot\Delta t -T) \cdot H(t- i\cdot\Delta t -T) \tag{5-23}$$

where the strain response to one haversine cycle at crack geometry a_0 is: (5-24)

$$\varepsilon_{sin}(t) := \sigma_0\cdot\left[\frac{1}{R_1}\cdot\sin(\omega\cdot t) + \frac{1}{\eta_1\cdot\omega}\cdot(1-\cos(\omega\cdot t)) + \frac{1}{\eta_2\cdot(\omega^2+\alpha^2)}\cdot\left(\alpha\cdot\sin(\omega\cdot t) - \omega\cdot\cos(\omega\cdot t) + \omega\cdot e^{-\alpha\cdot t}\right)\right]$$

And the strain response to one haversine cycle at crack geometry a_1 is: (5-25)

$$\varepsilon'_{\sin}(t) := \sigma'_0 \cdot \left[\frac{1}{R_1} \cdot \sin(\omega \cdot t) + \frac{1}{\eta_1 \cdot \omega} \cdot \left(1 - \cos(\omega \cdot t)\right) + \frac{1}{\eta_2 \cdot \left(\omega^2 + \alpha^2\right)} \cdot \left(\alpha \cdot \sin(\omega \cdot t) - \omega \cdot \cos(\omega \cdot t) + \omega \cdot e^{-\alpha \cdot t}\right) \right]$$

The permanent strain at the location A after cyclic load from 1 to N cycles are applied can be obtained by:

$$\varepsilon_p(\text{cycles 1 to N}) = \lim_{t\to\infty} \varepsilon(t)$$

$$= \sum_{i=0}^{N1-1} \lim_{t\to\infty} \{\varepsilon\sin(t- i\cdot\Delta t) \cdot H(t- i\cdot\Delta t) + \varepsilon\sin(t- i\cdot\Delta t -T) \cdot H(t- i\cdot\Delta t -T) \}$$

$$+ \sum_{i=N1}^{N-1} \lim_{t\to\infty} \{\varepsilon'\sin(t- i\cdot\Delta t) \cdot H(t- i\cdot\Delta t) + \varepsilon'\sin(t- i\cdot\Delta t -T) \cdot H(t- i\cdot\Delta t -T)\}$$

$$\varepsilon_p(\text{cycles 1 to N}) = \sum_{i=0}^{N1-1} \frac{2\sigma_0}{\eta_1\omega} + \sum_{i=N1}^{N-1} \frac{2\sigma'_0}{\eta_1\omega} \qquad (5\text{-}26)$$

Thus, for the new crack geometry, the strain at location A is composed of: 1) strain history due to loads from time 0 to N_1 when crack length was a_0, and 2) strain history due to loads after N_1 to the current N under a_1 crack length. Figure 5-16 illustrates this strain history.

In other words, the strain history from the previous crack length geometry serves as the initial condition for the new crack geometry. The new crack geometry does not change the history of strain that was induced by load history acting prior to the new crack geometry.

The dissipated creep strain energy (DCSE) is the nonreversible energy associated with the permanent strain presented in Equation (5-4). The total DCSE at a location A is an accumulation of individual DCSE caused by each load cycle. Therefore, the amount of total DCSE that is induced by load cycles 1 to N_l in the previous crack length will be also taken as an initial damage for the current crack geometry.

The complete details of damage accumulation during the crack growth are presented in Appendix D.

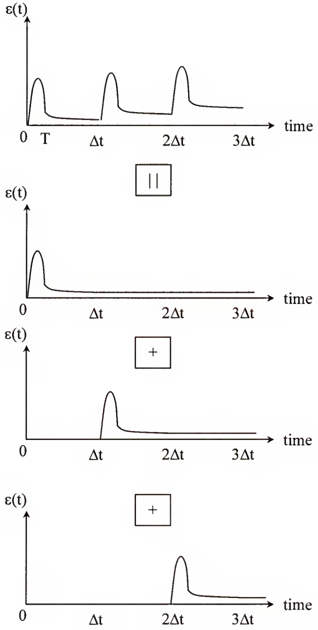

Figure 5-15. History of Strain is Composed of a Superposition of Individual Strains Induced at Different Time.

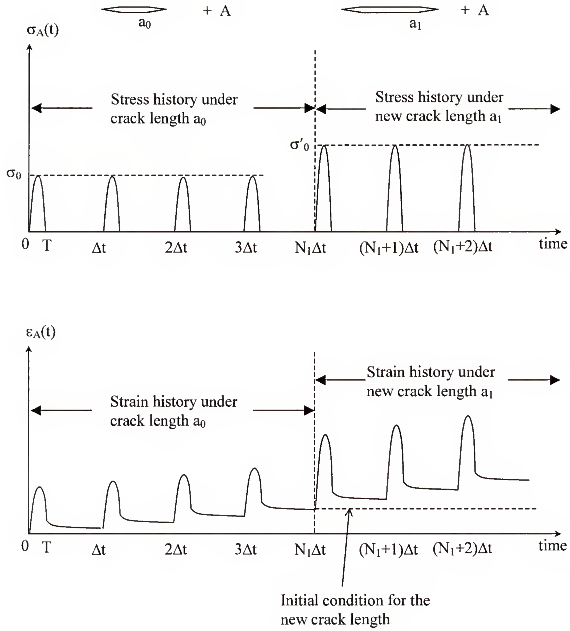

Figure 5-16. History of Stress and Strain During the Crack Propagation.

5.6 Critical Zone Vicinity and Direction of Crack Growth

Previously, the key features of the HMA fracture simulator for defining stepwise crack growth and micro-damage are well established. The method is now able to simulate when and how much a crack will grow, i.e. the rate of crack growth. However, another important aspect, the direction of crack growth, still needs to be addressed.

Fundamentally, the tensile-mode of cracking allows the crack to propagate in the direction perpendicular to the maximum tensile principal stress (Anderson 1995; Broek 1986). Due to its unique geometrical and loading conditions, the indirect tension test always has the maximum tensile stresses acting on a vertical plane through the center of its circular disk, which causes the crack to predominantly develop in this plane (Roque et al. 1999). But in a general problem, the direction of principal tensile stress is unknown and may deviate during the development of crack growth. Moreover, the wandering of load positions between cycles of loads is likely to cause the directional variation of the principal tensile stress between the cycles, which should result in the uncertainty of crack growth direction. Thus, a sound method of determining crack growth direction is required.

A solution to this issue is to define a grid of critical zones that cover a range of possible crack growth directions. Figure 5-17 illustrates an example of a radial grid of seven critical zones (ABCDEFG) located in front of a crack tip in the indirect tension test. Each zone has the same length and is set apart from other zones at the same angle of 9°. The amount of dissipated creep strain energy on each zone is then determined as described in Section 5.4. A plot of the DCSE variation on these directional zones for the indirect tension test is shown in Figure 5-18.

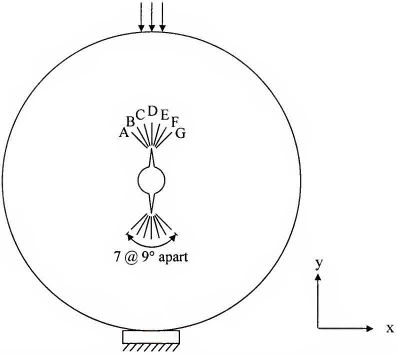

Figure 5-17. Geometry of Grid of Critical Zones. Seven Zones (ABCDEFG) Locate in Front of Crack Tip.

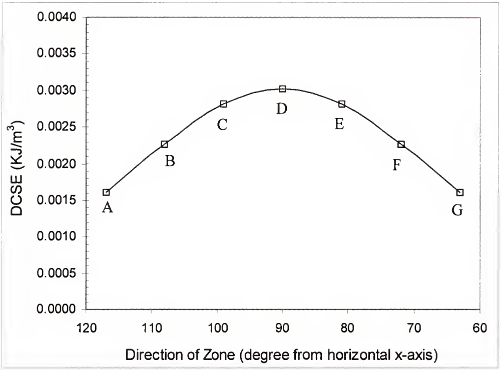

Figure 5-18. DCSE Variation in the Critical Zone Vicinity Caused by One Load Cycle.

Knowing the DCSE variation in the vicinity of these critical zones, we can locate the direction of maximum DCSE within this range. In this case, the maximum DCSE locates at the 90° from the horizontal x-axis, which match the actual crack growth in the vertical direction. Only when this maximum DCSE reaches the damage threshold, a macro-crack develops from the existing crack by the length of the critical zone in the direction of the maximum DCSE.

The number of zones in the radial grid and angular spaces between the zones should be selected such that they can sufficiently capture the maximum value of DCSE. Although, a grid of seven zones covering a 54-degree range (9 degree gap between two consecutive zones) was successfully used in the indirect tension example above, there might be other grid options with fewer number of zones that is also sufficient to locate the direction and amount of maximum DCSE. Furthermore, a grid with fewer zones is more efficient in term of computation time during the crack growth prediction. In the following, we will investigate the possibility of a three-zone grid.

5.6.1 Three-Zone Grid: Case 1

A grid of three zones (XYZ) with 18-degree gap angle between two consecutive zones is investigated. The middle zone (Y) is located at 90 degrees from the horizontal x-axis. The locations of three zones (XYZ) are shown in Figure 5-19. Figure 5-20 illustrates the DCSE variation of zones XYZ comparing to the actual DCSE variation from the grid ABCDEFG presented earlier.

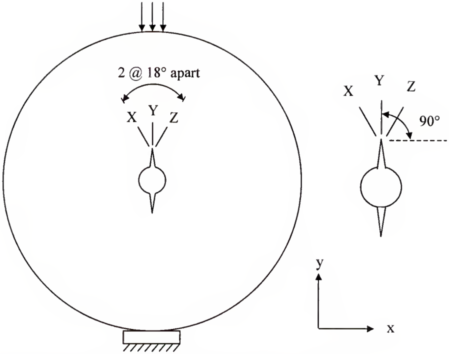

Figure 5-19. Location of a Grid of Three Critical Zones: Case 1.

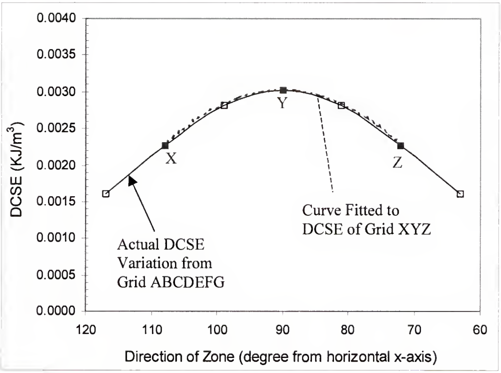

Figure 5-20. DCSE Variation for Three-Zone Grid: Case 1.

In Figure 5-20, a 2nd degree polynomial is fitted to the DCSE variation of XYZ. It appears that the fitted polynomial matches the actual DCSE variation from the grid ABCDEFG very well. It gives exactly the same value and direction of maximum DCSE as illustrated in the actual variation from the grid ABCDEFG.

5.6.2 Three-Zone Grid: Case 2

In this case, a grid of three zones (X′Y′Z′) with the same 18-degree gap angle between two consecutive zones as in the case 1 is used. But the middle zone, Y′, is now located at 99 degrees from the horizontal x-axis. The zones X′ and Z′ are located at 108 and 72 degrees respectively from the horizontal x-axis. The locations of three zones (X′Y′Z′) are shown in Figure 5-21. The center of the grid X′Y′Z′ appears to deviate from the crack growth direction (vertical line) by 9 degrees. Thus, this case will serve as a test for the three-zone grid whether it is capable of capturing a crack growth in the direction away from its center zone. Figure 5-22 illustrates the DCSE variation of zones X′Y′Z′ comparing to the actual DCSE variation from the grid ABCDEFG presented earlier.

In Figure 5-22, a 2nd degree polynomial is fitted to the DCSE variation of X′Y′Z′. The fitted curve does not perfectly match the actual DCSE variation from the grid ABCDEFG. However, the fitted polynomial yields the correct angle of maximum DCSE at 90 degrees from the horizontal x-axis. The value of maximum DCSE from the X′Y′Z′ fitted curve is slightly lower than the maximum DCSE as illustrated in the actual variation from the grid ABCDEFG.

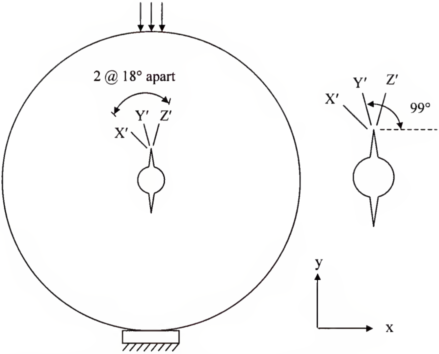

Figure 5-21. Location of a Grid of Three Critical Zones: Case 2.

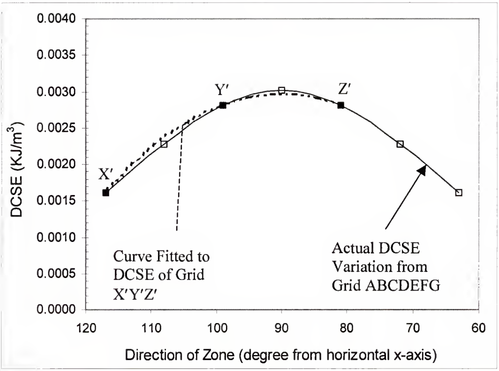

Figure 5-22. DCSE Variation for Three-Zone Grid: Case 2.

In conclusion, the grid of three zones with 18-degree gap angle between two consecutive zones can be considered sufficient to capture the maximum DCSE and its direction. To obtain the most accurate result of direction and value of maximum DCSE, the center of the three-zone grid should be located in the direction of current crack line, which is considered to be the most possible direction of crack propagation.

The fitted 2nd degree polynomial to the three values of DCSE variation will become useful in determination of the direction and value of maximum DCSE. The direction of maximum DCSE can be obtained by solving for the zero of the derivative of the 2nd degree polynomial. The value of maximum DCSE is the value of the polynomial corresponding to the peak angle.

However, the three-zone grid may not be applicable in some situations, in which a crack growth is found highly deviated from one step to another step. In this type of problem, a grid of more number of zones to cover wider range of possible directions should be considered.

5.7 Verification of HMA Fracture Simulator

In the following, examples are presented of the use of the HMA crack growth simulator for simulating the crack growth in the Superpave Indirect Tension Test (IDT) under cyclic loading conditions. The objective of these examples was to predict a relationship between the crack length in the specimen and the number of load repetitions (a-N relationship). The a-N relationship obtained with the proposed method will be compared to those obtained from measured laboratory results.

In the Superpave IDT, a hot-mix asphalt disk specimen 150mm (6in) in diameter and approximately 25mm (1in) thick with an 8 mm (0.315 in) hole at the center was subjected to cyclic haversine loads, with 0.1 second loading and 0.9 second rest periods per loading cycle. A coarse-graded Superpave asphalt mix and a fine-graded Superpave asphalt mixes were previously produced and tested by Honeycutt (2000) and Zhang (2000). The aggregate used in all four mixes was oolitic limestone from South Florida. This is an aggregate commonly used in Florida mixes. All mixes were 12.5-mm (0.49in) nominal maximum aggregate size. The gradations of both mixes are shown in Table 5-1. The asphalt used was an AC-30 asphalt, which corresponded to a PG 67-22. The design asphalt contents for the mixtures, as shown in Table 5-2, were determined at Ndesign = 109 revolutions to achieve 4% air void according to Superpave specifications. The design mixes were then reproduced at air void levels of approximately 7 percent to conduct the cracking performance tests, in which the specimens were subjected to repeated loading and the crack growth was observed. Similarly, the following tests were performed on specimens without center holes: strength test, creep test, and the resilient modulus test. The first three tests provided the material-related inputs for the modeling, while the fracture test provided the observed a-N relationship for comparison purposes. The fracture-related properties of both mixes are also given in Table 5-2. The complete details of the mixes can be found in Honeycutt (2000) and Zhang (2000).

In the IDT crack growth experiment, the crack length was interpreted from measured deformations between gauge points located across the center of the specimen at 3.81 mm (1.5 inches) apart from each other. The experimental crack length was then calculated from these deformations by using a predetermined relationship between the gauge deformations and the theoretical crack length. The relationship was obtained from the modeling of the IDT specimen at various crack lengths. The details on the development of this relationship can be found in Roque, Zhang and Zankar (1999).

Table 5-1. Superpave Coarse-Graded and Fine-Graded Gradations

Sieve Size mm (inch)	Coarse-graded % Passing	Fine-graded % Passing
19 (3/4)	100	100
12.5 (½)	97.4	95.5
9.5 (3/8)	90.0	85.1
4.75 (#4)	60.2	69.3
2.36 (#8)	33.1	52.7
1.18 (#16)	20.3	34.0
0.6 (#30)	14.7	22.9
0.3 (#50)	10.8	15.3
0.15 (#100)	7.6	9.6
0.075 (#200)	4.8	4.8

Table 5-2. Input Properties of the Superpave Coarse-Graded and Fine-Graded Mixes

Property	Unit	Coarse-graded	Fine-graded
Asphalt Content	%	6.5	6.3
Voids in Mineral Aggregate	%	15.4	15.6
Dissipated Creep Strain Energy @10°C	KJ/m^3	3.63	2.81
Tensile Strength @10°C	MPa	2.55	2.70
Creep Compliance: D_1 @10°C	1/GPa	0.0552	0.0831
Creep Compliance: m @10°C	-	0.796	0.656

The results of the crack length versus number of load repetitions (a-N) relationship for the Superpave mixes are presented in Figures 5-24 and 5-25. In Figure 5-24, the laboratory data points are the average of results obtained from experiments performed on two samples of a coarse-graded mixture at the similar level of tensile stress (0.95 MPa or

138 psi) at 10°C temperature. In Figure 5-25, the laboratory results were obtained from an experiment performed on one sample of fine-graded mix under tensile stress of 1.01 MPa (146 psi) at 10°C temperature.

For crack growth predictions, the IDT samples were modeled as a two-dimensional linear elastic isotropic material under plane stress loading conditions. Each specimen was modeled with 124 DD elements and a few more DD elements were added successively to model the 25-mm crack growth as shown in Figure 5-23. The length of the critical zone used for each crack extension step was one half of the maximum aggregate size, 6-mm zone length. The resulting HMA crack growth simulation modeled cracks initiating from both the top and the bottom of the center hole in the specimen based on the solution. Likewise, the cracks continued to propagate in a stepwise manner in the vertical direction due to the tensile stress concentration located ahead of the crack tips along the centerline of the IDT disk specimens.

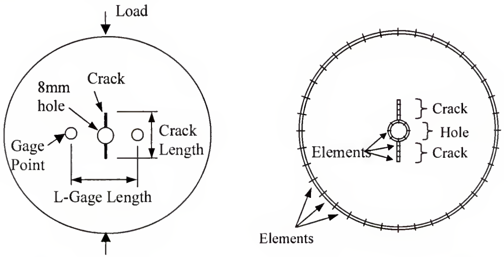

Superpave IDT Schematic

Representative Model in DDM

Figure 5-23. Superpave IDT with Vertical Crack and its Representative DD Model.

The resulting a-N relationships from the predicted model for the coarse-graded and fine-graded mixtures are presented in Figure 5-24 and 5-25, respectively, along with those obtained from the experimental results from the fracture tests.

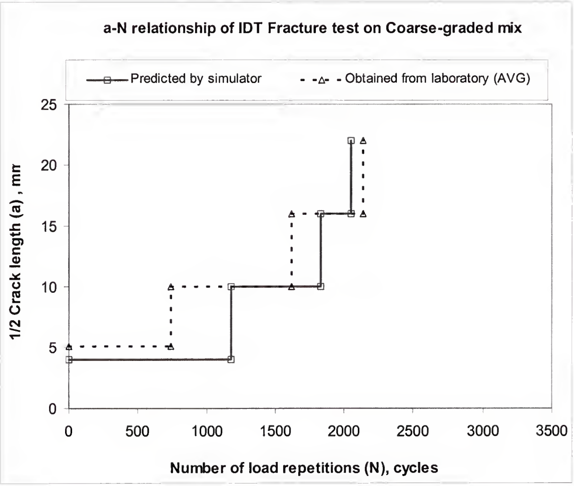

Figure 5-24. Crack Growth Characteristics of the Superpave Coarse-Graded Mix Obtained from Laboratory Results and from the HMA Fracture Simulator.

Although the predictions shown in Figures 5-24 and 5-25 did not match up exactly with the testing results, the HMA crack growth simulator captured a similar crack growth pattern that appeared in the Superpave coarse-graded and fine-graded mixes. Variation between two experiments on the same mixture is expected due to natural testing variability in the Superpave IDT test and other volumetric factors, such as slight differences in air voids, etc.

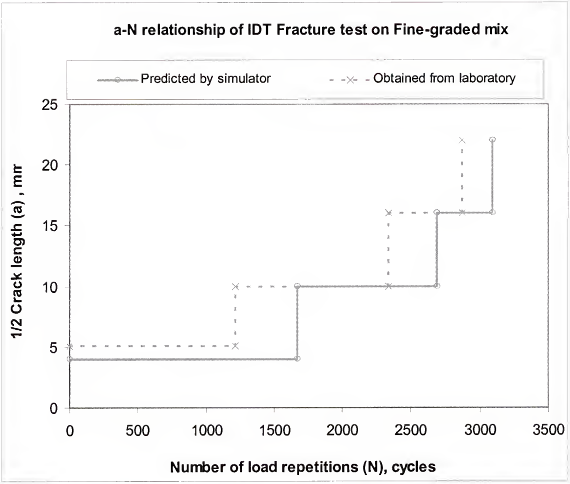

Figure 5-25. Crack Growth Characteristics of the Superpave Fine-Graded Mix Obtained from Laboratory Results and from the HMA Fracture Simulator.

CHAPTER 6
ANALYSIS AND FINDINGS

This Chapter presents the application of the newly developed displacement discontinuity element-based HMA fracture mechanics crack growth simulator to some typical asphalt pavement configurations. These applications include the verification of the simulator with some field pavement sections; and evaluation of some key parameters that affect how cracks develop in asphalt layer.

6.1 Verification with Field Pavement Sections

In this section, the HMA fracture simulator is used to evaluate the cracking performance of four asphalt pavement sections. These sections varied diversely in their cracking performance. The past survey of these sections allows us to compare their performance in a relative manner. Based on their field and laboratory data, the HMA fracture simulator will be applied to simulate the cracking development in these sections.

6.1.1 Pavement Sections

The studies of the pavement sections used were conducted earlier by Sedwick (1998) and Jajliardo (2003). Their evaluation included performance surveying, laboratory testing of samples obtained from coring, and in situ non-destructive testing. The sections were chosen in Florida to be evaluated as part of an ongoing longitudinal wheel path cracking study.

The sections from the study performed by Sedwick (1998) include: two locations of I10 in Madison county, and two locations of US301 in Bradford county as shown in Table 6-1. The sections from Jajliardo's (2003) study are from two locations of I75 in

Charlotte county as shown in Table 6-1. The average crack depth of each section was measured from coring or trench cuts through locations where longitudinal surface cracks were visible. Truck traffic was heavy for all sections with annual equivalent single axle loads (ESALs) and average annual daily traffic (AADT) shown in Table 6-2. The ages, depths of cracking, and performance ranking are also presented in Table 6-2.

Table 6-1. Location of Sections.

Abbreviation	Route	County	Travel Direction	Milepost
I10MW1	I-10	Madison	Westbound (West)	23.685-29.045
I10MW2	I-10	Madison	Westbound (East)	29.045-32.690
US301BN	US 301	Bradford	Northbound	0.000-8.120
US301BS	US 301	Bradford	Southbound	0.000-8.120
I75-1U	I-75	Charlotte	N/A	0.0-11.8
I75-1C	I-75	Charlotte	N/A	11.8-22.0

Table 6-2. General Description of Field Sections.

Section	AADT	Annual ESALs (x 1000)	Age as of 1997 (years)	Crack Depth mm.(in.)	Performance
I10MW1	17780	546	10	5.08 (0.2)	Good
I10MW2	17780	546	10	66.04 (2.6)	Poor

Section	AADT	Annual ESALs (x 1000)	Age as of 1997 (years)	Crack Depth mm.(in.)	Performance
US301BN	20200	558	13	71.12 (2.8)	Poor
US301BS	20200	558	13	86.36 (3.4)	Worst

Section	AADT	Annual ESALs (x 1000)	Age as of 2003 (years)	Crack Depth mm.(in.)	Performance
I75-1U	34500	6702	14	Uncracked	Good
I75-1C	42000	7443	15	56.13 (2.21)	Poor

The structural information of the sections is obtained from field measurement and laboratory tested of cored samples. The asphalt layer thicknesses of the sections were measured from field cores. Base layer thicknesses for the sections were measured in the field after cores were removed. The layer moduli were obtained from analysis of falling weight deflectometer results performed on the uncracked areas of the sections. Table 6-3 summarizes the results of layer thickness and modulus. Note that the moduli of the asphalt layers in Table 6-3 were obtained from resilient modulus tests at 10°C performed on samples obtained from field cores.

Table 6-3. Layer Thickness and Modulus of Field Sections.

Section	Layer Property	Asphalt (at 10°C)	Base	Subbase	Subgrade
I10MW1	Thickness	127 (5)	254 (10)	305 (12)	–
	Modulus	8931 (1295)	586 (85)	414 (60)	241 (35)
I10MW2	Thickness	127 (5)	254 (10)	305 (12)	–
	Modulus	6690 (970)	586 (85)	414 (60)	241 (35)
US301BN	Thickness	203.2 (8)	203.2 (8)	305 (12)	–
	Modulus	8483 (1230)	517 (75)	379 (55)	262 (38)
US301BS	Thickness	127 (5)	203 (8)	305 (12)	–
	Modulus	4738 (687)	448 (65)	276 (40)	207 (30)
I75-1U	Thickness	159 (6.25)	305 (12)	305 (12)	–
	Modulus	10910 (1582)	441 (64)	352 (51)	248 (36)
I75-1C	Thickness	165.1 (6.5)	305 (12)	305 (12)	–
	Modulus	11138 (1615)	379 (55)	345 (50)	207 (30)

Remark: Thickness is displayed in mm. (in.)
Modulus is displayed in MPa (ksi)

The general environmental of the I10 and US301 sections was considered similar given their proximity to one another. North-central Florida has a humid climate with average yearly air temperatures possibly between 20 and 25 °C. The I75 sections are located in south Florida and their average yearly air temperature would be higher. The temperature condition that is the most critical for cracking damage in asphalt layer should be in winter when asphalt material becomes stiffer and more fragile at low temperatures. Even though, the cracking damage in reality is a result of cumulative damage that occurs at various environmental conditions throughout the history of pavement, it is too complicated for the fracture simulator to account for all of those conditions at this stage. Moreover, the purpose of the crack predictions at this point is to compare the relative performance of these sections. Thus, rather than performing analysis at various pavement conditions, a pre-selected condition that is considered critical for cracking damage will be applied to the crack growth prediction for all sections. For this reason, we will conduct the cracking predictions of all sections with properties of the asphalt layer at 10 °C and properties of other layers as shown in Table 6-3. Table 6-4 shows the properties of asphalt layers at 10°C that obtained from laboratory tests performed on samples from the field cores as provided by Sedwick (1998) and Jajliardo (2003).

Table 6-4. Properties of Asphalt Concrete Layers at 10°C.

Section	Resilient Modulus, M_R MPa (ksi)	Tensile Strength, S_t MPa (psi)	Fracture Energy Limit FE KJ/m^3 (lb·in/in^3)	Dissipated Creep Strain Energy Limit DCSE KJ/m^3 (lb·in/in^3)
I10MW1	8931 (1295)	1.82 (264)	2.45 (0.355)	2.262 (0.328)
I10MW2	6690 (970)	1.78 (171)	1.052 (0.1526)	0.9483 (0.1375)
US301BN	8483 (1230)	1.13 (164)	0.3475 (0.05039)	0.2722 (0.03947)
US301BS	4738 (687)	.931 (135)	0.119 (0.01726)	0.02777 (0.004026)
I75-1U	10910 (1582)	2.01 (292)	2 (0.290)	1.813 (0.263)
I75-1C	11138 (1615)	1.65 (239)	1.103 (0.160)	0.9793 (0.142)

Table 6-4. Continued.

Section	Maximum Aggregate Size mm.(in.)	Poison Ratio	Creep Compliance $D(t) = D_0 + D_1 t^m$		
			D_0 MPa^{-1} (psi^{-1})	D_1 MPa^{-1} (psi^{-1})	m
I10MW1	12.7 (0.5)	0.37	147×10^{-6} (1.015×10^{-6})	1005×10^{-7} (6.932×10^{-7})	0.579
I10MW2	12.7 (0.5)	0.38	308×10^{-7} (2.127×10^{-7})	1354×10^{-7} (9.339×10^{-7})	0.576
US301BN	12.7 (0.5)	0.40	1165×10^{-7} (8.033×10^{-7})	1036×10^{-7} (7.144×10^{-7})	0.357
US301BS	12.7 (0.5)	0.33	179×10^{-6} (1.236×10^{-6})	658×10^{-7} (4.541×10^{-7})	0.474
I75-1U	12.7 (0.5)	0.38	685×10^{-7} (4.724×10^{-7})	1287×10^{-7} (8.876×10^{-7})	0.436
I75-1C	12.7 (0.5)	0.46	948×10^{-7} (6.549×10^{-7})	1095×10^{-7} (7.549×10^{-7})	0.471

6.1.2 Pavement Modeling

The pavement structure is modeled as a four-layer inhomogeneous body in the viscoelastic displacement discontinuity method. Since these four sections have only a slightly different in layer thickness, the same boundary discretization will be used for all sections. The extent of the model covers 9906 mm. (390 in.) width and 5080 mm (200 in.) depth for the subgrade layer. The four-layer pavement model is composed of 104 quadratic elements that cover all boundaries including interfaces between layers. The total number of elements is distributed to 41 elements for the asphalt concrete layer, 30 elements for the base layer, 22 elements for the subbase layer, and 10 elements for the subgrade layer. A number of smaller-sized elements are placed in the top layer especially around the tire location to capture the critical areas where there is bending action. The larger-sized elements are placed in the lower layers and in the area far away from the tire.

Figure 6-1 illustrates the DDM model that is used for all pavement sections. The thicknesses of the asphalt layer (H_1), the base layer (H_2) and the subbase layer (H_3) are variable and given in Table 6-3, but the subgrade layer thickness is fixed at 5080 mm (200 inches.) In Figure 6-1, the pavement model is created without any elements being used for representing side boundaries. This is because the width of the model extends so far that the influence of side-boundary elements (if present) are minimal at the area of interest. Thus, it is unnecessary to include side boundaries into the model. An example in Chapter 3 confirmed this modeling approach.

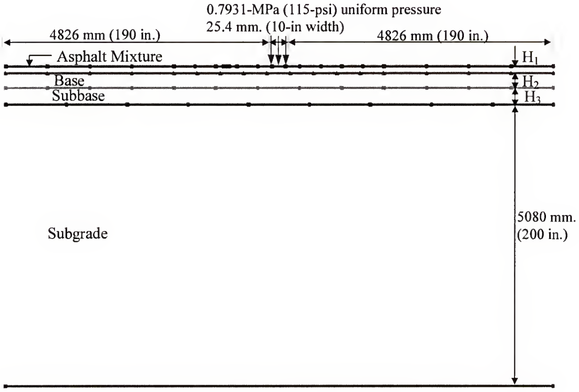

Figure 6-1. Displacement Discontinuity Method Model for All Pavement Sections.

The base, subbase, and subgrade layers are treated as linear-elastic materials whose Young moduli are given in Table 6-3. For their Poison ratio, a typical set of values is used throughout all sections, namely 0.35 for base layer, 0.4 for subbase layer, and 0.45 for subgrade layer. The asphalt layer is considered as a viscoelastic material. Its creep compliance function is described by the Power law equation, $D(t)=D_0+D_1t^m$, as described earlier in Chapters 4 and 5. Its Poisson's ratio function is taken as constant with time according to the Superpave indirect creep test specification (Roque et al. 1997). To obtain the transformed compliance, we utilize Equation 4-77:

$$\bar{J}(s) = L\{\ D(t)\ \} = \frac{D_0}{s} + \frac{D_1\Gamma(m+1)}{s^{m+1}}$$

$$s\,\bar{J}(s) = \frac{D_0 s^m + D_1\Gamma(m+1)}{s^m}$$

where $\Gamma(z)$ is the Euler Gamma function: $\Gamma(z) = \int_0^\infty t^{z-1}\, e^{-t}\, dt$

The transformed modulus is then obtained by:

$$s\,\bar{E}(s) = 1/\,s\,\bar{J}(s) = \frac{s^m}{D_0 s^m + D_1\Gamma(m+1)} \tag{6-1}$$

To obtain the shear modulus, we utilize Equation 4-78:

$$s\,\bar{G}(s) = \frac{s\bar{E}(s)}{2(1+\bar{v}(s))}$$

where $\bar{v}(s)$ in the above equation is the constant Poison ratio (v), i.e. $\bar{v}(s) = v$.

The transformed shear modulus and Poison ratio become

$$s\,\bar{G}(s) = \frac{1}{2(1+v)}\,\frac{s^m}{D_0 s^m + D_1\Gamma(m+1)} \tag{6-2}$$

$$\bar{v}(s) = v \tag{6-3}$$

The constants for compliance and Poison ratio for asphalt layer of each pavement section are given in Table 6-4.

For the boundary conditions of the pavement model, the elements at the bottom boundary are prescribed with zero displacements for both shear and normal components to represent a rigid foundation. The bottom boundary conditions in terms of time and transformed variables are written as:

$$u_s(t), u_n(t) = 0 \; ; \; t \geq 0 \tag{6-4}$$

$$\bar{u}_s(s) = L\{u_s(t)\} = \frac{0}{s} = 0 \tag{6-5}$$

$$\bar{u}_n(s) = L\{u_n(t)\} = \frac{0}{s} = 0 \tag{6-6}$$

For elements located at the top boundary of pavement, they are prescribed with zero shear and zero normal tractions to represent a free surface condition, except for the element at the location of tire contact where the tire load is applied. The top boundary condition in time and transformed variables are written as:

$$\sigma_s(t), \sigma_n(t) = 0 \; ; \; t \geq 0 \tag{6-7}$$

$$\bar{\sigma}_s(s) = L\{\sigma_s(t)\} = \frac{0}{s} = 0 \tag{6-8}$$

$$\bar{\sigma}_n(s) = L\{\sigma_n(t)\} = \frac{0}{s} = 0 \tag{6-9}$$

The 9000-lb dual tire is modeled as a 254-mm (10-in) strip of 0.7931-MPa (115-psi) uniformly distributed vertical pressure applied to the element at the center of surface boundary. The load is applied to the pavement in the form of a haversine function to represent the time-dependent manner of a truck passing. The time variation of the haversine load follows the same pattern as specified in the Superpave indirect tension test (Roque et al. 1997), in which the duration of on-off load is 0.1 second for one passing and followed by a 0.9 second resting period. The time-dependent functions of a passing tire are written as follows:

$$\sigma_s(t) = 0 \;\; ; \;\; t \geq 0 \tag{6-10}$$

$$\sigma_n(t) = (0.79\ \text{MPa})\cdot\{\ \sin[\omega t]\cdot H(t-0) + \sin[\omega(t-T)]\cdot H(t-T)\ \} \tag{6-11}$$

where $T = 0.1$ second and $\omega = \pi/T = 10\pi$

The transform functions of the tire load become

$$\bar{\sigma}_s(s) = L\{\sigma_s(t)\} = \frac{0}{s} = 0 \tag{6-12}$$

$$\bar{\sigma}_n(s) = L\{\sigma_n(t)\} = 0.79\cdot\left(\frac{\omega}{s^2+\omega^2}\right)\cdot[1+\exp(-T\cdot s)]\quad \text{MPa} \tag{6-13}$$

To represent the traffic cycles, the same tire load is then repeated at every second and at the same position on the pavement. Figure 6-2 illustrates the time function of the load repetition. This loading pattern may not completely resemble a real traffic condition in which a number of various loading magnitudes and speeds are expected. But since all sections were subjected to similar amount of annual traffic (Table 6-2), applying equivalent load repetitions should still result in the same prediction of relative performances as in the use of real traffic condition.

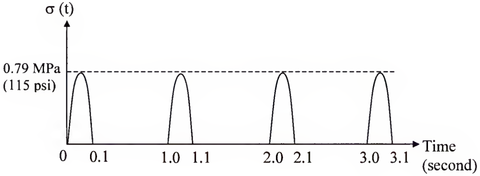

Figure 6-2. Time-Dependent Characteristic of Traffic Loads.

6.1.3 Crack Growth Prediction

The field observations indicated that cracking that occurred in these pavement sections were top-down longitudinal wheel path cracking (Sedwick 1998; Jajliardo 2003). Myers (2000) and Myers et al. (2001) investigated the major causes of top-down longitudinal cracking in asphalt pavements and found that the development of top-down cracking was mainly caused by the tensile stress at the surface of the asphalt layer. This tensile stress was induced by the bending action of the asphalt layer. When the tensile stress is applied to a small discontinuity (e.g. small crack or groove) at the pavement surface, which may be present by a variety of reasons, it results in a substantial stress concentration that may lead to crack growth in a downward direction from the discontinuity. It was found that this evidence became the most critical when the discontinuity was located about 635 to 1016 mm. (25 to 40 inches) away from the center of the tire, where the exact critical location is slightly variable due to the bending response of pavement structure.

Since all pavement sections in this study were actually subjected to longitudinal top-down cracking, only surface initiated top-down cracking will be considered in the crack growth prediction. Furthermore, the prediction will start the crack development from a pre-existing small crack (discontinuity) at the surface of pavement. The location on the pavement surface for a crack to start from will be determined from the location of maximum surface tensile stress.

Figure 6-4 illustrates the horizontal stresses at surface of all uncracked pavement sections. The horizontal stress at the bottom of asphalt layer and the vertical displacement at the pavement surface are also presented in Figure 6-5 and 6-6 for reference. Based on

Figure 6-4, the location of maximum surface tensile stress of each pavement section is obtained and listed in Table 6-5.

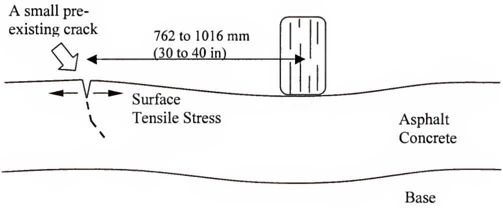

Figure 6-3. The Critical Condition of Top-Down Longitudinal Surface Cracking.

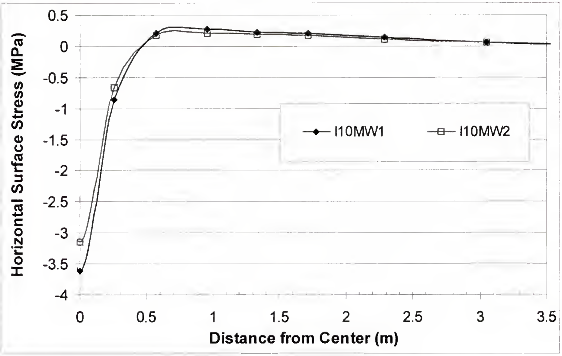

Figure 6-4. Horizontal Stresses at the Surface of Pavements.

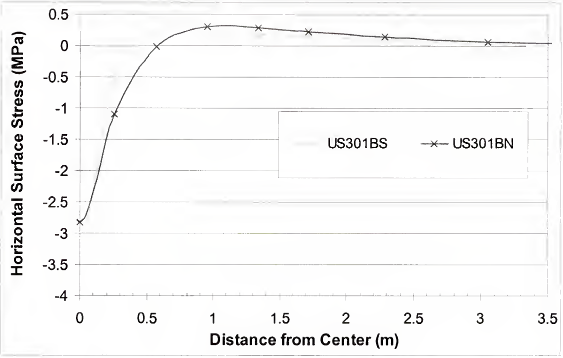

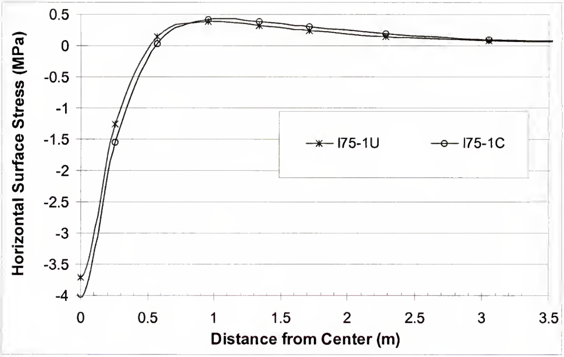

Figure 6-4. Continued

Table 6-5. Location of Maximum Tensile Stress at Surface of Pavement.

Section	Location of Max. Tensile Stress from Center of Tire, mm. (in.)
I10MW1	952.5 (37.5)
I10MW2	952.5 (37.5)
US301BN	1016 (40.0)
US301BS	762 (30.0)
I75-1U	952.5 (37.5)
I75-1C	952.5 (37.5)

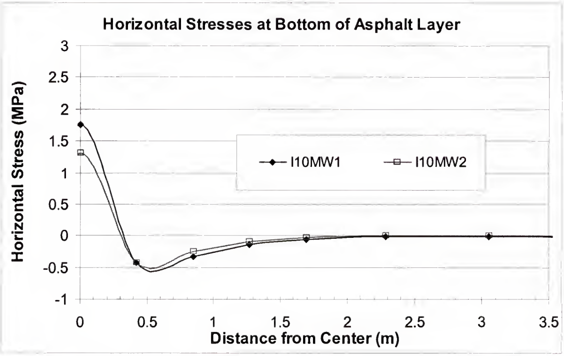

Figure 6-5. Horizontal Stresses at the Bottom of Asphalt Layers.

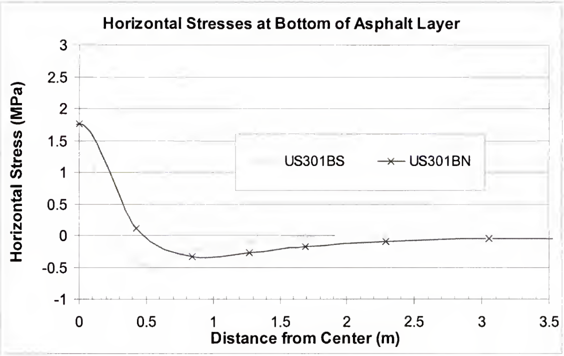

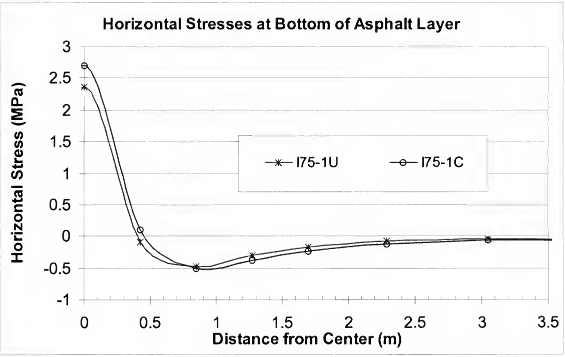

Figure 6-5. Continued.

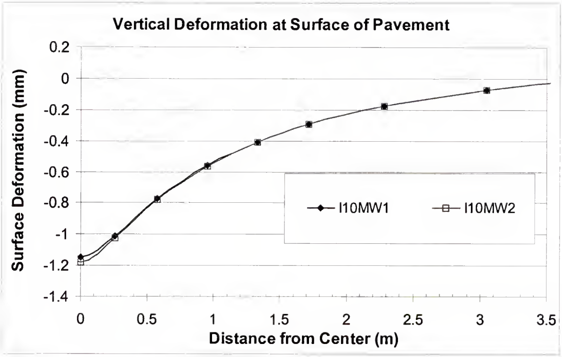

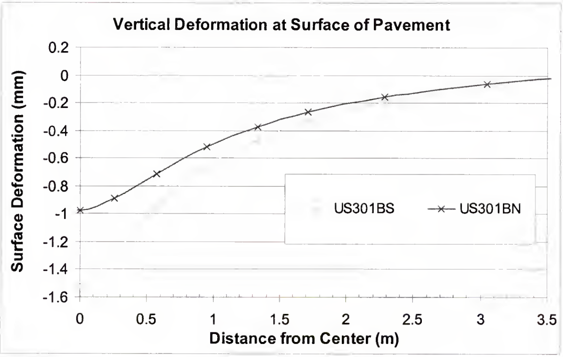

Figure 6-6. Vertical Deformations at the Surface of Pavements.

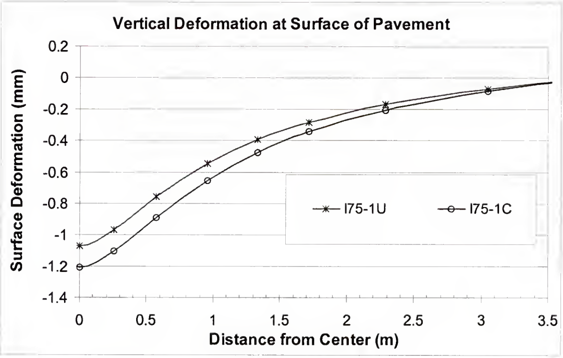

Figure 6-6. Continued.

6.1.4 Crack Growth Simulation

6.1.4.1 First crack growth step

To begin the process of crack growth prediction, a DD element representing a small crack of 6.35-mm (0.25-inch) length is placed at the location of maximum tensile stress of each pavement section. The crack growth simulation is then started from this initial condition.

As described in Chapter 5, the fracture simulator first locates a grid of three critical zones at the tip of the small crack. The length of a critical zone is defined by one-half of maximum aggregate size of the asphalt mixture, which is 6.35-mm (0.25-in) length. The HMA fracture simulator then calculates the dissipated creep strain energy (DCSE) occurring in these zones, which is induced by a cycle of tire load. Once the DCSE per cycle on these zones are known, accumulation of total DCSE on these zones during the load repetition can be calculated. If the maximum DCSE in the grid of the critical zone reaches or exceeds the DCSE threshold, a macro-crack will develop from the tip of the small existing crack in the direction of the maximum DCSE. The crack is set to propagate by the length of a critical zone (6.35 mm or 0.25 in). Thus, the new crack length now equals 12.7 mm (0.5 in.) An example of calculation of the first step of crack growth prediction for the pavement section I10MW1 is presented in the following.

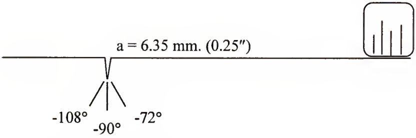

DCSE in the grid zones for crack length = 6.35 mm. (0.25 in.)

Grid Angle	DCSE per 1 cycle (KJ/m^3)	Cumulative DCSE at 72,999 cycles (KJ/m^3)
-108.0	2.6434×10^{-5}	$2.6434 \times 10^{-5} \times 72999 = 1.930$
-90.0	3.0988×10^{-5}	$3.0988 \times 10^{-5} \times 72999 = 2.262$
-72.0	2.6594×10^{-5}	$2.6594 \times 10^{-5} \times 72999 = 1.941$

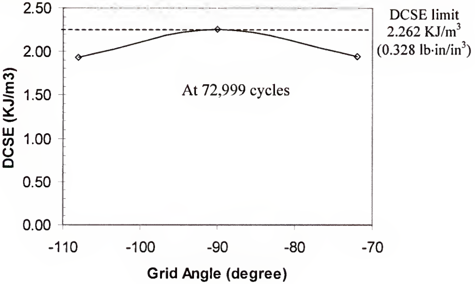

In this example, the rate of DCSE increment on the grid zones is found to range from 2.6434 x10^{-5} to 3.0988 x10^{-5} KJ/m^3 per loading cycle. As a result, the peak value of cumulative DCSE reaches the threshold at 2.262 KJ/m^3 at 72,999 cycles. The corresponding peak angle (i.e. the direction from the horizontal of the maximum DCSE) is found to be at –89.8 degree. Thus, the crack propagates from the existing crack tip of 6.35-mm (0.25-in) depth to 12.7-mm (0.5-in) depth approximately in the vertical direction (-89.8 degree from horizontal direction) at this moment of time.

6.1.4.2 Second crack growth step

For crack growth prediction in the next crack growth step, a new grid of critical zones is located in front of the new crack tip. The amount of DCSE accumulated at the locations that are being monitored in the new grid, which is caused by the history of load cycles applied during the previous crack geometry (6.35-mm or 0.25-in depth), must be obtained before determining the new set of DCSE due to the new load applications at the new crack geometry (12.7-mm or 0.5-in depth). An example calculation of the second step of crack growth prediction is presented in the following.

During the period of 6.35-mm (0.25-in) crack depth, the loading cycles from 0 to 72,999 caused cumulative damages to the three-zone grid at 0.2603, 0.3244, and 0.2622 KJ/m^3. After the 72,999th cycle, the rate of DCSE increment under the new crack geometry of 12.7-mm (0.5-in) depth increases substantially because the grid zones are now located very close to the crack tip. It was found that the peak value of cumulative DCSE reaches the threshold at 2.262 KJ/m^3 at the 113,590th cycle. The corresponding peak angle is at 89.7 degree. Therefore, the crack propagates by the length of critical zone (6.35 mm or 0.25 in) at approximately vertical direction (89.7 degree from horizontal direction).

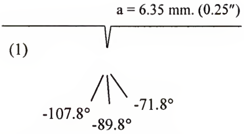

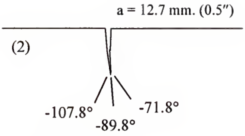

(1) DCSE in the grid zones for crack length = 6.35 mm. (0.25 in.)

Grid Angle	DCSE per 1 cycle (KJ/m^3)	Cumulative DCSE at 72,999 cycles (KJ/m^3)
-107.8	3.5663×10^{-6}	$3.5663 \times 10^{-6} \times 72999 = 0.2603$
-89.8	4.4437×10^{-6}	$4.4437 \times 10^{-6} \times 72999 = 0.3244$
-71.8	3.5913×10^{-6}	$3.5913 \times 10^{-6} \times 72999 = 0.2622$

(2) DCSE in the grid zones for crack length = 12.7 mm. (0.50 in.)

Grid Angle	DCSE per 1 cycle (KJ/m^3)	Cumulative DCSE at 113,590 cycles (KJ/m^3)
-107.8	4.1375×10^{-5}	$0.2603 + 4.1375 \times 10^{-5} \cdot (113590-72999) = 1.940$
-89.8	4.7737×10^{-5}	$0.3244 + 4.7737 \times 10^{-5} \cdot (113590-72999) = 2.262$
-71.8	4.1513×10^{-5}	$0.2622 + 4.1513 \times 10^{-5} \cdot (113590-72999) = 1.947$

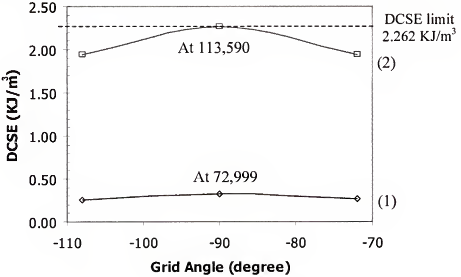

6.1.4.3 Subsequent crack growth steps

After the second step, the fracture simulator continues in the same manner to simulate the crack growth in subsequent crack growth steps by repeating the process previously described. Figure 6-8 illustrates the geometry of crack growth prediction and its corresponding number of load cycles when the crack geometry changes at each step for pavement section I10MW1. The stepwise crack growth geometry for all other sections is very similar to Figure 6-8, which appears to propagate in approximately vertical direction. Thus, their repetitions will not be presented here. The rate of crack growth is shown in Figure 6-9 and 6-10 for crack length vs. number of load repetition plot.

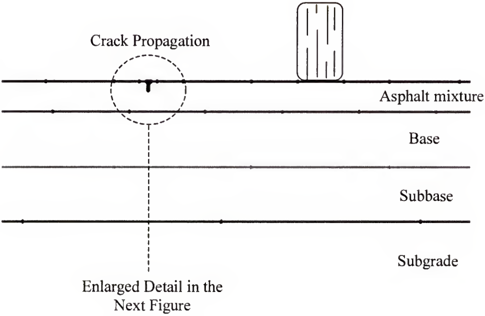

Figure 6-7. Top-Down Cracking Development in Asphalt Pavements.

Step 0: 6.35-mm (0.25-in) crack depth N= 0

Step 1: 12.7-mm (0.50-in) crack depth N=72,999 cycles

Step 2: 19.05-mm (0.75-in) crack depth, N=113,590 cycles

Step 3: 25.4-mm (1.0-in) crack depth N=146,059 cycles

Figure 6-8. Geometry of Crack Growth Prediction for Pavement Section I10MW1.

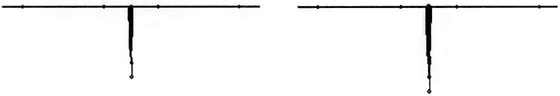

Step 4: 31.75-mm (1.25-in) crack depth, N= 176,736 cycles

Step 5: 38.1-mm (1.5-in) crack depth, N= 208,447 cycles

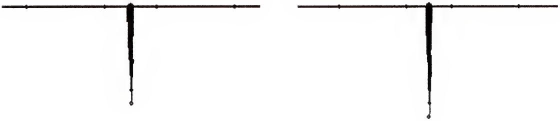

Step 6: 44.45-mm (1.75-in) crack depth, N= 243,219 cycles

Step 7: 50.8-mm (2.0-in) crack depth, N= 283,030 cycles

Figure 6-8. Continued.

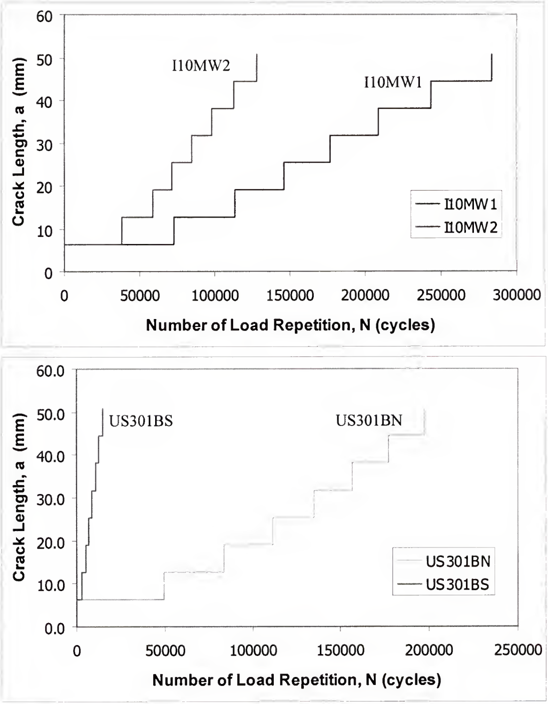

Figure 6-9. Prediction of Crack Growth Rate for Pavement Sections I10MW1, I10MW2, US301BN, and US301BS.

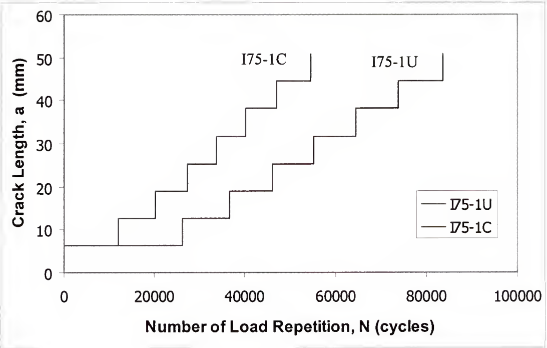

Figure 6-10. Prediction of Crack Growth Rate for Pavement Sections I75-1U and I75-1C.

6.1.5 Interpretation of Results

6.1.5.1 I10 sections

First, let us consider the pair of pavement sections I10MW1 and I10MW2. Table 6-3 indicates that these two sections are identical in structural thickness of all layers, and their moduli of base, subbase, and subgrade are also equal. The only difference between them is the properties of asphalt materials. The asphalt mixture in section I10MW1 has a higher dissipated creep strain energy threshold and a lower creep rate than the mixture in section I10MW2 (Table 6-4). This results in better resistance to cracking. The crack growth rate in Figure 6-9 indicates that at the number of load cycles when section I10MW2 has a 50.8-mm (2-in) crack length, section I10MW1 has only 19.05-mm (0.75-in) crack length. The prediction resembles the observation in the field (Table 6-2) where section I10MW1 had 5.08-mm (0.2-in) crack depth and section I10MW2 had 55.04-mm (2.6-in) crack depth.

6.1.5.2 I75 sections

For the pair of I75 sections, Jajliardo (2003) indicated that the I75-1U section was an uncracked section, while the I75-1C was a moderately cracked section. Since the HMA crack growth simulator always assumes that a crack develops in the pavement, every pavement under its prediction will undergo crack propagation. However, a well-performing pavement section should have a slower rate of crack growth prediction than a poor section. The rate of crack growth prediction for the I75 sections in Figure 6-10 indicates that the I75-1U section has a slower crack growth rate than the I75-1C section, thus it is determined to be a better performing section, which agrees with the field performance comparison.

6.1.5.3 US301 sections

The crack growth prediction for section US301BS indicates that it has an extremely fast crack growth rate, i.e. the worst cracking resistance. Again, the crack growth prediction agrees with the actual performance of the US301BS section. The US301BS was found to be a heavily cracked section with a large area of surface cracking and its crack depth was greater than three inches. The extremely poor performance of US301BS is due to its exceptionally low dissipated creep strain energy threshold. For pavement section US301BN, its crack growth rate from prediction appears to perform much better than the section US301BS. However, the field survey (Sedwick 1998) indicated that the section US301BN was also heavily cracked, but not as poor as the section US301BS. The reason for the misprediction of the relative performance of section US301BN may be because the m-value of US301BN was very low (0.357), even lower than that of the I75 and I10 sections. As explained in Chapter 4 and 5, the m-value controls the incremental rate of dissipated creep strain energy. Thus, a very low m-value would result in a significantly slower rate of damage and consequently a slower rate of crack growth prediction. If we consider the fracture energy and dissipated creep strain energy thresholds of the US301BN section, their extremely low thresholds suggest that this section should perform very poorly. Hence, this may imply that there might be other factors contributing to the cracking mechanism of asphalt pavements with very low energy thresholds. On the other hand, it might be only due to the incorrect data interpretation of the US301BN section. At this point, we cannot conclude any particular reason due to the insufficient information, and will leave it to a future study.

6.2 Direction of Crack Growth in Asphalt Pavement

Myers (2000) indicated that longitudinal wheel path cracks initiate from the surface of the pavement and traveled in the downward direction. However, the cracks were observed not to always propagate vertically throughout the layer. Based on observation from multiple field core samples cut through the locations of longitudinal cracks, it was revealed that the top-down crack path stayed on vertical direction only for a short distance (less than one inch) from the surface, after which its path deviated from the vertical direction. Myers (2000) investigated the crack growth direction using a numerical analysis of flexible pavement with a small crack located at the surface and 20 to 30 inches away from the center of the tire. It was found that the orientation of the major principal tensile stress at the crack tip area was approximately on the plane of a 30 degree angle away from the vertical plane.

Now let us consider the direction of crack growth predicted for the field sections in Section 6.1. From Figure 6-8, the crack propagates approximately in the vertical direction throughout its entire course. A possible explanation for this issue is that in the prediction, a starting crack was placed at the location of maximum surface tensile stress. From the bending action in the pavement, a condition of zero or minimal shear stress is usually found at the section of maximum horizontal stress. Thus, it is likely that the direction of principal tensile stress along the vertical section of where the starting crack was located is in horizontal direction. As a result, the crack propagated nearly in the vertical direction. Therefore, a question is whether the crack will deviate from the vertical direction, if the starting crack is placed at a distance away from the location of maximum tensile stress. In the following, this question will be investigated by the crack growth simulator.

The DDM model of section I10MW1 is reused for this study. Previously, a starting crack was placed at a distance of 952.5 mm (37.5 inches) away from the center of tire and resulted in the crack growth in a vertical direction. At this time, the starting crack was moved to a location 571.5 mm (22.5 inches) from the center of tire, i.e. 381 mm (15 inches) closer to the tire. At this location, the shear stress on the vertical section should increase substantially. A crack growth prediction is then started from this location. Figure 6-11 shows the geometry of the growing crack at each crack step. It indicates that the direction of crack growth deviates 10 degrees from vertical plane at 31.75-mm (1.25-in) crack depth, and becomes 16 degrees from vertical plane at 38.1-mm (1.5-in) crack depth.

In the real traffic situation, the vehicle wheel path does not always repeat itself on the same location on pavement. A number of vehicles may wanders left or right in an amount of few inches from the average position of wheel path. This wheel path wandering will cause a substantial shear stress at the crack tip and cause the micro-damage accumulated in the direction deviating from the vertical direction. It may imply that the cause of the deviation of crack growth direction observed in the field core is actually due to the wandering of tire position.

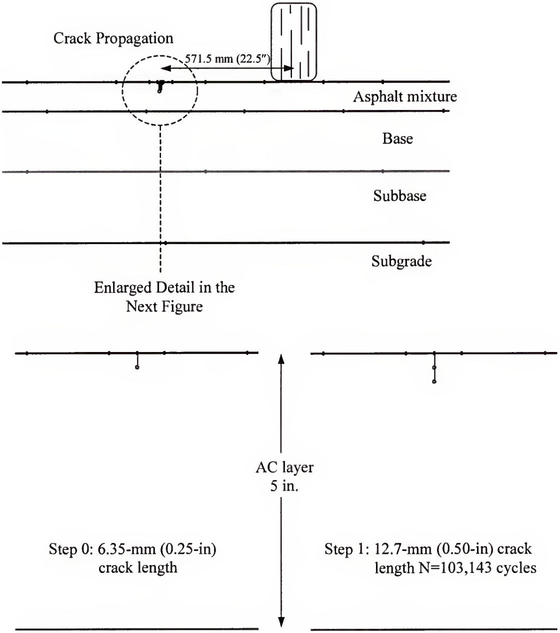
Crack Propagation
571.5 mm (22.5")
Asphalt mixture
Base
Subbase
Subgrade
Enlarged Detail in the Next Figure
AC layer
5 in.
Step 0: 6.35-mm (0.25-in) crack length
Step 1: 12.7-mm (0.50-in) crack length N=103,143 cycles

Figure 6-11. Crack Growth Geometry of Section I10MW1 for Crack Located 381 mm. (15 Inches) Closer to the Tire.

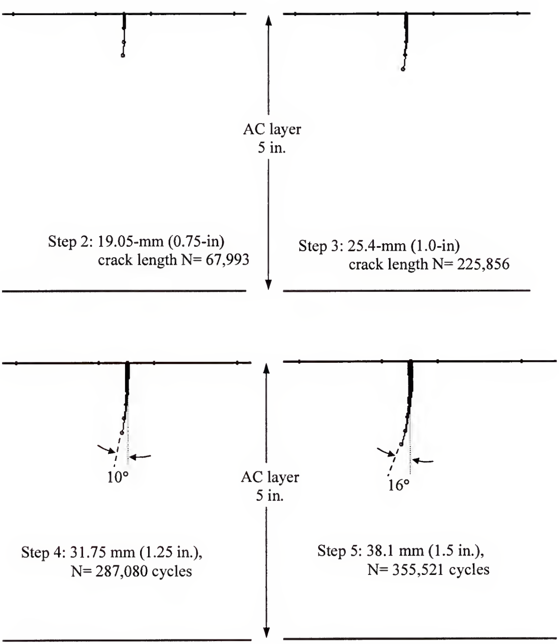
AC layer
5 in.
Step 2: 19.05-mm (0.75-in) crack length N= 67,993
Step 3: 25.4-mm (1.0-in) crack length N= 225,856
10°
AC layer
5 in.
16°
Step 4: 31.75 mm (1.25 in.), N= 287,080 cycles
Step 5: 38.1 mm (1.5 in.), N= 355,521 cycles

Figure 6-11. Continued.

6.3 Residual Stress in Flexible Asphalt Pavements

As described earlier in Chapter two, a number of fatigue cracking approaches consider the tensile stress/strain at the bottom of asphalt layer as a sole contribution to cracking damage. Regardless of the time-dependent response of asphalt pavement due to the repeated loads, these approaches consider only the maximum tensile stress/strain in their cracking formulas. According to most flexible pavement analysis, the maximum bending tensile stress always appears at the bottom of asphalt layer under the center of a tire. Accordingly, the tensile stress at the surface of asphalt layer is considerably lower in magnitude. This evidence is also shown in the stress plots in Figures 6-4 and 6-5. It should suggest there is a better chance that cracking damage develops from the bottom of the asphalt layer. Instead, longitudinal surface cracking was found in many cases as the primary deterioration mechanism of flexible pavements (Sedwick 1998; Garcia 2002). The author feels there is one issue that may not have been considered in the past. The mechanism of how the asphalt layer, a viscous material, interacts with the base layer, relatively an elastic material, in a time-dependent manner may lead to a better understanding of cracking mechanism in asphalt pavements.

6.3.1 Investigation Approach

Besides being able to predict crack growth in asphalt pavements, the HMA fracture simulator provides a framework for the viscoelastic displacement discontinuity method that is capable of analyzing the time-dependent response of a multi-layer pavement structure. In this problem, it will be used to monitor the response of asphalt pavements at the asphalt-base interface. In this study, a three-layer flexible pavement is considered. An assumption of perfect bonding without any local sliding between the asphalt and base layers must be made. In addition, the base and subgrade materials are assumed to be linear elastic materials. The properties of the asphalt mixture, base, and subgrade materials are given in Table 6-6. The properties of asphalt mixture are from the Superpave coarse-graded mix that was used in Chapter 5. The properties of base and subgrade materials are taken from the range of material properties from the field sections found in Sedwick (1998).

Table 6-6. Material Properties of a Flexible Pavement Structure.

Material	Description	Properties
Asphalt Mixture	Creep Compliance, $D(t)= D_0+D_1t^m$, MPa^{-1} (psi^{-1})	$D_0 = 455 \times 10^{-6}$ (3.14×10^{-6}) $D_1 = 552 \times 10^{-6}$ (3.81×10^{-7}) $m = 0.796$
	Poison Ratio, ν	0.5
Base	Elastic Modulus, E, MPa (psi)	345 (50,000)
	Poison Ratio, ν	0.35
Subgrade	Elastic Modulus, E, MPa (psi)	138 (20,000)
	Poison Ratio, ν	0.4

With the same approach used in Section 6.1 (Equations 6-2 and 6-3), the transformed shear modulus and transformed Poison ratio of the asphalt mixture are:

$$s\overline{G}(s)=\frac{1}{2(1+\nu)}\,\frac{s^m}{D_0 s^m + D_1\Gamma(m+1)} \tag{6-2}$$

$$\overline{\nu}(s) = \nu \tag{6-3}$$

The model of the three-layer flexible pavement is composed of 88 quadratic elements as shown in Figure 6-12. The asphalt surface layer has 40 elements, the base layer has 33 elements, and the subgrade layer has 15 elements. The model covers the pavement extent of 390-in width and 222-in depth under two-dimensional plane strain condition. The dimension of each layer is shown in Figure 6-12.

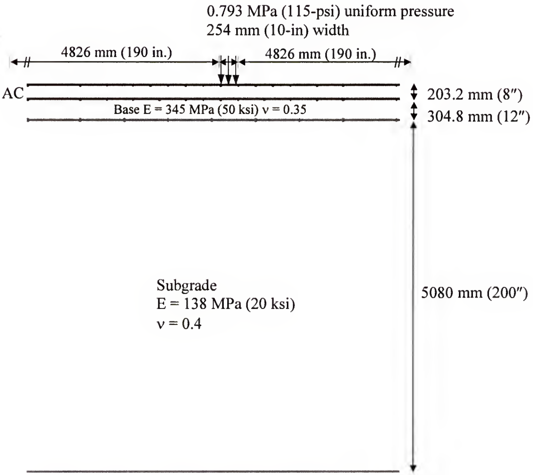

Figure 6-12. Model of Three-Layer Pavement.

For the boundary conditions of the pavement model, the elements at the bottom boundary are prescribed with zero displacements on both shear and normal components to represent a rigid foundation. The bottom boundary condition in time and transformed variables are written as:

$$u_s(t), u_n(t) = 0 \; ; \; t \geq 0 \tag{6-14}$$

$$\bar{u}_s(s) = L\{u_s(t)\} = \frac{0}{s} = 0 \tag{6-15}$$

$$\bar{u}_n(s) = L\{u_n(t)\} = \frac{0}{s} = 0 \tag{6-16}$$

For elements located at the top surface of the pavement, they are prescribed with free of tractions, except for the element at the location of tire contact where the tire load is applied. The boundary conditions for elements at surface are:

$$\sigma_s(t), \sigma_n(t) = 0 \ ; \ t \geq 0 \tag{6-17}$$

$$\bar{\sigma}_s(s) = L\{\sigma_s(t)\} = \frac{0}{s} = 0 \tag{6-18}$$

$$\bar{\sigma}_n(s) = L\{\sigma_n(t)\} = \frac{0}{s} = 0 \tag{6-19}$$

A 254-mm (10-in) strip of 0.793-MPa (115-psi) uniformly distributed vertical pressure is applied to the element at the center of surface boundary to represent a 4,083-kg (9,000-lb) dual tire. The pavement will be subjected to five cycles of equivalent load repetition. In each cycle, a uniform pressure is applied immediately to the pavement and left constant for a period of 0.1 second. Then it is removed suddenly from the pavement. Each of five cycles is applied at every second. The time-dependent function of a cycle of load application is written as follows:

$$\sigma_s(t) = 0 \ ; \ t \geq 0 \tag{6-20}$$

$$\sigma_n(t) = (0.793 \text{ MPa}) \cdot \{ H(t-0) - H(t-T) \} \tag{6-21}$$

where $T = 0.1$ second.

The transform functions of the load become

$$\bar{\sigma}_s(s) = L\{\sigma_s(t)\} = \frac{0}{s} = 0 \tag{6-22}$$

$$\bar{\sigma}_n(s) = L\{\sigma_n(t)\} = 0.793 \text{ MPa} \cdot \frac{1}{s} [1 - \exp(-T \cdot s)] \qquad (6\text{-}23)$$

Figure 6-13 illustrates the time functions of the uniformly distributed pressure.

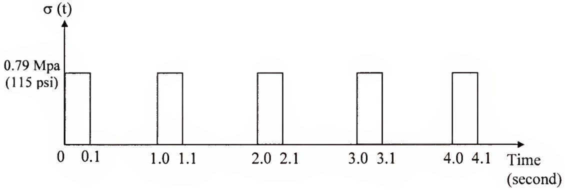

Figure 6-13. Time-Dependent Characteristic of Load Applications.

6.3.2 Interpretation of Time-Dependent Response in Asphalt Concrete Layer

The results of time-dependent stresses at the bottom and surface of asphalt layer below the center of uniformly distributed pressure are shown in Figures 6-14 to 6-17.

First, let us consider the case of a single cycle of load applied to the pavement. During the loading period of 0.1 second, the applied load causes significant bending stresses in the asphalt layer - tensile stress at the bottom and compressive stress at the surface of asphalt layer below the center of the tire. The high bending stresses then diminish after the load was removed at the end of 0.1 seconds. However, it appears that there are residual stresses remaining after the load was removed as illustrated in Figures 6-14 and 6-15. These residual stresses are in the opposite direction of the high stresses that occur during the loading period. This is because the elasticity of the base layer is attempting to return back to its undeformed-shape position after the load was removed, therefore pushing the asphalt layer back in the upward direction, and causing compressive stress at the bottom and tensile stress at the top of asphalt layer (Figure 6-18). The residual stresses appear to decrease gradually during the resting period of 0.9 seconds and tend to disappear at long times. Even though, the residual stresses after one cycle of load application are small in magnitude. Figure 6-16 and 6-17 reveal that the magnitudes of residual stresses are increasing incrementally when multiple loading cycles are applied repeatedly. Thus, the continual repeated loading without a long resting period may result in a considerable level of residual tensile stress at the surface of pavement under the tire area and residual compressive stress at the bottom of the asphalt layer.

Figures 6-16 and 6-17 also indicates that the rate of residual compressive stress accumulation at the bottom of the asphalt layer is apparently faster than the rate of residual tensile stress accumulation at the surface of the pavement. It suggests that the residual compressive stress may prevent the cracking damage to occur at the bottom of asphalt layer. But whether the residual tensile stress at the surface of pavement can incrementally increase to a level that can cause surface-initiated longitudinal cracking is still in question. And perhaps it is possible to have a certain structural combination of asphalt concrete and base layers that accentuates the residual stresses. Hence, the residual stress problem itself requires a more comprehensive study.

Furthermore, the evidence of asphalt-base interaction shows that the cracking mechanism in flexible pavements is possibly more complex than the classical approach, which considers only one snapshot of maximum pavement response. However, the fundamentals of the classical approach are also based on the bending mechanism of layered structures, which serves as a governing mechanism in the new hypothesis.

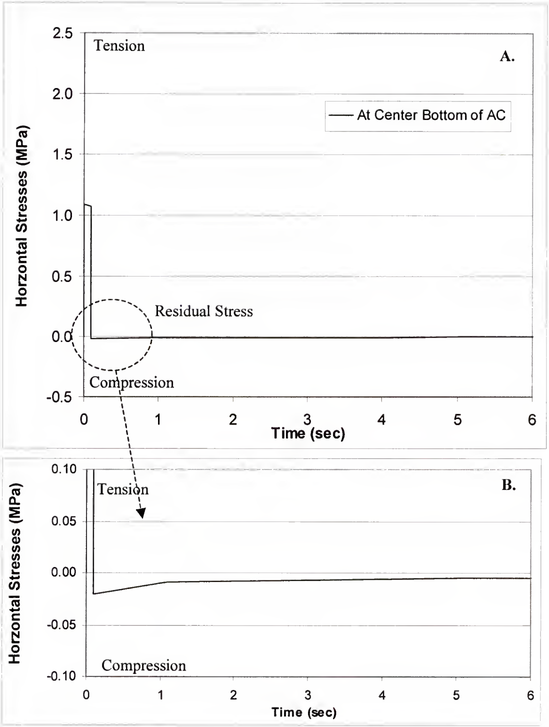

Figure 6-14. Horizontal Stress at Bottom of Asphalt Layer Below Center of Tire Caused by One Loading Cycle. A) Overall Scale, B) Enlarged Scale for Residual Stress.

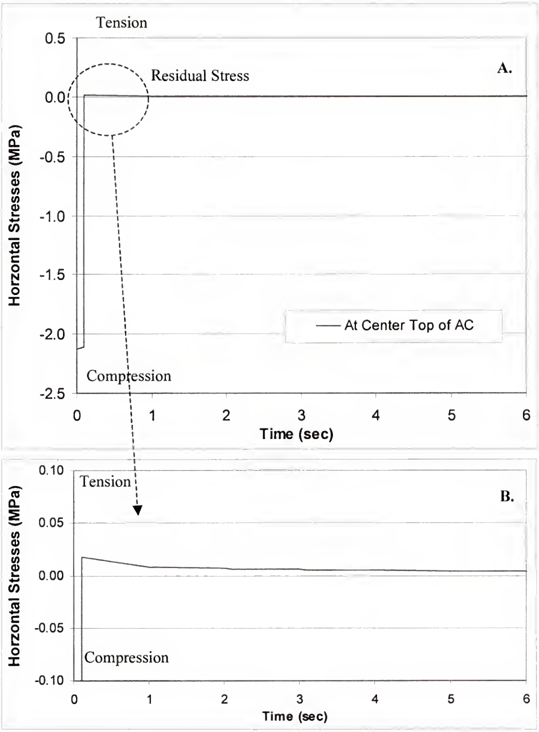

Figure 6-15. Horizontal Stress at Surface of Pavement Below Center of Tire Caused by One Loading Cycle. A) Overall Scale, B) Enlarged Scale for Residual Stress.

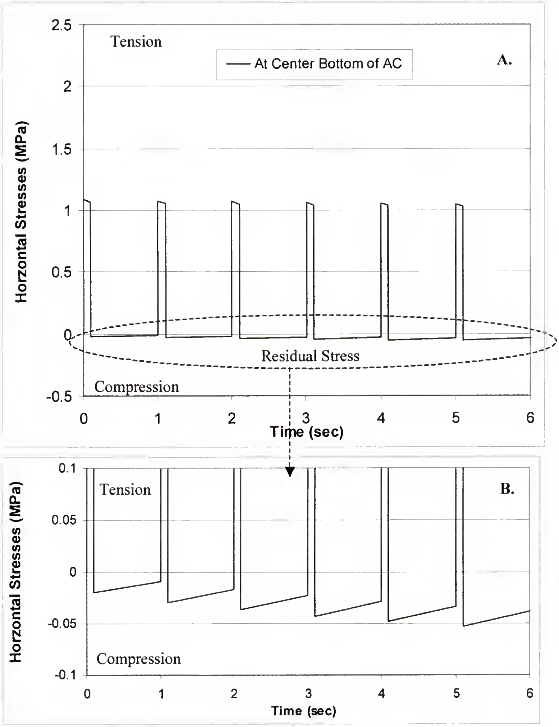

Figure 6-16. Horizontal Stress at Bottom of Asphalt Layer Below Center of Tire Caused by Multiple Loading Cycles. A) Overall Scale, B) Enlarged Scale for Residual Stress.

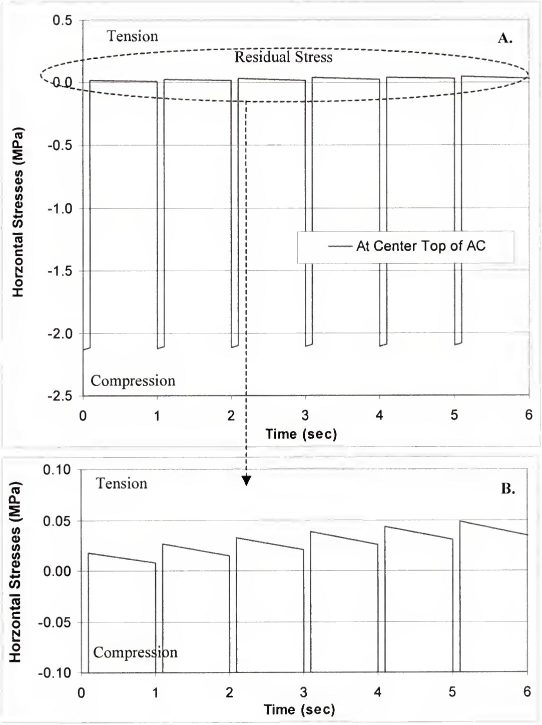

Figure 6-17. Horizontal Stress at Surface of Pavement Below Center of Tire Caused by Multiple Loading Cycles. A) Overall Scale, B) Enlarged Scale for Residual Stress.

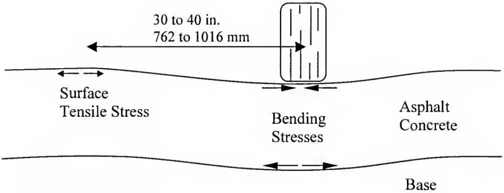

(A) During loading

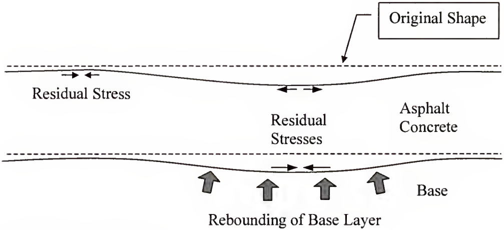

(B) After load was removed

Figure 6-18. Pavement Responses During and After a Load Application.

6.4 Effect of Stiffness Gradient

A parametric study of the effects of temperature condition on the mechanism for surface crack development was conducted by Myers (2000). It was indicated that the stiffness gradients within the asphalt surface layer, which were induced by temperature differentials in the asphalt layer, could significantly promote the critical condition for surface crack development and propagation. Myers (2000) found that there are several environmental conditions that typically occurred in the asphalt surface layer during a day including:

1. Uniform temperature distribution (i.e. no differential) throughout the asphalt surface layer
2. Sharpest temperature gradient located near surface of pavement
3. Highest temperature differential between the surface and the bottom of the asphalt layer
4. Rapid cooling nears the surface of the asphalt layer. This condition represents the case of sudden rain event.

Based on several analyses for stiffness gradients of those temperature cases, Myers (2000) discovered that the case of highest temperature differential (Case 3) had the strongest influence in elevating a significant magnitude of tensile stress concentration in front of the crack tip, thus accelerating the surface crack development in asphalt surface layer. In that analysis, a typical winter-season temperature gradient of 1.1°C per centimeter (5°F per inch) of asphalt concrete thickness was used in the case of highest temperature differential.

In this study, the crack growth predictions that are presented in the previous sections are all based on a uniform stiffness throughout the thickness of asphalt layer. In the following, we will investigate whether the temperature-induced stiffness gradient that is induced by temperature differential in an asphalt surface layer has any prominent influence in the field pavement sections. Some of the field pavement sections that were presented previously will be used to evaluate the effect of stiffness gradient.

6.4.1 Investigation Approach

Since the current HMA fracture simulator is only limited to predicting crack propagation within a homogeneous isotropic layer. A prediction of crack growth in asphalt mixture with non-uniform mixture properties due to the temperature gradient is not possible at this time. Moreover, the crack growth from one material layer to another material layer is beyond its capability at this time. Therefore, we will investigate the influence of temperature-induced stiffness gradient by considering whether there is a significant change in tensile stress concentration at the surface crack when the condition of asphalt layer changes from uniform-stiffness case to stiffness-gradient case.

6.4.1.1 Stiffness Gradients

The pavement sections of I10MW2 and I75-1C will be considered for the temperature-induced stiffness gradients. The resilient modulus of asphalt mixtures at three different temperatures of the corresponding field sections are given in Table 6-7. These values of resilient modulus were obtained from the Superpave indirect tensile test at low temperature (Roque et al. 1997). The values for pavement section I10MW2 were obtained from Sedwick (1998), and those for pavement section I75-1C was obtained from Jajliardo (2003). The thickness and moduli of base, subbase, and subgrade layers for these pavement sections are kept exactly the same as presented earlier in this chapter (Table 6-3).

The temperature variation within the asphalt concrete layer is obtained by introducing the rate of temperature differential of 1.1°C per centimeter (5°F per inch) of asphalt concrete thickness as suggested by Myers (2000) to the asphalt concrete layer. Figure 6-18 illustrates the temperature differential in asphalt concrete layer for those pavement sections. A low temperature starts at the surface of asphalt concrete layer; it then increases constantly (1.1°C per centimeter depth) until it reaches the highest temperature at the bottom of layer. Note that the average temperature is kept at 10°C at the middle of layer such that a comparison with the case of uniform stiffness of 10°C can be made.

In order to introduce stiffness gradients into an asphalt concrete layer, the whole layer is split into several sub-layers with equal thickness of about 40.64 to 43.18 mm (1.6 to 1.7 inches) (Figure 6-19). The average temperature in each sub-layer is then obtained from the temperature variation. After that, the modulus at the corresponding temperature in each sub-layer is obtained by interpolating from the resilient modulus at three different temperatures as given in Table 6-7. The asphalt concrete sub-layers in Figure 6-19 are applied to the base-subbase-subgrade structure for using in the stress analysis. Figures 6-20 and 6-21 show the details of pavement structures for the cases of stiffness gradient and uniform stiffness.

Table 6-7. Resilient Modulus at Three Temperatures for I10MW2 and I75-1C.

Pavement Section	Temperature	Resilient Modulus MPa (ksi)
I10MW2	-10°C	11959 (1,734)
	0°C	8641 (1,253)
	10°C	6690 (970)
I75-1C	0°C	16883 (2,448)
	10°C	11138 (1,615)
	20°C	7752 (1,124)

6.4.1.2 Pavement modeling

The linear elastic displacement discontinuity method is used to model these pavement sections in Figure 6-20 and 6-21. The similar modeling approach as presented earlier in Section 6.1 is used to model the pavement structure in this investigation. But more layers are added to represent the sub-layers of asphalt concrete.

The model for pavement sections I10MW2 and I75-1C are composed of a number of the quadratic elements to cover the pavement extent of 9.9-m width and more than 5.6-m depth (390-in x 222-in) under two-dimensional plane strain condition. The exact depths of the models depend on the thicknesses of the pavement sections, which are presented in Figures 6-20 and 6-21. Figure 6-22 shows an example of the DDM model for pavement section I10MW2 with sub-layers. A 12.7-mm (0.5-in) crack is also introduced to the surface of each pavement section to accentuate the tensile stress concentration in front of the crack tip. The details of number of elements for each section are presented as follows:

I10MW2 section

- For the case of uniform stiffness, the total number of elements used is 105 elements. The asphalt surface layer is treated as a single homogeneous layer with 43 elements. The numbers of elements in other layers are 30 elements for the base layer, 22 elements for the subbase layer, and 10 elements for the subgrade layer.

- For the case of stiffness gradient, the asphalt concrete layer is split into three sub-layers shown in Figure 6-20. Since the thicknesses of sub-layers are small, more elements with smaller sizes are required in the sub-layers. The total number of elements used in the model is 450 elements. The numbers of elements used in the asphalt concrete sub-layers are 120 elements for the uppermost sub-layer, 114 elements for the second sub-layer, and 114 elements for the third sub-layer. The numbers of elements in other layers are 70 elements for the base layer, 22 elements for the subbase layer, and 10 elements for the subgrade layer.

I75-1C section

- For the case of uniform stiffness, the total number of elements used is 177 elements. The asphalt surface layer is treated as a single homogeneous layer with 93 elements. The numbers of elements in other layers are 52 elements for the base layer, 22 elements for the subbase layer, and 10 elements for the subgrade layer.
- For the case of stiffness gradient, the asphalt concrete layer is split into four sub-layers shown in Figure 6-21. The total number of elements used in the model is 431 elements. The numbers of elements used in the asphalt concrete sub-layers are 103 elements for the uppermost sub-layer, 88 elements for the second sub-layer, 78 elements for the third sub-layer, and 78 elements for the fourth sub-layer. The numbers of elements in other layers are 52 elements for the base layer, 22 elements for the subbase layer, and 10 elements for the subgrade layer.

The elastic Young moduli of all layers including the sub-layers for each pavement section are given in Figures 6-20 and 6-21. For the boundary conditions of the pavement sections, the elements at the bottom boundary are prescribed with zero displacements on both shear and normal components to represent a rigid foundation. For elements located at the top surface of the pavement, they are prescribed with free of tractions, except for the elements at the location of tire contact where the tire load is applied. To represent a 4083-kg (9,000-lb) dual tire, a 254-mm (10-in) strip of 0.793-MPa (115-psi) uniformly distributed vertical pressure is applied to the elements underneath the tire contact area at the center of surface of pavement.

Figures 6-23 and 6-24 illustrate the results of tensile stress distributions in front of the crack in vertical direction for the pavement sections I10MW2 and I75-1C.

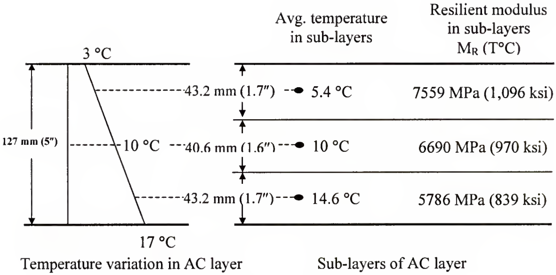

Stiffness Gradient of Asphalt Concrete Layer in Section I10MW2.

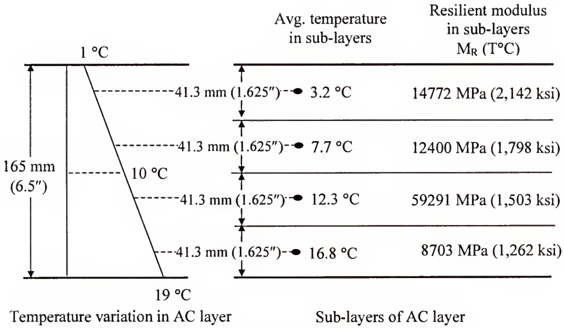

Stiffness Gradient of Asphalt Concrete Layer in Section I75-1C.

Figure 6-19. Stiffness Gradients in Asphalt Concrete Sub-layers.

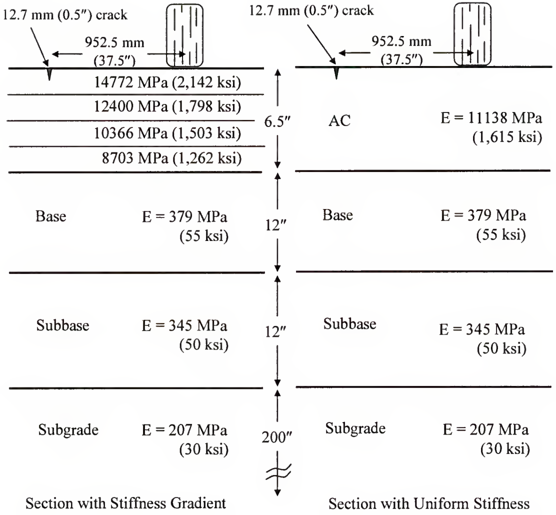

Figure 6-20. Pavement Structure of I75-1C for Stiffness Gradient Case and Uniform Stiffness Case.

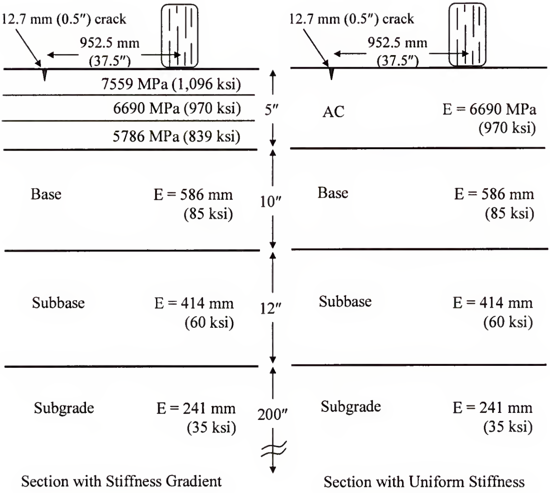

Figure 6-21. Pavement Structure of I10MW2 for Stiffness Gradient Case and Uniform Stiffness Case.

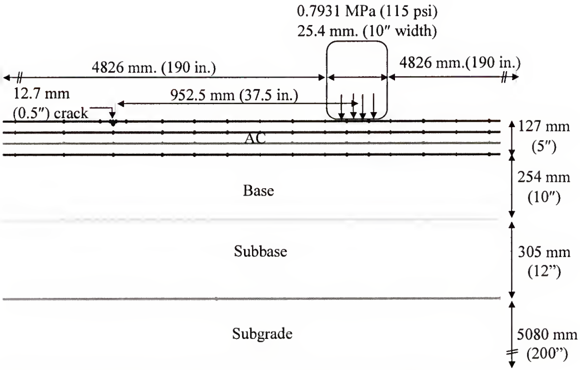

Figure 6-22. DDM Model of Pavement Section I10MW2 with Sub-Layers.

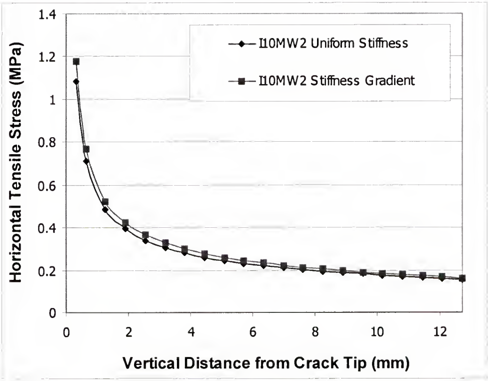

Figure 6-23. Tensile Stress Distribution in Front of Crack Tip for Section I10MW2.

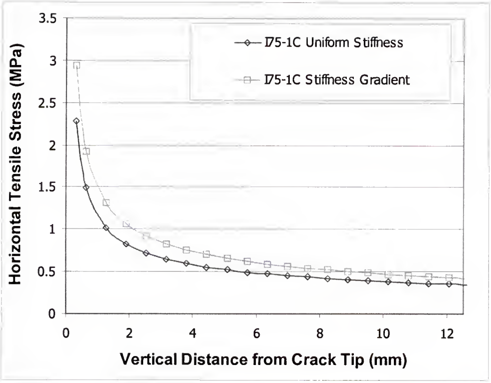

Figure 6-24. Tensile Stress Distribution in Front of Crack Tip for Section I75-1C.

6.4.1.3 Stress intensity factor (K_I)

In fracture mechanics, the tensile stress distribution in front of a crack tip is usually expressed by the following equation (Anderson, 1995):

$$\sigma_t(r) = \frac{K_I}{\sqrt{2\pi r}} \qquad \text{as r approaches zero} \qquad (6\text{-}24)$$

where r is the distance measured from the crack tip in the direction of crack angle. The K_I is defined as the stress intensity factor in tensile mode of cracking. Thus, the K_I is the indicator telling how large of stress concentration in front of crack tip. Instead of plotting the tensile stress concentration, the K_I can be referred to as an indicator of how critical the tensile stress develops. The K_I can be determined by linearly extrapolating from the plotted distribution of $\sigma_t \sqrt{2\pi r}$ versus r. This approach of determining K_I was also used in the work of Myers (2000). Figure 6-25 shows an example of K_I determination for the case of pavement section I75-1C. The results of K_I values for the cases of uniform stiffness and stiffness gradient are shown in Figure 6-26.

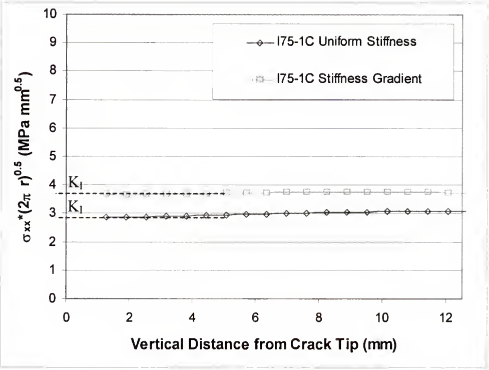

Figure 6-25. Determination of the Stress Intensity Factor for Section I75-1C.

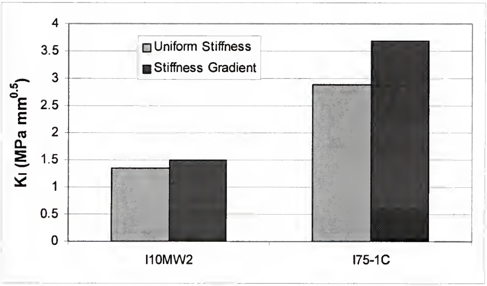

Figure 6-26. Stress Intensity Factors of Sections I10MW2 and I75-1C.

6.4.1.4 Reference sections for critical stiffness gradients

In addition, another four pavement sections that were presented in Myers (2000) are also included for K_I analysis. The details of these sections are shown in Figure 6-27. For the first section, a 203.2-mm (8-in) asphalt concrete with uniform stiffness of 5517 MPa (800 ksi) was placed on base, and subgrade structure with the base modulus of 138 MPa (20 ksi) (softer base). In the second section, the asphalt concrete layer is divided into five sub-layers with stiffness gradient. The second section also used the same base and subgrade structure as in the first section. The third and fourth sections are the same as the first and second section respectively, but the base stiffness were changed to 303 MPa (44 ksi) (stiff base). All four sections from Myers (2000) had a 12.7-mm (0.5-in) crack located at the distance 762 mm (30 inches) away from the center of the tire.

These four pavement sections from Myers (2000)' work were only extended to cover 2235-mm (88-in) total width and 2794-mm (110-in) total depth, which are considered smaller than the models used for the pavement sections I10MW2 and I75-1C. However, we will proceed with the Myers (2000)' original dimension for a comparison purpose. In addition, the DD elements will be placed on the side boundaries to compensate for the limited width of the model. The details of number of DD elements for each section are presented as follows:

- For the first and third sections, the total number of quadratic elements including a 12.7-mm (0.5-in) crack is 94 elements. The asphalt concrete layer is treated as a homogeneous uniform stiffness layer with 44 elements. The numbers of elements in other layers are 28 elements for the base layer, and 22 elements for the subgrade layer.
- For the second and fourth sections, the total number of quadratic elements including a 12.7-mm (0.5-in) crack is 256 elements. The asphalt concrete layer is split into five sub-layers shown in Figure 6-27. The numbers of elements used in the asphalt concrete sub-layers are 47 elements for the uppermost sub-layer, 40 elements for the second sub-layer, 38 elements for the third sub-layer, 38 elements

for the fourth sub-layer, and 39 elements for the fifth sub-layer. The numbers of elements in other layers are 32 elements for the base layer, 22 elements for the subgrade layer.

The elastic Young moduli of all layers including the sub-layers for these pavement sections are given in Figure 6-27.

For the boundary conditions of the pavement sections, the elements at the bottom boundary are prescribed with zero displacements on both shear and normal components to represent a rigid foundation. For elements located at the top surface of the pavement, they are prescribed with free of tractions, except for the elements at the location of tire contact where the tire load is applied.

To represent a 4,083-kg (9,000-lb) dual tire, a 254-mm (10-in) strip of 0.7931-MPa (115-psi) uniformly distributed vertical pressure is applied to the elements underneath the tire contact area at the center of surface of pavement. For elements located on the side boundaries of the pavement, they are set to no deformation in the horizontal direction, but they can freely displace in the vertical direction.

The results of K_I of these two sections, which are analyzed by the linear elastic displacement discontinuity method, are shown in Figure 6-28. The original values of K_I that were presented in Myers (2000) are also included in the Figure 6-29 for comparison with the DDM method.

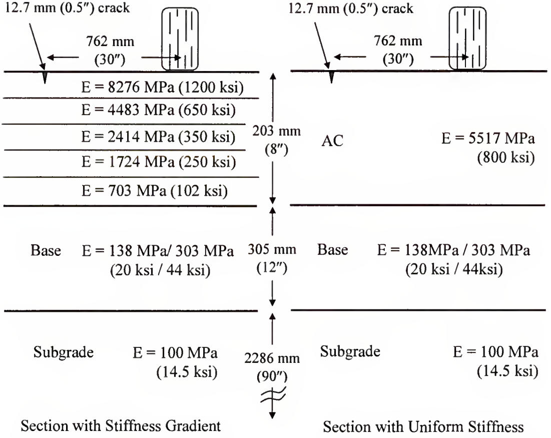

Figure 6-27. Pavement Structures for Stiffness Gradient Case and Uniform Stiffness Case According to Myers (2000).

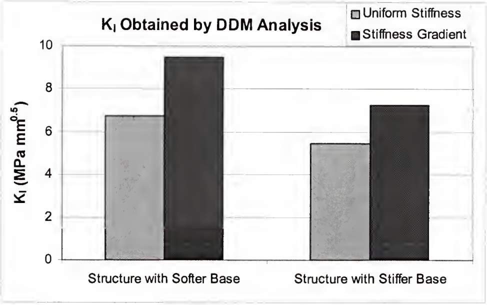

Figure 6-28. Stress Intensity Factors Obtained from DDM for the Reference Section (Myers 2000).

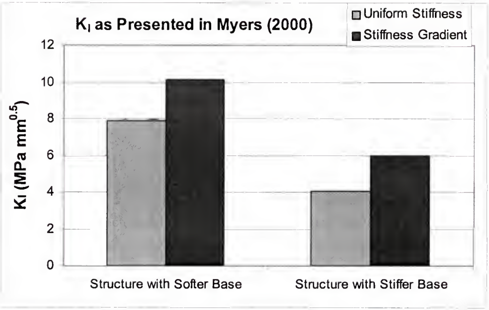

Figure 6-29. Stress Intensity Factors as Presented by Myers (2000) for the Reference Section (Myers 2000).

6.4.2 Intrepretation of Results

For the pavement section I10MW2, Figure 6-26 illustrates that the stress intensity factor (K_I) of the stiffness gradient case is slightly higher than K_I of the uniform stiffness case. But in pavement section I75-1C, the section with stiffness gradient causes a significant increase in the stress intensity factor (K_I) when compared to its case of uniform stiffness. This discrepancy also shows in plotted tensile stress concentration in Figures 6-23 and 6-24. The I10MW2 section with stiffness gradient results in only 0.06897-MPa (10-psi) higher tensile stress at the crack tip than the case of uniform stiffness. But for pavement section I75-1C, the tensile stress at the crack tip in the case of stiffness gradient becomes 0.6896-MPa (100-psi) higher than the case of uniform stiffness. This unparallel influence of stiffness gradient is most likely because of the variation of modulus in each asphalt mixture. In section I10MW2, the modulus at the top sub-layer is only 1772 MPa (257 ksi) higher than the one at the bottom sub-layer, while in section I75-1C, the modulus in the top sub-layer is 6069 MPa (880 ksi) higher than the bottom sub-layer. The pavement sections from Myers (2000) also confirm this, in which the modulus difference of 1,098 ksi results in a great increase of stress intensity factor as shown in Figures 6-28 and 6-29. Also, a thicker asphalt concrete layer may contribute in promoting a higher stiffness gradient, because the temperature differential between the top and bottom of the layer is greater in value.

Another factor that can play an important role in elevating the tensile stress concentration is the stiffness ratio between the asphalt concrete layer and the base layer. Figures 6-28 and 6-29 illustrate that for two pavement sections with the same asphalt concrete layer, the section with a softer base layer can result in a much higher stress intensity factor, i.e. higher tensile stress concentration, than the section with a stiffer base layer. The difference of the base stiffness in the soft and stiff base layers is only 166 MPa (24 ksi), but it can cause a great difference in stress intensity factor (about 3.48 $MPa \cdot mm^{0.5}$/100 $psi \cdot in^{0.5}$). Therefore, it is not only the stiffness gradient that can accentuate the critical conditions for cracking development, but also the overall pavement structural effect.

CHAPTER 7
CONCLUSIONS AND RECOMMENDATIONS

7.1 Conclusions

Recent work at the University of Florida has led to an improved understanding of the cracking behavior of asphalt mixtures, resulting in the development of a new viscoelastic fracture mechanics-based crack growth law, entitled "HMA fracture mechanics" (Zhang 2000; Zhang et al. 2001; and Birgisson et al. 2002b).

In this study, the fundamental cracking threshold and crack growth mechanism of the HMA fracture mechanics is taken as the basis in the development of an innovative method for simulating the viscoelastic response and cracking behavior of hot mix asphalt materials and pavements.

The framework of the HMA crack growth simulator is based on the displacement discontinuity boundary element method that has the following abilities:

- Detailed geometry of structure can be modeled such that the effect of the structural geometry on stress-displacement around cracks is captured.
- Physical cracks are modeled with a series of displacement discontinuity elements that span the length of the crack. The tensile stress concentration in front of a crack is also included naturally.
- Crack propagation is simply modeled by adding more elements to the series of elements that represent the existing crack.
- A nonhomogeneous layered structure such as pavement structure can be considered in the simulator.

Furthermore, the displacement discontinuity framework is extended to cover the linear viscoelasticity of asphalt mixtures by incorporating the Burgers and power law models through the correspondence principle. This allows the framework to:

- Model time-dependent characteristic of loads such as constant or haversine loads,
- Capture the time-dependent stress-displacement response of the overall structure, and
- Obtain the dissipated creep strain energy, i.e. micro-cracking damage, in the vicinity of a crack, which is the key to the crack growth prediction.

In addition, the following important aspects involved in the modeling of the crack growth mechanism are implemented:

- Appropriate definition of critical zone length that controls the stepwise crack growth.
- Framework for determining the direction of crack development is included.

The resulting HMA fracture mechanics-based crack growth simulator is potentially able to model and predict the crack growth in asphalt mixtures under general loading conditions. The key features of the HMA crack growth simulator may be summarized as follows:

- Crack development at low temperature is accounted for and is governed by the same four mixture parameters, which can all be obtained using relatively simple and well established tests using the Superpave IDT.
- A threshold concept is used to delineate between healable microdamage and non-healable macrocracking: if the threshold is not exceeded, only healable micro-damage develops; however, non-healable macro-damage (crack initiation or growth) results once the threshold is exceeded.
- Time-dependent loading conditions are considered.
- Stresses and creep strain energies are calculated within a linear viscoelastic constitutive model, and the resulting crack growth is determined based on a damage threshold framework.

- The displacement discontinuity boundary element method reduces the dimension of the problem by one, since only the boundary is discretized. This translates into significant savings in computational effort.
- The displacement discontinuity boundary element method is more efficient than finite element methods for modeling cracks, because of the explicit representation of cracks at the element level (each element can be regarded as a crack).
- Modeling crack growth in the asphalt mixture layer in a pavement structure is made possible by the nonhomogeneous layered displacement discontinuity method with the higher-order element to capture the bending action of pavement structure.

The HMA crack growth simulator is then verified with the HMA crack growth observations in the laboratory and relative cracking performances of field pavement sections.

In the verification with the laboratory crack growth results, the simulator was verified only with the Superpave IDT testing results due to the limitations of available experimental results. The simulator was used to predict the crack growth behavior of two HMA mixtures tested under cyclic loading conditions at low temperature in the Superpave IDT. The predicted crack growth behavior was shown to compare reasonably well with the experimental IDT results.

In the verification with the actual crack growth in asphalt pavements, three pairs of field pavement sections with known performances were used as references. The material and structural properties of these field pavement sections were used as the input for the HMA crack growth simulator. The HMA crack growth simulator predicts the top-down cracking on these pavement sections that were driven by the surface tensile stress. It appeared that the relative cracking performance between a pair of pavement sections predicted by the HMA fracture simulator is consistent with the field observations on these pair of pavement sections. Also, the crack growth simulator was able to explain observed changes in crack growth direction, which appeared in the field observations.

The verification with laboratory results and field observations confirmed that the HMA fracture mechanics-based crack growth simulator worked reasonably well. Additional study on residual stresses revealed that the bottom-up cracking may be prevented from occurring by the development of residual stress that is a result of asphalt concrete-base interaction. It also suggested that the surface tensile stress may not be the only mechanism for top-down cracking, there may be a possible condition for the residual tensile stress at the surface of pavement to become critical.

Furthermore, the study on the effect of stiffness gradient in asphalt concrete layer indicated that the stiffness gradient could accentuate the critical condition for crack development at the surface of pavements.

This infers that the proper condition and possible mechanism for top-down crack growth are still not clearly identified.

7.2 Recommendations

Evidences in the crack growth predictions for pavement sections suggested that the cracking performance of the flexible pavement is not only controlled by the properties of the asphalt mixture in the surface layer. The combination of the stiffnesses and thicknesses of asphalt surface layer and the lower layers is also the key to improve the cracking resistance of flexible pavements. This should also hold true for both surface-initiated top-down cracking and conventional bottom-up fatigue cracking. The following further studies are recommended:

- Identification of the proper conditions that are critical for cracking damage. The environmental effects and overall pavement structure should be considered.
- The evidence of residual stresses in asphalt concrete layer may be the key reason for describing the top-down versus bottom-up cracking mechanisms. A detailed study with the conditions in favor of the residual stresses is suggested.

- The study and implementation of the cohesive zone element to simulate the stress condition in front of the crack tip, which may lead to a more accurate mechanism at the crack tip.

APPENDIX A
HOOKE'S LAW

According to the Hooke' s law, the stress-strain in an elastic solid material has a linearly proportional relationship as follows:

$$\sigma = E \cdot \varepsilon \tag{A-1}$$

where

σ and ε are one dimensional stress and strain, and

E is material constant defined as the Young modulus.

For a three-dimensional generalized Hooke's law, the stress-strain relations for an isotropic, linearly elastic material can be written in the form:

$$\varepsilon_{xx} = \frac{1}{E}[\sigma_{xx} - \nu(\sigma_{yy} + \sigma_{zz})] \tag{A-2}$$

$$\varepsilon_{yy} = \frac{1}{E}[\sigma_{yy} - \nu(\sigma_{xx} + \sigma_{zz})] \tag{A-3}$$

$$\varepsilon_{zz} = \frac{1}{E}[\sigma_{zz} - \nu(\sigma_{xx} + \sigma_{yy})] \tag{A-4}$$

$$\varepsilon_{xy} = \frac{1}{2G}\sigma_{xy} \qquad \varepsilon_{xz} = \frac{1}{2G}\sigma_{xz} \qquad \varepsilon_{yz} = \frac{1}{2G}\sigma_{yz} \tag{A-5}$$

$$\sigma_{xx} = \frac{2G}{1-2\nu}[(1-\nu)\varepsilon_{xx} + \nu(\varepsilon_{yy} + \varepsilon_{zz})] \tag{A-6}$$

$$\sigma_{yy} = \frac{2G}{1-2\nu}[(1-\nu)\varepsilon_{yy} + \nu(\varepsilon_{xx} + \varepsilon_{zz})] \tag{A-7}$$

$$\sigma_{zz} = \frac{2G}{1-2\nu}[(1-\nu)\varepsilon_{zz} + \nu(\varepsilon_{xx} + \varepsilon_{yy})] \tag{A-8}$$

$$\sigma_{xy} = 2G\,\varepsilon_{xy} \qquad \sigma_{xz} = 2G\,\varepsilon_{xz} \qquad \sigma_{yz} = 2G\,\varepsilon_{yz} \tag{A-9}$$

where

G is shear modulus, $G = \dfrac{E}{2(1+\nu)}$, and

ν is Poisson's ratio.

The above three-dimensional stress-strain relations can also be written in index notation as follow:

$$\varepsilon_{ij} = \frac{1}{2G}\,[\sigma_{ij} - \frac{\nu}{1+\nu}\sigma_{kk}\,\delta_{ij}] \tag{A-10}$$

$$\sigma_{ij} = 2G\,[\varepsilon_{ij} + \frac{\nu}{1-2\nu}\,\varepsilon_{kk}\,\delta_{ij}] \tag{A-11}$$

where

δ_{ij} is the Kronecker delta; $\delta_{ij} = 1$ if $i = j$, $\delta_{ij} = 0$ if $i \neq j$,

index i, j represent x or y components, and

index kk represents summation of components—e.g. $\sigma_{kk}=\sigma_{xx} + \sigma_{yy} + \sigma_{zz}$.

APPENDIX B
FORMULATION FOR DISPLACEMENT DISCONTINUITY ELEMENT

Quadratic Element

As described in the chapter 3, the solutions of stress-displacement for the displacement discontinuity method are

$$u_x = [-2(1-\nu)\,\psi_{,y} + y\,\psi_{,xx}] + [\,(1-2\nu)\,\phi_{,x} + y\,\phi_{,xy}] \quad \text{(B-1)}$$

$$u_y = [-(1-2\nu)\,\psi_{,x} + y\,\psi_{,xy}] + [-2(1-\nu)\,\phi_{,y} + y\,\phi_{,yy}] \quad \text{(B-2)}$$

$$\sigma_{xx} = 2G\,[-2\,\psi_{,xy} - y\,\psi_{,xyy}] + 2G\,[-\phi_{,yy} - y\,\phi_{,yyy}] \quad \text{(B-3)}$$

$$\sigma_{yy} = 2G\,[y\,\psi_{,xyy}] + 2G\,[-\phi_{,yy} + y\,\phi_{,yyy}] \quad \text{(B-4)}$$

$$\sigma_{xy} = 2G\,[-\psi_{,yy} - y\,\psi_{,yyy}] + 2G\,[y\,\phi_{,xyy}] \quad \text{(B-5)}$$

where

$$\phi_{,x} = \frac{1}{4\pi(1-\nu)} \int_{-a}^{a} D_y(\xi)\frac{x-\xi}{(x-\xi)^2+y^2}\,d\xi \quad \text{(B-6)}$$

$$\phi_{,y} = \frac{1}{4\pi(1-\nu)} \int_{-a}^{a} D_y(\xi)\frac{y}{(x-\xi)^2+y^2}\,d\xi \quad \text{(B-7)}$$

$$\psi_{,x} = \frac{1}{4\pi(1-\nu)} \int_{-a}^{a} D_x(\xi)\frac{x-\xi}{(x-\xi)^2+y^2}\,d\xi \quad \text{(B-8)}$$

$$\psi_{,y} = \frac{1}{4\pi(1-\nu)} \int_{-a}^{a} D_x(\xi)\frac{y}{(x-\xi)^2+y^2}\,d\xi \quad \text{(B-9)}$$

$D_i(\xi)$ is the variation of displacement discontinuity over the element

Let us define

$$f_{,x} = \frac{1}{4\pi}\int_{-a}^{a} D_i(\xi)\frac{x-\xi}{(x-\xi)^2+y^2}d\xi$$

$$f_{,y} = \frac{1}{4\pi}\int_{-a}^{a} D_i(\xi)\frac{y}{(x-\xi)^2+y^2}d\xi \qquad \text{(B-10)}$$

For the quadratic element, $D_i(\xi)$ or the variation of displacement discontinuity along the element is described by the 2nd degree polynomial with three specified nodal points, $D_i(1)$, $D_i(2)$, and $D_i(3)$.

$$D_i(\xi) = \left(-\frac{1}{\sqrt{3}}\frac{\xi}{a} + \frac{2}{3}\left(\frac{\xi}{a}\right)^2\right) D_i(1) + \left(1 - \frac{4}{3}\left(\frac{\xi}{a}\right)^2\right) D_i(2) + \left(\frac{1}{\sqrt{3}}\frac{\xi}{a} + \frac{2}{3}\left(\frac{\xi}{a}\right)^2\right) D_i(3) \quad \text{(B-11)}$$

Substitute $D_i(\xi)$ into the Equation B-3 to obtain

$$f_{,x} = \left[-\frac{1}{\sqrt{3}}I_2 + \frac{2}{3}I_3\right] D_i(1) + \left[I_1 - \frac{4}{3}I_3\right] D_i(2) + \left[\frac{1}{\sqrt{3}}I_2 + \frac{2}{3}I_3\right] D_i(3) \qquad \text{(B-12)}$$

$$f_{,y} = \left[-\frac{1}{\sqrt{3}}II_2 + \frac{2}{3}II_3\right] D_i(1) + \left[II_1 - \frac{4}{3}II_3\right] D_i(2) + \left[\frac{1}{\sqrt{3}}II_2 + \frac{2}{3}II_3\right] D_i(3) \qquad \text{(B-13)}$$

where

$$I1 = \frac{1}{4\cdot\pi}\cdot\int_{-a}^{a}\frac{x-\xi}{(x-\xi)^2+y^2}d\xi \qquad \text{(B-14)}$$

$$I2 = \frac{1}{4\cdot\pi}\cdot\int_{-a}^{a}\frac{x-\xi}{(x-\xi)^2+y^2}\cdot\frac{\xi}{a}d\xi \qquad \text{(B-15)}$$

$$I3 = \frac{1}{4\cdot\pi}\cdot\int_{-a}^{a}\frac{x-\xi}{(x-\xi)^2+y^2}\cdot\left(\frac{\xi}{a}\right)^2 d\xi \qquad \text{(B-16)}$$

$$II1 = \frac{1}{4 \cdot \pi} \cdot \int_{-a}^{a} \frac{y}{(x-\xi)^2 + y^2} \, d\xi \tag{B-17}$$

$$II2 = \frac{1}{4 \cdot \pi} \cdot \int_{-a}^{a} \frac{y}{(x-\xi)^2 + y^2} \cdot \frac{\xi}{a} \, d\xi \tag{B-18}$$

$$II3 = \frac{1}{4 \cdot \pi} \cdot \int_{-a}^{a} \frac{y}{(x-\xi)^2 + y^2} \cdot \left(\frac{\xi}{a}\right)^2 d\xi \tag{B-19}$$

The $f_{,x}$ and $f_{,y}$ in vector forms can be written as

$$f_{,x} = \mathbf{I} \cdot \mathbf{D_i} \qquad \text{and} \qquad f_{,y} = \mathbf{II} \cdot \mathbf{D_i} \tag{B-20}$$

where the vector terms are

$$\mathbf{I} = \{\, [-\frac{1}{\sqrt{3}} I_2 + \frac{2}{3}\, I_3] \quad [\, I_1 - \frac{4}{3}\, I_3] \quad [\frac{1}{\sqrt{3}} I_2 + \frac{2}{3}\, I_3] \,\} \tag{B-21}$$

$$\mathbf{II} = \{\, [-\frac{1}{\sqrt{3}} II_2 + \frac{2}{3}\, II_3] \quad [\, II_1 - \frac{4}{3}\, II_3] \quad [\frac{1}{\sqrt{3}} II_2 + \frac{2}{3}\, II_3] \,\} \tag{B-22}$$

$$\mathbf{D_i} = \{\, D_i(1) \quad D_i(2) \quad D_i(3) \,\} \tag{B-23}$$

Thus, Equations B-1 to B-5 should become

$$u_x = [-2\, \mathbf{II} + \frac{y}{1-\nu}\, \mathbf{I}_{,x}] \cdot \mathbf{D_s} + [\frac{1-2\nu}{1-\nu}\, \mathbf{I} + \frac{y}{1-\nu}\, \mathbf{I}_{,y}] \cdot \mathbf{D_n} \tag{B-24}$$

$$u_y = [-\frac{1-2\nu}{1-\nu}\, \mathbf{I} + \frac{y}{1-\nu}\, \mathbf{I}_{,y}] \cdot \mathbf{D_s} + [-2\, \mathbf{II} + \frac{y}{1-\nu}\, \mathbf{II}_{,y}] \cdot \mathbf{D_n} \tag{B-25}$$

$$\sigma_{xx} = \frac{2G}{1-\nu} [-2\, \mathbf{I}_{,y} - y\, \mathbf{I}_{,yy}] \cdot \mathbf{D_s} + \frac{2G}{1-\nu} [-\mathbf{II}_{,y} - y\, \mathbf{II}_{,yy}] \cdot \mathbf{D_n} \tag{B-26}$$

$$\sigma_{yy} = \frac{2G}{1-\nu} [y\, \mathbf{I}_{,yy}] \cdot \mathbf{D_s} + \frac{2G}{1-\nu} [-\mathbf{II}_{,y} + y\, \mathbf{II}_{,yy}] \cdot \mathbf{D_n} \tag{B-27}$$

$$\sigma_{xy} = \frac{2G}{1-\nu}\ [\text{-}\mathbf{II}_{,y} - y\ \mathbf{II}_{,yy}] \cdot \mathbf{D}_s + \frac{2G}{1-\nu}\ [\ y\ \mathbf{I}_{,yy}] \cdot \mathbf{D}_n \tag{B-28}$$

The derivatives components of **I** and **II** vectors are presented as follows:

For I1 terms,

$$I1 = \frac{1}{4 \cdot \pi}\left(\frac{\ln\left(r_2^{\,2}\right)}{2} - \frac{\ln\left(r_1^{\,2}\right)}{2}\right) \tag{B-29}$$

where $r_1 = (x-a)^2 + y^2$ (B-30)

$r_2 = (x+a)^2 + y^2$ (B-31)

$$I1,x = \frac{1}{4 \cdot \pi} \cdot \left[\frac{(x+a)}{r_2^{\,2}} - \frac{(x-a)}{r_1^{\,2}}\right] \tag{B-32}$$

$$I1,y = \frac{1}{4 \cdot \pi} \cdot \left(\frac{y}{r_2^{\,2}} - \frac{y}{r_1^{\,2}}\right) \tag{B-33}$$

$$I1,yy = \frac{1}{4 \cdot \pi} \cdot \left(\frac{1}{r_2^{\,2}} - \frac{2y^2}{r_2^{\,4}} - \frac{I}{r_1^{\,2}} + \frac{2y^2}{r_1^{\,4}}\right) \tag{B-34}$$

For I2 terms,

$$I2 = \frac{I}{4 \cdot \pi \cdot a}\left(-2a + y \cdot \operatorname{atan}\left(\frac{y}{x-a}\right) - y \cdot \operatorname{atan}\left(\frac{y}{x+a}\right) + \frac{x}{2} \cdot \ln\left(r_2^{\,2}\right) - \frac{x}{2} \cdot \ln\left(r_1^{\,2}\right)\right) \tag{B-35}$$

$$I2,x = \frac{I}{4 \cdot \pi \cdot a} \cdot \left(\frac{-y^2}{r_1^{\,2}} + \frac{y^2}{r_2^{\,2}} + \frac{1}{2} \cdot \ln\left(r_2^{\,2}\right) + \frac{x(x+a)}{r_2^{\,2}} - \frac{I}{2} \cdot \ln\left(r_1^{\,2}\right) - \frac{x(x-a)}{r_1^{\,2}}\right) \tag{B-36}$$

$$I2,y = \frac{1}{4 \cdot \pi \cdot a} \cdot \left(\operatorname{atan}\left(\frac{y}{x-a}\right) - \operatorname{atan}\left(\frac{y}{x+a}\right) + \frac{y(x-a)}{r_1^{\,2}} - \frac{y(x+a)}{r_2^{\,2}} + \frac{x \cdot y}{r_2^{\,2}} - \frac{x \cdot y}{r_1^{\,2}}\right) \tag{B-37}$$

$$I2,yy = \frac{I}{4 \cdot \pi \cdot a} \cdot \left[\frac{2 \cdot (x-a)^3}{r_1^{\,4}} - \frac{2 \cdot (x+a)^3}{r_2^{\,4}} + \frac{x}{r_2^{\,2}} - 2 \cdot \frac{x \cdot y^2}{r_2^{\,4}} - \frac{x}{r_1^{\,2}} + 2 \cdot \frac{x \cdot y^2}{r_1^{\,4}}\right] \tag{B-38}$$

For I3 terms,

$$I3=\frac{1}{4\cdot\pi\cdot a^2}\cdot\left[-2\cdot a\cdot x+2\cdot x\cdot y\cdot \operatorname{atan}\left(\frac{y}{x-a}\right)-2\cdot x\cdot y\cdot \operatorname{atan}\left(\frac{y}{x+a}\right)+\frac{\left(y^2-x^2\right)}{2}\cdot\ln\left(r_1{}^2\right)-\frac{\left(y^2-x^2\right)}{2}\cdot\ln\left(r_2{}^2\right)\right] \tag{B-39}$$

$$I3,x=\frac{1}{4\cdot\pi\cdot a^2}\cdot\left(-2\cdot a+2\cdot y\cdot \operatorname{atan}\left(\frac{y}{x-a}\right)-2\cdot\frac{x\cdot y^2}{r_1{}^2}-2\cdot y\cdot \operatorname{atan}\left(\frac{y}{x+a}\right)+2\cdot\frac{x\cdot y^2}{r_2{}^2}-x\cdot\ln\left(r_1{}^2\right)\right.$$
$$\left.+\left(y^2-x^2\right)\cdot\frac{(x-a)}{r_1{}^2}+x\cdot\ln\left(r_2{}^2\right)-\left(y^2-x^2\right)\cdot\frac{(x+a)}{r_2{}^2}\right) \tag{B-40}$$

$$I3,y=\frac{1}{4\cdot\pi\cdot a^2}\cdot\left[2\cdot x\cdot \operatorname{atan}\left(\frac{y}{x-a}\right)+2\cdot\frac{x\cdot y\cdot(x-a)}{r_1{}^2}-2\cdot x\cdot \operatorname{atan}\left(\frac{y}{x+a}\right)-2\cdot\frac{x\cdot y\cdot(x+a)}{r_2{}^2}+y\cdot\ln\left(r_1{}^2\right)\right.$$
$$\left.+\frac{\left(y^2-x^2\right)\cdot y}{r_1{}^2}-y\cdot\ln\left(r_2{}^2\right)-\frac{\left(y^2-x^2\right)\cdot y}{r_2{}^2}\right] \tag{B-41}$$

$$I3,yy=\frac{1}{4\cdot\pi\cdot a^2}\cdot\left[4\cdot\frac{x\cdot(x-a)^3}{r_1{}^4}-4\cdot\frac{x\cdot(x+a)^3}{r_2{}^4}+\ln\left(r_1{}^2\right)-\ln\left(r_2{}^2\right)+\frac{4\cdot y^2}{r_1{}^2}-\frac{4\cdot y^2}{r_2{}^2}+\frac{y^2-x^2}{r_1{}^2}-\frac{y^2-x^2}{r_2{}^2}\right.$$
$$\left.-2\cdot\frac{y^2\cdot\left(y^2-x^2\right)}{r_1{}^4}+2\cdot\frac{y^2\cdot\left(y^2-x^2\right)}{r_2{}^4}\right] \tag{B-42}$$

For II1 terms,

$$II1=\frac{1}{4\cdot\pi}\left(\operatorname{atan}\left(\frac{y}{x-a}\right)-\operatorname{atan}\left(\frac{y}{x+a}\right)\right) \tag{B-43}$$

$$II1,y=\frac{1}{4\cdot\pi}\left(\frac{x-a}{r_1{}^2}-\frac{x+a}{r_2{}^2}\right) \tag{B-44}$$

$$II1,yy=\frac{1}{4\cdot\pi}\left[\frac{-2(x-a)\cdot y}{r_1{}^4}+\frac{2(x+a)\cdot y}{r_2{}^4}\right] \tag{B-45}$$

For II2 terms,

$$II2 = \frac{1}{4\cdot\pi\cdot a}\cdot\left(\frac{y}{2}\cdot\ln\left(r_1^{\,2}\right) - \frac{y}{2}\cdot\ln\left(r_2^{\,2}\right) + x\cdot\operatorname{atan}\left(\frac{y}{x-a}\right) - x\cdot\operatorname{atan}\left(\frac{y}{x+a}\right)\right) \tag{B-46}$$

$$II2,y = \frac{1}{4\cdot\pi\cdot a}\cdot\left[\frac{x\cdot(x-a)}{r_1^{\,2}} - \frac{x\cdot(x+a)}{r_2^{\,2}} + \frac{1}{2}\cdot\ln\left(r_1^{\,2}\right) - \frac{1}{2}\cdot\ln\left(r_2^{\,2}\right) + \frac{y^2}{r_1^{\,2}} - \frac{y^2}{r_2^{\,2}}\right] \tag{B-47}$$

$$II2,yy = \frac{1}{4\cdot\pi\cdot a}\cdot\left[\frac{-2\cdot x\cdot(x-a)\cdot y}{r_1^{\,4}} + \frac{2\cdot x\cdot(x+a)\cdot y}{r_2^{\,4}} + \frac{3\cdot y}{r_1^{\,2}} - \frac{3\cdot y}{r_2^{\,2}} - \frac{2y^3}{r_1^{\,4}} + \frac{2y^3}{r_2^{\,4}}\right] \tag{B-48}$$

For II3 terms,

$$II3 = \frac{1}{4\cdot\pi\cdot a^2}\cdot\left[2a\,y + x\cdot y\cdot\ln\left(r_1^{\,2}\right) - x\cdot y\cdot\ln\left(r_2^{\,2}\right) + \left(x^2 - y^2\right)\cdot\operatorname{atan}\left(\frac{y}{x-a}\right) - \left(x^2 - y^2\right)\cdot\operatorname{atan}\left(\frac{y}{x+a}\right)\right] \tag{B-49}$$

$$II3,y = \frac{1}{4\cdot\pi\cdot a^2}\cdot\left(2\cdot a + x\cdot\ln\left(r_1^{\,2}\right) + \frac{2\cdot x\cdot y^2}{r_1^{\,2}} - x\cdot\ln\left(r_2^{\,2}\right) - \frac{2\cdot x\cdot y^2}{r_2^{\,2}} - 2\cdot y\cdot\operatorname{atan}\left(\frac{y}{x-a}\right)\right.$$

$$\left. + 2\cdot y\cdot\operatorname{atan}\left(\frac{y}{x+a}\right) + \frac{\left(x^2 - y^2\right)\cdot(x-a)}{r_1^{\,2}} - \frac{\left(x^2 - y^2\right)\cdot(x+a)}{r_2^{\,2}}\right. \tag{B-50}$$

$$II3,yy = \frac{1}{4\cdot\pi\cdot a^2}\cdot\left[\frac{6\cdot x\cdot y}{r_1^{\,2}} - \frac{4\cdot x\cdot y^3}{r_1^{\,4}} - \frac{6\cdot x\cdot y}{r_2^{\,2}} + \frac{4\cdot x\cdot y^3}{r_2^{\,4}} - 2\cdot\operatorname{atan}\left(\frac{y}{x-a}\right) - \frac{4y\cdot(x-a)}{r_1^{\,2}}\right.$$

$$\left.\frac{-2y\cdot\left(x^2 - y^2\right)\cdot(x-a)}{r_1^{\,4}} + 2\cdot\operatorname{atan}\left(\frac{y}{x+a}\right) + \frac{4y\cdot(x+a)}{r_2^{\,2}} + \frac{2y\cdot\left(x^2 - y^2\right)\cdot(x+a)}{r_2^{\,4}}\right. \tag{B-51}$$

Constant Element

For I1 terms,

$$I = \frac{1}{4\cdot\pi}\left(\frac{\ln\left(r_2^{\,2}\right)}{2} - \frac{\ln\left(r_1^{\,2}\right)}{2}\right) \tag{B-52}$$

where $r_1 = (x-a)^2 + y^2$ (B-53)

$r_2 = (x+a)^2 + y^2$ (B-54)

$$I,x = \frac{1}{4\cdot\pi}\cdot\left[\frac{(x+a)}{r_2^{\,2}} - \frac{(x-a)}{r_1^{\,2}}\right] \tag{B-55}$$

$$I,y = \frac{1}{4\cdot\pi}\cdot\left(\frac{y}{r_2{}^2} - \frac{y}{r_1{}^2}\right) \tag{B-56}$$

$$I,yy = \frac{1}{4\cdot\pi}\cdot\left(\frac{1}{r_2{}^2} - \frac{2y^2}{r_2{}^4} - \frac{1}{r_1{}^2} + \frac{2y^2}{r_1{}^4}\right) \tag{B-57}$$

For II terms,

$$II = \frac{1}{4\cdot\pi}\left(\operatorname{atan}\left(\frac{y}{x-a}\right) - \operatorname{atan}\left(\frac{y}{x+a}\right)\right) \tag{B-58}$$

$$II,y = \frac{1}{4\cdot\pi}\left(\frac{x-a}{r_1{}^2} - \frac{x+a}{r_2{}^2}\right) \tag{B-59}$$

$$II,yy = \frac{1}{4\cdot\pi}\left[\frac{-2(x-a)\cdot y}{r_1{}^4} + \frac{2(x+a)\cdot y}{r_2{}^4}\right] \tag{B-60}$$

Crack-Tip Element

From Equations (3-51) and (3-52),

$$\mathrm{I} = \frac{1}{4\pi}\int_0^{2a} \frac{x-\xi}{(x-\xi)^2+y^2}\cdot\sqrt{\frac{\xi}{a}}\,\mathrm{d}\xi \tag{B-61}$$

$$\mathrm{II} = \frac{1}{4\pi}\int_0^{2a} \frac{y}{(x-\xi)^2+y^2}\cdot\sqrt{\frac{\xi}{a}}\,\mathrm{d}\xi \tag{B-62}$$

By analytical integration, we can obtain

$$I := \frac{1}{4\pi\sqrt{2a}}\cdot\left[-4\cdot\sqrt{a} - \frac{1}{2}\cdot\sqrt{r+x}\cdot\log\left[\frac{2a - 2\sqrt{a\cdot(r+x)} + r}{2a + 2\sqrt{a\cdot(r+x)} + r}\right] + \sqrt{r-x}\cdot\arctan\left[\frac{2\sqrt{a\cdot(r-x)}}{r-2a}\right]\right] \tag{B-63}$$

$$II := \frac{1}{4\pi\sqrt{2a}}\cdot\left[\frac{y}{2\cdot\sqrt{r+x}}\cdot\log\left[\frac{2a - 2\sqrt{a\cdot(r+x)} + r}{2a + 2\sqrt{a\cdot(r+x)} + r}\right] + \frac{y}{\sqrt{r-x}}\cdot\arctan\left[\frac{2\sqrt{a\cdot(r-x)}}{r-2a}\right]\right] \tag{B-64}$$

where $r = \sqrt{x^2+y^2}$

APPENDIX C
SOLUTIONS OF ONE-DIMENSIONAL VISCOELASTIC PROBLEMS

Viscoelastic Material under Continuous Sine Stress

A viscoelastic material is subjected to the uniaxial tensile stress. The time-dependent function of the tensile stress is in a continuous sine function as follows:

$$\sigma(t) = \sigma_0 \sin \omega t \tag{C-1}$$

The corresponding Laplace transformed stress is

$$\overline{\sigma}(s) = \sigma_0 (\frac{\omega}{s^2 + \omega^2}) \tag{C-2}$$

The strain response induced by the stress becomes

$$\overline{\varepsilon}(s) = \overline{\sigma}(s) \cdot s\overline{D}(s) \tag{C-3}$$

Apply the Burgers viscoelastic model as the material compliance:

$$s\overline{D}(s) = \frac{1}{R_1} + \frac{1}{\eta_1 s} + \frac{1}{\eta_2 (s + R_2/\eta_2)} \tag{C-4}$$

Thus,

$$\overline{\varepsilon}(s) = \sigma_0 (\frac{\omega}{s^2 + \omega^2}) \cdot \left[\frac{1}{R_1} + \frac{1}{\eta_1 s} + \frac{1}{\eta_2 (s + R_2/\eta_2)} \right] \tag{C-5}$$

The transformed strain is then inverted to the solution in the time variable:

$$\varepsilon(t) := \sigma_0 \cdot \left[\frac{1}{R_1} \cdot \sin(\omega \cdot t) + \frac{1}{\eta_1 \cdot \omega} \cdot (1 - \cos(\omega \cdot t)) + \frac{1}{\eta_2 \cdot \left(\omega^2 + \alpha^2\right)} \cdot \left(\alpha \cdot \sin(\omega \cdot t) - \omega \cdot \cos(\omega \cdot t) + \omega \cdot e^{-\alpha \cdot t}\right) \right] \tag{C-6}$$

where $\alpha = R_2/\eta_2$

If only creep strain is interested, only the compliance of the Maxwell dashpot is used

$$s\overline{D}_p(s) = \frac{1}{\eta_1 s} \tag{C-7}$$

And the result of time-dependent strain becomes

$$\varepsilon_p(t) = \frac{\sigma_0}{\eta_1 \omega}(1\text{-}\cos\omega t) \tag{C-8}$$

Viscoelastic Material under a Half-Sine Stress

For a single half-sine stress

$$\sigma_{1\text{-cycle}}(t) = \sigma(t) + H(t\text{-}T)\,\sigma(t\text{-}T) \tag{C-9}$$

where T is the period of one half sine, T = π/ω

$$\sigma_{1\text{-cycle}}(t) = \sigma_0 \sin\omega\, t + H(t\text{-}T)\,\sigma_0 \sin\omega(t\text{-}T) \tag{C-10}$$

The Laplace transformed version of the half sine stress is

$$\overline{\sigma}_{1-\text{cycle}}(s) = \overline{\sigma}(s) + e^{-sT}\overline{\sigma}(s) \tag{C-11}$$

$$\overline{\sigma}_{1-\text{cycle}}(s) = \sigma_0\left(\frac{\omega}{s^2+\omega^2}\right)(1+e^{-sT}) \tag{C-12}$$

The strain response induced by this stress in transformed variable is written as

$$\overline{\varepsilon}_{1\text{-cycle}}(s) = \sigma_0\left(\frac{\omega}{s^2+\omega^2}\right)\cdot\left[\frac{1}{R_1}+\frac{1}{\eta_1 s}+\frac{1}{\eta_2(s+R_2/\eta_2)}\right](1+e^{-sT}) \tag{C-13}$$

The transformed strain is then inverted to the solution in the time variable:

$$\varepsilon_{1\text{-cycle}}(t) = \varepsilon(t) + H(t\text{-}T)\,\varepsilon(t\text{-}T) \tag{C-14}$$

where $\varepsilon(t)$ is the solution of strain in the case of continuous sine stress: (C-15)

$$\varepsilon(t) := \sigma_0\cdot\left[\frac{1}{R_1}\cdot\sin(\omega\cdot t) + \frac{1}{\eta_1\cdot\omega}\cdot(1-\cos(\omega\cdot t)) + \frac{1}{\eta_2\cdot(\omega^2+\alpha^2)}\cdot\left(\alpha\cdot\sin(\omega\cdot t) - \omega\cdot\cos(\omega\cdot t) + \omega\cdot e^{-\alpha\cdot t}\right)\right]$$

APPENDIX D
DAMAGE ACCUMULATION AND CRACK GROWTH

Single Haversine Load

A linear viscoelastic material is subjected to a one-dimensional uniform tensile stress field. First, consider the tensile stress in a sine function, the time-dependent stress is written as

$$\sigma(t) = \sigma_0 \sin \omega t \qquad \text{(D-1)}$$

where σ_0 is the amplitude of tensile stress, $\omega = \pi/T$ is the radial frequency, and T is the period of the sine function from 0 to π.

The sine stress function in transform domain is

$$\sigma(t) = \sigma_0 \sin \omega t \qquad \rightarrow \qquad \bar{\sigma}(s) = \sigma_0 \left(\frac{\omega}{s^2 + \omega^2}\right) \qquad \text{(D-2)}$$

where s is the transform variable.

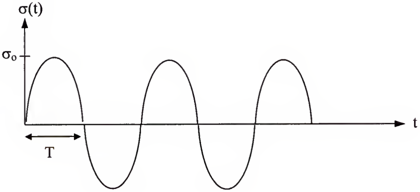

Figure D-1. Stress in Sine Function.

A haversine stress function can be obtained by imposing the sine stress function with another identical sine stress function at the period of T. This superposition is shown in Figure D-2. The haversine stress functions in time domain and transform domain are written as

$$\sigma(t) = \sigma_0 \sin \omega t + \sigma_0 \sin \omega(t-T) \cdot H(t-T) \tag{D-3}$$

$$\bar{\sigma}(s) = \sigma_0 \left(\frac{\omega}{s^2+\omega^2}\right) + \sigma_0 \left(\frac{\omega}{s^2+\omega^2}\right) e^{(-sT)} \tag{D-4}$$

where H(t-T) is a unit step function.

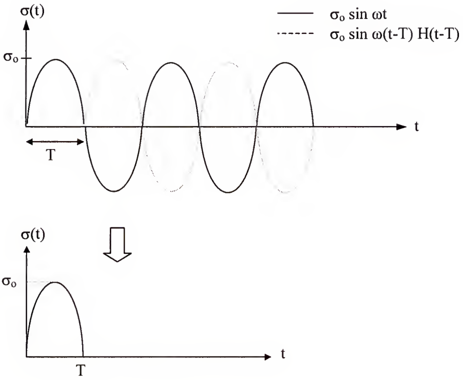

Figure D-2. Haversine Stress Function.

The total strain response due to the haversine stress function is obtained by utilizing the stress-strain relation:

$$\varepsilon(t) = \int_0^t J(t-\tau) \frac{\partial}{\partial t}\sigma(\tau)\, d\tau \quad \rightarrow \quad \bar{\varepsilon}_A(s) = \bar{J}(s) \cdot s\, \bar{\sigma}_A(s) \tag{D-5}$$

If the Burgers linear viscoelastic model is used to represent the material, the transform compliance is in the following form:

$$\bar{J}(s)\cdot s = \frac{1}{R_1} + \frac{1}{\eta_1 s} + \frac{1}{\eta_2 (s + R_2/\eta_2)} \tag{D-6}$$

where R_1, R_2, η_1, η_2 are coefficients of springs and dashpots in the Burgers model.

The total strain in transform domain is obtained by substituting $\bar{J}(s)\cdot s$ and $\bar{\sigma}_A(s)$ into (D-5).

$$\bar{\varepsilon}_A(s) = [\sigma_0 (\frac{\omega}{s^2+\omega^2}) + \sigma_0 (\frac{\omega}{s^2+\omega^2})\, e^{(-sT)}]\, [\frac{1}{R_1} + \frac{1}{\eta_1 s} + \frac{1}{\eta_2 (s + R_2/\eta_2)}] \tag{D-7}$$

$$\bar{\varepsilon}_A(s) = (1+e^{-sT})[\frac{\sigma_0}{R_1}\frac{\omega}{s^2+\omega^2} + \frac{\sigma_0}{\eta_1 s}\frac{\omega}{s^2+\omega^2} + \sigma_0 \frac{1}{\eta_2(s+R_2/\eta_2)}\frac{\omega}{s^2+\omega^2}] \tag{D-8}$$

The total strain in time domain is then obtained by taking the Lapace inversion of the above equation to arrive at

$$\varepsilon(t) = \frac{\sigma_0}{R_1}\sin \omega t + \frac{\sigma_0}{\eta_1 \omega}(1-\cos \omega t) + \frac{1}{\eta_2(\omega^2+\alpha^2)}(\alpha \sin \omega t - \omega \cos \omega t + \omega\, e^{-\alpha t}) +$$

$$H(t\text{-}T)\{\frac{\sigma_0}{R_1}\sin \omega(t\text{-}T) + \frac{\sigma_0}{\eta_1 \omega}[1-\cos \omega(t\text{-}T)] +$$

$$\frac{1}{\eta_2(\omega^2+\alpha^2)}[\alpha \sin \omega(t\text{-}T) - \omega \cos \omega(t\text{-}T) + \omega\, e^{-\alpha(t\text{-}T)}]\} \tag{D-9}$$

where $\alpha = R_2/\eta_2$

A reduced form of the above equation becomes

$$0 \le t \le T,\quad \varepsilon(t) = \frac{\sigma_0}{R_1}\sin \omega t + \frac{\sigma_0}{\eta_1 \omega}(1-\cos \omega t) + \frac{1}{\eta_2(\omega^2+\alpha^2)}(\alpha \sin \omega t - \omega \cos \omega t + \omega\, e^{-\alpha t})$$

$$t \ge T,\qquad \varepsilon(t) = \frac{2\sigma_0}{\eta_1 \omega} + \frac{\omega}{\eta_2(\omega^2+\alpha^2)}(1+e^{\alpha T})\, e^{-\alpha t} \tag{D-10}$$

The stress and strain functions of one haversine cycle are shown in Figure D-3. The permanent strain component, $\varepsilon_p(t)$, in the total strain is obtained by taking the limit of the total strain at $t \to \infty$.

$$\varepsilon_p(t) = \lim_{t\to\infty} \varepsilon(t) = \frac{2\sigma_0}{\eta_1\omega}, \quad t \geq T \qquad \text{(D-11)}$$

In other words, the permanent strain is the strain that is produced by the external dashpot element in the Burgers model. This dashpot element is the representative of the permanent response of the linear viscoelastic material. The permanent strain component during the time 0 and T should have the following form:

$$\varepsilon_p(t) = \frac{\sigma_0}{\eta_1\omega}(1-\cos\omega t), \qquad 0 \leq t < T. \qquad \text{(D-12)}$$

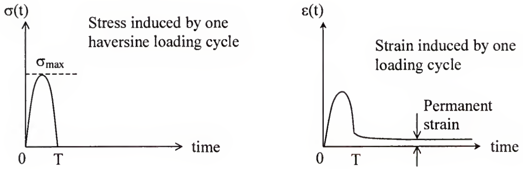
σ(t)
Stress induced by one haversine loading cycle
σmax
0
T
time
ε(t)
Strain induced by one loading cycle
Permanent strain
0
T
time

Figure D-3. Stress and Strain Induced by a Single Haversine Load.

The dissipated creep strain energy induced by a cycle of haversine stress is determined by

$$W_p(t) = \int_0^t \sigma(\tau)\,\dot{\varepsilon}_p(\tau)\,d\tau \qquad t \geq T \qquad \text{(D-13)}$$

where $\dot{\varepsilon}_p(\tau)$ is the rate of permanent strain, $\dot{\varepsilon}_p(t) = \frac{\partial}{\partial t}\varepsilon_p(t)$.

The integral can be separated into two parts: the period before and after the time T.

$$W_p(t) = \int_0^T \sigma(\tau)\,\dot{\varepsilon}_p(\tau)\,d\tau + \int_T^t \sigma(\tau)\,\dot{\varepsilon}_p(\tau)\,d\tau \tag{D-14}$$

Since $\sigma(t) = 0$ and $\frac{\partial}{\partial t}\varepsilon_p(t) = 0$ at $t \geq T$, thus the above equation reduces to

$$W_p(t) = \int_0^T \sigma(\tau)\,\dot{\varepsilon}_p(\tau)\,d\tau, \qquad t \geq T$$

$$W_p(t) = \int_0^T \sigma_0 \sin \omega\tau \,\frac{\partial}{\partial t}\left[\frac{\sigma_0}{\eta_1 \omega}(1-\cos \omega\tau)\right] d\tau, \qquad t \geq T$$

$$W_p(t) = \int_0^T \sigma_0 \sin \omega\tau \left(\frac{\sigma_0}{\eta_1} \sin \omega\tau\right) d\tau, \qquad t \geq T$$

$$W_p(t) = \frac{\sigma_0^2}{\eta_1}\left[\frac{\tau}{2} - \frac{\sin \omega\tau \cdot \cos \omega\tau}{2\omega}\right]_{\tau=0}^{\tau=T}, \qquad t \geq T$$

$$W_p(t) = \frac{\sigma_0^2}{\eta_1}\frac{T}{2}, \qquad t \geq T \tag{D-15}$$

This means the dissipated creep strain energy, $W_p(t)$, induced by a haversine stress remains the same amount even after the period of haversine, i.e. it is an unrecoverable product.

Cyclic Haversine Loads

The cyclic haversine stress function is used to represent the action of repeated loads. It is written in the following form:

$$\sigma(t) = \sigma_0 \left[\sin \omega t + \sin \omega(t-T)\cdot H(t-T)\right] +$$

$$\sigma_0\,[\sin\omega(t-\Delta t)\cdot H(t-\Delta t)+\sin\omega(t-\Delta t-T)\cdot H(t-\Delta t-T)]\;+$$

$$\sigma_0\,[\sin\omega(t-2\cdot\Delta t)\cdot H(t-2\cdot\Delta t)+\sin\omega(t-2\cdot\Delta t-T)\cdot H(t-2\cdot\Delta t-T)]+\ldots \qquad \text{(D-16)}$$

where Δt is the shifted period between each haversine cycle. Figure D-4 illustrates the characteristic of the cyclic haversine stress. The stress function in transform domain becomes

$$\bar{\sigma}(s)=\sigma_0\left(\frac{\omega}{s^2+\omega^2}\right)[1+e^{-sT}]\;+$$

$$\sigma_0\left(\frac{\omega}{s^2+\omega^2}\right)[1+e^{-sT}]\,e^{-s\Delta t}\;+$$

$$\sigma_0\left(\frac{\omega}{s^2+\omega^2}\right)[1+e^{-sT}]\,e^{-s2\Delta t}+\ldots \qquad \text{(D-17)}$$

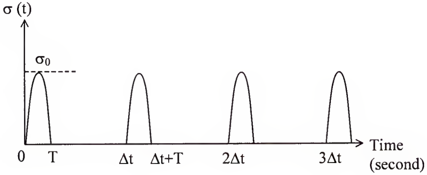

Figure D-4. Stress Function of Cyclic Haversine Loading

The transform total strain response to the cyclic haversine stress can be obtained

$$\bar{\varepsilon}(s)=\bar{J}(s)\cdot s\,\bar{\sigma}_A(s)$$

$$\bar{\varepsilon}(s)=\left[\sigma_0\left(\frac{\omega}{s^2+\omega^2}\right)(1+e^{-sT})\right]\left[\frac{1}{R_1}+\frac{1}{\eta_1 s}+\frac{1}{\eta_2(s+R_2/\eta_2)}\right]+$$

$$\left[\sigma_0\left(\frac{\omega}{s^2+\omega^2}\right)(1+e^{-sT})\,e^{-s\Delta t}\right]\left[\frac{1}{R_1}+\frac{1}{\eta_1 s}+\frac{1}{\eta_2(s+R_2/\eta_2)}\right]+$$

$$[\sigma_0 (\frac{\omega}{s^2+\omega^2})\ (1+e^{-sT})\ e^{-s\,2\Delta t}\ ]\ [\frac{1}{R_1}+\frac{1}{\eta_1 s}+\frac{1}{\eta_2(s+R_2/\eta_2)}]+\ldots$$

$$\bar{\varepsilon}\,(s) = (1+e^{-sT})[\frac{\sigma_0}{R_1}\ \frac{\omega}{s^2+\omega^2}+\frac{\sigma_0}{\eta_1 s}\ \frac{\omega}{s^2+\omega^2}+\sigma_0\ \frac{1}{\eta_2(s+R_2/\eta_2)}\ \frac{\omega}{s^2+\omega^2}]+$$

$$e^{-s\Delta t}(1+e^{-sT})[\frac{\sigma_0}{R_1}\ \frac{\omega}{s^2+\omega^2}+\frac{\sigma_0}{\eta_1 s}\ \frac{\omega}{s^2+\omega^2}+\sigma_0\ \frac{1}{\eta_2(s+R_2/\eta_2)}\ \frac{\omega}{s^2+\omega^2}]+$$

$$e^{-s\,2\Delta t}(1+e^{-sT})[\frac{\sigma_0}{R_1}\ \frac{\omega}{s^2+\omega^2}+\frac{\sigma_0}{\eta_1 s}\ \frac{\omega}{s^2+\omega^2}+\sigma_0\ \frac{1}{\eta_2(s+R_2/\eta_2)}\ \frac{\omega}{s^2+\omega^2}]+\ldots \tag{D-18}$$

The total strain in time domain is then obtained by taking the Lapace inversion of the above equation to arrive at

$$0\le t\le T,\quad \varepsilon(t) = \frac{\sigma_0}{R_1}\sin\omega t+\frac{\sigma_0}{\eta_1\omega}(1-\cos\omega t)+\frac{1}{\eta_2(\omega^2+\alpha^2)}(\alpha\sin\omega t-\omega\cos\omega t+\omega\, e^{-\alpha t})$$

$$T\le t\le \Delta t,\quad \varepsilon(t) = \frac{2\sigma_0}{\eta_1\omega}+\frac{\omega}{\eta_2(\omega^2+\alpha^2)}(1+e^{\alpha T})\, e^{-\alpha t}$$

$$\Delta t\le t\le \Delta t+T,\quad \varepsilon(t) = [\frac{2\sigma_0}{\eta_1\omega}+\frac{\omega}{\eta_2(\omega^2+\alpha^2)}(1+e^{\alpha T})\, e^{-\alpha t}]+[\frac{\sigma_0}{R_1}\sin\omega(t\text{-}\Delta t)$$

$$+\frac{\sigma_0}{\eta_1\omega}(1-\cos\omega(t\text{-}\Delta t))+\frac{1}{\eta_2(\omega^2+\alpha^2)}(\alpha\sin\omega(t\text{-}\Delta t)-\omega\cos\omega(t\text{-}\Delta t)+\omega\, e^{-\alpha(t-\Delta t)})]$$

$$\Delta t+T\le t\le 2\Delta t,\quad \varepsilon(t) = [\frac{2\sigma_0}{\eta_1\omega}+\frac{\omega}{\eta_2(\omega^2+\alpha^2)}(1+e^{\alpha T})\, e^{-\alpha t}]+$$

$$[\frac{2\sigma_0}{\eta_1\omega}+\frac{\omega}{\eta_2(\omega^2+\alpha^2)}(1+e^{\alpha T})\, e^{-\alpha(t-\Delta t)}] \tag{D-19}$$

From the above equation, the total strain response is actually the result of superposition of individual haversine total strain at different time shifting (Δt, 2Δt, 3Δt,

…). Figure D-5 illustrates the total strain response and its superposition components. This superposition method is called the Boltzmann's superposition principle (Findley et al. 1976).

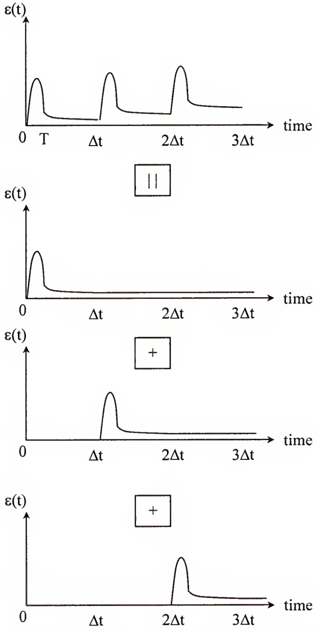

Figure D-5. History of Strain is Composed of a Superposition of Individual Strains Induced at Different Time.

Now considering the permanent strain induced by the cyclic haversine stress, the permanent strain function can be extracted from the total strain function by considering only the η_1 terms.

$$0 \leq t \leq T, \quad \varepsilon_p(t) = \frac{\sigma_0}{\eta_1 \omega}(1 - \cos \omega t)$$

$$T \leq t \leq \Delta t, \quad \varepsilon_p(t) = \frac{2\sigma_0}{\eta_1 \omega}$$

$$\Delta t \leq t \leq \Delta t + T, \quad \varepsilon_p(t) = [\frac{2\sigma_0}{\eta_1 \omega}] + [\frac{\sigma_0}{\eta_1 \omega}(1 - \cos \omega(t - \Delta t))]$$

$$\Delta t + T \leq t \leq 2\Delta t, \quad \varepsilon_p(t) = \frac{2\sigma_0}{\eta_1 \omega} + \frac{2\sigma_0}{\eta_1 \omega} \qquad \text{(D-20)}$$

and so on.

The dissipated creep strain energy after multiple haversine cycles is determined as follows:

$$W_p(t) = \int_0^t \sigma(\tau)\, \dot{\varepsilon}_p(\tau)\, d\tau$$

Since $\sigma(t) = 0$ and $\frac{\partial}{\partial t}\varepsilon_p(t) = 0$ outside the haversine load period, the above integral can be reduced to

$$W_p(t) = \int_0^T \sigma(\tau)\, \dot{\varepsilon}_p(\tau)\, d\tau + \int_{\Delta t}^{\Delta t + T} \sigma(\tau)\, \dot{\varepsilon}_p(\tau)\, d\tau + \int_{2\Delta t}^{2\Delta t + T} \sigma(\tau)\, \dot{\varepsilon}_p(\tau)\, d\tau + \ldots \qquad \text{(D-21)}$$

$$W_p(t) = \int_0^T \sigma_0 \sin \omega\tau \, \frac{\sigma_0}{\eta_1} \sin \omega\tau \, d\tau + \int_{\Delta t}^{\Delta t + T} \sigma_0 \sin \omega(\tau - \Delta t) \, \frac{\sigma_0}{\eta_1} \sin \omega(\tau - \Delta t) \, d\tau +$$

$$\int_{2\Delta t}^{2\Delta t+T} \sigma_0 \sin \omega(\tau-2\Delta t) \frac{\sigma_0}{\eta_1} \sin \omega(\tau-2\Delta t)\, d\tau + \ldots \qquad \text{(D-22)}$$

$$W_p(t) = \int_0^T \sigma_0 \sin \omega\tau \frac{\sigma_0}{\eta_1} \sin \omega\tau\, d\tau + \int_0^T \sigma_0 \sin \omega\tau \frac{\sigma_0}{\eta_1} \sin \omega\tau\, d\tau +$$

$$\int_0^T \sigma_0 \sin \omega\tau \frac{\sigma_0}{\eta_1} \sin \omega\tau\, d\tau + \ldots \qquad \text{(D-23)}$$

$$W_p(t) = \frac{\sigma_0^2}{\eta_1} \frac{T}{2} + \frac{\sigma_0^2}{\eta_1} \frac{T}{2} + \frac{\sigma_0^2}{\eta_1} \frac{T}{2} + \ldots \qquad \text{(D-24)}$$

Hence, the total dissipated creep strain energy is a summation of individual dissipated creep strain energy.

Crack Geometry Change

Since the solutions of the viscoelastic boundary value problem is applicable to the correspondence principle only if the traction and displacement boundaries remain unchanged. It also infers that a boundary extension, i.e. crack growth, during the period of loading is omitted. But since the dissipated creep strain energy induced by a load cycle completes at the end of haversine period and remains constant after worth, we only need to employ the correspondence principle during the loading period to obtain the amount of DCSE induced by that individual load cycle. During the resting period, the individual DCSE is added to the total DCSE, and a stepwise crack growth can be made without breaking the correspondence principle.

Let us assume that the geometry of the crack is changed immediately after the load cycle of N. Considering a location A away from the crack, the total dissipated creep strain energy at this location that has been induced by the haversine loads from cycle 1 to N before the crack growth is

$$W_p(t) = \int_0^T \sigma_0 \sin \omega\tau \, \frac{\sigma_0}{\eta_1} \sin \omega\tau \, d\tau + \int_{\Delta t}^{\Delta t+T} \sigma_0 \sin \omega(\tau-\Delta t) \, \frac{\sigma_0}{\eta_1} \sin \omega(\tau-\Delta t) \, d\tau +$$

$$\int_{2\Delta t}^{2\Delta t+T} \sigma_0 \sin \omega(\tau-2\Delta t) \, \frac{\sigma_0}{\eta_1} \sin \omega(\tau-2\Delta t) \, d\tau + \ldots +$$

$$\int_{N\Delta t}^{N\Delta t+T} \sigma_0 \sin \omega(\tau-N\Delta t) \, \frac{\sigma_0}{\eta_1} \sin \omega(\tau-N\Delta t) \, d\tau \qquad \text{(D-25)}$$

$$W_p(t) \text{ after the } N^{th} \text{ cycle} = \sum_{i=1}^{N} \frac{\sigma_0^2}{\eta_1} \frac{T}{2} \qquad \text{(D-26)}$$

where T is a constant representing the period of a haversine load.

The above equation suggests that the total DCSE is permanent and stays unchanged with time, thus it is now taken as the initial condition under the new crack geometry. For the load cycle after the crack growth, the dissipated creep strain energy is calculated by

$$W_p(t) = \sum_{i=1}^{N} \frac{\sigma_0^2}{\eta_1} \frac{T}{2} + \int_{(N+1)\Delta t}^{t} \sigma(\tau - (N+1)\Delta t) \; \dot{\varepsilon}_p(\tau - (N+1)\Delta t) \, d\tau \qquad \text{(D-27)}$$

Figure D-6 illustrates the total strain response and the total dissipated creep strain energy before and after the crack growth.

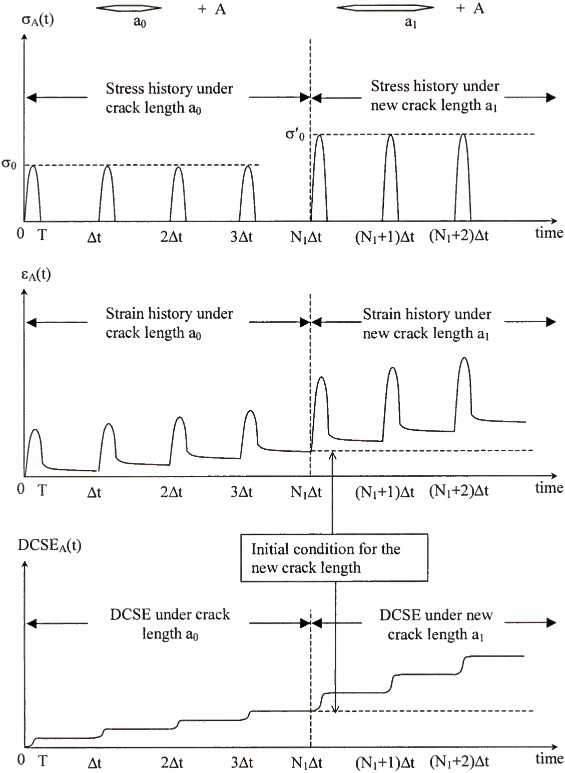

Figure D-6. Strain and total DCSE Under the Current Crack Geometry is Composed of Strain History of the Previous Crack Geometry.

LIST OF REFERENCES

ABAQUS Standard User Manual version 6.2. Hibbitt, Karlsson & Sorensen, Inc., Pawtucket, RI, 2001.

ADINA Software Program, a product of ADINA R & D, Inc., more details in http://www.adina.com, accessed March 2003.

Anderson, T.L. Fracture Mechanics Fundamentals and Applications. 2nd Edition. CRC Press, New York, 1995.

Atkinson, K.E. An Introduction to Numerical Analysis. 2nd Edition. John Wiley & Sons, New York, 1989.

Birgisson, B. A Two-Dimensional Dynamic Direct Boundary Element Method for Piecewise Homogeneous Elastic Media. Ph.D. Dissertation, University of Minnesota, Minneapolis, MN, 1996, 231p.

Birgisson, B., and S.L. Crouch. Elastodynamic Boundary Element Method for Piecewise Homogeneous Media. International Journal for Numerical Methods in Engineering, Vol. 42, 1998, pp. 1045-1069.

Birgisson, B., R. Roque, B. Sangpetngam, and Z. Zhang. Hot Mix Asphalt Fracture Mechanics: A Fundamental Crack Growth Law for Asphalt Mixtures. Journal of the Association of Asphalt Paving Technologists, Vol. 71, 2002b. (Accepted).

Birgisson, B., B. Sangpetngam, and R. Roque. Prediction of the Viscoelastic Response and Crack Growth in Asphalt Mixtures Using the Boundary Element Method. Transportation Research Record, Vol. 1789, 2002a, pp. 129-135.

Birgisson, B., C. Soranakom, J.A.L. Napier, and R. Roque. Simulation of the Cracking Behavior of Asphalt Mixtures Using Random Assemblies of Displacement Discontinuity Boundary Elements. 15th ASCE Engineering Mechanics Conference, Columbia University, New York, 2002c.

Birgisson, B., C. Soranakom, J.A.L. Napier, and R. Roque. Modeling of Microstructure and Fracture Behavior of Asphalt Mixtures Using a Boundary Element Approach. ASCE Journal of Civil Engineering Materials, in press 2003.

Bobet, A., and H.H. Einstein. Numerical Modeling of Fracture Coalescence in a Model Rock Material. International Journal of Fracture, Vol. 92, No. 3, 1999, pp.221-252.

Broek, D. Elementary Engineering Fracture Mechanics fourth revised edition. Kluwer Academic Publishers, Hingham, MA, 1986.

Buttlar, W.G., and R. Roque. Development and Evaluation of the Strategic Highway Research Program Measurement and Analysis System for Indirect Tensile Testing at Low Temperatures. Transportation Research Record, Vol. 1454, 1994, pp.163-171.

Cooper, K.E., and P.S. Pell. The Effect of Mix Variables on the Fatigue Strength of Bituminous Materials, LR663, Transport and Road Research Laboratory, U.K. 1974.

Crawford, A.M., and J.H. Curran. Higher-Order Functional Variation Displacement Discontinuity Elements. International Journal of Rock Mechanics and Mining Sciences & Geomechanics Abstracts, Vol. 19, 1982, p.143-148.

Crawford, A.M., and J.H. Curran. A Displacement Discontinuity Approach to Modeling the Creep Behavior of Rock and its Discontinuities. International Journal for Numerical and Analytical Methods in Geomechanics, Vol. 7, 1983, p. 245-268.

Crouch, S.L. Analysis of Stresses and Displacements Around Underground Excavations: An Application of the Displacement Discontinuity Method. Geomechanics Report to the National Science Foundation, University of Minnesota, Minneapolis, MN, 1976.

Crouch, S.L., and A.M. Starfield. Boundary Element Methods in Solid Mechanics. Unwin Hyman Inc., Cambridge, MA, 1990.

Crump K. S. Numerical inversion of Laplace transforms using a Fourier series approximation. Journal of the Association for Computing Machinery, Vol. 23, 1976, p. 89-96.

Findley, W.N., J.S. Lai, and K. Onaran. Creep and Relaxation of Nonlinear Viscoelastic Materials with an Introduction to Linear Viscoelasticity. Dover Publications, Inc., New York, 1976.

Flugge W. Viscoelasticity (2nd edition). Springer-Verlag, New York, 1975.

Garcia, O.F. Asphalt Mixture and Loading Effects on Surface-Cracking of Pavements. Master's thesis, University of Florida, Gainesville, FL, 2002.

Gomez, M., and M.R. Thompson. Mechanistic Design Concepts for Full Depth Asphalt Concrete Pavements, Civil Engineering Studies, Transportation Engineering Series No.41, University of Illinois at Urbana-Champaign, 1984.

Guzina, B.B. On the Analysis of Wave Motions in a Multi-Layered Solid. Quarterly Journal of Mechanics and Applied Mathematics, Vol. 54, No. 1, 2001, pp. 13-37.

Haddad, Y.M. Viscoelasticity of Engineering Materials. Chapman & Hall, New York, 1995.

Honeycutt, K.E. Effect of Gradation and Other Mixture Properties on the Cracking Resistance of Asphalt Mixtures. Master's thesis, University of Florida, Gainesville, FL, 2000, 158pp.

IMSL Fortran Mathematical Library, a product of Visual Numerics, Inc., more details in http://www.vni.com, accessed April 2003.

Jacobs, M.M.J., P.C. Hopman, and A.A.A. Molenaar. Application of Fracture Mechanics Principles to Analyze Cracking in Asphalt Concrete. Journal of the Association of Asphalt Paving Technologists, Vol.65, 1996, pp.1-39.

Jajliardo, A. Development of Specification Criteria to Mitigate Top-Down Cracking. Master's thesis, University of Florida, Gainesville, FL, 2003.

Kim, Y.R., H-J. Lee, and D.N. Little. Fatique Characterization of Asphalt Concrete Using Viscoelasticity and Continuum Damage Theory, Journal of the Association of Asphalt Paving Technologists, Vol. 66, 1997, pp. 520-569.

Komoriya, K., T. Yoshida, and H. Nitta. "WA-DA-CHI-WA-RE" Surface Longitudinal Cracks on Asphalt Concrete Pavement. In 80th Annual Meeting (CD-ROM), TRB, National Research Council, Washington, DC, 2001, paper number TRB 01-0432.

Lee, H.J., J.S. Daniel, and Y.R. Kim. Laboratory Performance Evaluation of Modified Asphalt Mixtures for Inchon Airport Pavements, Intern. J. Pavement Engineering, Vol. 1, No. 2, 2000, pp.151-169.

Lee, H.J., and Y.R. Kim. Viscoelastic Constitutive Model for Asphalt Concrete under Cyclic Loading, Journal of Engineering Mechanics, Vol. 124, No. 1, 1998a, pp. 32-40.

Lee, H.J., and Y.R. Kim. Viscoelastic Continuum Damage Model of Asphalt Concrete with Healing, Journal of Engineering Mechanics, Vol. 124, No. 11, 1998b, pp. 1224-1232.

Love, A.E.H. A Treatise on a Mathematical Theory of Elasticity. 4th Edition. Dover, New York, 1944.

LSDYNA Software Program, a product of Livermore Software Technology Corporation, Livermore CA, more details in http://www.lstc.com, accessed March 2003.

Maron, M.J. Numerical Analysis A Practical Approach. 2nd Edition. Macmillan Publishing Company, New York, 1987.

Monismith, C.L., and J.A. Epps. Asphalt mixture Behavior in Repeated Flexure. In Transportation and Traffic Engineering, University of California, Berkeley, CA, 1969.

Myers, L.A. Development and Propagation of Surface-Initiated Longitudinal Wheel Path Cracks in Flexible Highway Pavements. Ph.D. Dissertation, University of Florida, Gainesville, FL, 2000.

Myers, L.A., R. Roque, and B. Birgisson. Propagation Mechanisms for Surface-Initiated Longitudinal Wheel Path Cracks. In 80th Annual Meeting (CD-ROM), TRB, National Research Council, Washington, D.C., 2001, paper number TRB 01-0433.

Myre, J. Fatigue of Asphalt Pavements. In Proceedings, Third International Conference on Bearing Capacity of Roads and Airfields, the Norwegian Institute of Technology, Tapir, 1990.

Napier, J.A.L. Numerical Studies of Time-Dependent Failure and Implications for the Predictions of Time to Failure. In Proc., 37th U.S. Rock Mechanics Symposium, Vail, CO, 1999, pp. 911-917.

Narayanan, G.V., and D.E. Beskos. Numerical Operational Methods for Time-Dependent Linear Problems. International Journal for Numerical Methods in Engineering, Vol. 18, 1982, pp.1829-1854.

Newcomb, D.E., A.A. Bu-bushait, J.P. Mahoney, and J. Sharma. State-of-the-Art on Pavement Overlay Design Procedures, Vol.1, Report No. WA-RD 65.1, Washington State Department of Transportation, Olympia, WA, 1983.

Newcomb, D.E., Z. Wei, and M. Stroup-Gardiner. Investigation of Large Stone Mixtures. Final Report for Minnesota Department of Transportation, Report No.94-09, December 1993, 96pp.

Rauhut, J.B., R.L. Lytton, and M.I. Darter. Pavement Damage Functions for Cost Allocation – Vol.2 – Descriptions of Detailed Studies, FHWA-RD-84-019, Federal Highway Administration, Washington, DC, 1984.

Roque, R., B. Birgisson, B. Sangpetngam, and Z. Zhang. Crack Growth Behavior of Asphalt Mixtures and Its Relation to Laboratory and Field Performance. In Ninth International Conference on Asphalt Pavement, International Society for Asphalt Pavements, Copenhagen, 2002.

Roque, R., and W.G. Buttlar. The Development of a Measurement and Analysis System to Accurately Determine Asphalt Concrete Properties Using the Indirect Tensile Mode, Journal of the Association of Asphalt Paving Technologists, Vol. 61, 1992, pp. 304-332.

Roque, R., W.G. Buttlar, B.E. Ruth, M.Tia, S.W. Dickison, and B. Reid. Evaluation of SHRP Indirect Tension Tester to Mitigate Cracking in Asphalt Pavements and Overlays. Final Report to the Florida Department of Transportation. University of Florida, Gainesville, FL, August 1997, 364pp.

Roque, R., L.A. Myers and B. Birgisson. Evaluating Measured Tire Contact Stresses to Predict Pavement Response and Performance. Transportation Research Record Vol. 1716, 2000, pp. 73-81.

Roque, R., Z. Zhang, and B. Sankar. Determination of Crack Growth Rate Parameters of Asphalt Mixtures Using the Superpave Indirect Tension Test (IDT). Journal of the Association of Asphalt Paving Technologists, Vol. 68, 1999, pp. 404-433.

Sangpetngam, B., B. Birgisson, and R. Roque. Development of an Efficient Hot Mix Asphalt Fracture Mechanics-Based Crack Growth Simulator. Journal of the Transportation Research Board, in press 2003.

Schapery, R.A. Correspondence Principles and a Generalized J-Integral for Large Deformation and Fracture Analysis of Viscoelastic Media. Int. J. Fracture, Vol. 25, 1984, pp. 195-223.

Sedwick, S.C. Effect of Asphalt Mixture Properties and Characteristics on Surface-Initiated Longitudinal Wheel Path Cracking. Master thesis, University of Florida, Gainesville, FL, 1998.

Shou, K.J., and S.L.Crouch. A Higher Order Displacment Discontinuity Method for Analysis of Crack Problems. International Journal of Rock Mechanics, Minearl Science and Geomechanics Abstracts, Vol. 32, No. 1, 1995, pp. 49-55.

Siebrits, E., B. Birgisson, A.P. Peirce, and S.L. Crouch. On the Numerical Stability of Time Domain Boundary Element Methods. International Journal for Blasting and Fragmentation, Vol. 1, No. 3, 1997, pp. 305-316.

Siebrits, E., and S.L. Crouch. A Two-Dimensional Elastodynamic Displacement Discontinuity Method. International Journal of Numerical Methods in Engneering, Vol. 37, 1994, pp. 3229-3250.

Siebrits, E., H. Gu., and J. Desroches. An improved pseudo-3D hydraulic fracturing simulator for multiple layered materials. In Computer Methods and Advances in Geomechanics, Balkema, Rotterdam, 2001, pp.1341-1345.

Siebrits, E., and A.P. Peirce. Hydraulic Fracturing in Laminated Reservoirs. In Three-Dimensional and Advanced Hydraulic Fracture Modeling, Workshop Proceedings in Conjunction with 4th North American Rock Mechanics Symposium, Seattle, July 29, 2000, pp.1-12.

Sokolnikoff, I.S. Mathematical Theory of Elasticity. 2nd Edition. McGraw-Hill, New York, 1956.

Sousa, J.B., G. Way, and J. Harvey. Performance-Based Mix Design and Field Quality Control for Asphalt-Aggregate Overlays. Transportation Research Record, Vol. 1543, 1996, pp. 46-62.

Thompson, M.R. ILLI-PAVE Based Full-Depth Asphalt Concrete Pavement Design Procedure, In Proceedings, Sixth International Conference on Structural Design of Asphalt Pavements, Ann Arbor, MI, 1987.

Thompson, M.R., and K. Cation. A Proposed Full-Depth Asphalt Concrete Thickness Design Procedure, Civil Engineering Studies, Transportation Engineering Series No.45, University of Illinois at Urbana-Champaign, 1986.

Tschoegl, N.W. The Phenomenological Theory of Linear Viscoelastic Behavior: An Introduction. Springer-Verlag, New York, 1989, 769 p.

Uhlmeyer, J.S., K. Willoughby, L.M. Pierce, and J.P. Mahoney. Top-Down Cracking in Washington State Asphalt Concrete Wearing Courses. Transportation Research Record, Vol. 1730, 2000, pp. 110-116.

Zhang, Z. Identification of Suitable Crack Growth Law for Asphalt Mixtures Using the Superpave Indirect Tensile Test (IDT). Ph.D Dissertation, University of Florida, Gainesville, FL, 2000.

Zhang, Z, R. Roque, and B. Birgisson. Evaluation of Laboratory Measured Crack Growth Rate for Asphalt Mixtures. Journal of the Transportation Research Board, Vol. 1767, 2001, pp. 67-75.

Zhang, Z., R. Roque, B. Birgisson, and B. Sangpetngam. Identification and Verification of a Suitable Crack Growth Law (with Discussion). Journal of the Association of Asphalt Paving Technologists, Vol. 70, 2001, pp. 206-241.

BIOGRAPHICAL SKETCH

Boonchai Sangpetngam was born and raised by his lovely parents in Bangkok, Thailand, since 1972. In 1992, he graduated with the bachelor's degree in civil engineering from Chulalongkorn University in Thailand. After that, he worked as a civil engineer in the local companies and earned three years of experience in building construction and highway design.

In 1997, he was awarded the International Road Federation Fellowship and moved to the United States to pursue his graduate study at the University of Florida.

In his master's degree study, Boonchai and Dr. David Bloomquist, his advisor, participated in the evaluation of a rigid pavement drainage project that was sponsored by the Florida Department of Transporatation. Boonchai graduated the master's degree in civil engineering (geotechnical engineering) in spring of 1999 from the University of Florida.

Immediately after graduation, he joined the materials group at the University of Florida and worked as a graduate research assistant with his doctoral advisors, Dr. Bjorn Birgisson and Dr. Reynaldo Roque, in many sponsored research projects including evaluation of wick drain design for the western dams at Hibbing Taconite Company, evaluation of longitudinal wheel path cracking in asphalt pavement, and implementation of Superpave indirect tensile test to mitigate cracking in pavements. Boonchai is currently completing the Doctoral of Philosophy degree in civil engineering at University of Florida.

I certify that I have read this study and that in my opinion it conforms to acceptable standards of scholarly presentation and is fully adequate, in scope and quality, as a thesis for the degree of Doctor of Philosophy.

Bjorn Birgisson

Bjorn Birgisson, Chair
Assistant Professor of Civil and Coastal
Engineering

I certify that I have read this study and that in my opinion it conforms to acceptable standards of scholarly presentation and is fully adequate, in scope and quality, as a thesis for the degree of Doctor of Philosophy.

Reynaldo Roque

Reynaldo Roque, Cochair
Professor of Civil and Coastal Engineering

I certify that I have read this study and that in my opinion it conforms to acceptable standards of scholarly presentation and is fully adequate, in scope and quality, as a thesis for the degree of Doctor of Philosophy.

Mang Tia

Mang Tia
Professor of Civil and Coastal Engineering

I certify that I have read this study and that in my opinion it conforms to acceptable standards of scholarly presentation and is fully adequate, in scope and quality, as a thesis for the degree of Doctor of Philosophy.

Michael McVay

Michael C. McVay
Professor of Civil and Coastal Engineering

I certify that I have read this study and that in my opinion it conforms to acceptable standards of scholarly presentation and is fully adequate, in scope and quality, as a thesis for the degree of Doctor of Philosophy.

B Sankar

Bhavani V. Sankar
Professor of Mechanical and Aerospace
Engineering

This dissertation was submitted to the Graduate Faculty of the College of Engineering and to the Graduate School and was accepted as partial fulfillment of the requirements for the degree of Doctor of Philosophy.

May 2003

Pramod P. Khargonekar
Dean, College of Engineering

Winfred M. Phillips
Dean, Graduate School